THE UNIVERSITY *of* EDINBURGH

Friction and the Flow of Concentrated Suspensions

James Alexander Richards

Doctor of Philosophy
The University of Edinburgh
February 2020

Abstract

Suspensions are ubiquitous in industrial processing, yet fundamental understanding of how they flow remains limited. Recent progress on shear-thickening suspensions of non-Brownian particles establishes the importance of direct mechanical contact and friction between particles. This represents a paradigm shift, linking wet suspensions to dry granular materials through a static jamming volume fraction. In this thesis I explore further the implications of mechanical contact in three ways.

Firstly in time-dependent flows, I show that large shear-rate fluctuations arise from a competition between rapid microscopic contact dynamics and the slow dynamics controlling how the suspension is sheared. I develop a dynamical-systems approach that graphically shows how an instability arises, indicates how to control the instability, and allows the extraction of a contact relaxation time that is inaccessible to conventional rheometry.

Next, more complex interparticle interactions are considered. I take the relevant effect to be a stress-dependent constraint on relative interparticle motion, e.g., sliding, twisting or rolling. Constraints lower the jamming volume fraction and can either form or break with stress. I show that an interplay between two constraint types can capture all classes of flow curve, with predictions compared against my own experimental or literature data. In particular, a yield stress behaviour is reproduced for rolling constraints being broken while sliding is constrained.

Finally, I investigate the protocol dependence of yield-stress suspension rheology. The complex experimental phenomenology is shown to be consistent with an adhesively-bonded compressive frictional contact network. The yield stress is hence related to jamming and constraints, rather than just resulting from interparticle attraction. This finding continues the transition of non-Brownian

suspension rheology from the colloidal to the granular frame and suggests novel ways to tune the yielding behaviour through the interparticle friction coefficient or flow protocols.

Lay summary

Mixtures of hard solid particles in a liquid, or *suspensions*, are widely important to our everyday life. In some cases this is obvious – many products in the kitchen or bathroom are suspensions (mustard, toothpaste, ...). In other cases, the importance of suspensions is less obvious, because they are involved in the manufacturing process. Thus, the manufacturing of the paper you might be reading this thesis on, or the concrete floor you are standing on, or the mining of the metals in your computer, all rely upon suspensions. The particles in these suspensions are too small for the naked eye to see, but are far larger than the molecules of the liquid that surrounds them. For some suspensions, in the case of something like milk, the incessantly-moving liquid molecules buffet the suspended particles into their own 'Brownian' motion. This thesis deals with the case of when the suspended particles are large enough (say, bigger than a hundredth of a millimeter) that this Brownian motion is negligible. At first sight, such non-Brownian suspensions may seem to present few challenges to science and technology. In fact, they show some very odd properties, especially when we want to make them flow.

The oddness of non-Brownian suspensions is easily demonstrated in the kitchen: a concentrated mixture of cornstarch and water can be poured, stirred or 'sheared' slowly, just like a liquid. But stir faster and you will find it turns solid, or jams, and it can even fracture. On a larger scale, this phenomenon of 'shear-induced jamming' underlies the surprising demonstration of 'running across cornstarch'.

Recently, there has been a revolution in understanding how these non-Brownian suspensions flow. It turns out that when the applied stress is large enough, it can push out the thin lubricating film of liquid between particles and drive them into frictional contact. The current understanding of this process is limited to situations where the particles do not stick to each other, and also when the flow is steady. In this thesis we extend the understanding of non-Brownian

suspension flow into unsteady flows (specifically, sudden periodic jamming), and to systems in which the particles are sticky (which turns out to be the majority of cases). We establish models to treat both unsteady flows and sticky particles, before validating these models through experiment. The most general of our achievements is to propose and validate a model of suspension flow inspired by the packing of dry sticky granular materials (think of bags of flour or icing sugar). This model should be generalisable to treat a broad range of suspensions actually found in industry.

Declaration

I declare that this thesis was composed by myself, that the work contained herein is my own except where explicitly stated otherwise in the text, and that this work has not been submitted for any other degree or professional qualification except as specified.

Some of the work presented in this thesis has been published in jointly authored articles and the contribution of the candidate to these articles is explicitly stated here. The work presented in Chapter 4 has previously been published in *Physical Review Letters* as *Competing Timescales Lead to Oscillations in Shear-Thickening Suspensions* by **J. A. Richards**, J. R. Royer, B. Liebchen, B. M. Guy, and W. C. K. Poon (supervisor) [1]. This study was conceived by J. A. Richards and W. C. K. Poon. The majority of experiments were carried out by the candidate, with a minority carried out by J. R. Royer, which are clearly indicated. A first draft of the manuscript was written by the candidate.

The work presented in Chapter 6 is being prepared for publication in the *Journal of Rheology* as *The role of friction in the yielding of adhesive non-Brownian suspensions* by **J. A. Richards**, B. M. Guy, E. Blanco, M. Hermes, G. Poy, and W. C. K. Poon [2]. All experiments were carried out by the candidate.

The work presented in Chapter 8 has previously been published in *Physical Review Letters* as *Constraint-based Approach to Granular Dispersion Rheology* by B. M. Guy, **J. A. Richards**, D. J. M. Hodgson, E. Blanco, and W. C. K. Poon (supervisor) [3]. A declaration of author contributions was included: B. M. G., **J. A. R.**, E. B., and D. J. M. H. performed experiments motivating the model. **J. A. R.** and W. C. K. P. conceptualized the work. **J. A. R.** and B. M. G. performed calculations. B. M. G., **J. A. R.**, and W. C. K. P. produced the final manuscript.

(*James Alexander Richards, February 2020*)

Acknowledgements

I would like to thank all those who, without them, this thesis would not have been possible. A great thanks goes to my supervisor, Wilson Poon, whose seemingly endless scientific curiosity has been invaluable in guiding and refining this research. I also owe much to those involved with work on suspension rheology in Edinburgh, in particular Ben Guy, as our discussions helped nucleate and develop many of the ideas in this thesis. Finally, I would like to gratefully acknowledge the funding of my PhD studies by the EPSRC Centre for Doctoral Training in Soft Matter and Functional Interfaces and AkzoNobel.

Contents

Chapter 1

Introduction

Mixtures of hard micron-sized particles in a background liquid are ubiquitous in industrial processing, as they allow a solid material to take a fluid form. These "non-Brownian suspensions" of solid particles can then be used to easily and quickly form a bulk solid of the required shape through either: a chemical reaction, as for cement [4]; cooling and solidification of the background liquid, as in chocolate with a suspension of sugar in cocoa butter [5]; or simply through drying, e.g. with a ceramic green body [6]. In all cases, an accurate predictive understanding of how these suspensions flow is desired. This is to ensure that they take and retain the desired shape, or that they can be readily pumped and transported.

With a Newtonian background solvent and non-Brownian hard-spherical particles, such suspensions, may appear at first sight to be simple. Indeed, a naïve dimensional analysis says that the resistance to flow relative to that of the background solvent, or relative viscosity, at steady-state should be a function of the solid volume fraction alone and independent of the applied stress [7]. However, in practice this is far from the case, and a veritable zoo of behaviours are observed. Suspensions can increase in viscosity with stress (shear thickening), decrease (shear thinning) or possess a varied combination. At high volume fractions, suspensions can even switch between solid-like and liquid-like behaviour. To understand this variety of behaviours is challenging, because a bridging of lengthscales from the nanometric particle surface details to the macroscopic flow is needed. Arriving at such an understanding is not purely an intellectual exercise; it is also important industrially, as unintended rheological responses can lead to

damaged equipment or defective products (and angry customers).

This desire for predictive understanding also reflects the fundamental challenge of condensed matter physics: to link microscopic properties to macroscopic behaviours and enable predictions. While this process has long been understood for systems that are in thermal equilibrium, a system such as a suspension proves a particular challenge: being a driven, many-body, non-equilibrium problem. Therefore, a bottom-up theoretical approach to suspensions is currently lacking; however, this does not mean we cannot make progress. Instead, we must turn to phenomenological models, in which we take a simplified microscopic picture, derive and solve a set of equations based upon this microscopic picture and test whether this can match experiment.

A recent paradigm shift occurred in suspension rheology with the development of a phenomenological model of this kind by Wyart and Cates [8], which views shear thickening as a stress-driven transition from a frictionless or lubricated state to a frictional state with particles in direct mechanical contact. Previously, the thin fluid films between particles were seen to always prevent contact. With this new microscopic insight it is now possible to think about how to control or tune shear thickening, even if a precise theory does not exist; and it is with this philosophy of guided empiricism that we shall go forward.

The purpose of this thesis is to develop our predictive understanding of suspensions. Based upon simple microscopically motivated pictures, we aim to build upon knowledge of the steady-state rheology of well-stabilised shear-thickening suspensions towards more complex, industrially relevant situations. Thus, from bulk rheology results we hope to infer the relevant particle-level interactions. It may seem perverse, given the stated aim of the thesis, that measurements are not made at the contact level; however, such "nanotribological" measurements remain challenging and are outside the scope of this thesis.

1.1 Thesis outline

After the introductory chapters, this thesis is separated into three main parts. In the first part, we begin by looking at shear-thickening suspensions of well-stabilised particles with purely repulsive interactions. Firstly, in Ch. 3 the development and testing of the Wyart and Cates (WC) phenomenological model

is described within the context of the suspension literature. Directly following this in Ch. 4, we extend the WC model to describe time-dependent experimental systems. From this we suggest and demonstrate a simple way of tuning large-amplitude instabilities in shear-thickening systems and we additionally extend the time-dependent model to extract a contact relaxation timescale.

In Part II, we begin to consider the effect of more varied particle-particle interactions on non-Brownian suspension rheology. This part does not begin with a literature review, because little literature as yet exists treating this topic in the new particle-contact paradigm. Instead, we approach suspensions with attractive interactions from the point of view and framework developed in Part I, introducing and describing results obtained under previous paradigms as we go along.

To start, in Ch. 5 a WC-like phenomenological model is laid out based upon "adhesive" particle contacts, which stop particles rolling relative to each other and are *broken* with stress, combined with frictional contacts that are *formed* with stress. This represents a minimal extension to describe a larger variety of flow curves within the underlying principles of the WC model. In the following two chapters we then explore and test the implications of this minimally-extended model. In Ch. 6 we probe the rheological response of a model yield-stress suspension through a series of steady-state, shear reversal and oscillatory rheological tests. Combining the results we reveal that the yield stress in a non-Brownian suspension arises from a percolating compressive frictional contact network stabilised by adhesive bonds and that this structure is formed by the applied shear stress itself. In Ch. 7 we then go on to show how the effect of dispersants, or polymeric surfactants, can be described within our new model. Importantly, our results imply that the key physical effect of a dispersant is to prevent frictional contact between particles when adhesion is relevant; this then suggests design principles for dispersants.

In the final part, Part III, we return to recast the model introduced in Ch. 5 into a general form. Starting from the WC model we generalise non-Brownian suspension rheology based upon general stress-dependent constraints, interpreting friction as simply any particle interaction that constrains sliding and adhesion as any that constrain rolling. We demonstrate how a simple combination of two such stress-dependent constraints, one increasing and one decreasing with stress, capture all cases of experimentally measured flow curve in suspensions and we make predictions that we compare against literature and our own experimental

measurements.

Taken together with previous work, the results reported in this thesis, by making steps forward in the fundamental understanding and interpretation of suspension rheology, can be used to help design and tune the processing of industrially-relevant complex suspensions But, before we can begin, we must first review the fundamental experimental technique of this thesis: rheology.

Chapter 2

Rheometry of non-Brownian suspensions

Rheology, a term coined from the Greek verb, 'ῥειν', to flow, is the study of flow or deformation. This thesis is focussed on suspension rheology. More specifically, rheometry is the measurement of flow and deformation. In rheometry the aim is to to deduce constitutive relations between force and deformation using measurements in simple 'rheometric geometries' that, ideally, have homogeneous strain and stress. In application, flows are not typically rheometric, e.g. in a pipe or while mixing, but in principle the deduced constitutive relations can be applied to model the flow using, for example, finite element methods. In this section, the practical aspects of the shear rheometry techniques that are used on non-Brownian suspensions throughout this thesis will be outlined; importantly, the limitations and possible sources of error will also be addressed, as knowledge of these is necessary to be confident in the interpretation of the collected data. Unless otherwise referenced, theoretical results are quoted from Ref. [9]. We will discuss rheometry in terms of steady, or time-independent, flow; although at many points in the thesis we will also undertake dynamic measurements and the additional complications introduced will be addressed at these points. In general, fluids can exert pressure forces and also undergo extensile, as well as shear, deformation, which occurs during, e.g., extrusion. However, these quantities are challenging to measure and interpret for non-Brownian suspensions [10], requiring specially adapted rheometers [11, 12]. They are not considered in this thesis and we focus exclusively on shear rheology.

2.1 Rheometric geometries

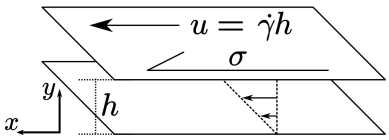

Figure 2.1 Idealised rheometric flow: shear flow between infinite sliding parallel plates. Geometry: plate separation, h, and relative velocity, u. Axes: x direction, fluid velocity; y direction, velocity gradient. Rheometric quantities: σ applied stress; $\dot{\gamma} = u/h$, shear rate.

As the experimental results and phenomenological models presented in this thesis deal only with shear, the force and deformation on a fluid element are described by only a single component shear strain, γ, and shear stress, σ. The idealised rheometric geometry is then a set of infinite sliding plates with a separation, or gap height, h, filled with the fluid or sample and with the upper plate moving at a velocity u relative to the bottom plate, Fig. 2.1. The fluid velocity is taken to be in the in x direction only, i.e. v_x, with velocity gradient in the y direction. It is now that, even in the idealised geometry, we must make our first key rheometric assumptions, which are that the velocity profile is linear across the gap, there is a no-slip boundary condition at the plates and that the sample is homogeneous. These assumptions allow us to write the local rate of shear deformation as a function of macroscopic quantities,

$$\dot{\gamma} = \frac{\mathrm{d}v_x}{\mathrm{d}y} = \frac{u}{h}. \tag{2.1}$$

In the steady state, force balance tells us that the stress, or average force per unit area, σ ($= \sigma_{xy}$), applied at the boundary is constant across the gap, and so the stress in the fluid is equal to the stress at the boundaries, σ. This assumption will hold for dynamic measurements as long as fluid inertia is negligible, and this is typically the case with the use of small gap heights and viscous fluids. With these assumption, we can therefore relate local fluid properties ($\dot{\gamma}$ and σ) to bulk quantities (velocity and force).

In a measurement one can apply either a force or a deformation and then measure one as a function of the other. In all cases it must be ensured that a steady state is reached after any change in the applied quantity. Whether it is appropriate to measure $\sigma(\dot{\gamma})$ or $\dot{\gamma}(\sigma)$ depends on the sample. Of course, such an idealised test using infinite rectilinear flow is not practicable, and while sliding plates can be

used for small deformations, to measure steady flow we must turn to rotational geometries.

2.1.1 Cone and plate

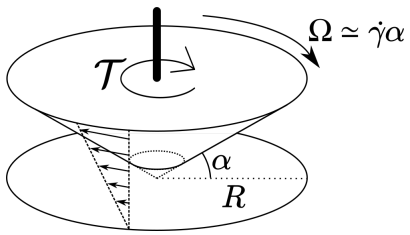

Figure 2.2 Cone-plate rheometric geometry. Geometry: plate radius, R, and cone angle, α (highly exaggerated for schematic purposes). Dotted line denotes truncation gap. Rheometric quantities: torque, $\mathcal{T}$, and angular velocity Ω. Shear rate, $\dot{\gamma} = \Omega/\alpha$ in small angle limit.

Even with a rotating geometry, using a cone-plate geometry it is still possible to apply a constant shear rate across the sample, with the fluid velocity in the azimuthal direction, Fig. 2.2. With an angular velocity, Ω, a radius, R, and a small angle, α (1°-2°), a homogeneous shear rate,

$$\dot{\gamma} = \frac{\Omega}{\alpha}, \tag{2.2}$$

is applied to the sample (in the small angle limit). The homogeneous shear rate makes it easy to relate the applied torque, $\mathcal{T}$, to the local stress,

$$\sigma = \frac{3\mathcal{T}}{2\pi R^3}. \tag{2.3}$$

The above analysis assumes that the cone touches the plate, in practice a truncated cone is used. The truncation gap ($\approx 50\,\mu\text{m}$) ensures that there is always a finite separation between the cone and plate to prevent the sample becoming trapped or jammed. Although the gap is sufficient for polymeric fluids or colloids, the typical gap is comparable to the maximum particle size for a non-Brownian suspension and use of a cone-and-plate geometry is precluded for our purposes.

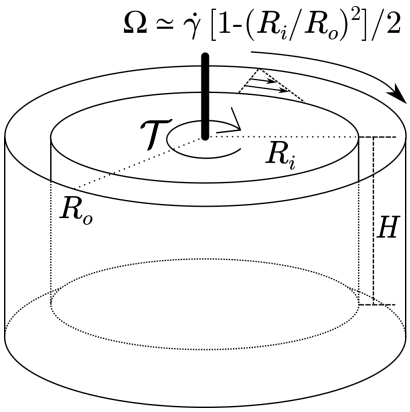

Figure 2.3 Couette-cylinder rheometric geometry. Geometry: inner cylinder radius, R_i, outer cylinder radius, R_o, and cylinder height, H (R_i/R_o highly exaggerated for schematic purposes). Rheometric quantities: torque, $\mathcal{T}$, and angular velocity Ω. Shear rate, $\dot{\gamma} = 2\Omega/[1-(R_i/R_o)^2]$ in small-gap limit.

2.1.2 Couette cylinders

To create a constant gap height in a rotating geometry, shear can be generated between two coaxial rotating cylinders, or Couette cylinders, Fig. 2.3.[1] We describe the geometry with an inner cylinder radius, R_i, outer cylinder radius, R_o, and height, H, while the cylinders rotate with a relative angular velocity, Ω. Here we discuss narrow-gap Couette cylinders, in which $1 - R_i/R_o \ll 1$.[2] Again assuming homogeneous flow and also neglecting end effects, i.e. $H \gg h$, we can calculate the shear stress at the inner cylinder, $\sigma = \sigma(R_i)$, in terms of the applied torque,

$$\sigma(\dot{\gamma}_{R_i}) = \frac{\mathcal{T}}{2\pi R_i^2 H}. \tag{2.4}$$

The shear stress weakly varies across the gap, as does the shear rate which we calculate from the rotation rate,

$$\dot{\gamma}(R_i) \approx \dot{\gamma}(R_o) \approx \frac{2\Omega}{1 - (R_i/R_o)^2}. \tag{2.5}$$

Therefore, a Couette-cylinder geometry may initially appear a suitable rheometric geometry for non-Brownian suspensions. However, there are a number of issues. These issues are primarily related to our assumption of a homogeneous sample, as

[1] Whether the inner or outer cylinder is rotated depends on rheometer design, although rotating the outer cylinder is desirable to eliminate secondary flow caused by Taylor vortices.

[2] The definition of a narrow gap would depend on the properties of the fluid being measured as this effects the necessary corrections [9].

in practice the solid volume fraction can show significant spatial variation with various causes. If the solid particles differ in density to the background fluid phase the sample can sediment and form a jammed solid at the bottom of the cylinder [13]. Volume fraction variation across the gap is also possible and this is driven by the variation in shear stress [14, 15].[3] Finally, the sample may even become inhomogeneous during loading. As the inner cylinder must be lowered into the outer cylinder, the sample is pumped up the walls of the cylinder and effectively extruded, a process that can cause large variations in volume fraction dependent on rate [16].

2.1.3 Parallel plate

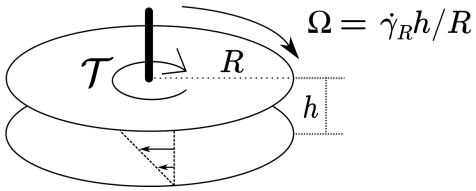

Figure 2.4 Parallel-plate rheometric geometry. Geometry: plate radius, R, and gap height, h (highly exaggerated for schematic purposes). Rheometric quantities: torque, $\mathcal{T}$, and angular velocity Ω. Rim shear rate, $\dot{\gamma} = \Omega R/h$.

And so, we must instead use a parallel plate geometry, consisting of two circular rotating plates of radius R, with separation h and relative angular velocity Ω, Fig. 2.4. This maintains a constant gap, unlike a cone-plate geometry, and avoids excessively stressing the sample during loading, as a Couette-cylinder geometry does.[4] However, quite clearly the shear rate will vary with the distance from the centre of rotation, r. This means that if the torque is measured at a single angular velocity only apparent quantities can be defined, that is we must assume that the sample behaves as a Newtonian liquid (so that viscosity does not depend on shear rate). In this case we report the rim shear rate,

$$\dot{\gamma}(R) = \dot{\gamma}_R = \frac{\Omega R}{h}. \tag{2.6}$$

[3]Refs. [14, 15] were conducted using wide-gap Couette cylinders. However, it is not apparent what constitutes a sufficiently narrow gap to prevent this effect and without direct visualisation of volume fraction variation we choose to avoid use of Couette cylinders entirely.

[4]Sedimentation will still be an issue in parallel plate geometry. However, instead of a yield stress appearing, as in Coeutte cylinders, sedimentation can lead to apparent shear thickening when the particles are resuspended at high stress [17]. To ensure that this does not occur measurements are made with both increasing and decreasing stress to check for long term time-dependent effects, such as sedimentation.

By assuming that the sample behaves as a Newtonian fluid, the torque on the geometry can be rewritten in terms of an apparent viscosity,

$$\mathcal{T} = 2\pi \int_0^R r^2 \sigma(r) \mathrm{d}r = 2\pi \int_0^R r^2 \eta_{\mathrm{app}} \frac{\Omega r}{h} \mathrm{d}r = \frac{\pi R^3}{2} \left(\frac{\Omega R}{h}\right) \eta_{\mathrm{app}}. \tag{2.7}$$

The apparent stress is then the assumed stress at the rim

$$\sigma_{\mathrm{app}} = \eta_{\mathrm{app}} \dot{\gamma}_R = \frac{2\mathcal{T}}{\pi R^3}. \tag{2.8}$$

Despite the variation of shear rate with radius, for some non-Newtonian fluids a simple single point correction can be made to try and account for this variation by using the shear rate at $0.76R$ to calculate η_{app}, instead of using the rim shear rate. For yield-stress fluids and shear-thinning samples this keeps the error between η_{app} and the true viscosity to within 2%. However, to more generally measure viscosities for non-Newtonian fluids we must probe a range of shear rates and stresses. By writing the torque on the plate as a function of the shear rate across the plate,

$$\mathcal{T} = 2\pi \int_0^R r^2 \sigma(r) \mathrm{d}r = 2\pi \int_0^{\dot{\gamma}_R} \left(\frac{R}{\dot{\gamma}_R}\right)^3 \dot{\gamma}^2 \sigma(\dot{\gamma}) \mathrm{d}\dot{\gamma}, \tag{2.9}$$

the torque can be differentiated with respect to $\dot{\gamma}_R$. The result can be rearranged to give the corrected viscosity for parallel plates,

$$\sigma(\dot{\gamma}_R) = \frac{\mathcal{T}}{2\pi R^3} \left(3 + \frac{\mathrm{d}\ln \mathcal{T}}{\mathrm{d}\ln \dot{\gamma}_R}\right). \tag{2.10}$$

This means that the non-Newtonian viscosity can be determined from an apparent stress or shear rate sweep. From this point on we then drop the distinction of the rime shear rate and report it as simply the shear rate, $\dot{\gamma}$. However, if the stress response of the sample changes discontinuously (or very sharply) with rate, this correction can break down. In such instances we are forced to report simply the apparent stress and viscosity. The correction also breaks down for dynamic measurements as the viscosity is no longer a function of shear rate alone. [5]

Of course, even when the correction can be applied a large number of assumptions are being made, in particular the assumption of no-slip boundary conditions. Here parallel plate geometries, in fact, possess two advantages. Firstly, the roughness of the plates can be easily adapted to minimise slip and this occurs approximately

[5] However, in some some studies this correction has been applied to time-dependent data [18].

when the roughness of the plates is matched to the particle size [19]. Too small a roughness and there is depletion of the particles near the surface causing slip along the surface, while if the roughness is too large the fluid can flow through the surface itself [20]. Although, the effectiveness of this roughening may be limited as the volume fraction increases [21]. To truly eliminate the effect of slip a series of measurements at different h can be made, from which the slip velocity can be deduced and corrected for [22]. As we are interested in trends rather than precise values when testing and comparing models to data in this thesis we do not apply this correction. Therefore, measurement at a single gap height of $\sim 1\,\text{mm}$ in a $20\,\text{mm}$ radius parallel plate geometry with appropriately selected roughness represents our chosen rheometric technique for non-Brownian suspension rheology.

2.2 A "window" on rheology

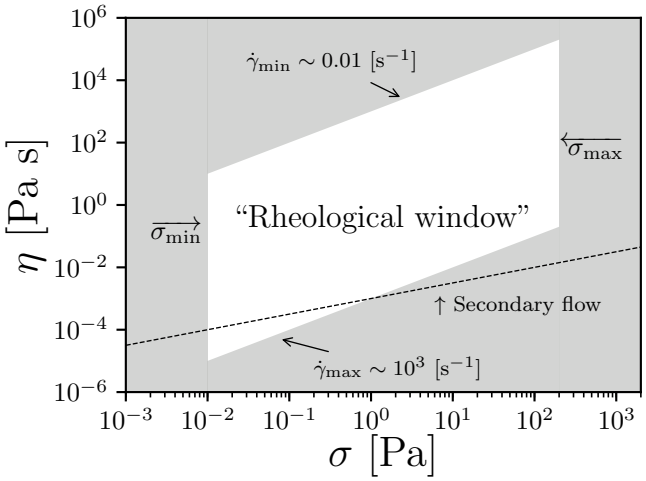

Figure 2.5 Outlining a rheological "window". Concept adapted from Refs. [23] and [24]. White region, approximate range of viscosities and stresses measurable in a parallel-plate geometry, grey region inaccessible. Measurable region bounded by: minimum shear stress, σ_{min}, set by instrument resolution or surface tension effects; maximum shear stress, σ_{max}, set by sample fracture; minimum shear rate, $\dot{\gamma}_{\text{min}}$, set by experiment time; and maximum shear rate, $\dot{\gamma}_{\text{min}}$, set by inertial ejection. Low-viscosity measurements additionally limited by generation of secondary flows, minimum measurable viscosity limit $\eta \propto \sigma^{1/2}$ [9], shown schematically.

Having explained our choice of a suitable rheometric geometry, we now turn to consider the limits on what we can measure. These limits restrict our

measurements of non-Brownian suspension properties to a "window" on the full flow curve or constitutive relation, Fig. 2.5. Throughout this thesis we typically present the relative viscosity, $\eta_r = \sigma/(\dot{\gamma}\eta_s)$, where we have divided by the viscosity of the background solvent, η_s, as a function of the stress, σ. Note that flow curves may be presented in this manner even for imposed shear rate measurements.

At low stress, measurements are restricted at $\sigma_{\min}$ by either the torque resolution of the instrument (0.1 µN m for a TA Instruments G2 equivalent to 0.01 Pa) or surface tension effects from contact line asymmetry [23]. At high stress the measurements are limited to $\sigma_{\max}$ by edge effects, chiefly sample fracture, at which point the surface tension of the background solvent can no longer contain the sample within the confines of the geometry. This upper stress limit was determined from visual inspection of the sample edge, with a typical value of $\sigma_{\max} \sim 200\,\text{Pa}$ [24]. In addition to limits on the measurable stress range, there are also limits on the shear rate range. Low shear rates are limited to $\dot{\gamma}_{\min}$ by the experimental time and this is itself limited by, e.g., drying or sedimentation of the sample.[6] Finally, the maximum shear rate, $\dot{\gamma}_{\max}$, is because of inertial sample ejection; together these limits give the observable "window" and typical values are shown in Fig. 2.5. For very low viscosity samples secondary flows can be generated (i.e. the fluid velocity is no longer exclusively in the azimuthal direction). This breaks our rheometric assumptions and this limit is shown schematically in Fig. 2.5 (dashed line). However, this effect should not impact the measurement of suspensions, as they are typically to viscous.

Outside of this window we can only project what the likely behaviour is from the response measured within the window. The best example of this is in the measurement of "yield stress fluids", in which measurements show that there is a minimum stress required for steady continuous flow [25]. As there is a minimum observable shear rate, it is then not possible to say if a sample behaves as a very viscous liquid or a solid at very low shear rates [26]. This ambiguity has caused a long-standing debate over the "yield stress myth"; however, a consensus has at least been reached on the fact that the yield stress represents an engineering reality [27].

[6] As a sample takes strain to reach steady state (see Ch. 4) the minimum shear rate sets the time of the experiment.

2.3 Conclusion

In this chapter we have briefly outlined the principle of shear rheometry: making measurements of a sample under well-defined shear flow to deduce a constitutive relation. After reviewing the set of commonly used rheometric geometries, we find that the parallel-plate geometry is best suited for non-Brownian suspensions. We have described the limitations of this geometry due to the spatially varying shear rate. For this selected geometry, the restrictions on measurements were enumerated, showing how they demarcate a window onto the flow curve, or constitutive relation. Even within the use of rheometric geometries, it is possible to perform many tests beyond steady shear and these can often help reveal the rheophysics. By rheophysics we refer to deducing the physics on the particle or structural level from rheometric measurements. However, such a process typically starts from a steady state flow curve (as transient techniques either perturb the steady-state or tend to it in the long-time or large-strain limit). In this spirit, we will now move on to the first main part of the thesis, which will begin with a literature review focussing on the understanding of the steady-state rheology of well-stabilised non-Brownian suspensions.

Part I

Shear thickening beyond the steady state

Chapter 3

Shear-thickening suspensions: a review

Historically the study of "hard-sphere" suspensions has been split into two distinct regimes: colloidal dispersions, focussing on suspensions of Brownian particles with diameter $d \lesssim 1\,\mu\text{m}$, and granular suspensions with $d \gtrsim 50\,\mu\text{m}$.

In the colloidal regime, the dominant physics is thermal, or Brownian. The relative viscosity, η_r, is determined solely by the solid volume fraction, ϕ, and the Péclet number, $\text{Pe} = \tau_\text{B}\dot{\gamma}$ [28]. The Péclet number is the ratio of the Brownian time, $\tau_\text{B} = 3\pi\eta_s d^3/k_\text{B}T$, the timescale for a particle to diffuse the distance of its own radius, to the timescale of the applied shear, $1/\dot{\gamma}$. At $\text{Pe} \ll 1$, particles have time to rearrange in response to the applied shear and the suspension remains close to the isotropic equilibrium state. The viscosity diverges at the glass transition, $\phi_g \approx 0.58$ for monodisperse spheres, above which particles are trapped in 'cages'. As Pe increases the suspension shear thins, reaching a plateau at $\text{Pe} \gg 1$; now particles no longer have time to randomise and the structure responds to the applied shear, becoming highly anisotropic. The viscosity of this plateau only diverges at random close packing, ϕ_rcp, the maximum density amorphous packing for spheres. For colloidal suspensions, stresses are transmitted hydrodynamically, through the suspending fluid. Such behaviour is universal for Brownian hard-particle suspensions and data for multiple systems can be collapsed [29], albeit with appropriate changes in ϕ due to measurement uncertainty [30].

In the granular regime, the dominant physics is instead related to the particle's

mass or momentum. The importance of inertia[1] is determined by the particle Reynolds number, Re_p, the ratio of inertial to viscous forces on the particle [7]. At low Re_p, a particle closely follows the streamlines of the suspending fluid, while at high Re_p[2] the particle trajectory is determined by its momentum. As an inertial granular medium is sheared it exerts a pressure through interparticle collisions. The particles want to expand and occupy a larger volume, a process known as dilation. In a suspension, however, the overall volume is typically fixed due to the solvent.[3] At fixed ϕ granular suspensions show inertial shear thickening with increasing Re_p ($\sigma \propto \dot{\gamma}^2$), a process known as Bagnoldian shear thickening [32]. In stark contrast to the colloidal regime, the dominant stress-transmission mechanism is via direct mechanical contact between particles.

An intermediate particle size regime is therefore defined between these two limits, where thermal motion is insignificant ($\mathrm{Pe} \ll 1$), but inertia is also negligible ($\mathrm{Re}_p \ll 1$); we refer to these as non-Brownian suspensions.[4] For hard particles (i.e. they are not significantly deformed by the applied stresses, such as in an emulsion) there seems to be no intrinsic stress-scale. Therefore, non-Brownian suspensions should have a constant relative viscosity, depending only on ϕ [7]. In practice they are, paradoxically, often highly non-Newtonian, with the viscosity depending strongly on the applied stress or shear rate and with the stress-transmission mechanism unclear (hydrodynamic or contact?). One of the most striking examples of this, and seen ubiquitously in the intermediate-size regime, is shear thickening, where the viscosity increases with the applied shear rate or stress.

In this chapter we review literature experimental data on shear-thickening suspensions, leading up to the development of the current phenomenological model based on stress-dependent frictional contacts. The use of this model to explain multiple inter-related experimental phenomena is then reviewed, before finally discussing unresolved issues at the microscale.

[1] Inertia can also effect suspension flow macroscopically, such that the flow is no longer laminar, e.g. the Couette-Taylor instability. This can manifest as apparent shear thickening, i.e. the stress increases faster than the apparent shear rate [31]. However, in this thesis we are most concerned with the local rheological properties of the suspension and we will consider bulk fluid inertia to be negligible.

[2] The crossover is in fact volume fraction dependent [7], precluding introducing specific critical values for Re_p.

[3] An important exception to this is when considering sedimented suspensions, although again this lies beyond the scope of this thesis.

[4] The requirements for the existence of this intermediate regime are detailed in Appendix A.

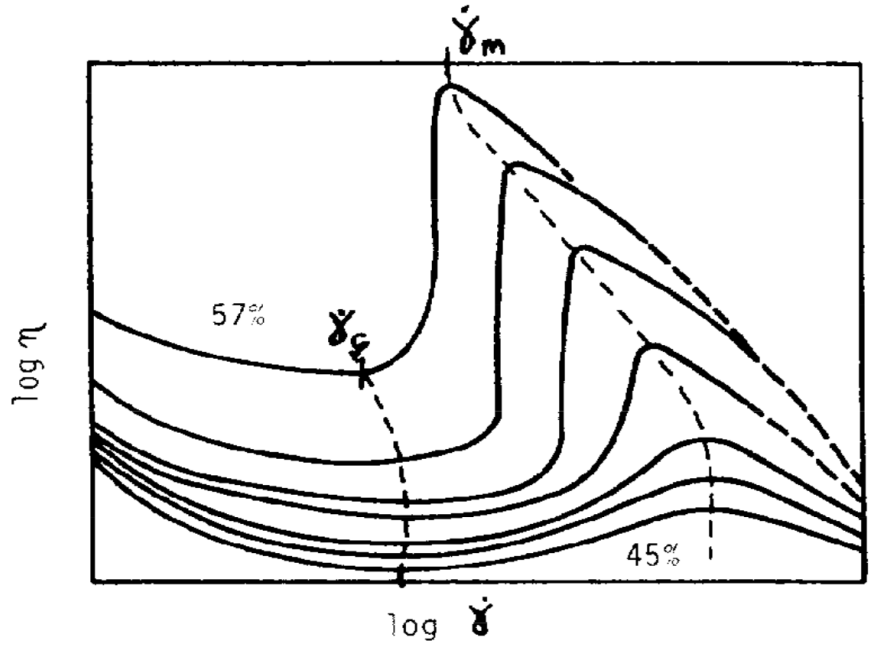

Figure 3.1 Schematic representation of flow curves for a shear-thickening suspension, viscosity, η, *vs* shear rate, $\dot{\gamma}$, with approximate solid volume fraction (labelled) as a parameter. Dashed lines: the loci of the onset shear rate for thickening, $\dot{\gamma}_c$, and the shear rate at the end of the shear-thickening region, $\dot{\gamma}_m$. Figure taken from Ref. [33].

3.1 Historical perspective

One of the first systematic reviews of experiments on shear-thickening suspensions was conducted by Barnes in 1989 [33]; this set out a schematic for a shear-thickening suspensions in the low-Re_p regime, plotted as a function of shear rate, Fig. 3.1. Suspensions initially shear thin, approaching a high-Pe plateau before the onset of shear thickening. With increasing ϕ, the onset shear rate for thickening, $\dot{\gamma}_c$, decreases and the rise in viscosity increases, also occurring over a narrower $\dot{\gamma}$ range. At high ϕ the increase in viscosity becomes sudden: the suspension shows discontinuous shear thickening (DST). At the end of the shear-thickening region, at $\dot{\gamma}_m$, continued shear thinning may be observed, although this is emphasised to be system specific. Compiling multiple data sets, it was identified that $\dot{\gamma}_c$ decreased with increasing solvent viscosity, $\dot{\gamma}_c \propto 1/\eta_s$, and increasing particle diameter, $\dot{\gamma}_c \propto d^{-2}$. It was therefore postulated that shear-thickening was *generic*, requiring only that the system is well dispersed, i.e. not aggregated by strong attractive interactions, and consists of hard particles, i.e. not an emulsion or foam. Inertia was ruled out as thickening was seen for small particles in viscous solvents. The experimental observation of shear thickening in

suspensions of non-aggregating solid particles was then thought to depend simply on whether it occurred at an accessible shear rate.

3.1.1 Hydrodynamic effects

Becuae shear thickening occurs generically for well-stabilised hard-particles with Pe $\gg 1$ and small Re_p, explanations for the viscosity increase centred around hydrodynamic interactions, in particular the notion of "hydroclustering" [34]. In this concept for shear-thickening, at a critical shear rate the hydrodynamic forces between particles overcome the stabilising forces which keep particles dispersed, such as electrostatic, steric [35] or entropic forces.[5] As the particles are pushed closer together the short-range hydrodynamic interactions, or lubrication forces, increase [38], hence the dissipation and the viscosity increase. Stokesian dynamics simulations, which include Brownian motion, hydrodynamic interactions[6] and conservative repulsive interactions, have only reproduced weak continuous shear thickening. This remains the case even at high volume fractions ($\phi \approx 0.58$) [39], and it is in contrast to the strong thickening seen experimentally at such ϕ [33].

A criterion to observe "hydroclusters" and strong hydrodynamic thickening was, however, deduced. Clustering should occur when the quiescent relaxation time of the contact (i.e. the time taken to separate under interparticle forces alone, after the removal of applied stress) is greater than the timescale for shear, $1/\dot{\gamma}_c$ [40]. The criterion could be satisfied by introducing enhanced hydrodynamics, such as slowed solvent permeation through a polymer brush coating. However, it is difficult to justify such an addition for electrostatically stabilised shear-thickening suspensions, e.g. silica. To observe strong thickening generically, as seen experimentally, would require unphysically-small particle gaps. As the hydrodynamic viscosity only increases logarithmically with decreasing gap, $\eta \propto \ln(1/z)$ [41], to see the multiple orders of magnitude rise in viscosity seen

[5] In sheared dense suspensions some of the effects of Brownian motion can be captured through a repulsive potential, for both shear thinning [36], as well as the onset stress for shear thickening [37].

[6] In general it is has been too computationally intensive to explicitly model the background solvent directly through the Navier-Stokes equations. The effect of the background fluid has therefore been included as a pairwise interaction between particles, calculated theoretically for two isolated particles. Such hydrodynamic interactions are in general long range, decaying as $1/z$. However, it has been shown in concentrated suspensions that the effect of hydrodynamic interactions on the suspension viscosity is dominated by interactions arising from short-range lubrication forces and a Stokes drag term, relative to the affine motion of the background solvent.

during DST would require gaps far below that at which the continuum background solvent assumption breaks down. At such gaps features such as surface roughness and the molecular scale must be considered. This paradox gives rise to the so-called 'small-gap problem' [31, 42].

3.2 Frictional shear thickening

In experimental observations of DST suspensions, several additional phenomena are observed which are not readily explainable through hydrodynamic interactions. At or around the onset of DST, a positive first normal stress difference is observed [43], this is a difference in the pressures exerted in the flow and gradient directions, i.e. in a cone-plate geometry the surfaces are pushed apart by the suspension. This positive normal stress difference is in stark contrast to the negative normal stress difference seen from simulations with hydrodynamic interactions alone [39]. Secondly, when slightly increasing the volume fraction of a DST suspension, there is now a transition at high stress to a 'pasty' state, which granulates [44]. Such granules are *statically* jammed, where hydrodynamic forces should vanish, but they can be relaxed back to a suspension by vibration, hence they are below random close packing and are not jammed by geometry alone. Finally, DST can be eliminated by the presence of an un-sheared reservoir of particles [45, 46] or soft boundaries [17]. Together these phenomena suggest that for DST to occur confinement is required to prevent particles expanding or dilating, and therefore that DST is related to jamming, with mechanical contacts that transmit stress directly across the sample.

Interestingly, the subtle role of confinement can explain why 'dilatancy' was originally discarded as an explanation for shear thickening by Metzner and Whitlock [47]. As dilatancy could only be visually observed from deformation of the free surface due to particles poking out, a particle size effect arises. The effective softness of the free surface depends on particle size: the maximum confining stress, $\sigma_{\max}$, is proportional to surface tension, Λ, and the inverse particle size, $\sigma_{\max} \propto \Lambda/d$ [17]. For small particles ($d \lesssim 1\,\mu\text{m}$) the free surface acts as a hard boundary and they do not significantly deform it so that no "dilation" is seen despite thickening. For large particles ($d \gtrsim 50\,\mu\text{m}$), the boundary is soft and dilation occurs. As the particles are not confined, jamming cannot

occur and no increase in viscosity is measured from direct stress transmission.[7] With "dilatancy" appearing neither necessary nor sufficient, explanations instead concentrated on suspension structure and hydrodynamic interactions [48].

3.2.1 Dry friction

If particles are in mechanical contact, as in the thickened state, interactions can be far more complex. A prime example is dry friction, where 'dry' emphasises the contrast to lubrication in the hydrodynamic regime. Friction is not a fundamental force, like electrostatic interactions, nor does it have a first principles derivation, as for steric or Van der Waals interactions [49]. Instead it arises from such fundamental forces through a hierarchical interaction of surface details: adhesion and contamination at contact areas, yielding and plastic deformation of asperities (protrusions in a rough surface); and elastic coupling of roughness over multiple lengthscales [50]. Only at the continuum level of bulk objects does the concept of a frictional force arise. It possesses several important attributes: it is non-conservative, the force is not purely a function of position, but a functional of position and velocity; it is dissipative, converting kinetic energy or work into thermal energy through the many microscopic degrees of freedom not directly considered; and below a threshold value it prevents motion independent of direction. As it is then a many-body non-equilibrium phenomenon, *ab initio* theories are not yet available and empirical or phenomenological models must be used in their place. One of the simplest and oldest is Coulomb's Law:

$$F \leq \mu_p N. \qquad (3.1)$$

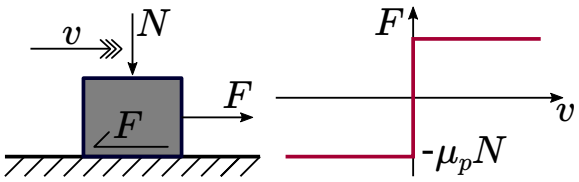

The maximum magnitude of the frictional force, F, depends solely on the normal load, N, via a proportionality constant, the static coefficient of friction, μ_p. The frictional force resists movement up to the threshold. Above this sliding occurs, with a frictional force $F = \mu_p N$ now opposing the motion of velocity v. In Coulomb friction there is no v dependence and the dynamic (sliding) friction coefficient is equal to the static coefficient. While this is originally an empirical

[7] As the particles are large at observable shear rates they are likely well within the thickened regime already [33] and with confinement the particles would jam at a critical strain, rather than strictly shear thickening.

model, *post hoc* justification has been developed [51]. The validity of many assumptions used in deriving Eq. 3.1 are often questionable, but its simplicity and ability to capture the essential features of friction mean that it is widely used in studying granular materials [50].

Motivated by the 'small-gap problem' and the possibility of mechanical contact as particles approached, Seto et al. introduced the Coulomb friction model into discrete-element method (DEM) simulations of repulsive suspensions [52]. Interactions between particles included: hydrodynamics, with the lubrication divergence cut-off to mimic surface roughness; electrostatic repulsion; and,at contact, Coulomb friction with $\mu_p = 1$. These simulations were the first to capture the key experimental features of shear-thickening suspensions: DST at high volume fractions ($\phi > 0.56$), continuous shear thickening (CST) at lower volume fractions and with both CST and DST having a critical onset stress. In previous simulations including only hydrodynamic and frictional interactions between rough spheres, quasi-Newtonian behaviour was found [53, 54]. To capture strong shear thickening, not only are frictional forces needed but repulsive forces between particles, which prevent contact until a critical stress is reached. At $\phi > 0.58$ particles were seen to jam, forming system spanning force networks that could support a static load. Flow only occurred at these volume fractions due to finite particle softness allowing deformation. The viscosity increase of CST at lower ϕ was then suggested to be the residue of this jamming transition. Without system spanning force networks the mechanism for the viscosity increase remained, however, unclear. Although, it was noted that friction must be important, as with $\mu_p = 0$ only weak hydrodynamic thickening was found at any volume fraction.

3.3 Wyart and Cates model

These observations were incorporated into a phenomenological model by Wyart and Cates (WC) [8], which identified the minimum 'ingredients' needed to capture the shear thickening seen in experiments and the simulations of Ref. [52]. The model considers (non-Brownian, non-inertial, density-matched) hard frictional spheres (diameter d) immersed in a solvent, viscosity η_s, with short ranged ($\ll d$) repulsive forces of maximum magnitude F^*. It is this repulsive force which introduces the additional stress-scale, a particle pressure $p^* \sim F^*/d^2$, and it is this that is needed to explain the non-Newtonian behaviour of suspensions in the

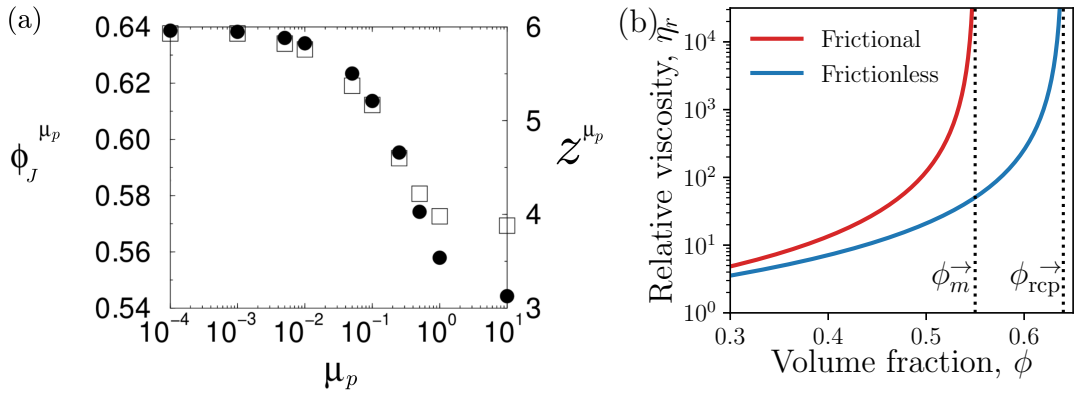

Figure 3.2 Effect of friction on jamming volume fraction. (a) Solid circles: friction dependent jamming volume fraction, $\phi_J^{\mu_p}$, as a function of interparticle friction coefficient, μ_p, for monodisperse spheres under isotropic compression. Open squares: corresponding drop in coordination number at jamming, $\mathcal{Z}^{\mu_p}$. Figure adapted from Ref. [57]. (b) Two-branch phenomenology for suspension viscosity. Blue: frictionless viscosity branch, relative viscosity, η_r as a function of volume fraction, ϕ, diverges at random close packing, $\phi_J(\mu_p \ll 0.1) = \phi_{\rm rcp} \approx 0.64$, according to Eq. 3.2. Red: frictional viscosity branch, diverging at $\phi_J(\mu_p \gg 0.1) = \phi_m \approx 0.55$.

intermediate size regime. At low particle pressure, $p \ll p^*$, the repulsive force prevents particles coming into mechanical, frictional contact and the suspension is lubricated. At high particle pressure, $p \gg p^*$, all particles are pushed into frictional contact and the suspension is frictional.

Unfortunately, in conventional suspension rheometry the particle pressure p is generally inaccessible; it is instead the shear stress, σ, that is measured. However, it is possible to simply consider functions of σ [8]. This is possible because the ratio of shear stress to particle pressure as a function of ϕ is comparable between the frictional regime, taken from one-off measurements using a unique permeable-boundary rheometer to allow variations in ϕ and measurement of p [11, 12], and the frictionless regime, taken from simulations [55]. Henceforth, we use functions of σ in place of p, with a stress-scale $\sigma^* \sim F^*/d^2$, and follow conventional application of the WC model [24, 56]. However, initial use of p encodes the importance of confinement: only under rigid boundaries which fix ϕ and impose a particle pressure is there a local constitutive relation, $\eta(\sigma, \phi)$, otherwise boundaries must explicitly be considered [31].

3.3.1 Phenomenological analysis

In the lubricated regime, $\sigma \ll \sigma^*$, the viscosity, η, will diverge at the jamming volume fraction for frictionless particles, $\phi_J = \phi_{\text{rcp}}$. In the frictional regime, $\sigma \gg \sigma^*$, the viscosity will now diverge at a lower volume fraction, $\phi_J = \phi_m < \phi_{\text{rcp}}$. This volume fraction will depend on the interparticle friction coefficient, μ_p. For isostatic compression, friction reduces ϕ_J from $\phi_{\text{rcp}} \approx 0.64$ for $\mu_p \ll 0.1$, to $\phi_J = \phi_{\text{rlp}} \approx 0.55$ for $\mu_p \gg 0.1$, random loose packing for monodisperse spheres [57], Fig. 3.2(a).[8]

Multiple functional forms have been used to capture the dependence of suspension viscosity on ϕ (see Ref. [28] and references therein). Here it is only important that η monotonically increases and diverges approaching a critical ϕ. For simplicity, for all σ we use the same Maron-Pierce [59], or Quemada [60], form for the relative viscosity,

$$\eta_r(\phi, \phi_J) \equiv \frac{\eta}{\eta_s} = \left[1 - \frac{\phi}{\phi_J(\sigma)}\right]^{-2}, \tag{3.2}$$

allowing the introduction of a stress-dependent jamming volume fraction, $\phi_J(\sigma)$, to capture the non-Newtonian behaviour. Shear thickening can then be seen as a stress-driven transition from a frictionless viscosity branch to a frictional branch, Fig. 3.2.

Wyart and Cates assumed the jamming volume fraction to be a linear interpolation between the two limiting jamming volume fractions based upon the proportion of frictional contacts, $\hat{f}$,

$$\phi_J(\sigma) = \phi_m \hat{f}(\sigma) + \phi_{\text{rcp}} \left[1 - \hat{f}(\sigma)\right]. \tag{3.3}$$

This proportion of frictional contacts is an increasing function of σ, rising from $f = 0$ ($\rightarrow \phi_J = \phi_m$) when $\sigma \ll \sigma^*$ to $f = 1$ ($\rightarrow \phi_J = \phi_{\text{rcp}}$) when $\sigma \gg \sigma^*$.[9] The qualitative behaviour of the model is preserved for a general set of functions that increase sufficiently rapidly with σ, see Supplemental Material of Ref. [8]. We choose a specific function, from Ref. [24], based on the proportion of contacts

[8] Although quoted limiting jamming volume fractions are based on isotropic compression of packings, similar values are found experimentally for shear jamming in the frictional case [58].

[9] Due to the short range nature of the repulsive force it is possible to define contacts unambiguously. $\hat{f}$ is then the proportion of contacts where the non-hydrodynamic normal force between the particles has exceeded the maximum force of the repulsive potential.

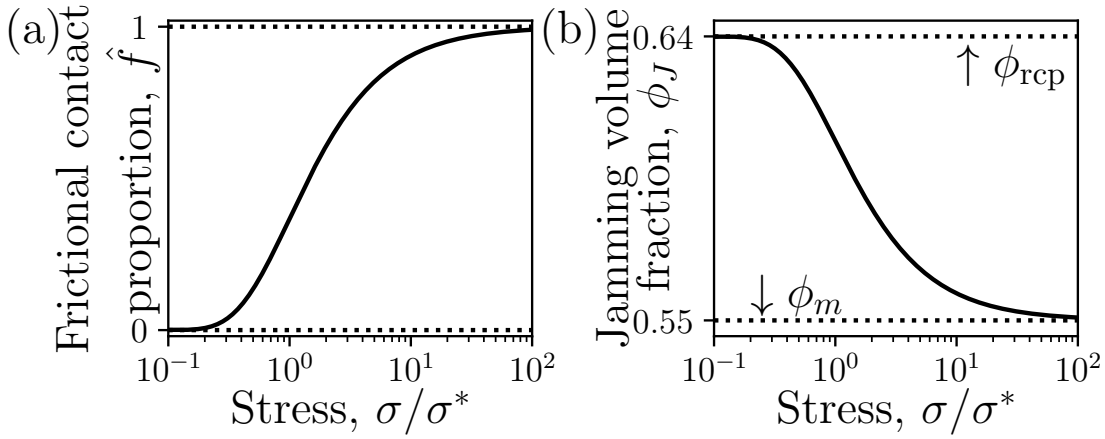

Figure 3.3 Stress dependence of underlying variables. (a) Solid line: proportion of frictional contacts, $\hat{f}$, as a function of reduced shear stress, σ/σ^*, relative to the onset stress for frictional contact, given by Eq. 3.4 with $\beta = 1$. Dashed lines, limiting values for $\sigma \to 0$ ($\hat{f} = 0$) and $\sigma/\sigma^* \to \infty$ ($\hat{f} = 1$). (b) Solid line: corresponding jamming volume fraction at which $\eta_r \to \infty$, ϕ_J, as a function of reduced shear stress, σ/σ^*. Dashed lines, limiting values for $\sigma \to 0$ ($\phi_J = \phi_{\rm rcp} = 0.64$) and $\sigma/\sigma^* \to \infty$ ($\phi_J = \phi_m = 0.55$).

exceeding a critical load in the force distribution of dry granular systems [61],

$$\hat{f}(\sigma) = \exp\left[-\left(\frac{\sigma^*}{\sigma}\right)^{\beta}\right], \tag{3.4}$$

with $\beta \approx 1$ [24]. The proportion of frictional contacts increases steeply around σ^*, Fig. 3.3(a), causing a corresponding decrease in ϕ_J, Fig. 3.3(b).

3.3.2 Qualitative behaviour

Equations 3.2, 3.3 and 3.4 together give a closed relation for the relative viscosity as a function of dimensionless stress, $\Sigma = \sigma/\sigma^*$, and volume fraction, $\eta_r(\Sigma, \phi)$, Fig. 3.4(a). With increasing volume fraction, for $\phi < \phi_m$, η_r transitions continuously between two plateau regions, with the extent of thickening increasing. The onset of frictional contact increases η_r by reducing the distance to jamming, without explicitly needing direct transmission of forces through system spanning networks.

Eventually, for $\phi > \phi_m$, η_r instead diverges with increasing stress. Replotting now with Σ *vs* dimensionless shear rate, $\dot{\Gamma}$, a more complex set of features becomes apparent, Fig. 3.4(b). In a range of volume fractions below ϕ_m, $\phi_{\rm DST} = 0.535 <$

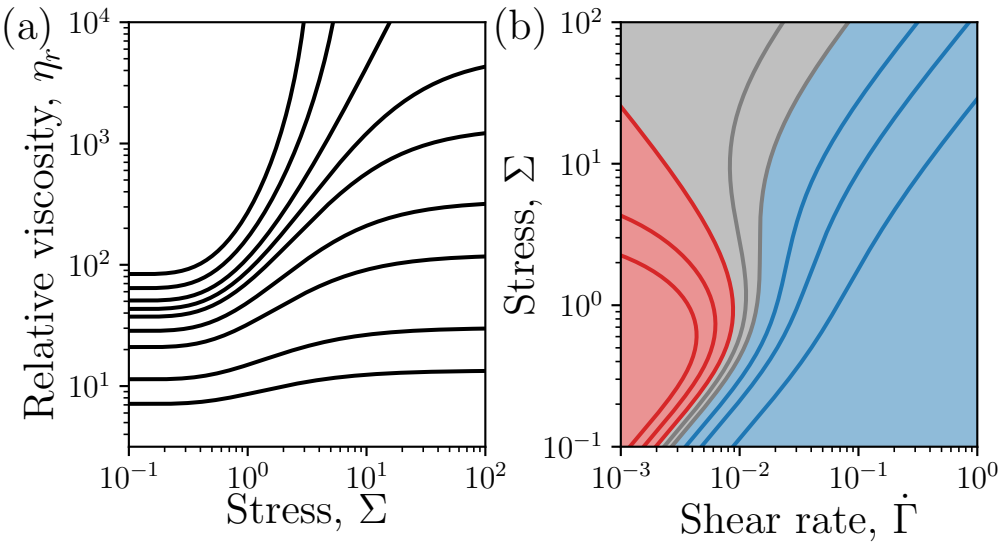

Figure 3.4 Flow curves from the WC model. (a) Relative viscosity, η_r, as a function of dimensionless stress, $\Sigma = \sigma/\sigma^*$, for volume fractions, $\phi = [0.40,\ 0.45,\ 0.50,\ 0.52,\ 0.535,\ 0.5425,\ 0.55,\ 0.56,\ 0.57]$, from bottom to top. WC-model parameters: $\phi_m = 0.55$, $\phi_{\text{rcp}} = 0.64$ and $\beta = 1$. (b) Flow curves from (a) replotted as Σ *vs* dimensionless shear rate, $\dot{\Gamma} = \eta_s\dot{\gamma}/\sigma^*$. Shaded regions, volume fractions exhibiting: blue, CST; grey, DST; red, shear jamming. Solid lines, ϕ as in (a), now left to right.

$\phi < \phi_m$, flow curves connecting two lines of constant slope (=viscosity) have a backwards bending region, $\mathrm{d}\dot{\Gamma}/\mathrm{d}\sigma < 0$, creating an $\mathcal{S}$-shaped flow curve.

In this range of ϕ, rheological measurements under increasing $\dot{\Gamma}$ would see a sudden jump in Σ from the frictionless state to a high-stress flowing frictional state at the point where the flow curve beings to bend backwards, $\dot{\Gamma}^+$, Fig. 3.5(a). When decreasing $\dot{\Gamma}$ from the thickened state, a similar drop to return to the low stress-state would occur, again as the flow curve bends backwards, but now at $\dot{\Gamma}^-$. Due to the $\mathcal{S}$ shape of the flow curves, the process is hysteretic: the decreasing $\dot{\Gamma}$ stress-drop occurs at a lower $\dot{\Gamma}$ than the increasing $\dot{\Gamma}$ jump. Under imposed Σ, there is now a region of applied stress, where $\mathrm{d}\dot{\Gamma}/\mathrm{d}\sigma < 0$, for which bulk flow is predicted to be unstable [62]. The WC-model flow curve should now only represent the local rheology. Similar behaviour and arguments are more familiarly used, with Σ and $\dot{\Gamma}$ inverted, for shear banding in yield-stress fluids with $\mathrm{d}\sigma/\mathrm{d}\dot{\gamma} < 0$ [62].

For $\phi > \phi_m$, there is no flowing upper branch, the flow curve bends backwards to $\dot{\Gamma} = 0$. Under increasing $\dot{\Gamma}$, once the backwards bending region is reached, with no flowing state to enter the model makes no specific predictions about the

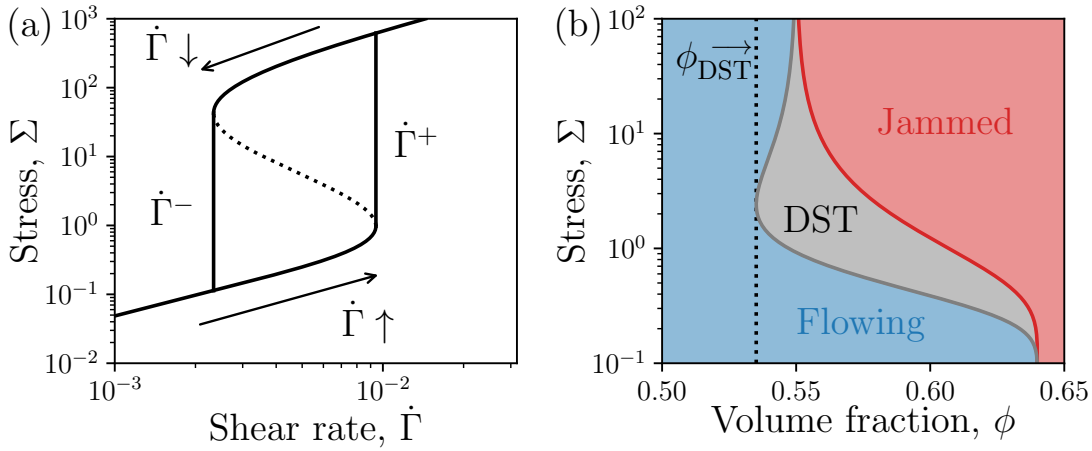

Figure 3.5 Categorising the behaviour of the WC model. (a) Schematic of hysteretic behaviour under imposed shear rate, $\dot{\Gamma}$, for $\phi = 0.548$. Hysteresis loop: stress jump under increasing $\dot{\Gamma}$ at $\dot{\Gamma}^+$ *vs* stress drop under decreasing $\dot{\Gamma}$ at $\dot{\Gamma}^-$. Solid line, states measurable under imposed rate; dashed line, backwards-bending region inaccessible under imposed $\dot{\Gamma}$. (b) Rheological phase diagram for WC model, in Σ-ϕ space. Red line, shear-jamming curve, where $\phi_J(\Sigma) = \phi$; grey line, DST curve, where $\mathrm{d}\dot{\Gamma}/\mathrm{d}\Sigma = 0$. Shaded regions: blue, stable flow, $\mathrm{d}\dot{\Gamma}/\mathrm{d}\Sigma \geq 0$; grey, backwards-bending flow curves, $\mathrm{d}\dot{\Gamma}/\mathrm{d}\Sigma < 0$; red, jammed, $\phi > \phi_J(\Sigma)$. Dashed line, minimum volume fraction at which $\mathrm{d}\dot{\Gamma}/\mathrm{d}\Sigma = 0$, $\phi_{\mathrm{DST}} = 0.535$.

flow. It predicts only that steady homogeneous flow is precluded. Under imposed Σ, there is again a region where bulk flow should be unstable, but a transition to a shear-jammed state ($\dot{\Gamma} = 0$) at high stress is also predicted. The changing qualitative behaviour with stress and volume fraction can be represented in a Σ-ϕ phase diagram, Fig. 3.5(b).

3.3.3 Testing the WC model: steady-state rheology

With a minimal set of ingredients, taking elements from established suspension rheology (Eq. 3.2) and dry granular packings (ϕ_{rcp}, ϕ_m) and only introducing the interpolation $\hat{f}(\Sigma)$ *de novo*, the model captures the qualitative features of shear thickening suspensions, Fig. 3.1: increasing thickening with increasing ϕ, followed by a transition to DST at $\phi \approx 0.55$. Such a schematic has been based on a broad range of systems [33], which do not in general meet the idealised picture of the WC model: additional stress-scales may be introduced due to non-density matched particles [31]; interaction ranges may be significant, e.g. in charge-stabilised systems [43]; particles may be close to the colloidal regime so

that Brownian motion cannot be neglected [35]; and aspherical or polydisperse particles can significantly change the limiting jamming volume fractions [44].

An attempt to meet the idealised picture of the WC model can be made using a near hard-sphere system, sterically-stabilised polymethylmethacrylate (PMMA) particles in a density and refractive-index matched solvent [24]. The steady-state rheology is shown to be consistent with the WC model, in particular validating the two-branch picture with critical volume fractions of $\phi_m \approx 0.55$ and $\phi_{\mathrm{rcp}} \approx 0.64$. Varying d, the onset stress, σ^* is found to scale with d^{-2}, such that at accessible stresses (say 0.1 to 1000 Pa): colloidal particles, $d \ll 1\,\mu\mathrm{m}$, are always frictionless; granular particles, $d \gg 50\,\mu\mathrm{m}$, are always frictional; and it is only in the intermediate-size regime that thickening occurs in the observable window.

As standard experimental rheometry can only access macroscopic quantities, e.g. stress or shear rate, to probe microscopically it is useful to analyse DEM simulations that reproduce the macroscopic experimental properties. The proportion of frictional contacts, $\hat{f}$, can be calculated [63], and indeed it is found to have the assumed ϕ-independent functional form, Fig. 3.6(a). Such simulations also allow verification of the presence of backwards bending flow curves below ϕ_m [64], as the small system size simulated allows the local flow curve to be probed without inhomogeneities developing, Fig. 3.6(b). As forces on the particle level can be identified, the contact network can be visualised, Fig. 3.6, demonstrating the development of frictional force chains (red) in the compressive direction as the suspension thickens.[10]

3.4 Testing the WC model: beyond standard rheometry

Up until this point, we have focussed almost entirely exclusively on the steady-state shear-stress response of homogeneous suspensions. Although an extensively researched aspect of suspensions, it represents only a subset of suspension behaviour, a far broader range of which is of interest in both industrial application and in investigating the underlying physics. Here we review several non-steady-shear experiments and explain how they support the frictional model of shear thickening.

[10]Interestingly, for volume fractions exhibiting DST, $\phi = 0.56$, the force contact network appears less anisotropic in the thickened state.

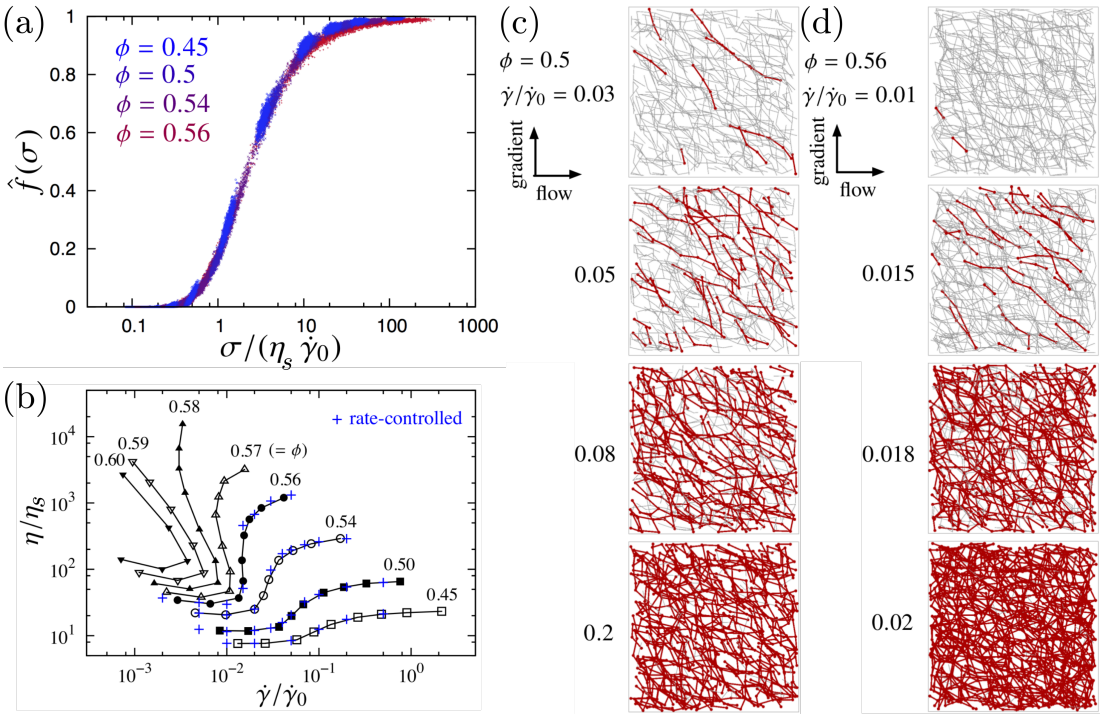

Figure 3.6 Revealing the microscopic behaviour of shear-thickening suspensions using simulations. (a) Fraction of frictional contacts, $\hat{f}(\sigma)$, as a function of stress for multiple $\phi < \phi_m$. Shear rate, $\dot{\gamma}$, normalised by $\dot{\gamma}_0 = 2F^*/3\pi\eta_s d^2$. Figure adapted from Ref. [63]. (b) Stress-controlled DEM simulations (black symbols) for a small system size; relative viscosity, η/η_s, *vs* non-dimensional shear rate, $\dot{\gamma}/\dot{\gamma}_0$. Blue symbols, rate controlled simulations in the CST regime. Figure adapted from Ref. [64]. (c) and (d) Force contact networks in simulations of shear-thickening suspensions. Frictionless contacts between particles are drawn with grey segments, with frictional contacts in red. Increasing shear rate (labelled) from top to bottom. (c) Change in contact network for a CST transition at $\phi = 0.50$. (d) A corresponding contact network for the DST transition at $\phi = 0.56$. Figures (c) and (d) adapted from Ref. [63].

3.4.1 Granulation

A prime example of an industrial process involving suspension flow is wet granulation, which allows more predictable handling and transport of fine powders in an agglomerated form. A high-volume-fraction suspension is sheared to form separate granules that remain jammed, this is a process seen in many shear thickening suspensions [44, 65]. The WC model gives physical insight into this process: the preparation of a suspension with $\phi_m < \phi < \phi_{\mathrm{rcp}}$ is possible at low stresses without forming frictional contacts; when sheared the suspension frictionally shear jams, homogeneous flow is not possible and granules form; finally, a confining pressure from surface tension keeps the particles in the jammed frictional state [66]. Similar arguments can be applied to dry granulation where the background solvent is gradually added to a sheared powder bed [67].

3.4.2 Shear reversal

As for suspensions in the intermediate size regime inertia is negligible, the Navier-Stokes equations governing the hydrodynamic interactions of the particles become time reversible.[11] Therefore, for a suspension at steady state (viscosity $\eta^{\infty}_{\mathrm{rev}}$) when shear is reversed, the hydrodynamic forces should remain fixed in magnitude but change direction. In contrast, the contact forces for hard particles should vanish immediately upon reversal [68]. This then allows the separation of the hydrodynamic contribution to the viscosity (η^{0}_{rev}, the viscosity immediately on reversal) and the contact contribution ($\eta^{\infty}_{\mathrm{rev}} - \eta^{0}_{\mathrm{rev}}$, the increase in viscosity from reversal to steady state), Fig. 3.7(a).[12] Applying this process at increasing applied shear rate allows the separation of the hydrodynamic and contact contributions through the shear-thickening transition, Fig. 3.7(b). For two model hard-sphere suspensions, the increase in the steady state viscosity is driven exclusively by an increase in the contact contribution, Fig. 3.7(b) and (d). Although, the reversal technique does not directly distinguish friction, only contact, the increasing contact contribution is consistent with frictional contact in the WC model and DEM simulations of reversal [70], Fig. 3.7(e). Again simulations allow microscopic analysis and the hydrodynamic contribution can be additionally separated from

[11] This requires the additional assumptions of solvent and particle incompressibility, along with neglection of gravity over the course of the measurement.

[12] Strictly, the decomposition of viscosity contributions only applies to hard-contact interactions, introducing finite-range repulsion, that can rapidly separate the particles on reversal, may change the apparent hydrodynamic contribution [69].

the contact contribution using particle-level forces, Fig. 3.7(f). The agreement between the two approaches in DEM simulations confirms the validity of deducing the contributions from the reversal viscosities, $\eta_{\mathrm{rev}}^{0/\infty}$. Therefore, the shear-reversal technique provides strong evidence for the validity of the frictional model of shear thickening and a useful technique to separate contributions to viscosity based on reversal symmetry arguments.

3.4.3 Avalanche angle

The presence of frictional mechanical contact in the the thickened state can also be cleverly demonstrated using techniques adapted from dry granular materials [71]. Allowing non-density matched particles to sediment in a drum and then by slowly rotating the drum, the avalanche angle, θ, can be found. This is the steepest angle that a pile can support its own weight at. Practically a quasi-static angle is measured, with a slowly flowing layer of particles moving down the surface of the slope. As gravity exerts both the shear stress, σ, and the confining pressure, p, the angle of the slope sets a ratio $\mu = \sigma/p = \tan(\theta)$ throughout the sample. Approaching jamming, i.e. with the drum rotated slowly, μ is an increasing function of the interparticle friction coefficient. For frictionless particles $\mu \approx 0.1 \Rightarrow \theta = 6^\circ$ [55] and in frictional suspensions $\mu \approx 0.4 \Rightarrow \theta \approx 25^\circ$ [72]. By measuring the quasi-static avalanche angle and macroscopic μ, the microscopic μ_p can then be deduced. Taking a shear-thickening suspension of silica spheres, in the un-thickened state (gravitational confining pressure in the flowing layer $p \ll \sigma^*$) $\theta = 6^\circ$, which shows that the particles behave as though frictionless. Increasing the ionic strength of the solvent, thus reducing the repulsive force between particles such that in the flowing layer $p \gg \sigma*$, $\theta \approx 30^\circ$, this implies that in the thickened state $\mu_p \gg 0$. Such an experiment succinctly demonstrates that static "dry contact" does exist in a shear-thickening suspension.

3.5 Returning to the microscale

So far we have focussed, at least experimentally, on the macro-scale, dealing with averaged stresses and viscosities. Microscopic forces have been inferred through scaling arguments and simulations. Although the techniques are beyond the scope of this thesis, it is instructive to discuss direct measurements of interactions on

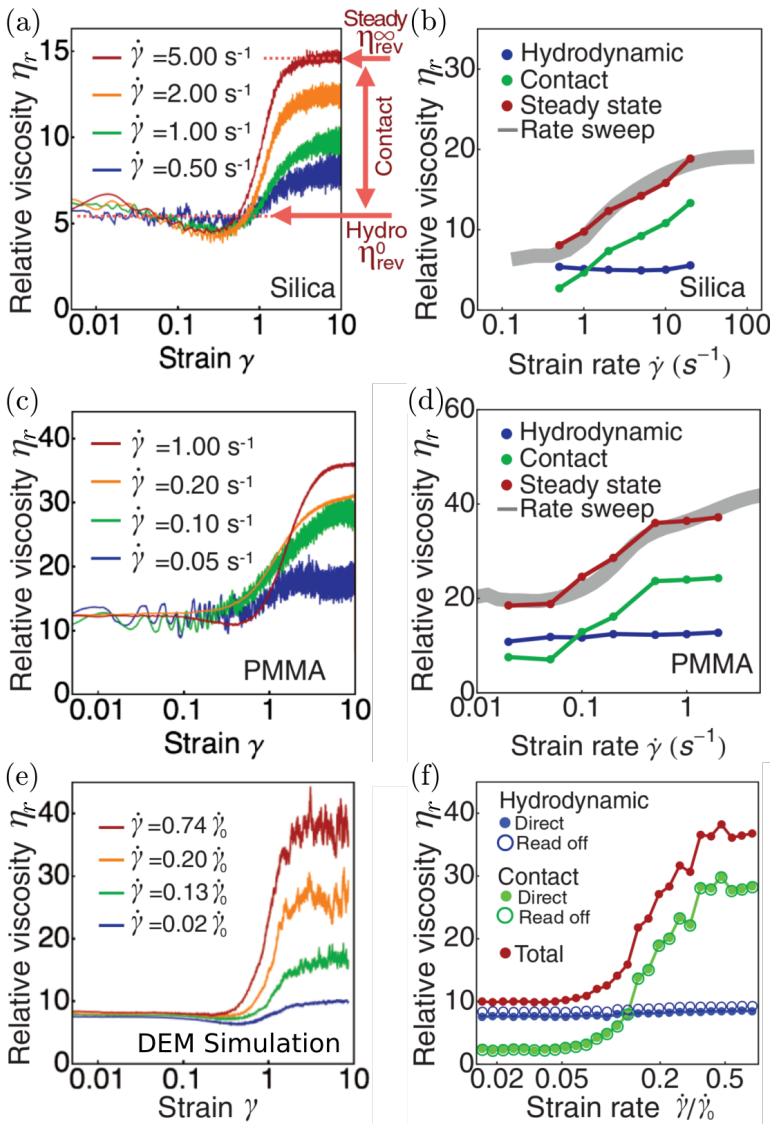

Figure 3.7 Separation of hydrodynamic and contact contributions to viscosity through shear reversal. (a) Strain-dependent reversal response for a silica suspension at $\phi = 0.49$: relative viscosity, η_r, as a function of reversal strain, γ, at various labelled shear rates, $\dot\gamma$. Red arrows indicate separation of viscosity components: total steady-state viscosity, $\eta^{\infty}_{\rm rev}$; hydrodynamic component on reversal, $\eta^{0}_{\rm rev}$; and contact contribution from increase, $\eta^{\infty}_{\rm rev} - \eta^{0}_{\rm rev}$. (b) Contributions to viscosity as a function of shear rate through the CST transition, as labelled. Grey, conventionally-measured steady-state viscosity from separate rate sweep. (c) and (d) Equivalent figures for sterically-stabilised PMMA in a silicone polymeric fluid at $\phi = 0.51$. (e) and (f) Equivalent figures for DEM simulations at $\phi = 0.51$, $\dot\gamma_0$ defined as in Fig. 3.6. Additionally displayed in (f) are direct readings of hydrodynamic and contact components of the stress. Figure adapted from Ref. [70].

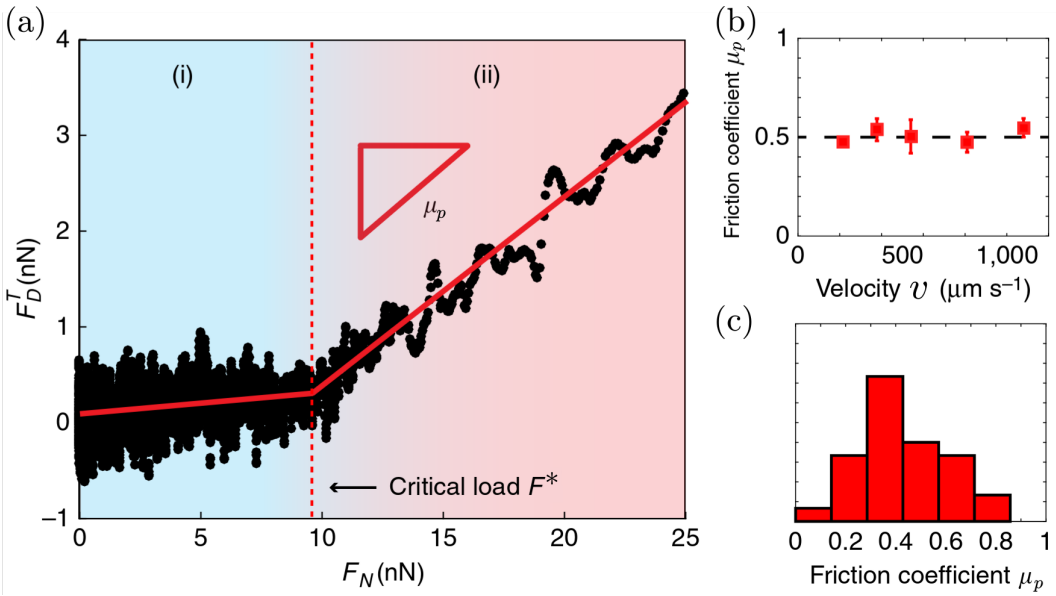

Figure 3.8 Particle-level interactions. (a) Dissipative component of tangential force, F_D^T, *vs* conservative normal load, F_N. Regions: (i) Lubricated region, $\mu_p \ll 1$; (ii) frictional region, $\mu_p \approx 0.5$. (b) Velocity dependence of measured friction coefficient. (c) Distribution of measured friction coefficients for multiple particle pairs. Adapted from Ref. [73].

the single particle level and the issues these raise for current models of shear thickening.

3.5.1 Atomic force microscopy

To investigate frictional interactions between microscopic particles both normal and tangential forces need to be simultaneously measured at low loads, typically nanonewtons. This can be accomplished using a quartz tuning fork atomic force microscope [73]. The technique has been successfully applied to a pair of $d = 0.6\,\mu\text{m}$ polyvinyl chloride (PVC) particles in plasticiser, which creates a sterically stabilised system [73]. With increasing normal load, at a critical force, $F^* \approx 10\,\text{nN}$, there is a transition: from a weak tangential interaction, consistent with hydrodynamic lubrication, to a stronger velocity-independent interaction, consistent with sliding friction with $\mu_p \approx 0.5$. The calculated μ_p is independent of velocity within the measured range, Fig. 3.8(b), which corresponds to the relative velocity of particles at thickening, $\sim \dot{\gamma}_c$. Using this technique it is not possible to measure static friction coefficients. The critical force, at the change in tangential interaction, corresponds well with the onset stress for shear thickening,

$F^*/d^2 \sim \sigma^*$, supporting the theory that shear thickening in suspensions is driven by the onset of friction between particles.

3.5.2 Dissipation mechanism

Directly studying the interaction between two particles emphasises that the challenge is ultimately to bridge scales: systematically relating the microscale, at the particle surface level, to macroscopic rheology. In the WC model the limiting jamming volume fractions, ϕ_m and ϕ_{rcp}, have a close relation to a physical process, static jamming with and without friction respectively. Away from jamming, the model relies on purely empirical equations. We now separately consider what processes drive dissipation and how they may scale.

In the lubricated regime all forces are hydrodynamic and scale as $\eta_s\dot{\gamma}$. All dissipation, which ultimately leads to the viscosity, must come from hydrodynamic forces, whether drag on particles due to non-affine motion [74] or lubrication forces. In the frictional regime, there is in fact the same scaling, although this does not mean that hydrodynamic forces dominate [7]. Mechanical contact forces between particles can be far larger than drag and lubrication close to jamming, $\eta_s\dot{\gamma}$ simply sets a scale for the contact forces. The dominance of contact forces is measured by the viscous number, J, which compares viscous forces to the confining pressure $J = \eta_s\dot{\gamma}/p$, and J goes to 0 at jamming, i.e. $\eta_r \to \infty$. If contact forces dominate at high η_r, this turns the question as to how dissipation away from pure hydrodynamic interaction occurs. (Note that normal forces for hard particles do not contribute to dissipation.)

In simulations systematically varying the interparticle friction coefficient in the Coulomb model [75], the dissipation mechanism is found to depend on μ_p and proximity to jamming, Fig. 3.9. Away from jamming, $J \gg 0$, dissipation is always dominated by solvent-mediated forces, with particles sliding (low μ_p) or rolling (high μ_p) relative to one another. However, close to jamming the dissipation mechanism depends on the value of μ_p. For $\mu_p \to 0$ there are obviously no frictional forces or dissipation; increasing μ_p, the dissipation directly from friction increases, as most contacts are still sliding (relative velocity) but against a frictional force. Direct frictional dissipation peaks at $\mu_p \approx 0.1$, above this contacts are now prevented from sliding by the large frictional forces. For large μ_p, dissipation is then again dominated by viscous drag, but now it is due to increased non-affine motion through the solvent approaching jamming [76].

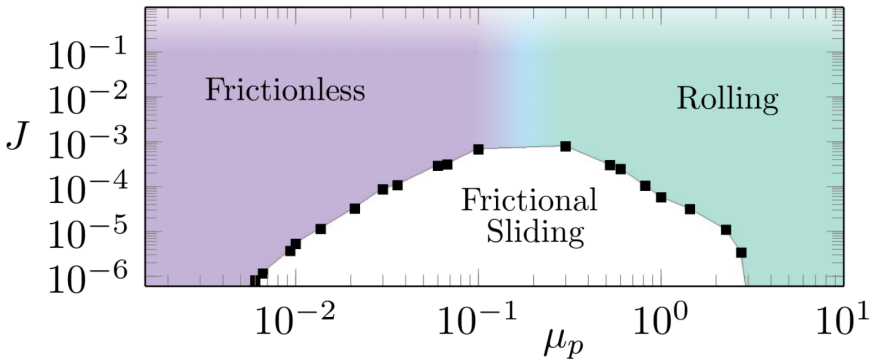

Figure 3.9 Microscopic dissipation mechanisms. Suspension dissipation regimes as a function of viscous number, $J = \eta_s\dot{\gamma}/p$ (the ratio of viscous forces to confining pressure), and interparticle friction coefficient, μ_p. Black squares, value of J at which direct dissipation from sliding friction is equal to viscous dissipation from solvent-mediated interactions. Regimes: frictionless (purple), particles predominantly slide (relative tangential motion) and dissipation viscously dominated; frictional sliding (white), particle predominantly slide but dissipation frictionally dominated; and rolling (green), particles predominantly roll and dissipation is viscously dominated. Adapted from Ref. [75].

3.5.3 Beyond the Coulomb model

Much of the literature since the introduction of the WC model has in fact focussed on sliding friction: sliding friction coefficients are measured in microscopic experiments [73, 77, 78] and the concept of dissipation direct from sliding friction has become entrenched [79]. Caution must, however, be urged on this point.

It should first be noted that measured friction coefficients are not large enough to explain the rheological response in the current framework. For DEM simulations to match the rheology of PVC suspensions[13], a larger interparticle friction coefficient must be used ($\mu_p = 1$ compared to 0.5 [73]), giving a lower frictional jamming volume fraction, Fig. 3.2(a). Similarly, for rough silica particles measured against equivalent flat surfaces, in the high normal load regime $\mu_p \lesssim 0.1$, and this is highly inconsistent with DST being seen for ϕ significantly below random close packing. Large decreases from ϕ_{rcp} to ϕ_m are generic for shear-thickening suspensions, seen in both PMMA [24] and silica suspensions [56], this implies that large high-stress friction coefficients ($\mu_p \gtrsim 1$) are generic.

Secondly, during microscopically-measured sliding contact, strong variation of

[13]Requiring relative shifts in ϕ to compensate for the high polydispersity of the PVC particles.

the tangential force is seen, approaching stick-slip motion, with maximum loads up to 5 times higher than the average [78]. Together, these suggest that it is *static*, rather than sliding, contact properties that are relevant to shear thickening, e.g. the minimum force required to slide from asperity interlock. To capture this behaviour one must go beyond the simple Coulomb model of friction. A static friction coefficient higher than the sliding friction coefficient would describe: stick-slip motion in particle-level measurements [78],[14] the large drop in maximum packing fraction from ϕ_{rcp} to ϕ_m and the moderate friction coefficients measured in sliding tests. If a static friction coefficient larger than the sliding coefficient does indeed exist, dissipation in shear-thickening suspensions would be due to induced non-affine motion, rather than directly from sliding friction, Fig. 3.9.

3.6 Conclusion and outlook

The discussion over the possible difference between static and sliding friction coefficients illustrates both the advantages and the limitations of the WC model. A major advantage is in giving an analytically tractable framework to interpret experimental results and a physical picture to understand how variations on the particle surface level lead to changes in the macroscopic rheology. Such insights are vital in industry, giving a handle on what particle properties to tune to give the desired effects, even when precise matching of model and experiment are not possible.

Equally though, there is a limit on the information about the microscale from the rheological response. For example, we can deduce that there is an enhanced tangential interaction between particles that is captured by a large friction coefficient in a Coulomb friction model. However, we cannot directly infer surface-level details on what that interaction is, e.g. asperity interlock, inter-digitating polymer brushes, etc. Similar ambiguity exists for the maximum repulsive force, F^*, between particles preventing frictional contact [24], hence the lack of detailed discussion to date on this aspect. Only through systematic variation of particle properties can deductions be made. For example, varying d, a constant force is found for sterically-stabilised PMMA particles, suggesting the origin of the repulsive force is from Brownian motion of the particle being truncated at

[14] Stick-slip motion, alternating between pinning and rapid motion, arises for such a decreasing friction coefficient when considering the measurement system, which is idealised as a block with mass attached to a spring moved at a constant velocity [50].

a contact lengthscale set by the stabilising polymer brush [24]. Thus, many questions remain open regarding details on the particle-surface level. However, the presence of mechanical contact in suspensions is now widely accepted and it is the ramifications of this insight that will form the theme of the rest of this thesis.

Chapter 4

Competing timescales lead to oscillations in shear-thickening suspensions

The WC model of frictional shear thickening deals with the steady-state: the fraction of frictional contacts is a function of stress alone, with no temporal dependence. While it may predict the onset of unsteady or inhomogeneous flow through backwards-bending or shear jamming flow curves, it cannot be applied to describe such spatio-temporally varying flows. The WC model is therefore restricted in application to fitting and predicting rheological behaviour in the continuously shear thickening regime, $\mathrm{d}\dot{\gamma}/\mathrm{d}\sigma > 0,\ \forall\ \sigma$. There is then a limit to the volume fraction at which shear-thickening suspension behaviour can be currently predicted, set by $\phi_{\mathrm{DST}} \lesssim \phi_m$, a volume fraction significantly below random close packing.

In industrial applications there is, however, a consistent demand for use of higher volume fraction suspensions: creating stronger concrete [80] and ceramics; allowing safer storage of mine tailings and reducing water usage in arid areas [81]; or reducing fat content in chocolate [5]. Large stresses must be applied to these suspensions during processing, transport, shaping or mixing. At these increased volume fractions instabilities may then occur. If they are not readily predictable or controllable, serious problems could arise, e.g. defects in products during shaping or damage to processing equipment.

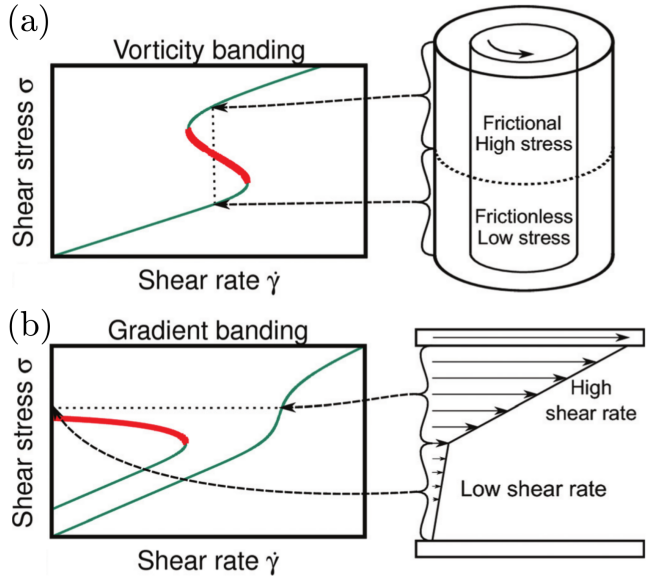

Figure 4.1 Banding in suspensions. (a) Schematic of vorticity banding for a suspensions with a homogeneous volume fraction, ϕ, in DST regime, $\phi_{\mathrm{DST}} < \phi < \phi_m$. Left, underlying flow curve with: green, stable regions, where $(\mathrm{d}\sigma/\mathrm{d}\dot{\gamma} > 0)$; and, red, unstable regions, where $(\mathrm{d}\sigma/\mathrm{d}\dot{\gamma} < 0)$. Right, geometry schematic: bands have common $\dot{\gamma}$ and different σ. (b) Schematic of gradient banding in an inhomogenous suspension split into region with a volume fraction below DST regime, $\phi < \phi_{\mathrm{DST}}$, and a region in the shear-jamming regime, $\phi > \phi_m$. Left, flow curve of shear jamming volume fraction, $\phi > \phi_m$ and CST volume fraction, $\phi < \phi_{\mathrm{DST}}$. Colours as in (a). Right, flow schematic: bands have a common σ and different $\dot{\gamma}$. Adapted from Ref. [82].

4.1 Unsteady flow phenomena

We should first briefly turn to why backwards-bending regions of the flow curve are expected to be unstable, following the arguments of Ref. [82]. Consider an initially homogeneous suspension with an applied average stress in this backwards-bending region and for which $\mathrm{d}\sigma/\mathrm{d}\dot{\gamma} < 0$. The shear rate across the sample (flow and vorticity directions) is always equal, but stress is not controlled locally. Regions with a higher than average viscosity (due to, e.g., fluctuations) will have a higher stress. This higher stress then drives the local viscosity even higher (as $\mathrm{d}\eta/\mathrm{d}\sigma > 0$), which further increases the stress, creating a vicious cycle. Similarly, areas of low viscosity will decrease further and the suspension is expected to separate into regions of high stress and regions of low stress, such

inhomogeneous flow is known as banding.[1] For bands aligned perpendicular to the flow direction, this is vorticity banding, Fig. 4.1(a). One might first expect this to be a stable solution; however, for the bands to be steady and without particle migration, they must have the same particle pressure. This fixes them to the same frictional state, $\hat{f}$ [8]. As the bands also share a common shear rate, the volume fractions must be the same, as flow curves $\sigma(\dot{\gamma}, \phi)$ do not cross. The two 'bands' are therefore identical, a contradiction, and steady vorticity banding is precluded.[2]

Banding could also occur across the gap, with bands having a common σ and differing $\dot{\gamma}$, a situation known as gradient banding, Fig. 4.1(b). Again, at steady-state particle pressure, p, must be equal between the bands, fixing the frictional state. In systems with a fixed interparticle friction coefficient, the macroscopic friction coefficient, $\mu = \sigma/p$, is a single-valued function of ϕ. As σ and p are equal in both bands, ϕ must again be equal: steady gradient bands are precluded.[3]

Flow in the backwards bending regime is therefore expected to be time dependent. This prediction is consistent with experimental observations of suspensions in the DST regime; under imposed stress sudden jamming events are seen, with rapid drops in $\dot{\gamma}$, Fig. 4.2(a) and Refs. [82, 85–88], while under imposed rate, σ can suddenly spike, Fig. 4.2(b) and Refs. [43, 89].

4.1.1 Probing local properties

The previous experiments, Fig. 4.2, all report macroscopic quantities, average stress and apparent shear rate, as standard shear rheometry cannot access the local quantities needed to see if the system bands. To examine the local velocities, stresses or volume fractions techniques beyond standard rheometry have recently been applied to suspensions in the DST regime.

Local stresses on the boundaries of a sheared suspension can be measured by

[1] Banding is 'expected' as such negative constitutive relations are generally found to have unstable homogeneous solutions [62], although as no general proof is to me, I cannot say it is a sufficient condition. It is also not a necessary condition: edge effects can induce apparent banding even without a negative local constitutive relation [83].

[2] Vorticity bands could be stabilised by normal stress differences, and cannot be fully ruled out. Such normal stress differences are not, however, found [84] and ultimately unsteady inhomogeneous flow is in fact observed, see below.

[3] A jammed band can coexist with a steady flowing band if the μ value in the jammed band can take on a different value to the limiting values of $\mu(\phi \to \phi_J^-)$.

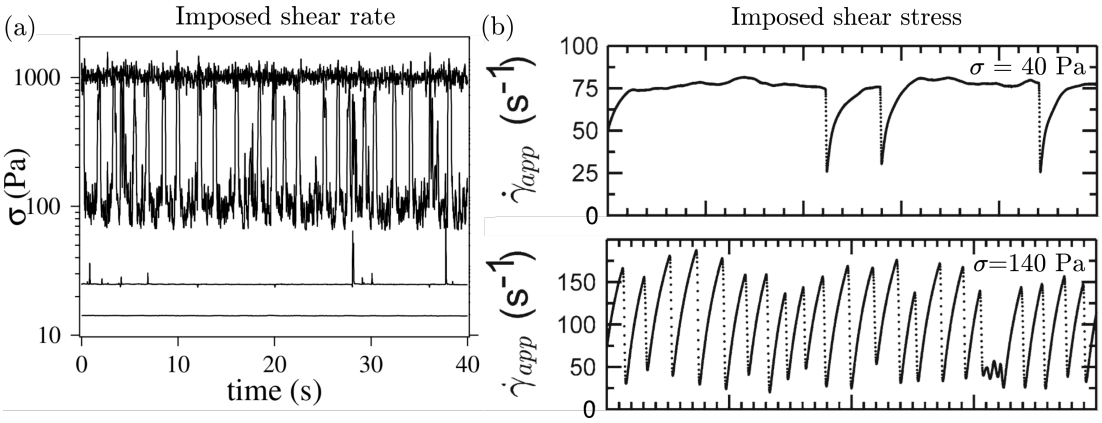

Figure 4.2 Transient jamming of shear-thickening suspensions. (a) Time-dependent measured shear stress under imposed shear rate for $\dot{\gamma} = 80\,\mathrm{s}^{-1}$, $190\,\mathrm{s}^{-1}$, $1000\,\mathrm{s}^{-1}$, $2200\,\mathrm{s}^{-1}$, listed for traces bottom to top. Adapted from Ref. [89]. (b) Time-dependent measured shear rate under imposed stress for 40 Pa (top) and 140 Pa (bottom). Adapted from Ref. [85].

monitoring the deflection of a thin, elastic coating on the geometry surface: boundary stress microscopy [90]. Under imposed average σ, the local stress remains homogeneous when ϕ is significantly below ϕ_m. Just below $\phi \approx \phi_m$, at the onset of thickening the stress becomes localised in travelling bands (layered in the flow direction) that accompany the appearance of a time-dependent shear rate, Fig. 4.3(a). Above $\phi \approx \phi_m$, there are transient static high-stress regions.[4] Unfortunately boundary stress microscopy can only report local stresses and local velocities must be measured separately, for example, using ultrasound velocimetry [91]. Shearing a cornstarch suspension in narrow-gap Couette cylinders, in the DST regime vorticity (not flow) bands form, with a flow-direction velocity signature, Fig. 4.3(b). With a highly system-specific response, this suggests a more complex coupling of variations in stress, velocity and volume fraction.

Unfortunately one cannot accomplish simultaneous measurements of all quantities of interest in a single experiment. In simulations, although all variations can be measured simultaneously, there are severe limitations on system size, and instabilities must be 'forced' by making the system large ($\gg d$) in only one dimension [92]. When the vorticity direction is large, travelling bands are seen, Fig. 4.3(c); however, with a velocity signature in only the vorticity direction, and

[4]The authors of Ref. [90] identify the first inhomogeneous regime as CST, as when time averaged $\mathrm{d}\dot{\gamma}/\mathrm{d}\sigma > 0$, nominally CST. Strong time dependence is seen and the effect of the soft boundaries are not clear, such inhomogeneous flow therefore suggests it is locally DST.

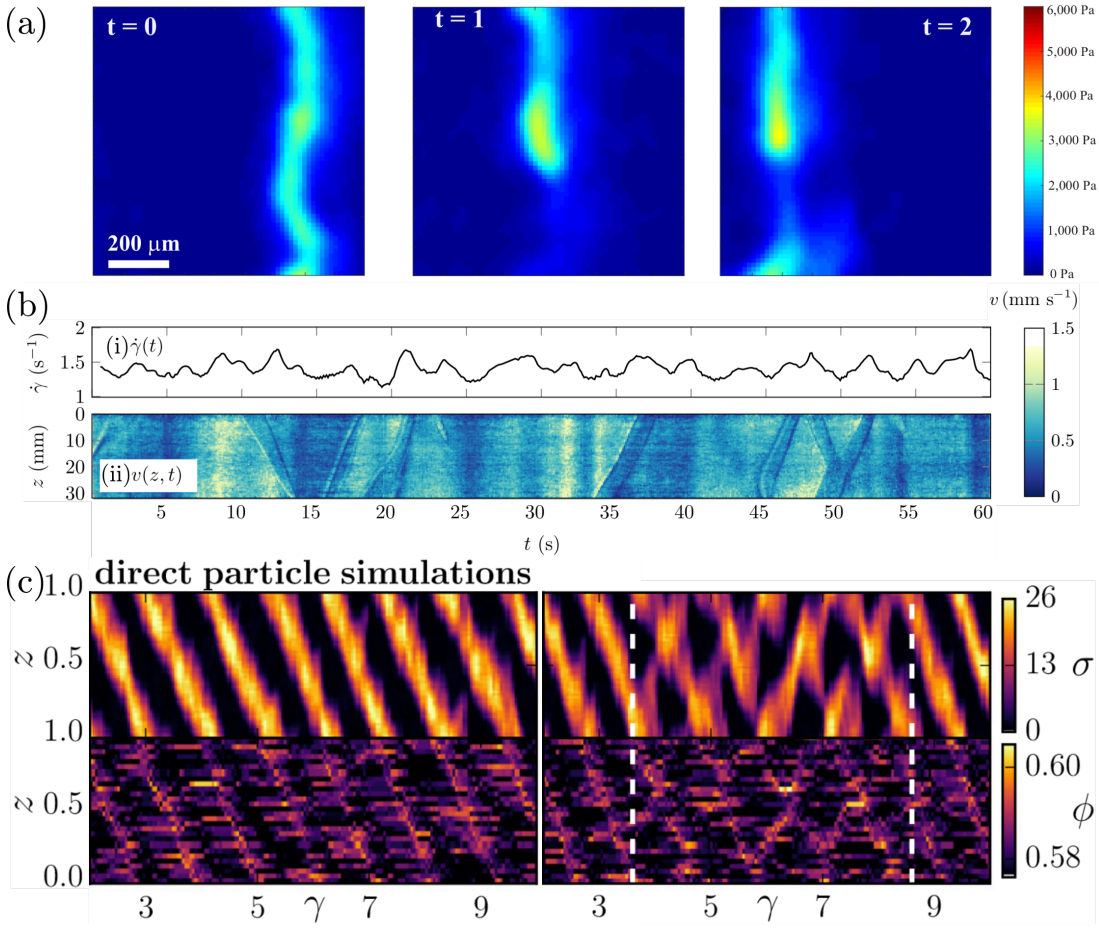

Figure 4.3 Locally-measured banding phenomena. All values are indicated by the corresponding colour gradient (far right). (a) Stress inhomogeneity in a silica suspension. Boundary stress microscopy images: local stress measured over time, frames left to right with total elapsed time 2/7 s. Stress-scale indicated by colour (far right) with flow direction to the right. Adapted from Ref. [90]. (b) Velocity inhomogeneity in a cornstarch suspension. (i) Macroscopic apparent shear rate, $\dot{\gamma}$, over time, t. (ii) Corresponding velocity in the flow direction measured using ultrasound and as a function of height, z (vorticity direction) and time, t. Velocity scale indicated by colour (far right). Adapted from Ref. [91]. (c) Stress and volume fraction inhomogeneities in DEM simulations. Top, stress variation as a function of z (spatial coordinate in vorticity direction) and strain, γ. Bottom, corresponding volume fraction variation, ϕ. Note that boundary conditions are periodic. Left, travelling bands regime; right, transient appearance of locally oscillating bands. Adapted from Ref. [92].

not the flow direction, the link to Ref. [91] is unclear. In summary, this leaves the picture of how shear-thickening suspensions behave dynamically deeply unclear, even in simple rheometric geometries. We therefore aim to find the minimal description of flow in the unstable regime, beginning with time-dependent but spatially homogeneous flow and focussing on describing highly asymmetric shear-rate oscillations at the onset of shear thickening [82, 85, 87, 88]. We believe that it is a necessary prelude to developing a more complete method to understand, interpret and tune instabilities in the DST regime in future work.

4.2 Constructing a minimal model

The state variable of the suspension in the WC model, describing the transition from a frictionless to frictional viscosity branch, is the steady-state fraction of frictional contacts, $\hat{f}$. At steady-state, this is determined entirely by the shear stress, i.e. $\hat{f}(\sigma)$, but when the system is evolving with time the fraction of frictional contacts must become a dynamic variable, $f(t)$. The structure of the frictional contact network depends on the applied stress [63], and it must adapt as the stress changes, consistent with the concept of 'fragile' granular materials [93]. Adaptation takes finite time; therefore, in general during non-steady flow, $f(t)$ will differ from the instantaneous steady-state value, e.g. on reversal [69, 70]. In constructing a suitable form for the evolution of $f(t)$, the WC model must be recovered at steady state: f must evolve towards $\hat{f}$. Secondly, as the WC model considers athermal inertialess spheres with short-range interactions, the development of the frictional contact network and the evolution of f will be driven by the accumulated strain (so changing with a rate $\mathrm{d}f/\mathrm{d}t \propto \dot{\gamma}$), see, e.g., the reversal response Fig. 3.7. Adapting previous work [64, 94] to the WC model, we use the simplest functional form to capture these properties,

$$\frac{\mathrm{d}f}{\mathrm{d}t} = -\frac{\dot{\gamma}}{\gamma_0}\left[f - \hat{f}(\sigma)\right], \tag{4.1}$$

with a characteristic strain scale, γ_0, and $\dot{\gamma} \geq 0$.[5] To relate $f(t)$ to the viscosity we use, as with $\hat{f}$ in the steady state, first Eq. 3.3 to calculate the jamming point,

$$\varphi_J(\sigma) \equiv \varphi_m f(\sigma) + \varphi_{\mathrm{rcp}}\left[1 - f(\sigma)\right], \tag{4.2}$$

[5]The strain scale, γ_0, may be different to the reversal strain scale, or the start up strain scale from a quiescent state [95], which relates to the *formation* of a contact network as our γ_0 is the strain scale for continued *evolution* of a contact network.

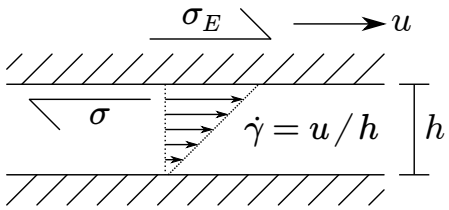

Figure 4.4 Schematic of an idealised rheometric geometry. Hatching, upper and lower plates with relative velocity, u, separation or gap hegith, h. Affine flow in sample (non-hatched region between plates) with shear rate, $\dot{\gamma} = u/h$. Sample stress, $\sigma = \eta\dot{\gamma}$ and external stress applied to plates, σ_E.

where φ is the weight fraction, which we will use in the rest of this Chapter due to the porosity of the main model system, cornstarch in glycerol-water [96]. A similarly modified form of Eq. 3.2 is then used for the relative viscosity,

$$\eta_r(\varphi, \varphi_J) = \frac{\eta}{\eta_s} = \left[1 - \frac{\varphi}{\varphi_J(\sigma)}\right]^{-2}. \tag{4.3}$$

We should note that using the steady-state WC-model equations to relate the dynamic $f(t)$ to η_r makes an implicit assumption that the suspension is completely described by the mean-field parameter, f. This is actually an incorrect assumption, as even for suspensions of a fixed frictional state, the structural evolution cannot be captured by even a rank-2 fabric tensor [97]. We shall discuss in §4.3 why this crudity may not doom the model.

4.2.1 Measurement-system dynamics

We have so far looked at the suspension dynamics in isolation; experimentally though, the suspension in a rheological test is part of a larger system, through which a deformation or stress is applied to a sample and the response measured. We now turn to consider the dynamics of a typical measurement system for imposed-stress rheometry. An external stress, σ_E, is applied through the system boundaries. In a rheometer, this is the 'geometry', which has far a higher mass than the suspension for a typical gap height, h, between the boundaries [98]. We therefore consider only the mass of the geometry and neglect the mass of the suspension, although for unusually large h ($\gg 1\,\mathrm{cm}$) the inertia of the suspension may also be significant [64, 94]. In the steady state, the applied stress is equal to the sample stress, $\sigma_E = \eta(\hat{f})\dot{\gamma}$, and the inertia of the geometry can be ignored. However, when $\mathrm{d}\dot{\gamma}/\mathrm{d}t \neq 0$, force balance between the geometry and the sample

gives

$$\rho_A h \frac{\mathrm{d}u}{\mathrm{d}t} = \sigma_E - \eta(f)\dot{\gamma}, \tag{4.4}$$

with ρ_A the geometry's areal density and u the velocity. Assuming homogeneous flow across the gap, $u = \dot{\gamma}h$, the equation of motion simplifies to

$$\rho_A h \frac{\mathrm{d}\dot{\gamma}}{\mathrm{d}t} = \sigma_E - \eta(f)\dot{\gamma}. \tag{4.5}$$

Physically this means that when $\mathrm{d}\dot{\gamma}/\mathrm{d}t > 0$, the sample stress is lower than σ_E, while when $\mathrm{d}\dot{\gamma}/\mathrm{d}t < 0$, the sample stress is higher. It is only though combining the suspension dynamics with the measurement-system dynamics that more complex behaviour arises.

4.2.2 Non-dimensionalisation

To begin to deduce the interaction between measurement system and suspension, we first measure time in units of the geometry inertial timescale, $t_i = \rho_A h/\eta_s$, and rewrite Eqs. 4.5 and 4.1 as:

$$\frac{\mathrm{d}\dot{\Gamma}}{\mathrm{d}\tau} = \Sigma_E - \eta_r(f)\dot{\Gamma} \equiv g_1(\dot{\Gamma}, f), \tag{4.6}$$

$$\frac{\mathrm{d}f}{\mathrm{d}\tau} = -\frac{\dot{\Gamma}}{\epsilon}\left[f - \hat{f}(\Sigma)\right] \equiv g_2(\dot{\Gamma}, f), \tag{4.7}$$

where $\tau = t/t_{\mathrm{i}}$. Other dimensionless variables are shear rate, $\dot{\Gamma} \equiv \mathrm{d}\Gamma/\mathrm{d}\tau = \dot{\gamma}\eta_s/\sigma^*$; applied stress, $\Sigma_E = \sigma_E/\sigma^*$; viscosity, $\eta_r = \eta(f)/\eta_s$; sample stress, $\Sigma = \eta_r(f)\dot{\Gamma}$; and strain, $\Gamma = \eta_s^2/(\rho_A h\sigma^*)$.

The geometry inertial timescale characterising the measurement system, t_i, then competes with the timescale for contact network evolution from Eq. 4.1 characterising the suspension dynamics, $t_{\mathrm{c}} = \gamma_0\eta_{\mathrm{s}}/\sigma^*$, to yield our key dimensionless parameter,

$$\epsilon = \frac{t_c}{t_i} \equiv \frac{\gamma_0\eta_s^2}{\rho_A h\sigma^*}. \tag{4.8}$$

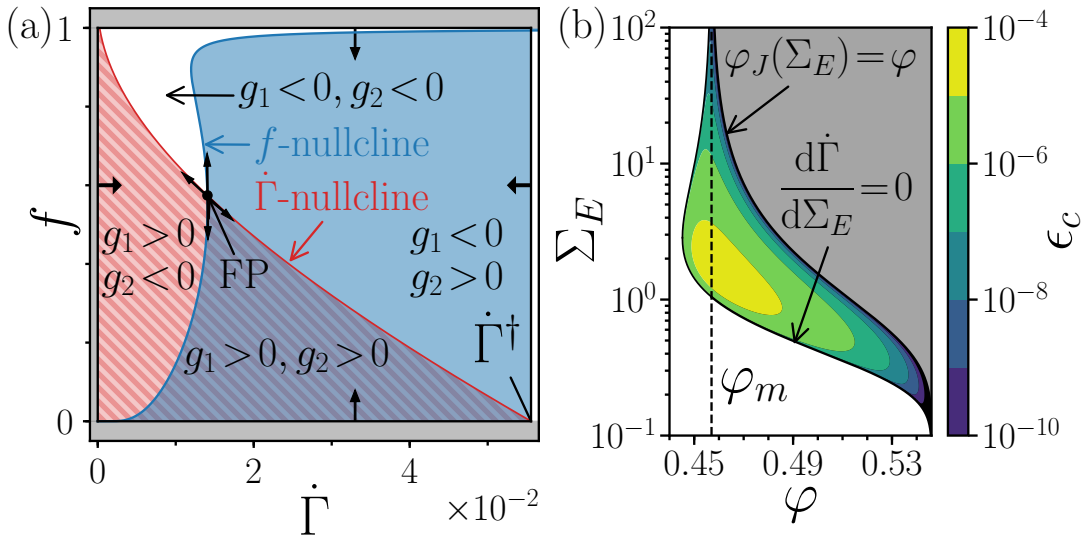

Figure 4.5 Limit-cycle behaviour for Eqs. 4.6 and 4.7. (a) Phase-plane schematic for DST regime, $\varphi_{\mathrm{DST}} < \varphi < \varphi_m$. Red line, $\dot{\Gamma}$-nullcline; red hatched shading, $g_1 > 0$; blue line, f-nullcline; blue shading, $g_2 > 0$. Fixed point (FP) at nullcline intersection, where $g_1 = 0$ and $g_2 = 0$. On the black rectangle, trajectories point inwards, indicating the existence of a limit cycle if FP is unstable. (b) Critical stability criterion value, ϵ_c, from Eq. 4.9, value indicated by colour bar (right). Solid black lines, $\epsilon_c = 0$, at DST onset, $\mathrm{d}\dot{\Gamma}/\mathrm{d}\Sigma_E = 0$, and shear jamming, $\varphi = \varphi_J(\Sigma_E)$; grey shading, shear jammed, $\varphi < \varphi_J(\Sigma_E)$.

4.3 Analysis of a minimal model

Coupling Eqs. 4.6 and 4.7, there are only two degrees of freedom $(\dot{\Gamma}, f)$; as such, the equations can only capture a steady state or a periodic limit cycle [99] and cannot describe the more complex time-dependent behaviour also seen [82, 91]. Analysis of the model can, however, still elucidate some of the essential physics of unsteady flow in shear-thickening suspensions.

4.3.1 Linear stability analysis

For a given weight fraction, φ, and external stress, Σ_E, a fixed point (FP) in the dynamical system occurs where the nullclines, $g_1 = 0$ ($\Rightarrow \mathrm{d}\dot{\Gamma}/\mathrm{d}\tau = 0$) and $g_2 = 0$ ($\Rightarrow \mathrm{d}f/\mathrm{d}\tau = 0$), intersect, Fig. 4.5(a). Performing a linear stability analysis, we examine the Jacobian [99], $J = \begin{pmatrix} \partial g_1/\partial\dot{\Gamma} & \partial g_1/\partial f \\ \partial g_2/\partial\dot{\Gamma} & \partial g_2/\partial f \end{pmatrix}$, which encodes the dynamics about the fixed point. The real parts of the eigenvalues of J determine whether small perturbations will decay (both have negative real parts, stable FP)

or grow (at least one positive real part, unstable FP). The fixed point becomes unstable, undergoing a Hopf bifurcation (both real components becoming positive simultaneously), if[6]

$$\epsilon < \epsilon_c = -\dot{\Gamma}\left(\frac{\mathrm{d}\dot{\Gamma}}{\mathrm{d}\Sigma_E}\right)\bigg|_{\mathrm{FP}}. \tag{4.9}$$

Since ϵ and $\dot{\Gamma}$ are both strictly positive, instability requires $\mathrm{d}\dot{\Gamma}/\mathrm{d}\Sigma_E < 0$, i.e. a backwards-bending flow curve, as previously expected to be required for instability.

Thus, the onset of DST ($\mathrm{d}\dot{\Gamma}/\mathrm{d}\Sigma_E = 0$) forms the lower boundary of our region of potential instability (when $\epsilon \to 0$), Fig. 4.5(b). The upper boundary of this region occurs at shear jamming (SJ), where $\varphi_J(\Sigma_E) = \varphi$ and the flow curve touches the vertical axis so that $\dot{\Gamma} = 0$. Above this boundary no flow is possible.[7] Between these two boundaries, $\epsilon_c(\varphi, \Sigma_E)$ peaks at a value $\epsilon_c^{\max} = 2 \times 10^{-5}$: instability may occur between DST and shear jamming whenever $\epsilon < \epsilon_c^{\max}$, Fig. 4.5(b). The value of $\epsilon_c^{\max}$, reported below for the primary model system of cornstarch in a 50 wt.% glycerol-water mixture (see §4.4 for details), depends weakly on the parameters of the underlying WC model: increasing with greater β and larger difference between ϕ_{rcp} and ϕ_m.

Physically, at such small ϵ ($t_i \gg t_c$), if the geometry is perturbed, e.g. to a slightly higher shear rate, the suspension would thicken before the geometry slows. The sample stress would then rise, driving $\hat{f}$ higher and causing further thickening in a vicious cycle, pushing the system away from the steady state. In contrast, if ϵ is larger ($\epsilon > \epsilon_c$), the geometry would instead lose momentum and return to the steady-state shear rate before the frictional contact proportion could increase and the suspension thicken: the system is stable to the perturbation.

4.3.2 Phase-plane analysis

However, the linear stability analysis only describes the system close to the fixed point. To determine the behaviour far away from steady state we must turn to a phase-plane analysis, in which trajectories in $\dot{\Gamma}$-f space depend parametrically on τ. Consider the regime $\varphi_{\mathrm{DST}} \leq \varphi < \varphi_m$ with $\mathcal{S}$-shaped flow curves.

[6] See Appendix B.1 for derivation.

[7] At the SJ boundary $\epsilon_c \to 0$; this is not just a boundary because flow is precluded above it.

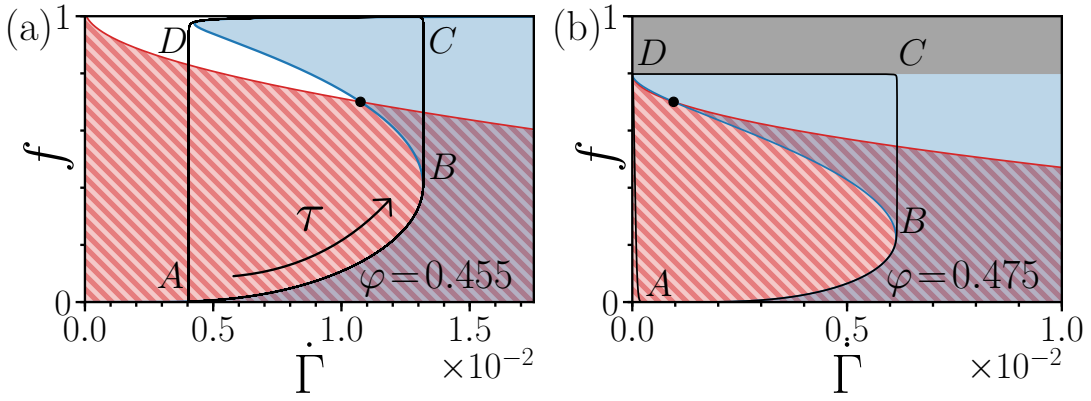

Figure 4.6 Limit-cycle behaviour for Eqs. 4.6 and 4.7. (a) Limit cycle for an $\mathcal{S}$-shaped flow curve: $\varphi = 0.455$ and $\Sigma_E = 3.0$. WC-model parameters: $\varphi_m = 0.457$, $\varphi_{\text{rcp}} = 0.546$ and $\beta = 0.94 \Rightarrow \phi_{\text{DST}} = 0.445$. Black line, numerical solution for $\epsilon = 10^{-9} \ll \epsilon_c$; shading as in Fig. 4.5(a). (b) Limit cycle for SJ flow curve; $\varphi_m = 0.475$ and $\Sigma_E = 3.0$; grey shading, shear jammed and flow forbidden, other parameters and shading as in (a).

The f-nullcline, Fig. 4.5(a), reflects the shape of the steady-state flow curve.[8] Trajectories are set by Eqs. 4.6 and 4.7, which show that trajectories point *inwards* everywhere on the rectangle defined by $\dot{\Gamma} = 0$, $\dot{\Gamma} = \dot{\Gamma}^{\dagger}$ (where the $\dot{\Gamma}$-nullcline intersects the $\dot{\Gamma}$ axis), $f = 0$ and $f = 1$, Fig. 4.5(a).[9] However, trajectories point *outwards* on any infinitesimally-small loop around the fixed point if it is unstable. If $\epsilon < \epsilon_c$, the Poincaré-Bendixson Theorem [99] then predicts a limit cycle in the region depicted in Fig. 4.5(a).

A numerically-calculated limit cycle with Σ_E in the DST regime is shown in Fig. 4.6(a). To understand the processes behind this cycle, we remove explicit time dependence and divide Eqs. 4.7 and 4.6 to obtain

$$\epsilon \left[\frac{\Sigma_E}{\dot{\Gamma}} - \eta_r(f) \right] = - \left[f - \hat{f}(\Sigma) \right] \frac{\mathrm{d}\dot{\Gamma}}{\mathrm{d}f}. \tag{4.10}$$

If ϵ is small, such that the left-hand side of Eq. 4.10 $\to 0$, to maintain equality this requires on the right hand side either $\mathrm{d}\dot{\Gamma}/\mathrm{d}f \to 0$ (vertical lines in phase space) or $f \to \hat{f}(\Sigma)$ (following the f-nullcline). Therefore, for small ϵ, starting at $(0, 0)$, the system follows the f-nullcline ($g_2 = 0$, $g_1 > 0$), Fig. 4.5(b), at a rate controlled by Eq. 4.6 (and hence set by t_i). At B, the system can no longer

[8] On the f-nullcline $f = \hat{f}(\Sigma)$ and as there is a one-to-one dependence of Σ to $\hat{f}$, see Eq. 3.4, the f-nullcline reflects the shape of the flow curve: sigmoidal, $\mathcal{S}$-shaped or shear jamming.

[9] This can be seen by inspection, as $\dot{\Gamma} = 0 \to g_1 > 0$, $\dot{\Gamma} = \Gamma^{\dagger} \to g_1 < 0$, $f = 0 \to g_2 > 0$ and $f = 1 \to g_2 < 0$.

follow the f-nullcline; the shear rate must continue to increase (as $g_1 > 0$), but the f-nullcline begins to bend backwards. Instead, there is a vertical jump to join the 'upper branch' of the f-nullcline at C. The system now follows the 'upper branch' of the f-nullcline with decreasing $\dot{\Gamma}$ ($g_2 = 0,\ g_1 < 0$), until it reaches D. Again, the system can no longer follow the f-nullcline, dropping vertically to A, and the process begins again: we have a limit cycle.

As a consistency check, the 'jump' BC, and hence the limit cycle, relies on $\dot{\gamma}$ not changing ($t \ll t_i$) as a large number of frictional contacts form and the suspension shear thickens ($t > t_c$), i.e. $\epsilon \ll 1$. This is the same physical requirement as for the loss of linear stability. During the large-amplitude cycle, f is then either close to steady state or making a large rapid jump, the precise details of which are unimportant. This binary behaviour may explain why the substitution of $\hat{f}$ for $f(t)$ is successful.

At higher weight fractions, $\varphi > \varphi_m$, Fig. 4.6(b), there is no flowing 'upper branch', instead the jump from B takes the suspension towards jamming at C, $\eta \to \infty$. For small but non-zero ϵ, the left-hand side of Eq. 4.10 is now large and negative. As $f < \hat{f}$ [Fig. 4.6(b) (blue region)], $\mathrm{d}\dot{\Gamma}/\mathrm{d}f$ must also be large and negative, so that the shear rate rapidly drops to D on the $\dot{\Gamma}$-nullcline. Now with $f > \hat{f}$, from D the system drops back to A, again giving a limit cycle. Note that the CD part of the limit cycle probes our system close to jamming. Unlike in conventional steady-state rheometry [14], our system should remain homogeneous: the time and strain needed to traverse CD is simply too short to allow finite particle migration.[10]

4.4 Experimental comparison

To validate our model, we first characterised a shear-thickening suspension known to show oscillations [82]. Cornstarch (Sigma Aldrich, particle diameter $\approx 14\,\mu\mathrm{m}$ and polydispersity $\approx 40\%$ from static light scattering [82]) was dispersed into a 50 wt.% glycerol-water mixture ($\eta_s = 6\,\mathrm{mPa\,s}$). We used a TA Instruments DHR-2 with roughened parallel plates (radius $R = 20\,\mathrm{mm}$ and $h = 1.0\,\mathrm{mm}$ for flow curves, $1.5\,\mathrm{mm}$ for time dependence). From the applied torque, $\mathcal{T}_E$, and

[10]Here we are disregarding bulk particle migration, migration could still occur on much smaller lengthscales, e.g. slip due to depletion near the geometry boundary. Slip as a driving effect, as in microchannels [100], can be ruled out, however, by the presence of oscillations for cross-hatched, roughened or smooth geometries [82].

measured angular velocity, Ω, we report rim shear rates, $\dot{\gamma} = \Omega R/h$, and apparent stresses, $\sigma_E = 2\mathcal{T}_E/\pi R^3$.[11] Cornstarch particles swell or are porous [96]; so, as stated earlier, we quote weight fractions, φ, using freshly-prepared samples and monitoring reproducibility.

4.4.1 Steady-state rheology of cornstarch

In a time-averaged stress sweep (constant σ_E for 30 s, averaging for final 20 s), Fig. 4.7(a), suspensions thicken from a low-stress region at $\sigma_E \lesssim 1\,\mathrm{Pa}$ with approximately constant viscosity (slope = 1 in a log-log σ-$\dot{\gamma}$ plot) to a high-stress viscosity plateau, at moderate φ, or until sample fracture at high φ. From plateau η_r values, the limiting ϕ_J can be determined using Eq. 4.3, with $\varphi_{\mathrm{rcp}} = 0.546 \pm 0.002$ from the minimum of η_r and $\varphi_m = 0.457 \pm 0.001$ from the maximum, Fig. 4.8(a). For a non-Newtonian fluid, as stated in Ch. 2, for parallel-plate measurements a correction must be applied to the apparent stress, σ_E. Writing the corrected stress,

$$\tilde{\sigma} = \frac{\mathcal{T}_E}{2\pi R^3}\left(3 + \frac{\mathrm{d}\ln\mathcal{T}_E}{\mathrm{d}\ln\Omega}\right), \tag{4.11}$$

the relative viscosity, $\eta(\tilde{\sigma})$, can then be used to find the onset stress for the WC model in the CST regime ($\varphi \leq 0.44$), Fig. 4.8(b), giving $\sigma^* = (5.1 \pm 0.3)\,\mathrm{Pa}$ and $\beta = 0.94 \pm 0.03$. Note that the correction cannot be applied in the DST regime (as a one-to-one relationship between σ and $\dot{\gamma}$ is assumed). Therefore, outside of fitting CST data to the WC model, we report apparent stresses throughout this chapter.[12]

Comparing with time-averaged flow curves at $\varphi > \varphi_m$, the WC model works until the predicted flow curve bends backwards, Fig. 4.7(a) (red dashed). Up to this point, the flow is steady: $\dot{\Gamma}$ is constant in time, Fig. 4.7(b). At higher stress, the flow starts to oscillate, Fig. 4.7(c), before becoming aperiodic, Fig. 4.7(d). To see if the model can capture the onset of unstable flow we are looking at two questions: does the model predict an instability? and secondly, does it correctly predict the form of the instability, e.g. frequency and amplitude? To determine this we first need to calculate both t_i and t_c.

[11] As in this chapter we primarily report apparent stresses, to denote the apparent stress we use σ rather than σ_{app}, and when referring to the corrected stress we use $\tilde{\sigma}$.

[12] The distinction between sample and applied stress is dropped for the corrected stress, as it is only applied for steady-state measurements.

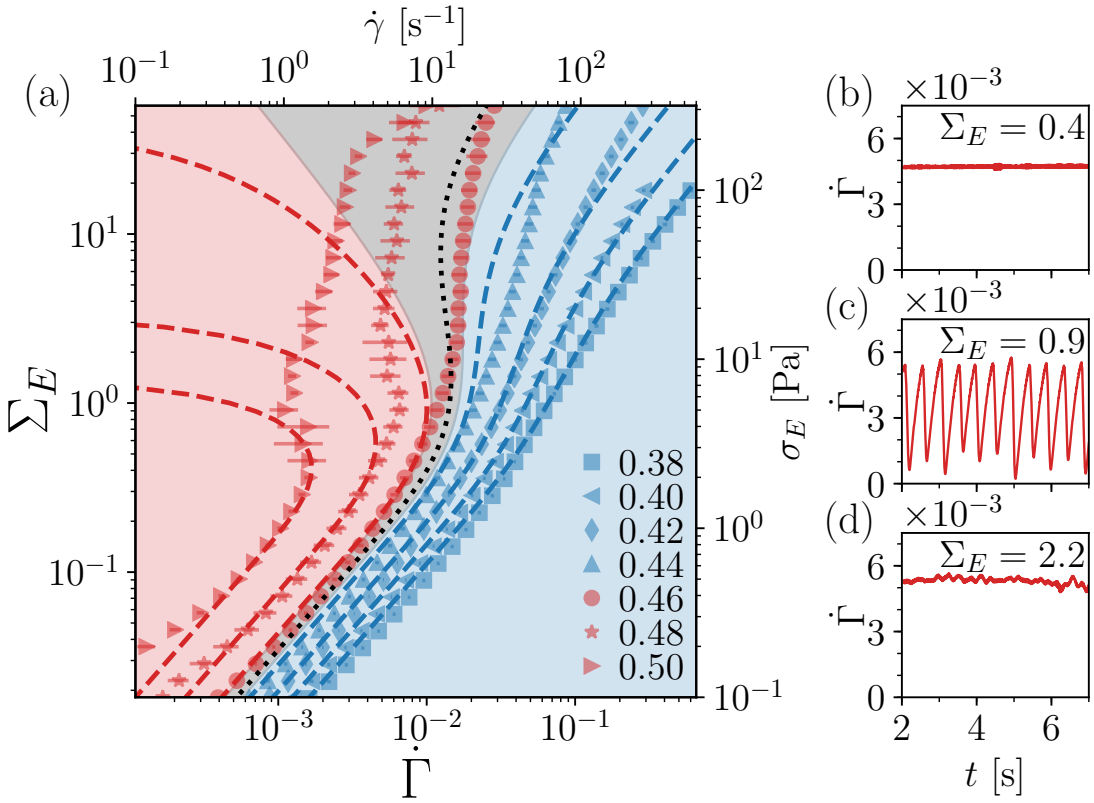

Figure 4.7 Imposed-stress rheology. (a) Flow curves: dimensionless stress *vs* dimensionless average shear rate, $\Sigma_E(\dot{\Gamma})$, and absolute, $\sigma_E(\dot{\gamma})$, at given weight fractions, φ. Dashed lines: WC model for $\varphi_m = 0.457$, $\varphi_{\mathrm{rcp}} = 0.546$, $\beta = 0.94$ ($\Rightarrow \varphi_{\mathrm{DST}} = 0.445$) and $\sigma^\star = 5.1\,\mathrm{Pa}$ at given φ (dashed) and $\varphi = 0.45$ (dotted). Blue, $\varphi < \varphi_{\mathrm{DST}}$; grey, $\varphi_{\mathrm{DST}} < \varphi < \varphi_m$; red, $\varphi > \varphi_m$. Symbols: Σ_E *vs* time-averaged $\dot{\Gamma}$ for cornstarch suspensions in a 50 wt.% glycerol-water mixture. Error bars denote standard deviation from three up-sweeps. (b)-(d) Time-dependent experimental shear rate, $\dot{\Gamma}(t)$, for $\varphi = 0.48$, showing respectively: (b) steady flow below the onset of shear thickening, (c) periodic shear-rate oscillations and (d) aperiodic flow at high stress.

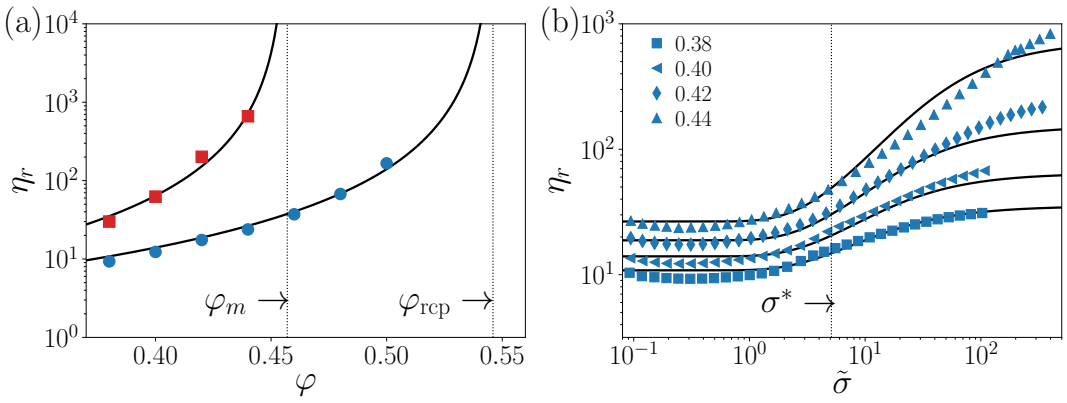

Figure 4.8 Fitting of the WC model to 50 wt.% glycerol-water cornstarch suspension rheology. (a) Plateau relative viscosity values, η_r, as a function of weight fraction, φ. Solid points, experimental minimum (blue circles) and maximum (red squares) relative viscosities. Solid lines are fits to Eq. 4.3 for $\min \eta_r$ and $\max \eta_r$, finding $\varphi_{\mathrm{rcp}} = 0.546 \pm 0.002$ and $\varphi_m = 0.457 \pm 0.001$ respectively. (b) Corrected steady-state rheological data (blue symbols, see legend for φ) and WC-model fit (solid black lines), with $\beta = 0.94 \pm 0.03$ and $\sigma^* = 5.1 \pm 0.3$, value denoted by dotted line.

4.4.2 Calculating the inertial timescale

To measure the inertial timescale, $t_i = \rho_A h/\eta_s$, we need the geometry's areal density in addition to the known background solvent viscosity and gap height. The areal density, ρ_A, was defined in Eq. 4.5, but for rectilinear flow of infinite parallel plates. However, experimentally rotational flows of finite plates are used. The rotational moment of inertia of the geometry, I,[13] must be converted into an equivalent areal density using the equation of motion for the angular velocity, Ω,

$$I\frac{\mathrm{d}\Omega}{\mathrm{d}t} = \mathcal{T}_E - \mathcal{T}, \tag{4.12}$$

with the applied torque from the rheometer, $\mathcal{T}_E$, resisted by the sample torque, $\mathcal{T}$. Using the previously established definitions for the rim shear rate ($\dot{\gamma} = \Omega R/h$) and apparent stress ($\sigma = 2\mathcal{T}/\pi R^3$) the equivalent areal density, ρ_A, is unambiguously defined:

$$\underbrace{\left(\frac{2I}{\pi R^4}\right)}_{\rho_A} h\frac{\mathrm{d}\dot{\gamma}}{\mathrm{d}t} = \sigma_E - \eta\dot{\gamma}. \tag{4.13}$$

[13]The moment of inertia is a combination of the instrument and the tool inertia, both measured in the TA Instruments TRIOS software.

The measured geometry moment of inertia, $I = 44\,\mu\text{Nms}^2$, then gives $\rho_A \equiv 2I/\pi R^4 = 175\,\text{kg}\,\text{m}^{-2}$ and thus, $t_i = 44\,\text{s}$.

4.4.3 Strain-dependent dynamics

To calculate the contact timescale, $t_c = \gamma_0\eta_s/\sigma^*$, the strain-scale for contact network evolution, γ_0, is needed. Since this is inaccessible from steady-state rheometry, we must turn to separate transient experiments. Measuring under imposed rate inertial dynamics are removed and the contact dynamics alone can be probed. From a slowly sheared state ($\sigma \ll \sigma^*$ and $f \approx 0$, for accumulated strain > 1),[14] applying a large shear rate, $\dot{\gamma}^+$ (such that $\sigma = \dot{\gamma}^+\eta(f=0) \gg \sigma^*$ and $\hat{f} \approx 1$), Eq. 4.1 reduces to a solution that is only dependent on the strain, γ, accumulated after the increase in $\dot{\gamma}$ to $\dot{\gamma}^+$,

$$f(\gamma) = 1 - \exp\left(-\frac{\gamma}{\gamma_0}\right). \tag{4.14}$$

Equation 4.14 assumes an instantaneous change in $\dot{\gamma}$; however, experimentally a finite time is required for $\dot{\gamma}$ to change and a new timescale is introduced, the instrument response time, t_s. The step response time can be neglected though, if it is much lower than the time for η to increase, i.e. $t_s \ll \gamma_0/\dot{\gamma}^+$. As t_s is fixed by rheometer choice, we instead must decrease the necessary $\dot{\gamma}^+$ through increasing η_s, using now an 85 wt.% glycerol-water background solvent to suspend cornstarch particles. Due to the uncertainty in volume fractions from porosity and the subsequent use of weight fractions, the steady-state rheology must be remeasured, see Appendix B.2 for details. Using the fitting procedure of §4.4.1, we find: $\varphi_m = 0.452 \pm 0.004$, $\varphi_{\text{rcp}} = 0.545 \pm 0.003$, $\beta = 0.81$ ($\Rightarrow \varphi_{\text{DST}} = 0.445$) and $\sigma^* = (1.3 \pm 0.2)\,\text{Pa}$. The background solvent viscosity, $\eta_s = 75\,\text{mPa}\,\text{s}$, is measured from centrifuged supernatant.[15]

Transient measurements were made using a TA Instruments ARES-G2 rheometer, with cross-hatched parallel plates ($R = 20\,\text{mm}$ and $h = 1\,\text{mm}$), reporting rim shear rates and apparent viscosity as a function of rim strain, γ. To ensure a large increase in viscosity and aid measurement, we use $\varphi \gtrsim \varphi_{\text{DST}}$, applying

[14] Required to develop an anisotropic structure in the frictionless state, otherwise the strain to develop an anisotropic particle structure from the quiescent state would be measured [95].

[15] $\eta_s = 75\,\text{mPa}\,\text{s}$ is less than the viscosity measured before suspension preparation, $110\,\text{mPa}\,\text{s}$, and suggests a lower glycerol proportion in the background solvent, with either dilution due to water stored in the porous cornstarch or preferential absorption of the glycerol by the cornstarch.

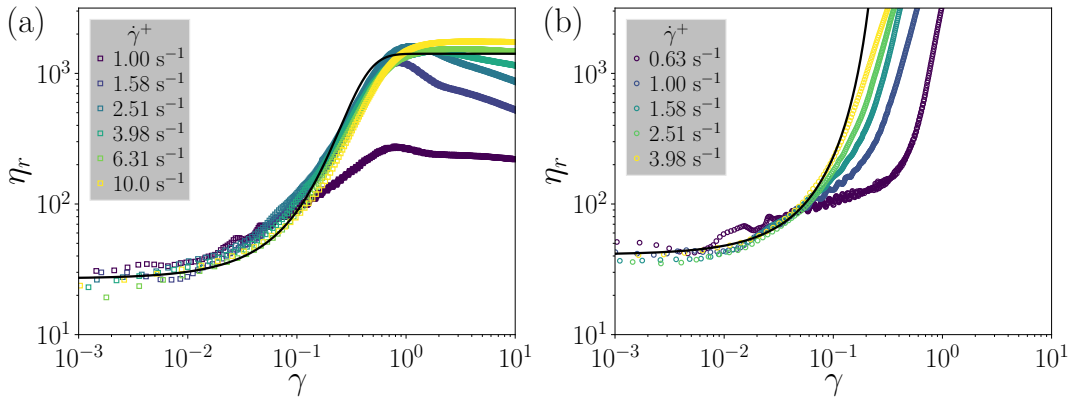

Figure 4.9 Strain-dependent relative viscosity response, $\eta_r(\gamma)$, to a step change in shear rate. (a) $\varphi = 0.44$ cornstarch suspension in an 85wt.% glycerol-water mixture. Open squares: response of η_r as a function of accumulated strain, γ, on changing $\dot{\gamma}$ from $0.01\,\mathrm{s}^{-1}$ to $\dot{\gamma}^+$, see legend. Black line: high $\dot{\gamma}^+$ limit model, using Eq. 4.14 with $\gamma_0 = 0.12$ in Eqs. 4.2 and 4.3, underlying steady-state WC-model parameters ($\varphi_m = 0.452$ and $\varphi_{\mathrm{rcp}} = 0.545$). Note: η_r values for the model have been shifted a factor of 0.4 to aid fitting by eye. (b) $\varphi = 0.46$, otherwise as (a).

$\dot{\gamma} = 0.01\,\mathrm{s}^{-1}$ before stepping to $\dot{\gamma}^+ \gtrsim 1\,\mathrm{s}^{-1}$ and measuring the response for 10 strain units, Fig. 4.9.[16] We show transient viscosity measurements, $\eta_r(\gamma)$, at multiple $\dot{\gamma}^+$ for $\varphi = 0.44$, Fig. 4.9(a), and $\varphi = 0.46$, Fig. 4.9(b), points.

For sufficiently high $\dot{\gamma}^+$ ($\geq 1.58\,\mathrm{s}^{-1}$, Fig. 4.9), the increase in viscosity occurs at a constant critical strain, with excellent collapse for $\varphi = 0.44$[17] and adequate collapse for $\varphi = 0.46$. An estimate of γ_0 can be extracted by comparison with the large $\dot{\gamma}^+$ limit prediction of $\eta_r(\gamma)$, that uses $f(\gamma)$ from Eq. 4.14 in Eqs. 4.2 and 4.3 (black trace). To aid in fitting the model prediction is shifted by a factor of 0.4 (as the error in γ, not η_r, must be minimised). A value of $\gamma_0 \approx 0.12$ is found to reasonably match viscosity traces for both $\varphi = 0.44$ and 0.46. This does not rule out variation of γ_0 over larger a range of φ, although these volume fractions would be beyond the range of interest for instabilities, $\varphi \sim \varphi_m$. Finally, to ensure that this analysis was valid, we must verifying that

[16] The large change in viscosity is required due to the high noise level inherent to transient measurements with the lack of temporal averaging. A large change in η means a commensurately large change in f. Note that Eq. 4.1 is derived for small changes in f [linear in $(f - \hat{f})$ it can be considered the first order term in a series expansion]; the technique will therefore find an approximation of γ_0.

[17] The drop in η_r after strong thickening is most likely due to radial particle migration, with $\dot{\gamma}$ variation in a parallel-plate geometry. Migration will then have also occurred in imposed-stress steady-state measurements for $\varphi \gtrsim \varphi_{\mathrm{DST}}$. However, note that when recording oscillations, significant migration would not be expected at the onset of oscillations due to the single up-sweep protocol.

the time for the suspension to thicken ($\gamma_0/\dot{\gamma}^+ = 0.08\,\mathrm{s}$ at $\dot{\gamma}^+ = 1.6\,\mathrm{s}^{-1}$) is larger than the instrument response time ($t_s = 0.02\,\mathrm{s}$). Indeed, this is the case and the change in $\dot{\gamma}$ can be approximated as an instantaneous step change with the stress response due to changes in f.

4.4.4 Model comparison

Thus, with $\gamma_0 \approx 0.12$, $t_c = \gamma_0\eta_s/\sigma^* = 1.1 \times 10^{-4}\,\mathrm{s}$. Combining t_c with $t_i = 44\,\mathrm{s}$ gives us our system parameter, $\epsilon = 2.7 \times 10^{-6}$. With $\epsilon \ll \epsilon_c^{\max} = 2 \times 10^{-5}$, we then expect the system to show oscillations over a range of Σ_E between DST onset and shear jamming, Fig. 4.5(b). Solving Eqs. 4.6 and 4.7 numerically, with $\varphi = 0.47$ and $\Sigma_E = 0.93$ (corresponding to the onset of oscillations in experiments), we find relaxation oscillations quantitatively matching experiments with no free parameters, Fig. 4.10(a).[18] Note that with highly asymmetric non-sinusoidal oscillations, Fig. 4.6(b), we are far away from the fixed point and the linear stability analysis no longer applies. With a slow increase in $\dot{\Gamma}$, followed by a rapid drop, the oscillation frequency is determined by the step AB and Eq. 4.6, Fig. 4.6(b). The frequency of small oscillations about the fixed point (given by the imaginary components of the eigenvalues of J) is unrelated to the limit cycle frequency, in contrast to the assumptions of Ref. [102].

The model well captures the frequency, amplitude and shape of oscillations. Although indicative of the model being valid, caution must be exercised: such dynamics will arise from coupling of Eq. 4.6 to a generic 'fast' f-relaxation. To probe Eq. 4.1, we must test the prediction of ϵ_c through variation of ϵ and the easiest way to do this is to vary η_s. By increasing the proportion of glycerol in the background solvent to 67 wt.% and increasing η_s from 6 mPa s to 15 mPa s, but leaving the geometry (i.e ρ_A and h unchanged), ϵ is increased to $2\times10^{-5} \approx \epsilon_c^{\max}$.[19] Sustained oscillations are no longer observed, with only damped oscillations in a narrow range of φ and σ_E, Fig. 4.10(b). Increasing η_s and ϵ further using an 85 wt.% glycerol-water background solvent ($\eta_s = 75\,\mathrm{mPa\,s}$), we can make $\epsilon \sim 3 \times 10^{-4} \gg \epsilon_c^{\max}$. As predicted, no shear-rate oscillations are observed across the DST regime, e.g. for $\varphi = 0.44$, Fig. 4.10(f). All results are consistent with

[18] Numerical integration was performed using the SciPy `odeint` package [101] and was checked for consistency against a forward Euler method. Effects of step size and specified numerical tolerance were monitored to ensure accuracy.

[19] Remeasuring the steady-state rheology for cornstarch in a 67 wt.% glycerol-water mixture, we find $\sigma^* = 2.3\,\mathrm{Pa}$, $\varphi_m = 0.447 \pm 0.003$, $\varphi_{\mathrm{rcp}} = 0.530 \pm 0.002$ and $\beta = 0.94 \rightarrow \varphi_{\mathrm{DST}} = 0.436$, see Appendix B.2 for flow curves.

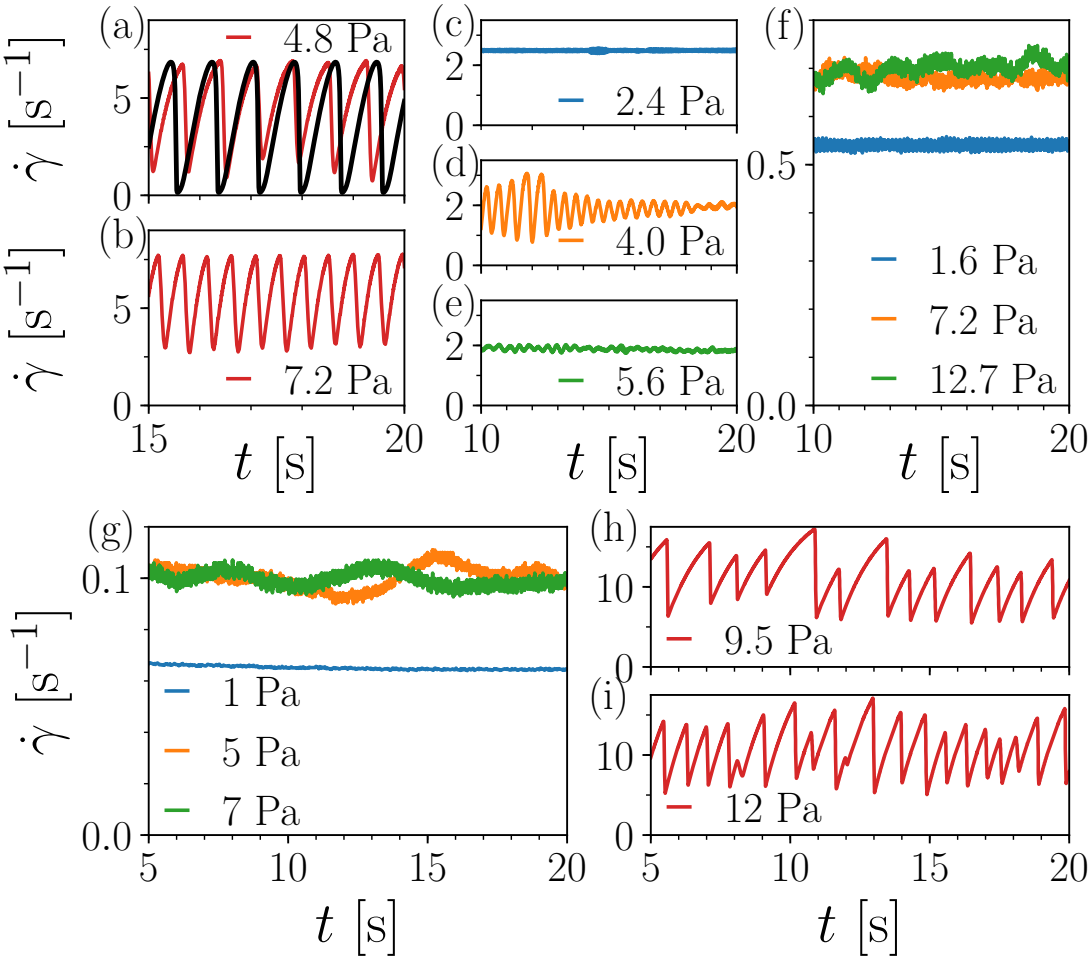

Figure 4.10 Tuning shear-rate oscillations for $\varphi \gtrsim \varphi_{\mathrm{DST}}$. (a)-(b) Low viscosity: cornstarch in a 50 wt.% glycerol-water mixture, $\varphi = 0.47$; relaxation oscillations. Red, experimental data; black, model: $\epsilon = 2.7 \times 10^{-6}$, flow curve parameters from Fig. 4.5. Traces aligned by eye. (c)-(e) Medium viscosity: cornstarch in a 67 wt.% glycerol-water mixture, $\eta_s = 15\,\mathrm{mPa\,s}$ at $\varphi = 0.45 \gtrsim \varphi_{\mathrm{DST}} \approx 0.44$; damped oscillations in a narrow range of stress. (f) High viscosity: cornstarch in an 85 wt.% glycerol-water mixture, $\varphi = 0.44 \gtrsim \varphi_{\mathrm{DST}} \approx 0.44$; DST with no relaxation oscillations. (g) 4 µm silica spheres in an 87 wt% glycerol-water mixture ($\eta_s = 151\,\mathrm{mPa\,s}$ and $\epsilon = 1 \times 10^{-4}$) at $\phi = 0.574 \gtrsim \phi_m = 0.57$; DST with no large shear-rate oscillations. (h)-(i) Silica in dimethyl-sulfoxide–water mixture ($\eta_s = 3.4\,\mathrm{mPa\,s}$ and $\epsilon = 2 \times 10^{-7}$) at $\phi = 0.58$; shear-rate oscillations.

our predicted $\epsilon_c^{\max}$ from independent measurements.

4.4.5 Silica comparison

Cornstarch, while a useful model system due to its amenability, is far from approaching the idealised picture of the WC model being aspherical, highly polydisperse, of unknown hardness and even of unknown volume fraction. To ensure that the model holds independent of system specifics, we turn to a suspension of near-monodisperse, hard 4 µm silica spheres in an aqueous background solvent. A similar system has been shown to be well described the WC model [56]. These experiments were carried out by J. R. Royer, motivated by the predictions of the preceding model.

Using an Anton Paar MCR 302 rheometer with roughened parallel plates ($R = 20\,\mathrm{mm}$, $h = 1\,\mathrm{mm}$ and $\rho_A = 400\,\mathrm{kgm}^{-2}$)), for a silica suspension in an 87 wt.% glycerol-water mixture ($\eta_s = 151\,\mathrm{mPa\,s}$ and $\sigma^* = 40\,\mathrm{Pa}$) we have $\epsilon = 1 \times 10^{-4} \gg \epsilon_c^{\max} = 2 \times 10^{-5}$. Consistent with the prediction of the model, no oscillations were seen in the DST regime [e.g. $\phi = 0.58 > \phi_m = 0.57$, Fig. 4.10(g)], see Appendix B.2 for time-averaged rheology. Decreasing ϵ to 2×10^{-7}, by changing the background solvent to an 80 wt.% dimethyl sulfoxide-water mixture ($\eta_s = 3.4\,\mathrm{mPa\,s}$ and $\sigma^* = 14.5\,\mathrm{Pa}$), strong relaxation oscillations were found, Figs. 4.10(h) and (i). The appearance of strong oscillations is again consistent with the predicted $\epsilon_c^{\max}$ for instability, showing the prediction is not system specific. We briefly note that as the system was tuned between extremes ($\epsilon \gg \epsilon_c^{\max}$ to $\epsilon \ll \epsilon_c^{\max}$), one cannot conclude about precise γ_0 values in different systems. In DEM simulations, a value of $\gamma_0 = 0.023$ has been reported [64], however values inconsistent with this have also been found [Supplemental material of Ref. [92] and personal communications (R. Radhakrishnan and J. Sun, 16$^{\text{th}}$ November 2018)].

4.5 Time-dependent relaxation

Up till this point we have focussed on the onset and presence of oscillations, e.g. Figure 4.10(a) pertaining to σ_E at the onset of DST. As σ_E increases beyond this point, the oscillation frequency, ν, increases [82, 86], and the agreement between model and experiment worsens, Fig. 4.11. As the suspension comes ever

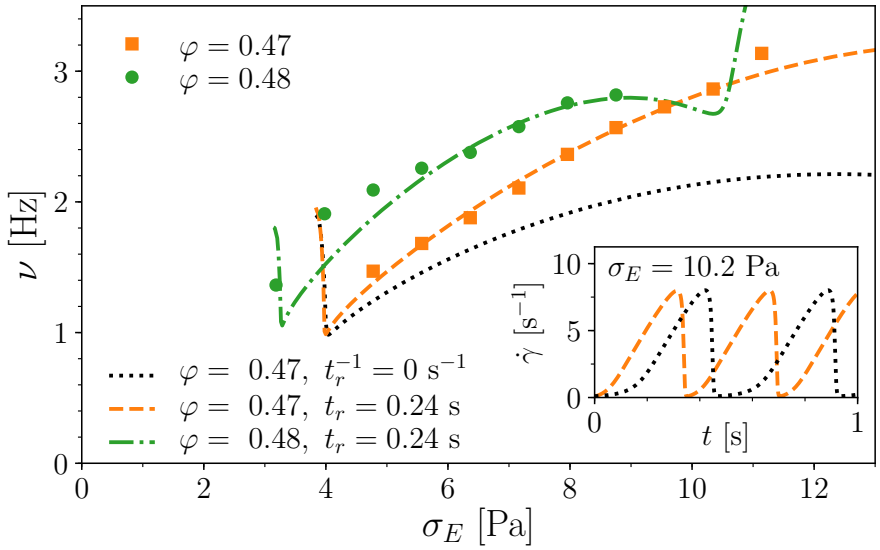

Figure 4.11 Oscillation frequency, ν, *vs* applied stress, σ_E. Points: ν for cornstarch in a 50 wt.% glycerol-water mixture taken from a Fourier transform of 30 s upwards stress sweep (excluding first 2 s) in steps of 0.796 Pa: $\varphi = 0.47$ (■), $\varphi = 0.48$ (●). Lines, model predictions for $\epsilon = 2.7 \times 10^{-6}$ (see legend). Inset: effect of additional time-dependent relaxation on oscillation shape.

closer to jamming, at the precipitous drop in $\dot{\Gamma}$, the strain-dependent *ansatz* for f-relaxation, Eq. 4.1, becomes increasingly ineffective. The predicted time taken to traverse DA in the limit cycle, Fig. 4.6(b), is lengthened compared to reality (cf. slow onset in Fig. 4.11 inset). From the higher experimental ν, we therefore infer the existence of an additional intrinsic, strain-independent, mechanism for relaxing f towards its steady-state value, as suggested in Ref. [103]. Eq. 4.1 is modified accordingly to read

$$\frac{\mathrm{d}f}{\mathrm{d}t} = -\left(\frac{\dot{\gamma}}{\gamma_0} + \frac{1}{t_r}\right)\left[f - \hat{f}(\sigma)\right], \tag{4.15}$$

introducing a relaxation time t_r. There are now two distinct contact relaxation mechanisms: dependent on strain ($\propto \dot{\gamma}/\gamma_0$) or time ($\propto 1/t_r$). The latter dominates as $\dot{\Gamma} \to 0$, increasing the relaxation rate of f near jamming and decreasing the time taken to traverse DA.

Fitting the $\nu(\sigma_E)$ data with this new model through variation of t_r, Fig. 4.11, gives a relaxation time of (0.24 ± 0.05) s.[20] Since $t_c/t_r = 5 \times 10^{-4} \ll 1$, the original strain-dependent mechanism dominates away from jamming. Only when

[20] Varying t_c/t_r from 4×10^{-4} to 6×10^{-4}, data for $\varphi = 0.47$ and 0.48 lies between the predicted $\nu(\sigma_E)$, with the exception of the first two data points for $\varphi = 0.48$.

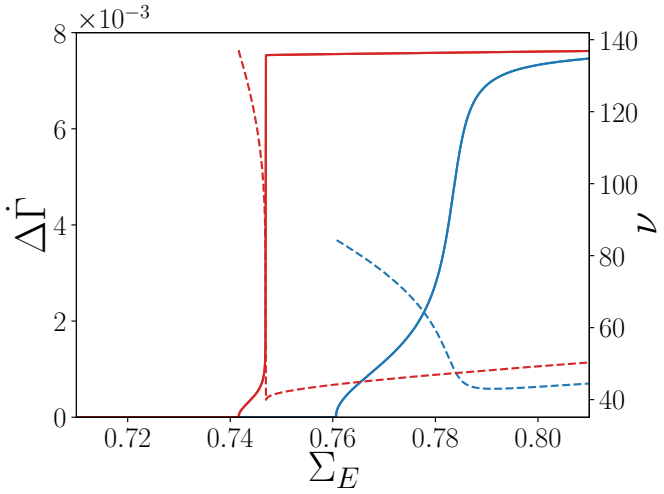

Figure 4.12 Characterising the limit cycle around the onset of instability. Solid lines: oscillation amplitude, $\Delta\dot{\Gamma}$, as a function of Σ_E at $\varphi = 0.47$. ϵ values: blue, $\epsilon = 2.7 \times 10^{-6}$; red, $\epsilon = 1.0 \times 10^{-6}$. WC-model parameters, as in §4.3: $\varphi_{\mathrm{rcp}} = 0.546$, $\varphi_m = 0.457$, $\beta = 0.94$. Both increasing and decreasing Σ_E are plotted. Dashed lines: corresponding limit cycle frequency, ν, measured in units of reciprocal dimensionless time, $\tau^{-1} = t_i/t$.

the shear rate drops, near jamming, does the additional term contribute. As this is where $f > \hat{f}$, the time-dependent relaxation contributes by *breaking* frictional contacts, not forming them. This can be verified by changing Eq. 4.15 so that the time-dependent f-relaxation only breaks contacts, i.e. $\Theta[f - \hat{f}(\sigma)]$, and it is found that for $t_c/t_r = 5 \times 10^{-4}$ there is no measurable change in $\nu(\sigma_E)$.

Importantly this gives some insight into possible physical interpretations of t_r. Conceptually, removing the applied stress on the suspension with a finite interaction range, the repulsive forces that give σ^* would push particles out of mechanical contact. The actual timescale would depend sensitively on the surface details that resist rapid separation by the repulsive force, again raising the issue of the 'small gap problem'. Interestingly, $t_r \approx 0.24\,\mathrm{s}$ is comparable to the relaxation time for cornstarch grains pushed into adhesive contact, $\sim 0.5\,\mathrm{s}$, and attributed to interactions of polymers on the cornstarch surface, suggesting that surface chemistry matters for suspension dynamics [104].

4.5.1 Onset behaviour

In fitting this value of t_r, the initial frequency spike predicted by the model was neglected, Fig. 4.11. Just above the onset of instability, our system undergoes

small-amplitude limit cycles. Additional applied stress causes a slow increase in amplitude, $\Delta\dot{\Gamma}$, with no measurable hysteresis, solid lines in Fig. 4.12. This behaviour is consistent with a supercritical Hopf bifurcation, see Appendix B.1. The corresponding frequency, ν (dashed lines), is large and initially decreases with Σ_E. Increasing the stress further, beyond this initial region, $\Delta\dot{\Gamma}$ begins to increase rapidly before plateauing and the corresponding frequency slowly increases. The first region occurs over a small range of Σ_E and, experimentally, small high-frequency oscillations in a narrow stress window ($\ll 0.1\,\mathrm{Pa}$) would not be resolvable. The model is then consistent with the sudden appearance of large amplitude oscillations with increasing frequency in experiment, despite the seeming prediction of a frequency spike. As an aside, the nature of the jump in amplitude depends on ϵ. Although for both $\epsilon = 2.7 \times 10^{-6}$ and 1.0×10^{-6}, the increase in $\Delta\dot{\Gamma}$ is sharp in terms of experimental stress resolution, for $\epsilon = 10^{-6}$ the transition is sharp within explored numerical resolution ($\delta\Sigma_E = 10^{-4}$). This is suggestive of a canard explosion, a transition over an exponentially small range of the control parameter [$\propto \exp(1/\epsilon)$] from a sinusoidal small amplitude oscillation to a large-amplitude relaxation oscillation. Such behaviour is seen in dynamical systems such as the forced Van der pol oscillator [105].

4.6 Conclusion and outlook

The mechanism we have proposed to explain relaxation oscillations in shear-thickening suspensions appears generic; relying only on the coupling of fast contact dynamics (Eq. 4.1) to a slow system equation, in this case geometry inertia (Eq. 4.5). Therefore, it is perhaps a puzzle why such oscillations have not been more widely reported. In the case of geometry inertia, one reason is the use of high-viscosity solvents, e.g. Ref. [56], thus giving $\epsilon \gg \epsilon_c^{\max}$. More prevalent could be the breakdown of simple shear flow, where surface tension no longer confines the sample [17, 24] as the stress peaks at C in the limit cycle causing fracture, e.g. Ref. [106]. Free surface effects such as this have been suggested to lead to aperiodic, apparently chaotic behaviour [91]. With only two dynamical variables, lacking spatial variation, our model cannot capture such inhomogeneous flow. It nevertheless well captures the development of relaxation oscillations *en route* to aperiodic unsteady flows, suggesting it is a first step towards a method of interpreting generic unsteady flows which *are* widely seen [89–91, 107].

In the shear-rate-oscillation regime our model generalised to Eq. 4.15 has allowed

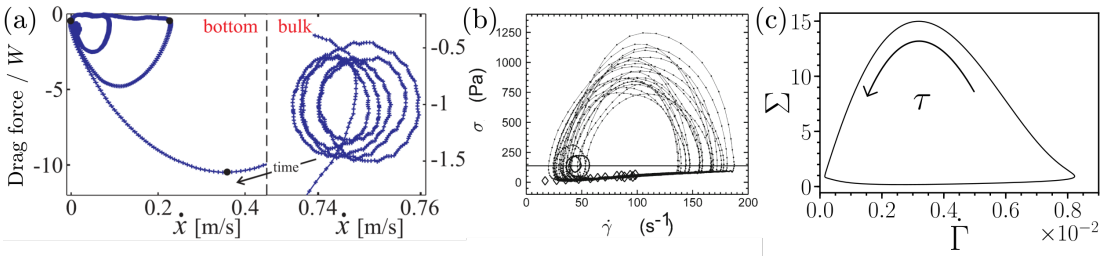

Figure 4.13 Limit cycles in high-volume fraction suspension flow. (a) Oscillations in the settling velocity of a ball in a cornstarch suspension. Parametric plot of drag force (normalised by ball weight, W) *vs* sedimentation speed, $\dot{x}$. Right: oscillations in the 'bulk'. Left: oscillations approaching the bottom. Adapted from Ref. [111]. (b) Shear-rate oscillations in the flow of polystyrene particle suspensions. Parametric plot of sample stress, σ, *vs* shear rate, $\dot{\gamma}$. Adapted from Ref. [85]. (c) Shear-rate oscillations in the model. Parametric plot of sample stress, Σ, *vs* shear rate, $\dot{\Gamma}$. Model parameters as in Fig. 4.10(a).

us to extract an intrinsic contact-relaxation timescale, t_r, which is difficult to access using other methods such as shear reversal [70] or cessation [103] due to instrument artefacts. Instead, our method of accessing t_r relies on modelling the coupling with one such artefact, viz., geometry inertia. The relaxation time becomes important in modelling the flow properties whenever the suspension comes close to jamming and the shear rate drops. Although the shear jamming regime is not accessed in standard shear rheometry, in application it is ubiquitous: chemical mechanical polishing slurries in the semiconductor industry [108], conching of chocolate [5], granulation [67] and even shear-thickening-fluid enhanced fabrics in body armour [109]. With our protocol for extracting this relaxation time, future work should be able to clarify the underlying physical mechanism, which may include particle softness [69], surface chemistry [110] or long-range repulsion [37].

Finally, we turn to the general applicability of the results in this chapter. Coupling between a system variable, significantly slower than the fast contact network dynamics, should be ubiquitous in all areas of high-volume-fraction suspension flow. Thus, for example, in vorticity banding, particle migration is slow [92]; in channel flow, particle rearrangement due to fluid permeation is slow [100, 112]; and in the settling of a ball in a suspension, the ball's inertial dynamics are slow [111]. Correspondingly relaxation-type oscillations, with periodic bursts of brief near-jamming episodes, have been observed in vorticity banding [92]; the micro-channel flow of polymethylmethacralate particles [100]

and the settling velocity of a ball in cornstarch [111]. To underline the common physics uniting these phenomena, compare in Fig. 4.13 the parametric plots of: (a) the velocity and drag for a sedimenting ball, (b) the sample stress and shear rate a suspension of polystyrene particles and the sample stress, and (c) shear rate in the model. For the oscillations in the velocity of a sedimenting ball there is even a sudden transition from small amplitude sinusoidal oscillations in the bulk to large-amplitude limit cycles approaching the bottom, cf. Fig. 4.12. It is therefore possible, perhaps likely, that the kind of physics we have modelled may be relevant far beyond the data sets presented here. By merely identifying the relevant 'slow' system variable, a comparison of timescales and a graphical phase-plane analysis could be used to qualitatively understand instabilities and tune their presence by informed variation of the competing timescales.

Part II

Suspension rheology beyond repulsive interactions

Chapter 5

A minimal extension to the WC model

In the first part of this thesis the focus lay solely upon "well-stabilised" suspensions with exclusively repulsive particle-particle interactions. However, we must remember that our investigation of suspensions is ultimately motivated by their widespread industrial application. Now, in the industrial application of suspensions mutually-attracting particles are widespread as complete stabilisation may not be possible to achieve: highly ionic backgrounds may prevent electrostatic stabilisation [25] or the use of adsorbed stabilisers may compromise product mechanical properties [113]. Alternatively, further components of a formulation may induce attraction between particles, with high molecular weight polymers bridging by adsorbing on two particles simultaneously [25] or immiscible solvents forming capillary bridges [114].[1] It may even be that attractive forces are desirable due to the rheological properties they bestow, with attractive force typically believed to lead directly to a yield stress [117].

We therefore seek to extend the WC model to encompass suspensions with more complex interactions than pure repulsion between particles. In this chapter, we shall introduce a generalised form of the WC model based upon a microphysical motivation. This extension consists of introducing a stress-dependent proportion of adhesive contacts, in direct analogy to the proportion of frictional contacts in the WC model. In such adhesive bonds interparticle attraction dominates over

[1] Note that due to the particle size in non-Brownian suspensions, depletion-type interactions are not relevant, with the typical roughness being comparable to the radius of gyration of a depletant [115] unless great care is taken, e.g. Ref. [116].

externally applied shear; as the applied stress increases the proportion of adhesive contacts then decreases. We will show how an interplay between the strength of these adhesive contacts and the onset stress for friction generate different types of flow curve. In the next two chapters this model is tested using experiments. Before, in the third and final part of the thesis, we then return to recast our friction-adhesion model in a yet more general manner that is independent of microphysics.

5.1 Introducing adhesive interactions

As stated, particles in suspensions that are not well-stabilised are mutually attracting; typically, this interparticle attraction is simply taken be expressible as the gradient an interparticle potential, $F = -\nabla U(\vec{r})$ [118]. However, we must now think about the further implications of the WC model on our view of suspension rheology. It is important to realise that when particles are in a frictional state that they can exert non-potential forces upon one another. Although the exact microphysical origins can be debated, with arguments for, e.g., asperity interlock [78, 119], hydrogen bonding [110] and polymer interdigitation [24], such forces must come from a finite contact area. Therefore, the WC model suggests that we must consider the effect of a finite contact area in suspension rheology.

We must now reflect upon what the combination of a finite contact area and attraction implies; for this we turn once again to inspiration from the dry granular literature. For dry micron-sized particles, attraction does not just act along the line of centres between particles, but it also introduces a resistance to rolling [120, 121]. That is to say, two contacting particles are prevented from rolling below a critical rolling torque, M^*. This critical rolling torque arises from a pinning lengthscale on the particle surface, i.e. there is a distance the contact can roll without breaking. This lengthscale, ξ, combines with the radial attractive force, F_a, to give the critical rolling moment, $M^* = F_a\xi$, and this lengthscale has been ascribed to the surface topography, specifically the roughness [120, 121]. We term such a contact an *adhesive* contact, to distinguish it from (potential-based) attraction, and the stress scale, or strength, of this adhesive contact can be related to the critical rolling torque via the particle diameter, $\sigma_a \sim M^*/d^3$.

To progress we need to change scale from the particle level to that of a packing of

particles. For a sheared granular medium with rolling resistance between particles (i.e. a torque with resists rolling between particles, but dependent on the total normal force between particles, rather than with a single critical rolling moment) there is an exponentially-tailed distribution of contact torques [122, 123], just as there is an exponential tail of large forces for normal and tangential forces [61]. Therefore, as the shear stress on a packing is increased, there will be a gradual breakage and mobilisation of adhesive contacts: first, the large torques in the exponential tail will mobilise some contacts even at a low applied stress; as the characteristic stress, σ_a, is reached most contacts will exceed the critical torque; before finally, when a stress much larger than σ_a is applied all adhesive contacts are broken. To capture this process, we introduce a stress-dependent proportion of adhesive contacts,

$$a(\sigma) = 1 - \exp\left[-\left(\frac{\sigma_a}{\sigma}\right)^{\kappa}\right]. \tag{5.1}$$

Note that we have simply chosen this functional form to mimic that used for the fraction of frictional contacts, but instead decreasing from $a(\sigma = 0) = 1$ to $a(\sigma \to \infty) = 0$ with stress. The exponent, κ, controls the rapidity of the cross-over from the adhesion-dominated to essentially adhesionless regime. For this chapter we will set $\kappa = 1$, along with the exponent for the fraction of frictional contacts, β, in Eq. 3.4,

$$f(\sigma) = \exp\left[-\left(\frac{\sigma^*}{\sigma}\right)^{\beta}\right]. \tag{5.2}$$

Note that as from this point on only steady-state models will be presented and we drop the distinction between the dynamic quantity, f and the steady-state value $\hat{f}$, choosing to simply write f for notational brevity.

When measuring the suspension rheology we do not have access to particle level details such as the proportion of adhesive contacts, instead we simply measure measure the viscosity or stress. Therefore, we need to consider the impact of the proportion of adhesive contacts on the suspension flow. For potential attraction the stress response is typically taken to be due directly to the strength of attraction and the tensile force it can exert [25]. Returning to reflect on the WC model, we must note that friction acts by lowering the jamming volume fraction. Therefore, to work out the effect of $a(\sigma)$ on the viscosity we need to infer the impact of adhesion on the jamming volume fraction.

To deduce the effect of adhesion on the jamming volume fraction we once again look to the dry granular literature. For packings of dry frictional and adhesive particles four limits are now observed [124]. In addition to the adhesionless

limits of random close packing and random loose packing, we now have the adhesive limits without fricion of "adhesive close packing", ϕ_{acp}, and with friction of "adhesive loose packing", ϕ_{alp}. The values of these jamming volume fraction limits have been measured using a ballistic deposition protocol to be $\phi_{\mathrm{alp}} = 0.14 < \phi_{\mathrm{acp}} \approx \phi_{\mathrm{rlp}} \approx 0.51 < \phi_{\mathrm{rcp}} = 0.64$ [124, 125]. Adhesive loose packing is a very low jamming volume fraction as an adhesive frictional contact is also taken to have a critical twisting torque, which confers bond rigidity in the adhesive limit; therefore, loose filamentous packings are stable. However, we require the jamming points under shear. Although for the frictional limit, ϕ_{rlp}, similar values are found for the jamming volume fraction using isotropic compression [57], sedimentation [58] and shear [126], we do not know that this is the case for ϕ_{alp}. To make qualitative predictions, we need only decide on the ordering of these four jamming volume fractions. But, to make quantitative predictions, we make what perhaps is the most parsimonious assumption that $\phi_{\mathrm{acp}} = \phi_{\mathrm{rlp}}$. Specifically, for calculational purposes in this chapter we use $\phi_{\mathrm{rcp}} = 0.64$, $\phi_{\mathrm{acp}} = \phi_{\mathrm{rlp}} = 0.55$ and $\phi_{\mathrm{alp}} = 0.30$.

To determine the stress-dependent jamming volume fraction, we must interpolate between four limits (ϕ_{alp}, ϕ_{acp}, ϕ_{rlp} and ϕ_{rcp}) using two variables, the proportion of adhesive contacts, $a(\sigma)$ (Eq. 5.1), and the proportion of frictional contacts, $f(\sigma)$ (Eq. 5.2). We choose the simplest (linear) interpolation:

$$\phi_J = \phi_{\mathrm{alp}} af + \phi_{\mathrm{acp}} a(1-f) + \phi_{\mathrm{rlp}}(1-a)f + \phi_{\mathrm{rcp}}(1-a)(1-f). \tag{5.3}$$

This interpolation assumes that there is no correlation between adhesive and frictional contacts. In the case that $a \to 0$, Eq. 5.3 reduces to ϕ_J in the WC model, Eq. 3.3. Finally, as in the WC model, we assume that the viscosity is given by the Maron-Pierce equation,

$$\eta_r = \left[1 - \frac{\phi}{\phi_J}\right]^{-2}. \tag{5.4}$$

We now have four parameters: the onset stress for frictional contact, σ^* and the critical stress for breaking adhesive contacts, σ_a, along with the two associated exponents, β and κ, controlling the rapidity of these processes. With these four parameters and the four limiting jamming volume fractions (ϕ_{rcp}, ϕ_{acp}, ϕ_{rlp} and ϕ_{alp}), there is the possibility of a complex interaction between friction and adhesion. However, in this chapter we will focus on three cases, building on the

WC model with an increasing strength of attraction relative to the onset stress for friction, i.e. σ_a/σ^*. We reserve a more general and wide-ranging discussion of other possibilities to Ch. 8.

In the case of zero adhesion, $\sigma_a/\sigma^* = 0$ ($\sigma^* = 1\,\mathrm{Pa}$), we obviously recover the WC model. The jamming volume fraction drops with stress from ϕ_{rcp} to ϕ_{rlp}, Fig. 5.1(a) (solid line). The viscosity is determined by the distance to jamming, so at a constant ϕ and increasing stress the distance to jamming decreases, the viscosity increases and flow curves show shear thickening, Fig. 5.1(b) [lines (purple to yellow) for $\phi = 0.20, 0.25, \ldots, 0.55, 0.60$]. At $\phi > \phi_{\mathrm{rlp}}$, a constant ϕ line in Fig. 5.1(a) now intersects $\phi_J(\sigma)$ and shear jamming is predicted above this point, i.e. that no flow is possible when ϕ_J drops below the sample's ϕ.

Now with weak adhesion, e.g. $\sigma_a/\sigma^* = 0.1$ ($\sigma_a = 0.1\,\mathrm{Pa}$ and $\sigma^* = 1\,\mathrm{Pa}$), the jamming volume fraction shows a non-monotonic dependence on stress, Fig. 5.1(c) (solid line). At low stress, $\sigma \approx \sigma_a$, ϕ_J initially increases as adhesive contacts are broken, before frictional contacts form as σ approaches and then exceeds σ^* and ϕ_J drops to ϕ_{rlp}. Where the two critical stresses are close to each other, ϕ_J does not increase fully to ϕ_{rcp} before frictional contacts begin to form, reaching only some lower ϕ_{max}. Correspondingly, flow curves at $\phi < \phi_{\mathrm{acp}} \approx \phi_{\mathrm{rlp}}$, show shear thinning from a low-shear plateau followed by thickening to a high-shear plateau, Fig. 5.1(d) [lines, as in (b)]. Only at high volume fractions, $\phi > \phi_{\mathrm{acp}} \approx \phi_{\mathrm{rlp}}$, does a yield stress develop; in this case $\phi_J > \phi$ at low stress and adhesive contacts must be broken with stress to unjam and flow steadily. At high stress, such yielding is predicted to be followed by shear jamming as $\phi > \phi_{\mathrm{rlp}}$. Interestingly, there is also a predicted range of volume fractions, $\phi_{\mathrm{max}} < \phi < \phi_{\mathrm{rcp}}$, in which dispersal to a suspension should be possible ($\phi < \phi_{\mathrm{rcp}}$) but with no steady-flow achievable ($\phi > \phi_{\mathrm{max}}$).

Finally, when the strength of adhesion is far greater than the onset stress for friction, $\sigma_a/\sigma^* \to \infty$ ($\sigma_a = 0.1\,\mathrm{Pa}$ and $\sigma^* = 0\,\mathrm{Pa}$), ϕ_J monotonically increases with stress, from ϕ_{alp} to ϕ_{rlp}, Fig. 5.1(e) (solid line). As the viscosity depends on the distance to jamming, the relative viscosity is also monotonically decreasing, Fig. 5.1(f) [lines, as in (b)]. For $\phi < \phi_{\mathrm{alp}}$, η_r decreases from a low shear plateau to a high shear plateau set by ϕ_{rlp}, the same plateau as in both the previous two cases. Above ϕ_{alp}, at low stress $\phi > \phi_J$ and adhesive contacts must be broken for the suspension to yield or unjam and flow. This unjamming or yield stress is given by the inversion of $\phi_J(\sigma)$, Fig. 5.1(e), as such it increases exponentially from ϕ_{alp} (note that ϕ_J is linear with σ plotted logarithmically) before diverging

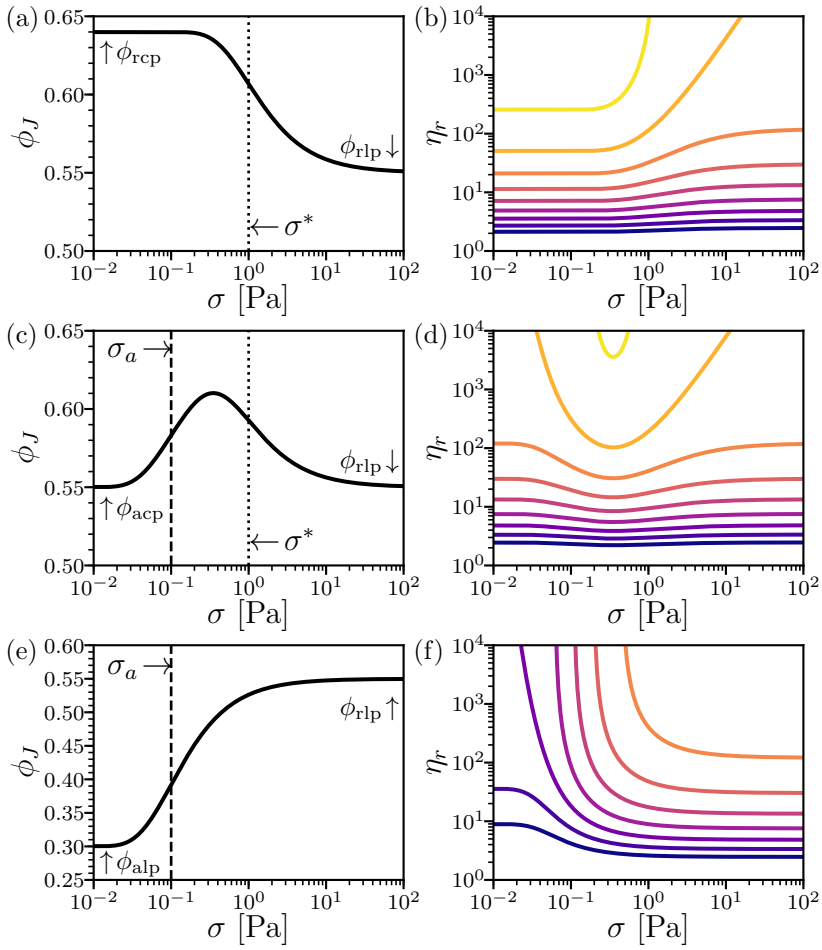

Figure 5.1 Introducing adhesion into the a WC-like framework for suspensions. (a) and (b) Case 1, finite onset stress ($\sigma^* = 1\,\text{Pa}$) and no adhesion ($\sigma_a = 0$), i.e. the WC model. (a) Jamming volume fraction, ϕ_J, *vs* stress, σ. Solid line, setting $a = 0$, Eq. 5.3 reduces to $\phi_J = f(\sigma)\phi_{\rm rlp} + [1 - f(\sigma)]\phi_{\rm rcp}$, with $f(\sigma) = \exp(-\sigma^*/\sigma)$, $\phi_{\rm rlp} = 0.55$ and $\phi_{\rm rcp} = 0.64$. Dotted line indicates value of σ^*. (b) Resultant flow curves: relative viscosity with stress, $\eta_r(\sigma)$ at volume fractions ϕ, spaced at 0.05 intervals from $\phi = 0.20$ to $\phi = 0.60$ indicated by color (purple to yellow). (c) and (d) Case 2, weak adhesion, $\sigma_a \ll \sigma^*$, with a finite onset stress ($\sigma_a = 0.1\,\text{Pa}$ and $\sigma^* = 1\,\text{Pa}$). (c) Jamming volume fraction, ϕ_J, *vs* stress, σ, from Eq. 5.3 (solid line), $f(\sigma)$ as in (a), with $a(\sigma) = 1 - \exp[-(\sigma_a/\sigma)^\kappa$. Parameters as in (a) and also with $\sigma_a = 0.1\,\text{Pa}$, $\phi_{\rm alp} = 0.30$, $\phi_{\rm acp} = \phi_{\rm rlp}$ and $\kappa = 1$. Dotted line denotes σ^* and dashed line denoted σ_a. (d) Resultant flow curves from ϕ_J in (c), volume fractions, ϕ, as in (b). (e) and (f) Case 3, strong adhesion with a negligible onset stress, $\sigma_a/\sigma^* \to \infty$, with $\sigma_a = 0.1\,\text{Pa}$ and $\sigma^* = 0\,\text{Pa}$. (e) Stress-dependent jamming volume fraction, $\phi_J(\sigma)$, for case 3. Solid line, Eq. 5.3 with $f = 1$ reduces to $\phi_J(\sigma) = a\phi_{\rm alp} + (1 - a)\phi_{\rm rlp}$, relevant parameters as in (a) and (c). Dashed line indicates value of σ_a. (f) Flow curves resulting from $\phi_J(\sigma)$ in (e). Volume fractions as in (b) and (d), note that $\phi \geq 0.55$ has no flowing state and is not plotted.

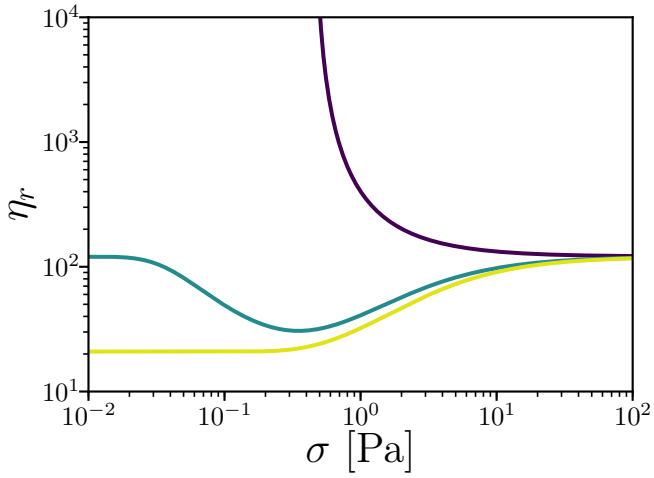

Figure 5.2 Tuning flow curve behaviour, various cases of the model at a fixed volume fraction, $\phi = 0.40$. Relative viscosity, η_r, *vs* stress, σ, at various adhesion strengths relative to the onset stress, using Eqs. 3.4, 5.1, 5.3 and 5.4. With decreasing adhesion strength: purple, strong adhesion with $\sigma_a = 0.1\,\text{Pa}$ and $\sigma^* \to 0$; green, weak adhesion with $\sigma_a = 0.1\,\text{Pa}$ and $\sigma^* = 1\,\text{Pa}$; and no adhesion (WC model), with $\sigma_a \to 0$ and $\sigma^* = 1\,\text{Pa}$.

as $\phi \to \phi_{\text{rlp}}$. Physically, as the volume fraction approaches random loose packing all adhesive contacts must be broken for the suspension to flow and, due to the distribution of torques, the required stress diverges. We must emphasise that when friction is present a yield stress arises at lower volume fractions because the jamming volume fraction is always higher without friction (ϕ_{alp} *vs* ϕ_{acp}).

5.2 Conclusion

If we now plot in Fig. 5.2 the three cases we have outlined above together at a single volume fraction, $\phi = 0.40$, this appears strikingly similar to the data presented by Ref. [127]. In this work Brown et al. proposed that a yield stress due to interparticle attraction 'covers up' shear thickening with increasing attraction. This microphysical picture was simulated using a discrete element by Singh et al. [118] and a model was developed in which a yield stress with a Herschel-Bulkley form is added to the shear thickening flow curve. Such an additive approach was stated to work as the yield stress due to potential-based attraction arises from an isotropic state, while, in contrast, shear thickening and jamming occur in an anisotropic sheared state.

Despite the seeming similarity in the steady state flow curves, in the following two

chapters we shall elucidate how our picture of suspension rheology being driven by friction and adhesion is fundamentally different. In Ch. 6, we demonstrate that interparticle friction plays a vital role in the yield stress of a model non-Brownian suspension and detail how this supports the model we have outlined in this chapter. Then in Ch. 7 we shall investigate how dispersants tune suspension behaviour between the cases of Fig. 5.1. By comparison with the model of this chapter we shall explain how controlling friction between particles effects the yield stress.

Interestingly, we will be able to do this without detailed knowledge of the microphysics that gives rise to our hypothesised frictional and adhesive contacts. Ultimately, this reflects the fact that the 'friction' and 'adhesion' we have been referring to in this chapter are merely any force on the particle level that prevents, respectively, relative sliding and relative rolling between particles. In this sense they are 'constraints' on relative interparticle motion and in the final part of this thesis we shall recast the model developed in this chapter in far more general terms along these lines. This generalised model forms a constraint-based approach to non-Brownian suspension rheology and makes predictions for further classes of flow curve, which we will explore alongside further detailing of the cases we have outlined in this chapter. However, we will not wait until the final part to introduce the terminology of 'constraints', so that in the following chapters we will refer to the model presented in this chapter as (one instance of) 'constraint rheology' and to frictional and adhesive contacts as constraints.

Chapter 6

Yielding in adhesive non-Brownian suspensions

While this thesis initially focussed on shear-thickening suspensions and particles with purely repulsive interparticle forces, the previous chapter introduced a framework for capturing more complex flow curves and interactions. It was hypothesised that yielding and shear thinning in non-Brownian suspension originated from the breaking of adhesive constraints with stress, specifically constraints on interparticle rolling, with the characteristic stress-scale for contact mobilisation given by a critical rolling moment, M^*. A suitable contact model was proposed, in which M^* originates from a combination of short-range attraction and a pinning lengthscale associated with the finite area of the contact, which we term adhesion.

Although the existence of a 'true' yield stress in soft matter systems has been debated [26], it is undeniably an engineering reality [117], with a critical "yield stress", σ_y, marking a transition between no flow and continual flow (which may depend on observation time [27]). Practically, this property is vital for control of how suspensions behave during processing. In some cases, sufficiently small values of the yield stress are required for spreading and levelling in, e.g., self-compacting concrete [80] or chocolate [128]; while in other cases, adequately large yield stresses are needed to retain a formed shape, e.g. for a ceramic green body [6], or to keep larger granular particles suspended [129].

In soft-matter systems the ability to resist deformation is typically thought to come from a homogeneous load-bearing structure that exists at rest; yielding

then consists of the deformation and break-up of this structure with increasing stress [117]. In attractive colloidal gels, flocs formed by diffusion span the system, while in colloidal glasses particles are prevented from flowing by caging from other particles. In soft-jammed systems, sometimes aided by potential-based attraction, for example emulsions, particles are in elastic contact with a sufficiently large number of neighbours to allow mechanical equilibrium. Yielding may be complex: in attractive colloidal glasses two-step yielding is observed, with attractive bond breakage preceding cage breakage [130]; however, the yield stress still originates from the quiescent structure and is largely insensitive to the measurement technique, although time-dependent effects often add complexity.

In quiescent non-Brownian hard-particle suspensions under no external load there is, in contrast, no process to form a load-bearing structure, such as diffusion or elasticity. Instead, the structure formed will depend sensitively on the previous shear history. Correspondingly, yield-stress measurements for an attractive non-Brownian suspension varies widely between different labs, techniques and rheological protocols [131]. This then hints at a fundamental difference in yielding between non-Brownian suspensions and many other soft solids. In this chapter, we reveal this fundamental difference through a combination of steady-shear and shear-reversal measurements on a model non-Brownian suspension, which show that the yield stress only develops under finite strain. The dynamics are shown to be consistent with the development of a compressive frictional contact network stabilised by adhesive bonds. This then implies that yielding to a steady flowing state is actually unjamming from a shear-jammed state through the breakage of adhesion-stabilised frictional contacts with increasing stress. This demonstrates that the yield stress measured from a steady-state flow curve, e.g. by fitting an empirical constitutive law such as the Herschel-Bulkley equation, is in fact due to a complex interplay between friction and adhesion.

To isolate the effect of adhesion we then prepare a state through oscillatory shear to relax or remove compressive frictional contact networks and measure an ‘adhesion only yield stress’. Finally, it is hypothesised that this adhesion only yield stress represents a frictionless lower bound to yielding measurements in adhesive non-Brownian suspension, with the steady-state yield stress representing a frictional upper bound. To support this assertion we show that an alternative protocol for measuring a yield stress gives a value that lies between these two bounds. Ultimately, this shows the sensitivity of non-Brownian suspensions to shear history due to their athermal nature and their fundamental difference from

colloidal systems.

6.1 Measuring 'the yield stress'

We begin by measuring the yield stress of a model cornstarch-in-oil suspension in two ways: by continuing in the same direction of shear as the pre-shear process and by reversing the direction of shear. Both protocols are shown to measure the same yield stress, which is this stress for transitioning from a jammed to a flowing state. The measured yield stress is consistent with the constraint-based model for a frictional suspension with rigid adhesive bonds being broken with stress. Crucially, the dynamics of the reversal measurements additionally show that an $\mathcal{O}(1)$ strain must be accumulated for this yield stress to develop. This is consistent with the formation of a compressive frictional contact network and shows how adhesion in a non-Brownian suspension requires a shear-induced frictional structure to generate the yield stress, rather than the yield stress simply resulting from adhesion alone.

Cornstarch[1] is typically dispersed in an aqueous solvent to form a shear-thickening suspension [132]. Instead, here we disperse it in sunflower oil (Flora, viscosity $\eta_s = 62\,\mathrm{mPa\,s}$, density $\rho_s = 0.92\,\mathrm{gcm^{-3}}$) by vortex mixing, stirring and then roller mixing for $\gtrsim 2\,\mathrm{h}$. In non-aqueous solvents cornstarch has previously been observed to form a yield-stress suspension at high solid-volume fraction [104, 133] and samples are seen to hold their shape, see Fig. 6.1. At low solid-volume fractions, non-aqueous cornstarch suspensions are also used as a model electro-rheological fluid, where the viscosity depends strongly on the applied electric field [134].

6.1.1 Steady shear

The steady-state rheology, in which the suspension is sheared in the same direction as the pre-shear step, was first measured under imposed shear rate with a TA Instruments ARES-G2 rheometer. All reported rheological measurements on suspensions in this chapter were made using cross-hatched parallel plates with

[1] Purchased from Sigma Aldrich with approx. 73% amylopectin and 27% amylose, diameter $d \approx 14\,\mu\mathrm{m}$ and polydispersity $\approx 40\%$ from static light scattering in a glycerol-water mixture [82], density $\rho_p = 1.45\,\mathrm{gcm^{-3}}$.

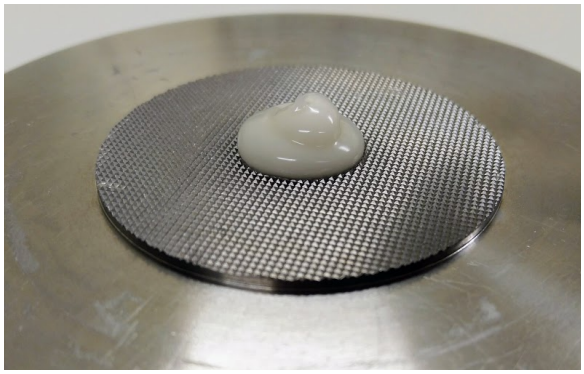

Figure 6.1 Visual appearance of a cornstarch-in-sunflower-oil suspension at ≈ 52% solid volume fraction on a cross-hatched plate, diameter 60 mm, approximately 5 min after pouring.

radius $R = 20\,\mathrm{mm}$, gap height $h = 1\,\mathrm{mm}$ and a serration depth of 0.25 mm. From the measured torque, $\mathcal{T}$, and applied angular velocity, Ω, we report the corrected stress, $\sigma = (\mathcal{T}/2\pi R^3)(3 + \mathrm{d}\ln\mathcal{T}/\mathrm{d}\ln\Omega)$ and relative viscosity $\eta_r = \sigma/(\dot{\gamma}\eta_s)$ from the rim shear rate, $\dot{\gamma} = \Omega R/h$. Where we do not correct for the varying rate across the parallel plate we report the apparent stress, $\sigma_{\mathrm{app}} = 2\mathcal{T}/\pi R^3$, and from this $\eta_{r,\mathrm{app}} = \sigma_{\mathrm{app}}/\dot{\gamma}$.

For experimental rheological measurements, as discussed in Ch. 2, there exists a limited observable "window", delineated by the white area in Fig. 6.2. The range of measurable stresses is restricted at the upper limit, $\sigma_{\max} \approx 180\,\mathrm{Pa}$, by sample fracture, where surface tension no longer confines either the particles [31] or, as observed in this case, the bulk sample, possibly due to normal stress differences [83]. At the lower limit, the minimum stress is set by either instrument resolution or particle sedimentation with a stress-scale $\sigma_{\min} \sim (\rho_p - \rho_s)gd \approx 0.05\,\mathrm{Pa}$. Similarly, the shear rate is limited to be below the point of inertial sample fracture [24], $\dot{\gamma}_{\max} \approx 400\,\mathrm{s}^{-1}$, and above a minimum, $\dot{\gamma}_{\min} = 0.01\,\mathrm{s}^{-1}$, that is simply set by the maximum possible length of the experiment. Within this "window" suspensions are initially pre-sheared at $\dot{\gamma} = \max[100\,\mathrm{s}^{-1}, \dot{\gamma}(\sigma_{\max})]$ for 100 s, before immediately dropping to $\dot{\gamma}_{\min}$ to begin a logarithmic up-sweep of the shear rate at 5 pts./decade. The step length is set by $\max(\gamma = 10, t = 10\,\mathrm{s})$, ensuring that a steady state is reached at each $\dot{\gamma}$ before averaging over time.

The resultant flow curves, $\eta_r(\sigma)$, plotting relative viscosity *vs* stress, are shown for multiple solid volume fractions, ϕ, from 0.35 to 0.53, see Fig. 6.2 (symbols). For all ϕ, suspensions shear thin with increasing stress and η_r decreases, approaching a plateau for $\phi \leq 0.45$. At higher volume fractions, any possible plateau is obscured by sample fracture at $\sigma_{\max} \approx 180\,\mathrm{Pa}$, with measurements beyond this denoted by

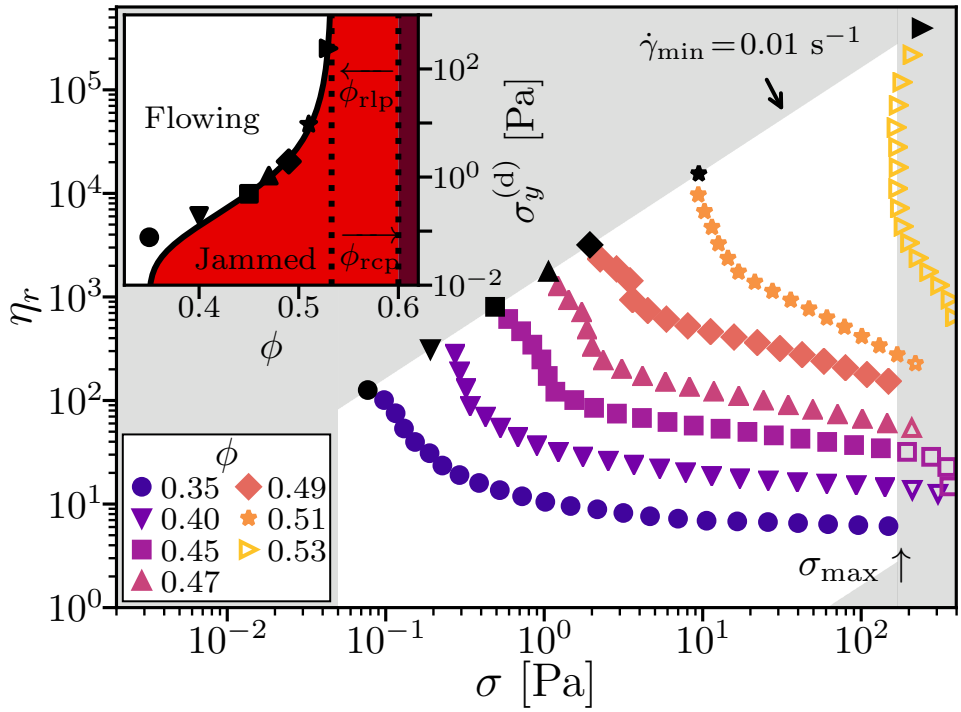

Figure 6.2 Steady-state rheology of an adhesive suspension. Cornstarch-in-oil suspension flow curves measured under imposed shear rate, $\dot{\gamma}$: relative viscosity, $\eta_r = \eta/\eta_s$, *vs* shear stress, σ. Grey, observable "window" limited by sample fracture, $\sigma_{\max} \approx 180\,\mathrm{Pa}$ [24] and minimum shear rate, $\dot{\gamma}_{\min} = 0.01\,\mathrm{s}^{-1}$. Points: data, for volume fraction, ϕ, see legend. Open symbols, $\sigma > \sigma_{\max}$; black points, $\sigma(\dot{\gamma}_{\min}) \equiv \sigma_y^{(\mathrm{d})}$. Inset: σ-ϕ jamming phase diagram from constraint-based rheology model. Points, $\sigma_y^{(\mathrm{d})}$ from main figure. Solid line, model unjamming stress discussed in §6.1.4, using Eq. 6.1, $\phi_J(\sigma) = \phi_{\mathrm{rlp}}(1-a) + \phi_{\mathrm{alp}}a$, and Eq. 6.2, $a(\sigma) = 1 - \exp(-(\sigma_a/\sigma)^\kappa)$ with parameters $\phi_{\mathrm{rlp}} = 0.533$, $\phi_{\mathrm{alp}} = 0.35$, $\sigma_a = 0.2\,\mathrm{Pa}$ and $\kappa = 0.55$. Shading: red, jammed, $\phi_J(\sigma) < \phi$; white, flowing, $\phi_J(\sigma) > \phi$; and maroon, $\phi > \phi_{\mathrm{rcp}} \sim 0.6$, dispersion not possible.

open symbols. Such flow curves suggest the presence of a yield stress and resemble those of some other non-Brownian suspensions, such as molten chocolate [5] or mineral slurries [135]. An estimate of the yield stress can be extracted from the steady-state stress at the lowest accessed shear rate, $\sigma_y^{(\mathrm{d})} = \sigma(\dot{\gamma}_{\mathrm{min}} = 0.01\,\mathrm{s}^{-1})$, where this is a dynamic measurement as it extrapolates from a flowing state. We find that $\sigma_y^{(\mathrm{d})}$ rapidly increases with ϕ, see Fig. 6.2 [inset], and appears to diverge in the vicinity of $\phi = 0.53$. Above the yield stress interpretation of $\eta_r(\sigma)$ may be complicated by banding, such that the apparent shear rate (and hence viscosity) no longer represents the local behaviour, see Appendix C for a further discussion. For samples at $\phi > 0.53$, a steady state was not reached at any applied shear rate and instead the samples formed a visible fracture plane with stick-slip motion occurring. We will return to an analysis of the extracted yield stress in §6.1.3, after introducing the complimentary shear-reversal measurements.

6.1.2 Shear reversal

For the measurement of the dynamic yield stress, the suspension was pre-sheared in the *same* direction that the measurements were made. We now perform the equivalent of previously-published shear-reversal experiments on repulsive shear-thickening suspensions [70], as reviewed in Ch. 3, where we investigate the response upon application of a stress in the opposite direction to the pre-shear. In a shear-reversal test on a non-adhesive suspension during pre-shear particles are in compressive contact and interact through both hydrodynamic and hard-sphere repulsion with sliding friction. When the direction of deformation is inverted, particles previously in compressive contact are now in tension with only hydrodynamic forces between them. Therefore, the drop in viscosity upon reversal gives the contact (frictional) contribution to the viscosity. This contact contribution requires an $\mathcal{O}(1)$ strain in the new shear direction to redevelop as a compressive contact network reforms. We now explore how this picture is changed with the addition of adhesive interactions between particles. After presenting a full data set, we focus first on the discussion of the long time-time, or steady-state, response after reversal, deferring discussion of the transient response immediately after reversal until Sec. 6.3.

We use a controlled-torque TA Instruments DHR-2 rheometer for reversal tests, and report the rim strain, γ, and applied stress, $\sigma = 3\mathcal{T}/2\pi R^3$, which is correct at yielding where $\mathrm{d}\ln\mathcal{T}/\mathrm{d}\ln\Omega = 0$. To reach a well-defined initial state, samples

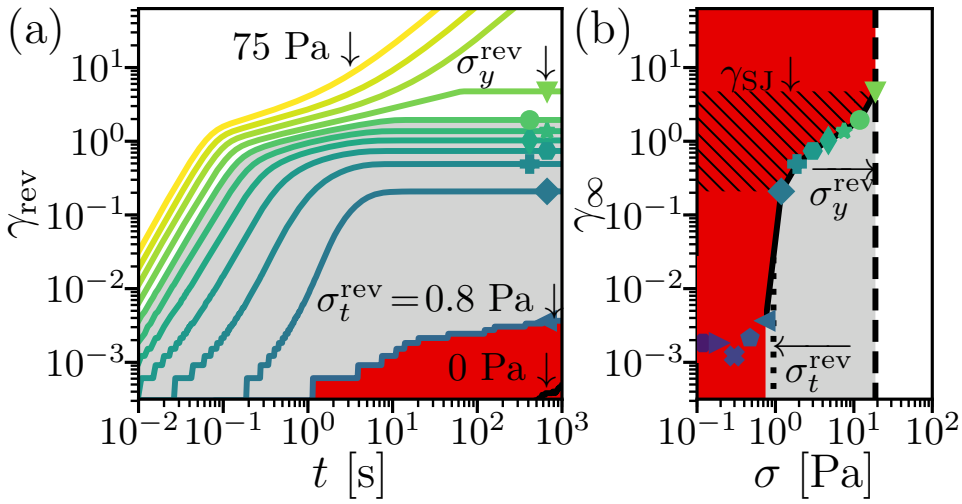

Figure 6.3 Transient behaviour upon reversal at $\phi = 0.51$. (a) Shear reversal yield-stress measurement with reverse pre-shear, showing time-dependent strain, $\gamma_{\rm rev}(t)$, for imposed stresses, σ, spaced logarithmically at 5 pts./decade from 0.075 Pa (showing from 0.8 Pa) to 75 Pa (teal to yellow) and 0 Pa (black). Stress, σ, for non-flowing states given by symbol and color from (b), and for flowing states $\sigma = 30$, 47 and 75 Pa. Shading, for regions identified in (b): red, $\sigma < \sigma_t^{\rm rev}$; grey, $\sigma_t^{\rm rev} < \sigma < \sigma_y^{\rm rev}$; and, white, $\sigma > \sigma_y^{\rm rev}$. (b) Transient-yield-stress interpretation. Long-time limiting strain, $\gamma_\infty(\sigma) \equiv \gamma(t = 10^3\,{\rm s})$, *vs* σ (symbols). Dotted line, $\sigma_t^{\rm rev}$, set by $\max[\Delta \log(\gamma_\infty)]$, or steepest slope; dashed line, $\sigma_y^{\rm rev}$, highest stress of a jammed state. Shading: white, flowing states; grey, transiently flowing states (will jam at γ_∞); and, red, non-flowing states that are inaccessible to our stress-controlled protocol. Hatched region, range of strains, $\gamma_{\rm SJ}$, for shear-jammed states.

were pre-sheared in the reverse (-γ) direction at high stress, 75 Pa $\lesssim \sigma_{\rm max}$, for 100 s and left quiescent (0 Pa) for a further 100 s. The sample was then stressed at a constant $\sigma < \sigma_{\rm max}$ in the opposite (+γ) direction for 1000 s. The time-dependent strain response, $\gamma_{\rm rev}(t)$, was measured, before removal of σ for 100 s to test for elastic recovery, repeating the series of steps over a range of stresses, σ, spaced logarithmically at 5 pts./decade from 0.075 Pa to 75 Pa. Some adjustments were made to the protocol for different volume fractions: for $\phi = 0.53$, the pre-shear stress was increased to 300 Pa to ensure flow; for $\phi \leq 0.40$, the pre-shear stress was decreased to 7.5 Pa to prevent $\dot{\gamma}_{\rm max}$ being exceeded and inertial ejection of the sample; and for $\phi \leq 0.47$ reversal tests were additionally repeated over a lower stress range of 3 mPa to 7.5 Pa.

To gain insight into the results we will first focus on data for a single volume fraction, $\phi = 0.51$, see Fig. 6.3(a). At $\sigma \lesssim 1.0$ Pa, there is a sub-linear growth of

$\gamma_{\rm rev}(t)$, denoted by red background shading. As the slope of $\gamma_{\rm rev}(t)$ is less than one, the shear rate is decreasing with time and the state is not flowing (even if it is slowly deforming). This is creep, its occurrence at $\sigma = 0\,\mathrm{Pa}$, Fig. 6.3(a) [black curve] and its σ independence below 1 Pa, see Fig. 6.3(b) [symbols], suggest that creep is a remnant of pre-shear. Above this stress range we see transient yielding (grey shading): the suspension initially flows, with $\gamma_{\rm rev} \propto t^2$. This constant-acceleration motion is an (inertial) instrument artefact, indicating an almost negligible viscosity. Above the 'transient yield stress', $\sigma_t^{\rm rev} = 1.0\,\mathrm{Pa}$, but below $\sigma = 20\,\mathrm{Pa}$, the suspension then re-jams at $\gamma_{\rm rev} \approx \mathcal{O}(1)$. This deformation is plastic, with negligible recoverable strain. We define $\gamma_\infty(\sigma)$, as the long-time-limit strain, estimated at $t = 10^3\,\mathrm{s}$, Fig. 6.3 [symbols]. Transient yielding at $\sigma_t^{\rm rev}$ is identified from the sharpest rise in $\mathrm{dln}\,\gamma_\infty/\mathrm{dln}\,\sigma$, see Fig. 6.3(b) [dotted line]. Only above a second higher critical stress, $\sigma_y^{\rm rev} = 20\,\mathrm{Pa}$, does the suspension continually flow (white shading) with $\gamma_{\rm rev} \propto t$, defining '*the* yield stress' for this reversal protocol, see Fig 6.3(b) [dashed line].[2] Between $\sigma_t^{\rm rev}$ and $\sigma_y^{|rmrev}$, there is then a range of γ_∞ for which the system shear jams, we label these strains $\gamma_{\rm SJ}$ specifically.

Note that for our later interpretation to be valid, the behaviour we report must be due to the reversal of the direction of shear and not just due to a change from the high-stress pre-shear state to a lower stress. We can verify that this is the case by a comparison with shear continuing in the same direction as the pre-shear, and indeed we find that the response is explicitly due to the reversal of the direction of shear in Appendix C.2.

6.1.3 Comparison of yield-stress measurements

We have now made two types of measurement on a cornstarch-in-oil suspension and in both we have identified a stress which characterises the transition to continuous flow. In the steady-state flow curves, $\sigma^{(\rm d)}$ is taken from the stress at the lowest applied shear rate, which we use in place of fitting an empirical model such as the Herschel-Bulkley model. From controlled-stress reversal measurements, $\sigma_y^{\rm rev}$ is taken as the stress separating a jammed state ($\dot\gamma \to 0$ as

[2] It should be noted that here we are using a 'rheological' interpretation of yielding, a transition to or from continual flow. In the study of engineering materials yielding may be defined as the onset of failure, either non-linear or plastic deformation [25]. In this sense $\sigma_t^{\rm rev}$ represents a 'yield stress', as it marks the onset of a large non-linear plastic deformation in $\gamma_\infty(\sigma)$.

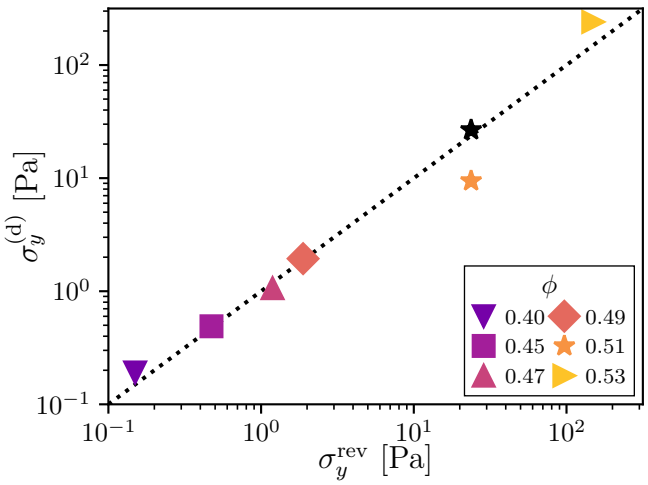

Figure 6.4 Comparison of yield-stress measurements. Steady-state flow curve yield stress, $\sigma_y^{(\mathrm{d})} = \sigma(\dot{\gamma}_{\mathrm{min}})$, from measurements under imposed-$\dot{\gamma}$ *vs* σ_y^{rev}, from controlled-σ reversal, coloured symbols. See inset legend for corresponding volume fractions, ϕ. Black symbol: peak stress observed during application of $\dot{\gamma}_{\mathrm{min}}$ at $\phi = 0.51$, for all other ϕ this measurement is equivalent to $\sigma_y^{(\mathrm{d})}$. Marker size represents the approximate precision in σ_y^{rev} of $\pm 10^{0.1}$ and the black dotted line shows equality of the two measurements, $\sigma_y^{(\mathrm{d})} = \sigma_y^{\mathrm{rev}}$.

$t \to \infty$) and a flowing state ($\dot{\gamma} > 0$ as $t \to \infty$) in the long-time limit. Comparing these two measurements across all volume fractions measured, Fig. 6.4, we find that there is near equality (symbols close to dotted line); however, there are two caveats to address.

First, at $\phi = 0.35$, although a finite $\sigma_y^{(\mathrm{d})}$ is measured, under imposed stress no jammed states are observed (i.e. $\sigma_y^{\mathrm{rev}} = 0\,\mathrm{Pa}$). Instead, only slow flow is measured and this volume fraction is merely strongly shear thinning. This highlights the limitation of extrapolating from finite shear rates and assuming $\dot{\gamma}_{\mathrm{min}} \approx 0\,\mathrm{s}^{-1}$. When measuring at a finite shear rate if the flow curve is vertical, i.e. $\mathrm{d}\eta_r/\mathrm{d}\sigma \to -\infty$ or $\mathrm{d}\sigma/\mathrm{d}\dot{\gamma} \to 0$, a value close to the $\dot{\gamma} \to 0$ limit and the yield stress should be measured, as is reasonably the case for $\phi \geq 0.45$, Fig. 6.4. However, if at $\dot{\gamma}_{\mathrm{min}}$ the flow curve is merely shear thinning ($\mathrm{d}\eta_r/\mathrm{d}\sigma \ll 0$) the yield stress will be overestimated by using $\sigma_y^{(\mathrm{d})} = \sigma(\dot{\gamma}_{\mathrm{min}})$. This effect can be compensated for by extrapolating from the measured flow curve and $\dot{\gamma}_{\mathrm{min}}$ to $\dot{\gamma} = 0$ using an empirical form, such as the Herschel-Bulkley equation. Indeed, the deviation of $\sigma_y^{(\mathrm{d})}$ above σ_y^{rev} as ϕ drops can already be seen at $\phi = 0.40$ and this could likely be compensated for by extrapolating to $\dot{\gamma} = 0$. However, for $\phi = 0.35$ a discrepancy would still exist when using an extrapolated value of $\sigma_y^{(\mathrm{d})}$. From imposed-stress measurements we have determined that there is no measurable

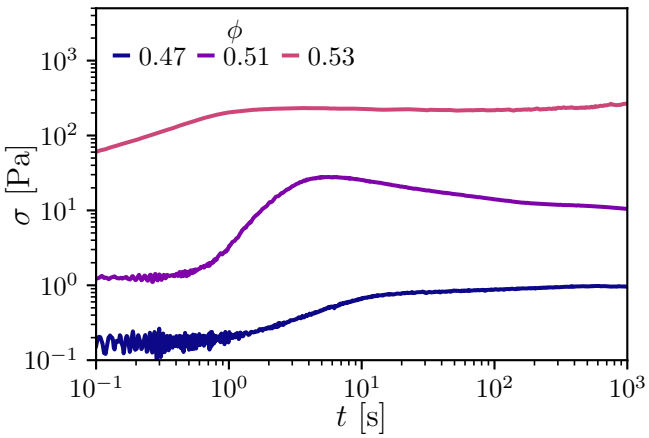

Figure 6.5 Time-dependent stress, $\sigma(t) \equiv 3\mathcal{T}(t)/2\pi R^3$, *vs* time, t, after application of an imposed shear rate, $\dot{\gamma}_{\text{min}} = 0.01\,\text{s}^{-1}$ for multiple volume fractions, ϕ (see legend).

yield stress $\sigma_y^{\text{rev}} < 3\,\text{mPa}$. Determining this requires measurements at lower shear rates which extend the rheological "window", e.g. under imposed stress, and it cannot be divined by extrapolation from higher shear rate measurements.

The second caveat is for the measurements at $\phi = 0.51$ (orange star, Fig. 6.4). While the magnitudes of $\sigma_y^{(\text{d})} = 10\,\text{Pa}$ and $\sigma_y^{\text{rev}} = 20\,\text{Pa}$ are comparable, closer agreement (black star) can be found by using the 'peak' stress reached during shear at $\dot{\gamma}_{\text{min}}$, purple trace in Fig. 6.5. A pronounced peak in $\sigma(t)$ at $\dot{\gamma}_{\text{min}}$ is only seen in this measurement at $\phi = 0.51$ and was not found in either other volume fractions or a repeat measurement with a new batch of cornstarch. The origin of the stress overshoot is not known, although such peaks have been associated with transient banding dynamics [136]. As we are interested in the trend and broad magnitude of the stress, rather than the precise values, we do not further discuss this discrepancy.

These two caveats not withstanding, we therefore consider both measurements as accessing the same quantity, which we shall call *the* yield stress, σ_y.

6.1.4 Discussion

So far, we have simply presented and described experimental results. We now turn to interpret these results and hence attempt to infer the particle level interactions and physical processes from which the yield stress arises. To do this the steady state-rheology is first evaluated in terms of the constraint model developed in Ch. 5 for a combination of frictional and adhesive contacts, before

we discuss whether the particle interactions so deduced are consistent with the strain dependence of the reversal response.

Comparison with the constraint-based rheology model

We begin by noting that the divergence of yield stress in the vicinity of $\phi = 0.53$, as described in §6.1.1, is at a substantially lower volume fraction than random close packing, $\phi_{\mathrm{rcp}} \approx 0.60$, a value taken from aqueous (repulsive) cornstarch suspensions when swelling has been corrected for [96]. Note that there is no need to correct for swelling for cornstarch in sunflower oil, as this phenomena is restricted to aqueous background solvents [137]. Instead of ϕ_{rcp}, the critical volume fraction, at $\phi \approx 0.53 \approx 0.88\phi_{\mathrm{rcp}}$, is consistent with the volume fraction of the high-shear viscosity divergence in shear-thickening suspensions, where in hard spheres $\phi_m \approx 0.86\phi_{\mathrm{rcp}}$ [57] and in aqueous cornstarch suspensions $\phi_m \approx 0.84\phi_{\mathrm{rcp}}$.[3] Assuming that the interparticle friction coefficient is not particularly sensitive to the background solvent, we may interpret our divergence as occurring at the frictional jamming volume fraction, $\phi_m \approx \phi_{\mathrm{rlp}}$.

A frictionally jammed system at $\phi \geq \phi_{\mathrm{rlp}}$ is not typically interpreted as having 'yield stress behaviour'. But if we reinterpret the (in principal) infinite stress needed for hard shear-jammed particles to flow [138], we can describe the state to which the yield stress diverges as a shear-jammed frictional packing. However, below ϕ_{rlp} a frictional suspension can flow at any stress, i.e. $\sigma_y = 0$; whereas, in our model suspension the yield stress is finite below $\phi \approx 0.53$, with a gradual decrease as ϕ drops further below ϕ_{rlp}. Within the constraint model this implies that there is an adhesive constraint that is broken with stress and that is in addition to the frictional constraint on sliding that has been switched on with stress at an inaccessibly small stress-scale (i.e. $\sigma^* \to 0$).

With contacts always in a frictional state, or $f = 1$, the jamming volume fraction only depends on the proportion of adhesive contacts, $a(\sigma)$, and Eq. 5.3 reduces to

$$\phi_J(\sigma) = \phi_{\mathrm{alp}} a(\sigma) + \phi_{\mathrm{rlp}}[1 - a(\sigma)], \tag{6.1}$$

with, as in Ch. 5, the proportion of adhesive contacts given by

$$a(\sigma) = 1 - \exp\left[-(\sigma_a/\sigma)^{\kappa}\right]. \tag{6.2}$$

[3] The ratio is taken from the critical weight fractions reported in Ch. 4 without correction to volume fractions.

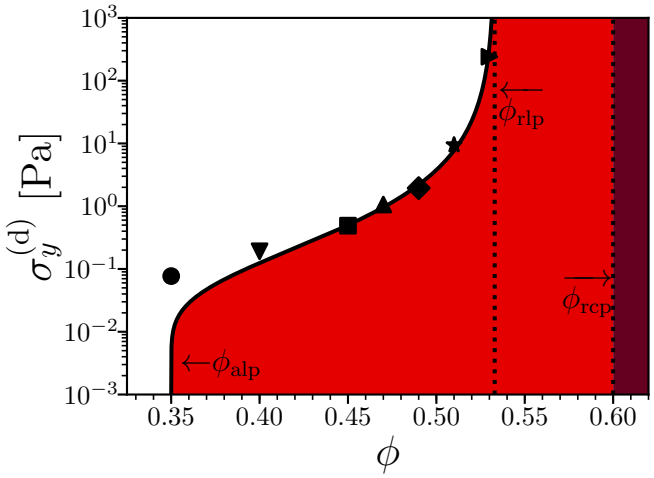

Figure 6.6 Comparison of constraint-based rheology model with dynamic yield-stress measurement. Black symbols, $\sigma_y^{(\mathrm{d})}$ as previously plotted in Fig. 6.2. Solid line, model unjamming stress from Eq. 6.1, $\phi_J(\sigma) = \phi_{\mathrm{rlp}}(1-a) + \phi_{\mathrm{alp}}a$, and Eq. 6.2, $a(\sigma) = 1 - \exp(-(\sigma_a/\sigma)^\kappa)$ with parameters: $\phi_{\mathrm{rlp}} = 0.533$, $\phi_{\mathrm{p}} = 0.35$, $\sigma_a = 0.2\,\mathrm{Pa}$ and $\kappa = 0.55$. Shading: red, jammed, $\phi_J(\sigma) < \phi$; white, flowing, $\phi_J(\sigma) > \phi$; and maroon, $\phi > \phi_{\mathrm{rcp}} \sim 0.6$, dispersion not possible.

The jamming volume fraction varies between ϕ_{rlp}, as $\sigma \to \infty$ with all adhesive bonds broken, and a lower "adhesive loose packing" (ϕ_{alp}), as $\sigma \to 0$ with all contacts bonded adhesively [125]. The yield stress is extracted from setting $\phi_J(\sigma) = \phi$, or inverting the inverting the plot of $\phi_J(\sigma)$ to give $\sigma_y(\phi)$. The minimum ϕ at which a yield stress exists is then ϕ_{alp} and, as stated, the yield stress diverges at ϕ_{rlp}.

A representative fit of this reduced model to $\sigma_y^{(\mathrm{d})}$ can then be made, Fig. 6.6. The two limiting jamming volume fractions are set by the qualitative behaviour of the yield stress: $\phi_{\mathrm{rlp}} = 0.533$ is set by the rapid increase in $\sigma_y^{(\mathrm{d})}$, while $\phi_{\mathrm{alp}} \approx 0.35$ is set by the sudden appearance of a measurable yield stress between $\phi = 0.35$ ($\sigma_y < 3\,\mathrm{mPa}$) and $\phi = 0.40$ ($\sigma_y^{(\mathrm{d})} = 0.2\,\mathrm{Pa}$). The two parameters from $a(\sigma)$, $\sigma_a = 0.2\,\mathrm{Pa}$ and $\kappa = 0.55$, are then chosen to match the data. Note that at low volume fractions there is a deviation between the model and the data; as detailed in §6.1.3, this represents the fact that $\sigma_y^{(\mathrm{d})}$ is measured at a finite shear rate, but is being compared to a $\dot{\gamma} \to 0$ prediction.

If adhesion is necessary to capture the yield stress in a non-Brownian suspension, then it is easy to interpret σ_y as simply 'the yield stress due to adhesion'. But such an interpretation would be simplistic to the point of being misleading. To see why this is the case, we turn to the lower limiting jamming volume fraction

of $\phi_{\text{alp}} \approx 0.35$.

First note that this is close to the shear induced percolation threshold for frictionless repulsive hard spheres measured from simulations, $\phi_p \approx 0.40$ [139].[4] In the frictionless case, the existence of a system-spanning contact network does not affect the rheological properties of the system. On the other hand, in our suspension, with a negligible onset stress for frictional contact ($\sigma^* \to 0$), the particles in a percolated cluster at ϕ_p will be in frictional contact. However, we know that this is not sufficient to jam the system, which requires $\phi \to \phi_{\text{rlp}} \approx 0.53$ [126]. But, if particles in a percolated frictional cluster are additionally stabilised by adhesive contacts with bond rigidity, this can render the cluster and hence the system rigid.[5] This will directly affect the rheology and manifest as a finite σ_y.[6] If this suggestion is correct, then the yield stress does not arise solely from adhesion; instead, friction must also play a role throughout the range in which we observe a finite yield stress, $0.35 \lesssim \phi < 0.53$. In other words, the constraint model implies that the yield stress arises from a shear-induced percolated frictional contact network stabilised by adhesive bonds. We will now turn to explain why our shear-reversal experiments in fact demonstrate that this is the case.

Insight from shear reversal

The crucial insight is that the percolation threshold is for a suspension under shear. It must take strain to form, as the structure is inherently anisotropic, with the percolating cluster orientated in the compressive direction. Upon reversal, this anisotropy leads to the strain dependence of the viscosity for non-Brownian suspensions [142] that has been used to illuminate the role of contact forces in suspensions [68, 70]. In §6.1.2, we showed that σ_y similarly takes strain to develop upon reversal: when applying a stress slightly below the yield stress, the suspension plastically deforms before shear jamming and supporting the applied

[4] Here we are comparing cornstarch directly to monodisperse hard spheres, which may be a reasonable approximation with the similar values for ϕ_{rcp}, 0.60 *vs* 0.64.

[5] Here we are comparing to the percolation volume fraction of frictionless hard spheres under shear. The presence of additional constraints would, however, reduce this value, e.g. the addition of fiction was observed to lower the percolation threshold in finite-sized systems by 3% [140]. We are also neglecting the effect of potential attraction, which at rest in a thermal system can change the percolation threshold due to phase separation and the formation of locally dense regions that are isostatic (rigid), which then percolate [141]. The presence of gel-like behaviour will be addressed in § 6.2.

[6] Bond rigidity requires an additional constraint on twisting, which has been previously taken to be a property of a frictional adhesive bond [125].

stress. Close to $\phi_{\rm rlp}$ at $\phi = 0.51 \approx \phi_{\rm rlp} - 0.02$, such shear jamming was observed over a range of strains $0.24 \leq \gamma_{\rm SJ} \leq 3$. Qualitatively this is strikingly similar to the behaviour of a non-adhesive frictional suspension upon reversal just above $\phi_{\rm rlp}$. In a non-adhesive frictional suspension the suspension flows freely upon reversal until a system spanning rigid cluster spans the system; the suspension shear jams at a strain of 0.6-0.8 for $\phi \approx \phi_{\rm rlp} + 0.01$ [138]. Interestingly, this comparison can continue. In our model suspension, as the applied stress is increased towards unjamming (i.e. $\sigma \to \sigma_y$), $\gamma_{\rm SJ}$ rapidly increases; while in a frictional suspension, as the friction coefficient is reduced, the strain required to shear jam also rapidly increases as unjamming is approached. We will discuss the ϕ dependence of shear jamming in adhesive non-Brownian suspensions later in §6.3. For now we emphasise that the strain dependence of the reversal response is consistent with the formation of a compressive percolated frictional contact network under shear that is stabilised by adhesive bonds. This interpretation of the yield stress then contrasts with the colloidal view of a gel, where the load bearing structure would exist at rest and support load in all directions without requiring a significant strain to be accumulated.

The reversal response of non-adhesive suspensions we have described and related to the behaviour of adhesive suspensions is ultimately related to the concept of fragility [93]. For hard (frictional) spheres at $\dot{\gamma} \to 0$, only compressive contact forces can be supported and in a shear-jammed packing the applied stress is supported through a network of compressive "force chains". However, when the load changes direction these force chains are no longer compressive: the system must plastically deform to create compressive force chains in the new direction to jam and support the load. If we now consider an *adhesive* suspension the situation is more complex. While there is still an asymmetry in the contact, a non-zero load can be supported in tension. It may now be tempting to take $\sigma_t^{\rm rev}$ (the lower critical stress in the reversal protocol below which the reversed stress can be supported without deformation) as the 'yield stress due to adhesion'. Again, as with σ_y, it is not so simple, and in §6.3 we will describe how the volume fraction dependence of $\sigma_t^{\rm rev}$ may arise from the precise reversal protocol. To measure adhesion in isolation a specific protocol must be devised.

6.2 Measuring adhesion alone using oscillatory shear

To measure the effect of adhesion alone we must remove the effect of friction. As we have established, friction appears to only have a significant effect on the rheology when compressive contact networks have been formed. A small-amplitude oscillatory test can be used to probe the system without forming new compressive frictional contact networks, provided that any existing contact network is first removed. Note that a freshly loaded state is not suitable as it will have been sheared in an unknown manner during loading, forming contact networks in unknown directions. We therefore turn to oscillatory shear itself to prepare the state, knowing that in non-adhesive suspensions repeated intermediate amplitude shear removes contacts due to the irreversibility of hard-sphere contacts [143]. A state prepared in by repeated small-amplitude oscillation will have no preferred direction of shear and we will label it the 'isotropic' state.[7] In colloidal systems large amplitude shear has also been used to produce a homogeneous state [144], while looking at dry granular systems this protocol could be seen as the analog of shaking a packing to measure ϕ_{rcp}, e.g. Ref. [145]. Preparing a reproducible 'isotropic' state through a decreasing amplitude sweep, we will show that this protocol can also measure a characteristic stress-scale for the strength of the 'isotropic' state. This stress-scale is found to be dramatically lower than the steady-state yield stress, which further enforces the importance of frictional contacts to the effect of adhesion on the rheology.

6.2.1 Methods

In oscillatory shear a sinusoidal strain, $\gamma(t) = \gamma_0 \sin(\omega t)$, with an amplitude, γ_0, and a fixed (anglular) frequency, $\omega = 10\,\mathrm{rad\,s^{-1}}$, is applied with a strain-controlled TA Instruments ARES-G2 rheometer. From the measured (apparent) stress response $[\sigma_{\mathrm{app}}(t) = 2\mathcal{T}(t)/\pi R^3]$ we report the so-called 'elastic modulus', G', from the stress response in phase with $\gamma(t)$, and the 'loss modulus', G'', from the stress response in phase with the rate of deformation, $\dot{\gamma}(t)$. Data is taken after

[7] This label contains the caveat that the protocol only ensures it does not have a preferred direction of shear in one axis. As the suspension is not sheared in the gradient or vorticity directions inhomogeneities from loading may still exist and we emphasise this restriction through the continued use of quotation marks for the word 'isotropic' throughout.

one delay cycle and averaged over 7 cycles. In a large amplitude oscillatory shear (LAOS) protocol, G' and G'' are then measured with changing strain amplitude, a 'strain sweep'.

The modulii are based upon the primary Fourier coefficients of $\sigma(t)$ and therefore a linear response is tacitly assumed. However, if the modulii are changing with γ_0 the response is non-linear: G' and G'' no longer completely describe the stress response as they do in the linear-viscoelastic regime. While G'' does retain meaning as a measure of dissipation during a cycle, interpretation of G' may be more nuanced. However, a physically relevant framework for the interpretation of the full non-linear response in suspensions is currently lacking, although progress is being made [146]. We therefore simply report the linear modulii.

Now to prepare an 'isotropic' state, the strain amplitude is increased logarithmically at 10 pts./decade from $\gamma_0^{\min} = 10^{-4}$ to a $\gamma_0^{\max}$, before decreasing the strain amplitude back down to $\dot{\gamma}_{\min}$. A consistent down sweep was found when the maximum strain amplitude was large enough to observe a sharp rise in G' with increasing γ_0 in the preceding up sweep, or 'strain hardening'. For all measurements with $\phi \leq 0.53$, $\gamma_0^{\max} = 10$ was used, while for $\phi > 0.53$ the maximum strain amplitude without sample fracture was used. We will now report the results of the down sweep and how a 'yield stress due to adhesion' can be extracted.

6.2.2 Results

To allow comparison with the previous section, §6.1.2, we will continue to present results for $\phi = 0.51$. From the modulii as a function of strain amplitude, see Fig. 6.7 (a) [inset], the modulii [G' (light blue circles), and G'' (orange squares)] are replotted as a function of the 'elastic stress', $\sigma' = G'\gamma_0$. If the modulii are frequency independent, σ' would represent the stress at zero frequency, $\omega \to 0$. An approximation to the static (i.e., $\omega \to 0$) stress-strain curve can be extracted by replotting again, with $\gamma_0(\sigma')$, see Fig. 6.7(b) [light blue circles]. The elastic stress has been plotted as if it is the 'independent variable' to compare with imposed-stress measurements of deformation, such as Fig. 6.3.

A critical stress-scale, $\sigma_{\text{osc}} = 0.03\,\text{Pa}$, can be defined where $\sigma'(\gamma_0)$ reaches a maximum, or $\gamma_0(\sigma')$ becomes vertical, see Fig. 6.7(b). This is also the stress at

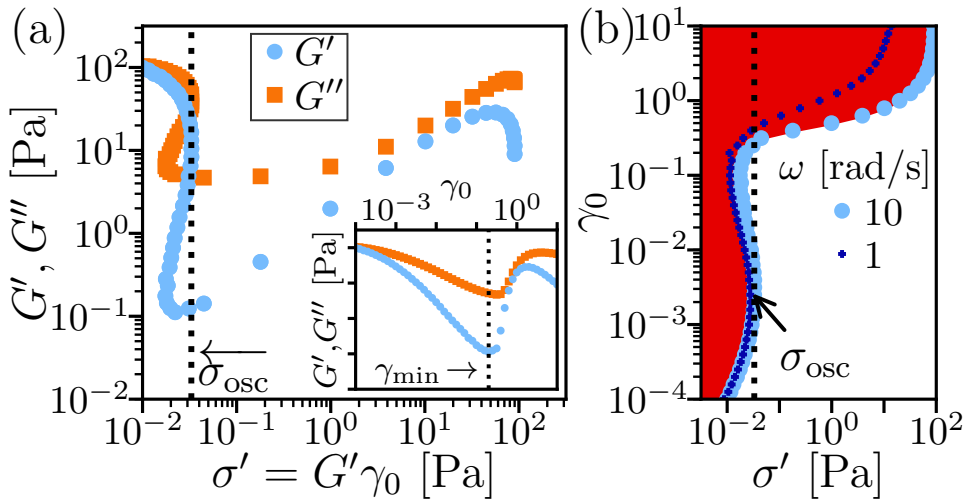

Figure 6.7 Large amplitude oscillatory shear at $\phi = 0.51$. (a) Oscillatory shear response with decreasing imposed strain amplitude, γ_0 (10 pts./decade), at (angular) frequency $\omega = 10\,\mathrm{rad\,s^{-1}}$. Elastic, G' (•), and loss, G'' (■), modulii, *vs* elastic stress component, $\sigma' = G'\gamma_0$. Inset: 'raw' data, modulii *vs* γ_0. (b) Yielding interpretation: γ_0 *vs* elastic stress component, σ', at $\omega = 1\,\mathrm{rads^{-1}}$ (+) and $10\,\mathrm{rads^{-1}}$ (•). Characteristic stress-scale, $\sigma_{\rm osc}$, defined where $\mathrm{d}\sigma'/\mathrm{d}\gamma_0 = 0$ at $\omega = 10\,\mathrm{rads^{-1}}$.

which the modulii drop sharply, Fig. 6.7 (a).[8] If $\gamma_0(\sigma')$ does represent a static load curve, this would correspond to the maximum stress that can be supported as a solid with a small deformation. This criterion has been found to accurately measure the yield stress of colloidal gels [147, 148]. Repeating the protocol at a lower frequency, $\omega = 1\,\mathrm{rad\,s^{-1}}$, we find that at small strains, $\gamma_0 \lesssim 0.1$, σ' is very weakly frequency dependent; this supports our assertion that the elastic stress offers a good approximation of the zero-frequency limit. In contrast, at large strain amplitudes, $\gamma_0 \gtrsim 1$, σ' appears to scale almost linearly with ω. In this non-linear and frequency-dependent regime we should no longer interpret $\gamma_0(\sigma')$ as a static load curve.

In the following discussion, §6.2.3, we are merely interested in characteristic stress-scales, for which the definition we have adopted for $\sigma_{\rm osc}$ should be adequate. However, before moving on, we note briefly that if precise values are desired the protocol dependence must be attended to. Repeating an additional up sweep, see Fig. 6.8(a), a threefold increase in the peak elastic stress-scale is observed. The defined stress-scale also varies weakly with the number of oscillations per measurement point, scaling approximately with the square root, shown in

[8] This is a 'drop' in the modulii if $G'(\sigma')$ and $G''(\sigma')$ are read conventionally, i.e. with increasing stress and strain, although the measurements were taken with decreasing strain.

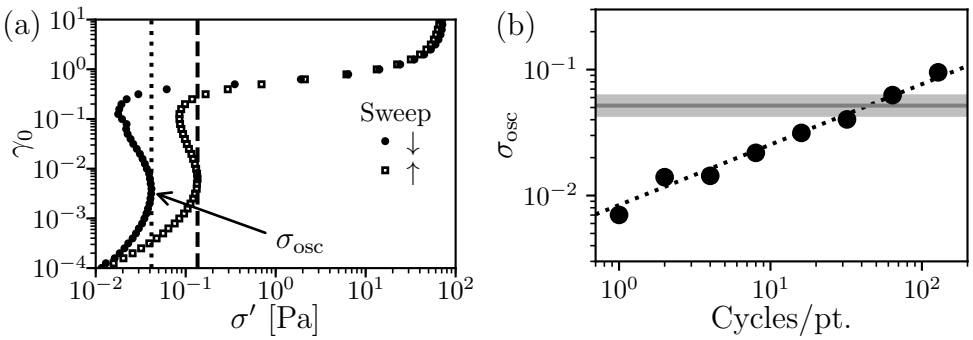

Figure 6.8 Protocol dependence of the characteristic oscillatory shear strength, $\sigma_{\rm osc}$. (a) Reversibility of LAOS strain amplitude sweep at $\phi = 0.51$: strain amplitude, γ_0, *vs* elastic stress, $\sigma' = G'\gamma_0$. Data taken at (angular) frequency $\omega = 10\,\mathrm{rad\,s^{-1}}$ and 10 pts./decade. Symbols: filled squares, first down sweep in γ_0 from $\gamma_0^{\rm max} = 10$ to $\gamma_0^{\rm min} = 10^{-4}$, measuring $\sigma_{\rm osc} = 0.042\,\mathrm{Pa}$; open squares, following up sweep from $\gamma_0^{\rm min}$ to $\gamma_0^{\rm max}$ with a peak elastic stress at 0.14 Pa, a threefold increase over $\sigma_{\rm osc}$ measured from the preceding amplitude down sweep. Note that a different batch of cornstarch was used in these experiments compared to those used for the data presented in Fig. 6.7. (b) Effect on $\sigma_{\rm osc}$ of number of shear cycles per point during down sweep at 10 pts./decade from $\gamma_0^{\rm max} = 10$ to $\gamma_0^{\rm min} = 10^{-4}$ at $\phi = 0.49$. Black circles, measured $\sigma_{\rm osc}$ as defined in Fig. 6.7, averaging over the second half of the number of cycles; dotted line, power law fit with $\sigma_{\rm osc} \propto (\text{Number of cycles/pt.})^{0.48}$; solid grey line, average strength of loaded sample from initial increasing strain amplitude up sweep taken before measurement of presented $\sigma_{\rm osc}$. This value is defined equivalently to $\sigma_{\rm osc}$. Light grey region, standard deviation in average loaded sample strength.

Fig. 6.8(b) for $\phi = 0.49$.

6.2.3 Discussion

The characteristic strength of the 'isotropic' state at $\phi = 0.51$, $\sigma_{\text{osc}} \sim 0.03\,\text{Pa}$, is much smaller than both $\sigma_y \approx 10\,\text{Pa}$ and $\sigma_t^{\text{rev}} = 1.0\,\text{Pa}$. Therefore, it may plausibly represent the strength of a percolated network held together solely by adhesion, with the compressive, frictional contribution having been removed by the oscillatory preparation protocol. The stress-scale, σ_{osc}, is therefore akin to the yield stress of a colloidal gel [25]. To test if this is a reasonable interpretation we can make a consistency check. We can estimate the strength of the adhesive bonds to be 6 nN using $\sigma_{\text{osc}} \approx U/d^3$, with $d = 14\,\mu\text{m}$ [82] and then converting to a force using an interaction length of 14 nm set by surface roughness [73]. Comparing this to a direct measurement of the pull-off force between cornstarch particles in a non-aqueous solvent of $\sim 20\,\text{nN}$ [104], we can see that they are of a similar magnitude and that this picture is consistent. Note, however, that the mechanism of structure formation is still different in a non-Brownian system. In a colloidal gel, the contacts are formed via diffusion, while in our non-Brownian system, the contacts are formed due to the externally-imposed shear strain.

With contact evolution being driven by imposed strain, this may partially explain the protocol dependence of σ_{osc} that leads us to term it only a characteristic stress-scale. Applying a moderate shear amplitude, $\gamma_0 \lesssim 0.1$, there may still be local plastic deformation and structural evolution that is an analog to the thermal coarsening and stiffening of colloidal gels with time [149]. This process may explain the rise in σ_{osc} with an increased number of oscillation cycles. An alternative explanation is that the bonds between particles strengthen with time. The adhesion force between cornstarch particles in non-aqueous solvents has previously been found to increase over time and explained as inter-digitation of biopolymers on the surface of cornstarch [104]. Such bond aging could also affect measurement of σ_y, although this remains to be investigated.[9]

Finally, we should address the definition of a strength from oscillatory shear measurements. So far we have put forward the peak elastic stress, σ_{osc}, forward

[9] We note that both measurements of the yield stress ($\sigma_y^{(\text{d})/\text{rev}}$) were taken from a previously flowing state, so if contacts did age it would represent a lower bound for the yield stress. It can therefore be robustly claimed that $\sigma_{\text{osc}} \ll \sigma_y$, and similarly with the reversal stress, $\sigma_t^{\text{rev}} < \sigma_y$. In contrast, caution would need to be taken if comparing precise values of σ_{osc} and σ_t^{rev}.

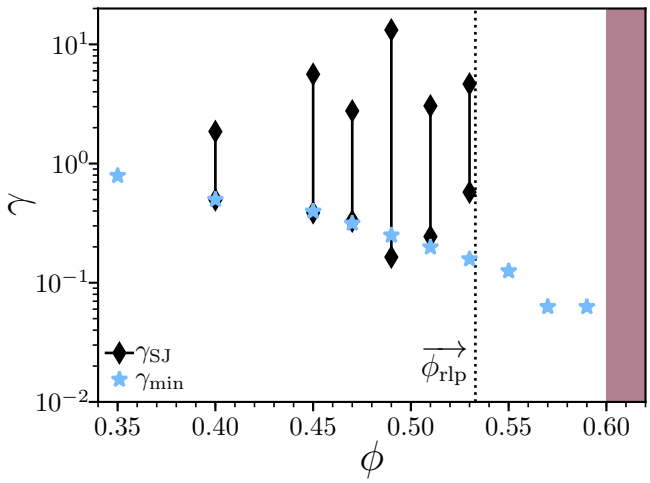

Figure 6.9 Volume fraction dependence of critical strains. Symbols: black connected diamonds, range of strains for shear jammed states upon reversal, γ_{SJ}, as defined in Fig. 6.3(b); blue stars, γ_{min}, strain at minimum of $G'(\gamma_0)$ in oscillatory shear, see Fig. 6.7(a) [inset] for definition.

as the definition of the strength measured using oscillatory shear, but a possible alternative definition should also be discussed. Most commonly the "cross-over" of the modulii is used to define a strength, the stress at which G' decreases below G'', e.g. Ref. [130].[10] In the typical case that $G' \gg G''$ for small γ_0 before sharply decreasing, the cross-over and elastic-stress definitions would be similar and the choice of definition inconsequential. In Fig. 6.7(a) [inset] at $\phi = 0.51$, the two modulii are almost equal at $\gamma_0 = 10^{-4}$ and the two definitions will differ greatly. The high G'' value is possibly due to the choice of a viscous background solvent. To compare their validity for approximating a strength measured in the low-shear-rate limit we can test their frequency dependence. While the peak in the elastic stress was shown to be ω independent, see Fig. 6.7(b), the cross-over definition entirely depends on ω in the range studied: 0 Pa at 10 rad s^{-1} and 0.035 Pa at 1 rad s^{-1}. This sensitivity reflects the linear frequency dependence of G'', which is dominated by the viscous solvent. Therefore, for this system, at the frequencies probed, the cross-over definition is not valid as measurement of the strength and we instead use the peak elastic stress, σ_{osc}.

6.2.4 Large-amplitude behaviour

The discussion of oscillatory shear has so far focussed solely on small to moderate amplitudes and the measurement of σ_{osc}; however, Fig. 6.7(a) [inset] clearly show a second set of features, a peak in G' and a concomitant rise in G''. These pronounced features have been observed in simulations of non-adhesive frictional suspensions, in which they were attributed to the formation of compressive frictional contacts and the resulting increase in viscosity [150]. Therefore, the peak in G' is not due to elastic effects, as a naïve interpretation might assume, but instead due to a strain-dependent viscosity. This interpretation is further supported by the near linear-dependence of G' upon ω in the high-strain region (i.e. viscous scaling) and shows the caution that must be taken in interpretation of linearly-defined modulii in LAOS.

To extract a strain-scale for the formation of frictional contacts in oscillatory shear, we take the strain at the minimum of $G'(\gamma_0)$ just before its sharp peak, γ_{min}, Fig. 6.7(a) [inset]. As a consistency check, γ_{min} (blue stars, Fig. 6.9) can be compared to the strain to shear jam upon reversal (black diamonds) across ϕ. The minimum strain to shear jam on reversal, i.e. the lower bound of γ_{SJ}, credibly corresponds to γ_{min} for $0.40 \leq \phi \leq 0.53$. Note that the strain scale does not go to zero at ϕ_{rlp}; instead, γ_{min} decreases approaching $\phi \approx 0.60$, consistent with ϕ_{rcp} and the shear-jamming behaviour of adhesionless frictional packings [138].

This indicates that the *strain* for the rise in G' can be associated with shear jamming and hence with the physical process that leads to the steady-state yield stress. However, we cannot necessarily equate a stress from oscillatory shear with σ_y. First, note that at an $\mathcal{O}(1)$ strain with $\omega = 10\,\text{rad}\,\text{s}^{-1}$ the shear rate, $\dot{\gamma} = \gamma_0\omega = 10\,\text{s}^{-1} \gg \dot{\gamma}_{\text{min}}$. This means that large-strain oscillatory shear corresponds to steady high-shear flow instead of 'yielding', which was previously suggested in, e.g., Ref. [151]. Consequently, the Cox-Merz rule precisely extracts the high-shear relative viscosity for $\phi = 0.47$, with $\sqrt{G'^2 + G''^2}/(\omega\eta_s) \approx G''/(\omega\eta_s) = 32$ at $\sigma \approx G''\gamma_0 = 200\,\text{Pa}$, cf. Fig. 6.2.[11]

Therefore, the high-strain-amplitude behaviour is consistent with the other rheological tests (steady-shear and reversal). It is also complimentary to our

[10] The stress is typically called 'the yield stress', but we reserve that term for steady shear in this work.

[11] An equivalent comparison was not possible at $\phi = 0.51$, with the stress at $\gamma_0 = 10$ far beyond σ_{max}.

picture of the reversal response being driven by the formation of an adhesively-stabilised frictional contact network with accumulated strain. The low-strain behaviour also more subtly supports our picture, as at $\phi = 0.51$, σ_{osc}, which we attribute to just adhesion alone, is much lower than the steady-state yield stress, which we attribute to the combined effects of adhesion and friction.

6.3 Protocol dependence in adhesive non-Brownian suspension rheology

We have now described how the steady-state yield stress, σ_y, arises from a fully-formed adhesion-stabilised compressive frictional contact network and we have also detailed how σ_{osc} represents the strength due to adhesion alone. This suggests that the two protocols should correspondingly form a frictional upper bound and a frictionless lower bound for measurements of 'a yield stress' in adhesive non-Brownian suspensions. Here 'a yield stress' represents the stress at the onset of a large plastic (inelastic) deformation. We will continue to restrict usage of 'the yield stress' and σ_y to refer to yielding to a continually-flowing state. Consistent with this assertion, we now show that another protocol for measuring 'a yield stress' lies between the two bounds. For this we choose the lower critical stress from the reversal protocol, σ_t^{rev}. We then provide a microstructural argument for its volume fraction dependence based upon our microphysical picture of friction and adhesion.

We begin by showing the volume fraction dependence of the steady-state yield stress, Fig. 6.10 (black diamonds), and how it can be accounted for using the constraint model from Fig. 6.6 (black line). In this instance, we are plotting the yield stress measured from reversal tests, σ_y^{rev}, whereas previously the model was compared with measurements taken from steady flow, $\sigma_y^{(\text{d})}$, Fig. 6.6. The use of σ_y^{rev} in place of $\sigma_y^{(\text{d})}$ emphasises that they are comparable measurements of the yield stress across the measured range of ϕ. Both the measurements and the model show that σ_y diverges as $\phi \to \phi_{\text{rlp}} \approx 0.53$, consistent with our previous remark that the yield stress is controlled by adhesion as well as friction. On the same plot, we now show the ϕ dependence of the characteristic stress from oscillatory measurements, σ_{osc}, Fig. 6.10 (blue circles). This quantity, remaining finite at $\phi > 0.53$, clearly diverges at a higher critical volume fraction. Fitting to a Krieger-Dougherty-like form (see caption for details), we find the point of

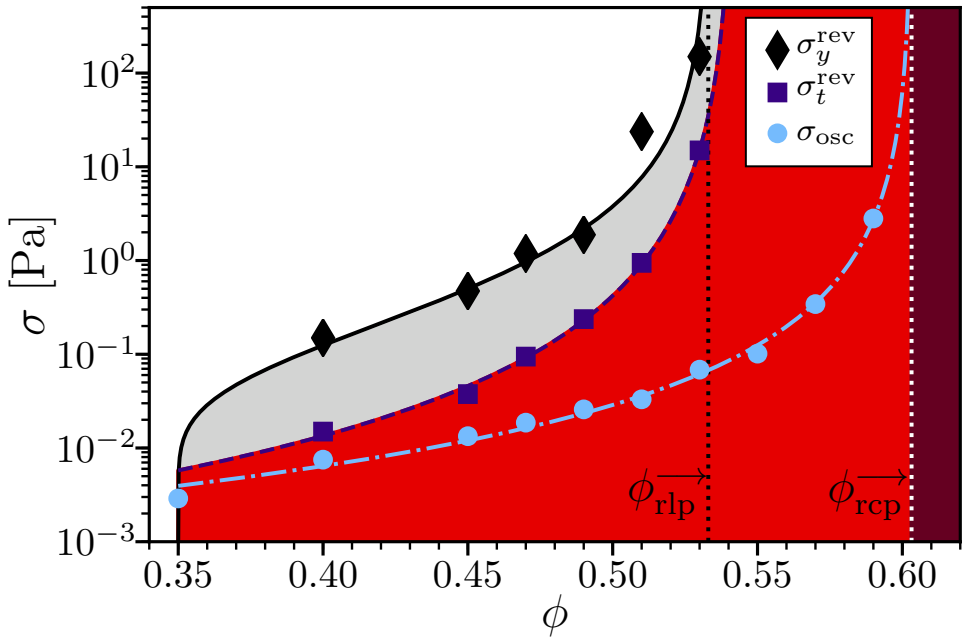

Figure 6.10 Dependence of defined stresses on volume fraction, ϕ. Symbols: black diamonds, yield stress from stress reversal, σ_y^{rev}; purple squares, transient yield upon reversal, σ_t^{rev}; light blue circles, characteristic strength of 'isotropic' state prepared through oscillatory shear, σ_{osc}. Lines: solid black, yield stress of constraint-based model, parameters as in Fig. 6.2; dashed purple, fit of σ_t^{rev} to $A(1-\phi/\phi_{\mathrm{crit}})^{-l}$, with $\phi_{\mathrm{crit}} = 0.541 \pm 0.002$ ($A = 3 \times 10^{-4}$ and $l = 2.8$); dot-dashed light blue, fit of σ_{osc} to $A(1-\phi/\phi_{\mathrm{rcp}})^{-l}$ to extract $\phi_{\mathrm{rcp}} = 0.603 \pm 0.003$ ($A = 5 \times 10^{-4}$ and $l = 2.2$); black dotted, ϕ_{rlp} from constraint-based model and $\sigma_y^{(\mathrm{d})}$ divergence; white dotted, ϕ_{rcp} from σ_{osc} divergence. Shaded regions: white, continuous flow; grey, jammed at steady-state but transient flow upon shear reversal; red, jammed at steady-state and no flow upon reversal; maroon, no dispersion possible.

divergence, at $\phi \approx 0.60$, to be consistent with $\phi_{\mathrm{rcp}} \approx 0.60$ from aqueous cornstarch suspensions [96]. The critical volume fraction for the divergence of σ_{osc} being ϕ_{rcp} is consistent with our suggestion that σ_{osc} measures the effect of adhesion without friction and the idea that the oscillatory preparation protocol is analogous to 'shaking' a dry granular packing to measure random close packing. Note, however, that the divergence in σ_{osc} at ϕ_{rcp} may be driven by changes in the effect of the oscillatory protocol approaching ϕ_{rcp}, rather than a divergence in a stress-scale resulting from adhesion alone. For example, it may be that the number of oscillations required to relax the frictional contact network diverges approaching ϕ_{rcp}.

Finally returning to the reversal transient stress identified in Fig. 6.3(b), σ_t^{rev}, we see that this measurement of 'a yield stress' lies between σ_y and σ_{osc} over all measured ϕ, Fig. 6.10 (purple squares). This is consistent with our notion that σ_y and σ_{osc} represent upper and lower bounds for yield-stress measurements. However, σ_t^{rev} has an intriguing volume fraction dependence: it appears to follow σ_{osc} at low ϕ ($\lesssim 0.45$), before rapidly increasing towards σ_y as it nears ϕ_{rlp}. Fitting a Krieger-Dougherty-like form, σ_t^{rev} appears to diverge close to ϕ_{rlp} at $\phi = 0.54$, Fig. 6.10(caption).[12]

We attribute the change in the volume fraction dependence of σ_t^{rev} to a change in the nature of the frictional contact network formed during the high stress pre-shear. We shall first describe how the structure formed during the pre-shear state changes with ϕ, before arguing how the structure would respond upon reversal in the presence of adhesive contacts and hence how σ_t^{rev} should change with ϕ.

The pre-shear state before reversal should approximate a sheared frictional non-Brownian suspension: as $\sigma \gg \sigma_a$, all adhesive bonds should be mobilised (i.e. broken), leaving frictional constraints alone. This supposition is supported by the plateau viscosity values of the steady-state flow curve reached at high stress that appear to be controlled by ϕ_{rlp}, see Appendix C.3. We therefore compare the microstructure of the pre-shear state to that of a frictional suspension, or equivalently a shear-thickening suspension at high stress ($\sigma \gg \sigma^*$), and use a schematic view of this structure (adapted from Ref. [93]) to illustrate the change in pre-shear state, Fig. 6.11. At moderate volume fractions, $\phi \lesssim \phi_{\mathrm{rlp}} - 0.08$, the frictional contact network exists primarily as linear force chains orientated in the

[12]Note that σ_t^{rev} is not defined above ϕ_{rlp}, as there is no steady flowing pre-shear state from which to apply the reversal protocol. A finite reversal stress from a shear jammed (non-flowing) state likely still exists, but it would not be directly comparable to σ_t^{rev}.

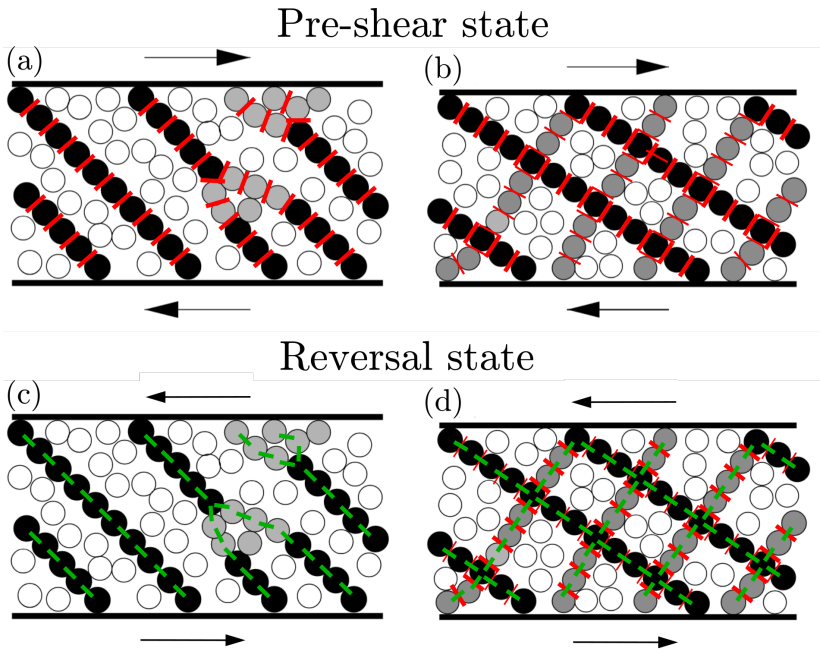

Figure 6.11 Schematic of contact force network during pre-shear and reversal. (a) and (b) Illustration of contact network formed during pre-shear step. Diagrams adapted and modified from Ref. [93]. (a) Compressive frictional contact network formed during pre-shear at a moderate volume fraction. Particles: shaded, part of contact force network or frictional "force-chains"; white, spectator particles. Red lines, compressive frictional contacts. (b) Contact network formed during pre-shear at a high volume fraction, i.e. approaching ϕ_{rlp}. Particle shading: black, compressive frictional force chains; grey, supporting frictional contact network; white, spectator particles. Red lines, frictional contacts. (c) and (d) State of contact network immediately upon reversal, i.e. from which σ_t^{rev} arises. (c) Contact network upon reversal at a moderate volume fraction showing relevant interparticle forces. Shaded particles, part of tensile adhesive force chains; green lines, adhesive contacts. (d) Contact network upon reversal at high volume fraction. Shading: black, part of tensile adhesive force chains, grey, particles part of adhesion-stabilised near-compressive frictional contact network. Lines indicate interparticle forces as in (a)-(c).

compressive direction, Fig. 6.11 [63]. As ϕ increases and approaches ϕ_{rlp}, there is a gradual transition in the form of the contact network from isolated linear force chains to an interconnected network of force chains (black particles) with a supporting frictional contact network (grey particles), Fig. 6.11(b) [63]. The supporting contact network is generated from the collision of repeatedly buckling force chains [93].[13] We now consider what the reversal response of such structures would be in the presence of adhesive bonds.

Upon cessation of shear, previously mobilised adhesive bonds would become significant, green lines in Fig. 6.11(c) and (d). Upon reversal at $\phi \leq 0.45$, Fig. 6.11(c), transient yielding would only involve tensile breakage of adhesive bonds along the (previously compressive) force chains. The transient reversal stress, σ_t^{rev}, would then be generated directly by the strength of adhesion without any contribution from frictional interactions [note the absence of compressive frictional contacts in Fig. 6.11(c) (red)]. This microstrucutral picture is consistent with σ_t^{rev} being of a similar magnitude to σ_{osc}, Fig. 6.10, as we have also associated σ_{osc} directly with adhesive bond breakage due to the removal of frictional contacts in the preparation protocol.

Finally, we consider cessation of shear at $\phi \gtrsim 0.45$. Adhesive interactions are again significant, Fig. 6.11(d) (green), but now adhesion would bond particles in both the force chains (black particles) and the supporting contact network (grey particles). When a reversed stress is applied, to transiently yield both the now tensile force chains and the adhesively-bonded supporting contact network must be broken. While force chains are formed in the compressive direction during pre-shear and become tensile upon reversal, the suporting contact network is orientated differently. Therefore, when the stress is reversed, there will be a compressive component acting between contacting particles in the supporting contact network. Frictional interactions will be relevant, Fig. 6.11(d) (red). To transiently yield at these high volume fractions will then require buckling of this now near-compressive adhesively-stabilised supporting contact network. In essence, at high volume fractions the contact network structure becomes less anisotropic, so that immediately upon reversal the contact structure is closer to that formed during steady shear. The transient reversal yield stress is then closer to the steady yield stress, although it does not become equal as the contact network formed during pre-shear is not truly isotropic. This remaining anisotropy

[13]Note that buckling of force chains will also occur in case (a), but due to the lower volume fraction a supporting contact network cannot form.

is revealed by the fact that reversal is still possible in a non-adhesive frictional suspension above ϕ_{rlp} and even up to ϕ_{rcp}. We therefore conclude that such a change in the pre-shear strucutre, when combined with adhesive bonds, could plausibly cause the large rise in σ_t^{rev} with increasing ϕ and the transition from a value close to σ_{osc} to an apparent divergence near ϕ_{rlp}.

The volume fraction dependence of σ_t^{rev} illustrates the sensitivity of the rheological response to structure due to the combined effects of friction *and* adhesion. It also acts as a cautionary tale, showing that great care must be taken during the pre-shear process when measuring 'a yield stress' in adhesive non-Brownian suspensions. However, such sensitivity does not just impact measurements, but it could also impact applications where a suspension is required to hold its shape. With the resistance to plastic deformation at $\gamma < \mathcal{O}(1)$ dependent on the shear history (remember σ_y requires strain to develop), the mechanical failure of a suspension will depend on the shear history and how it is loaded relative to the direction of that shear.

6.4 Conclusion

In this chapter we first demonstrated that the steady-state rheology of a model cornstarch-in-oil suspension is captured by the constraint-based rheology model, developed in Ch. 5. With the yield stress, defined as the minimum stress required for continual flow, becoming measurable at the percolation threshold under shear and diverging at random loose packing, we deduced that this is a frictional suspension with adhesive bonds that are broken with stress. Probing the system further, it was shown that the reversal response is consistent with this picture: the suspension must be strained to form a percolating adhesion-stabilised frictional cluster and for the yield stress to develop. This description of adhesive non-Brownian suspensions was then further tested. By preparing an 'isotropic' state using oscillatory shear, we measured the effect of adhesion alone. This revealed the importance of frictional contacts as the the suspension was much weaker when frictional contacts were relaxed by oscillatory shear.

The varied responses to the different rheological protocols applied exemplify the sensitivity of adhesive non-Brownian suspensions to shear history. Principally, we showed that the suspension can only support the yield stress when strained in the direction of the applied stress. This property is reminiscent of 'fragility' in dry

granular materials [93], ultimately, because the structure is formed by the stress itself. The *formation* of structure with shear represents a stark contrast with the colloidal view, where structure is formed at rest, supports stress equally in all directions, and is then only destroyed by shear. Such 'fragility'[14] has ramifications for tuning the behaviour of the system, because when the direction of shear is changed the suspension will be weaker, i.e. the reversal response in Fig. 6.3. Applying vibrations or orthogonal shear should then reduce the resistance of an adhesive non-Brownian suspension to flow and allow dynamic tuning of the flow behaviour, as has been shown in concentrated frictional suspensions [152–154].

[14]This is not strictly fragility, as defined by Cates et al. [93], as it can support a non-zero reversal stress; however, it shares may connections so it remains a useful concept, hence it remains in quotation marks.

Chapter 7

Analysing the effect of dispersants: towards a model industrial system

In this chapter we use the constraint-based rheology framework developed in Ch. 5 and validated in Ch. 6 to evaluate the effect of dispersants and illuminate their physical mechanism of action. Dispersants, surfactants that adsorb to the particle surface and are commonly taken as reducing interparticle attraction, are widely used to tune the flow behaviour of suspensions. As a dispersant can be simply added to a formulation, it represents an easier method of tuning the particle-particle interactions than, for example, changing the background solvent [104], permanently grafting a stabiliser during particle production (e.g., PHSA-stabilised PMMA) or changing the particle size distribution.

To analyse the effect of dispersants on a concentrated non-Brownian suspension we use a model system that is closer to an industrial system. One could argue that a major limitation of the work presented so far is the choice of main model system, cornstarch. It is not a nearly-hard-sphere particle with well-characterised interactions, such as silica or PMMA, nor is it necessarily representative of an industrial suspension. The only major advantages are its widespread application as a model system in rheology (e.g., Refs [15, 82, 95]) and its ease of use. We therefore develop a model aqueous mineral suspension of ground calcite in a glycerol-water mixture that mimics mine tailings, cement, ceramics and, indeed, similar mineral slurries, but without becoming highly multi-component or explicitly time dependent like, e.g., a mortar [4].

The price we pay for using a more realistic model system is that the rheological

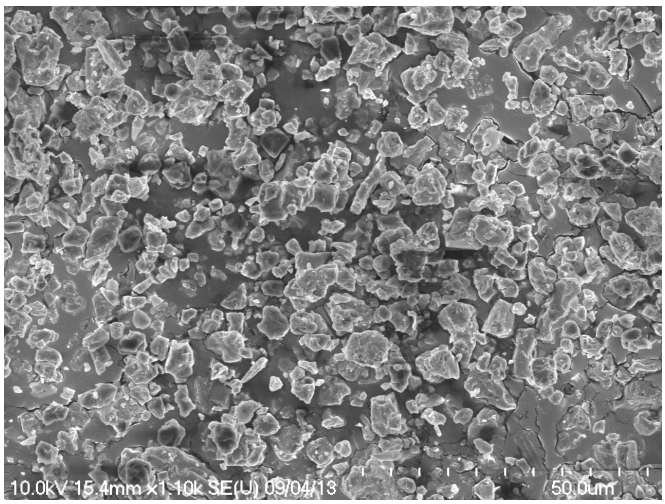

Figure 7.1 Scanning electron microscopy image of Eskal 500 ground calcium carbonate, 50 µm scalebar. Image courtesy of Elena Blanco.

results are less clean than for our previous model systems. Importantly, however, we will be able to demonstrate that the constraint-based rheology framework is useful for analysing general trends and guiding formulation practice without producing perfect fits to data. Without dispersant, bare calcite forms a yield-stress suspension that we show is comparable to the cornstarch-in-oil suspension of Ch. 6. We then show that there are two types of dispersant for forming "stabilised", or well-dispersed, suspensions: one which both reduces adhesion and increases the onset stress for friction, and another type which only increases the onset stress. However, both reduce the yield stress dramatically, so that tuning the onset stress for interparticle friction is the decisive mechanism for affecting the yield stress of non-Brownian suspensions.

Increasing the onset stress until $\sigma_a \ll \sigma^*$ means that when adhesion is relevant interparticle friction is not yet activated. We argue that σ^* is set by the removal of the dispersant from the surface due to shear. An unexpected way to improve dispersant design is therefore suggested: increasing adsorption strength (raising σ^*) rather than simply increasing separation to reduce attraction (lowering σ_a). This insight contrasts with the colloidal view and further supports the utility of the constraint-based model as a framework for thinking about non-Brownian suspension flow.

7.1 Ground calcium carbonate suspensions

As a model particle, we use Eskal 500 ground calcium carbonate (KSL Staubtechnik GmbH, 99 wt.% purity, primary impurity 0.45 wt.% magnesium oxide, density $2.7\,\mathrm{g/cm^3}$). Ground calcium carbonate (GCC) is widely used in manufacturing: to improve the finish and whiteness of paper; to act as a bulking agent for adhesives and fillers; or, to enhance the opacity and abrasion resistance of paint [155]. The GCC powder is quoted as having a limited quantity of 'fines' (3.6% below 0.9 µm) and no particles larger than 21 µm, with a volume weighted median diameter of 4 µm [156]. The particles are then highly polydisperse when compared to PMMA [24] or silica [56] model systems. However, the size range is not so broad (as in mortars and concretes) that the largest particles will become comparable to a typical rheometric gap ($\sim 1\,\mathrm{mm}$). If this was the case, a small number of particles could seize the instrument.[1] Therefore, a GCC powder represents an appropriate increase in complexity to determine if the framework developed in this thesis can capture and interpret the effect of dispersants on industrially relevant suspensions.

In application, calcite suspensions would typically be prepared with water as the background solvent; however, use of water alone presents various challenges that necessitate the use of glycerol-water mixtures instead. While solvent evaporation and drying are useful properties in paint or paper coating, for rheological characterisation it is less beneficial. At high solid volume fraction formation of a solid due to drying at the edge was observed; while at lower solid volume fraction, rapid sedimentation was visibly apparent. Using a glycerol-water mixture slows sedimentation by increasing the viscosity and reduces drying through the hygroscopy of glycerol.[2] The use of a tunable-viscosity background solvent also allows the stresses accessible at typical shear rates to be varied. The glycerol proportion did not appear to significantly impact the type of interaction between particles, because the rheology remains qualitatively unchanged when compared with a water background solvent in the small subset of tests for which a comparison was possible, see Fig. 7.2.

To prepare a suspension, Eskal 500 powder was added to a glycerol-water mixture

[1] The particle shape is also aspherical, Fig. 7.1, but importantly it is not formed of high-aspect-ratio rod-like particles, in which orientational ordering can cause additional time-dependent dynamics [157].

[2] An 85 wt% glycerol-water mixture is approximately at equilibrium with the relative humidity of 40% that experiments were conducted at [158].

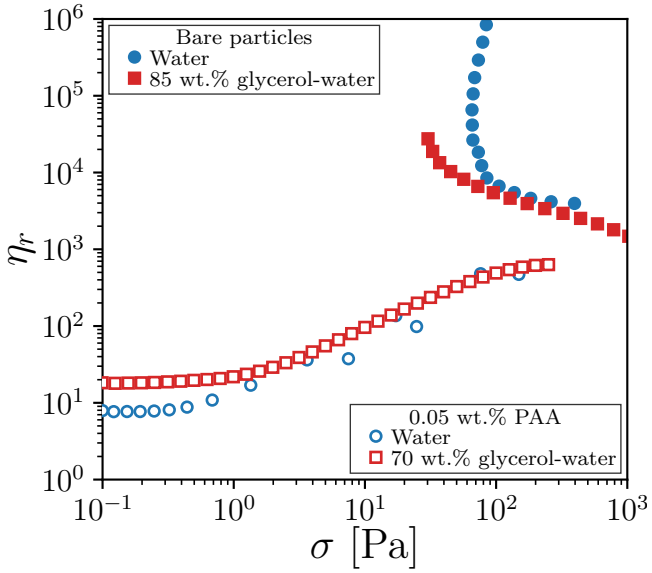

Figure 7.2 Tuning the background solvent at $\phi = 0.45$: relative viscosity, η_r *vs* stress, σ. Filled symbols, bare particles: blue circles, water background solvent; red squares, 85 wt.% glycerol-water mixture background, this is the system used for the data in Fig. 7.3. Protocol for water background solvent measurements as with glycerol-water background solvent. Open symbols, particles stabilised by 0.05 w/w% PAA: blue circles, water background solvent, protocol as in §7.3.1; red squares, 70 wt.% glycerol-water background, the composition used for the data in Fig. 7.6. Results with water background solvent are complicated by drying and sedimentation.

and to calculate ϕ we use literature values for the solvent density [158]. For samples with a dispersant, the dispersant is first dissolved into the glycerol-water mixture. The concentration is quoted in terms of a weight percentage of the calcite (w/w%) and the ratio is kept constant with changing solid volume fraction. Note that the dispersant mass is considered as additional to the suspension when quoting ϕ (i.e. as if subsequently added to a suspension). Literature values from Ref. [158] are used for the viscosity of the background solvent glycerol-water mixtures, as measured background solvent viscosities were found to correspond with the literature values with and without dispersant.

The powder was incorporated into the glycerol-water mixture through a combination of vortex mixing, followed by, at high volume fractions ($\phi \gtrsim 0.45$), mixing with a spatula, or, at lower volume fractions ($\phi \lesssim 0.45$), high-shear mixing, until a smooth suspension was achieved. Samples were then sealed and placed in an ultrasound bath for $\sim 5\,\text{min}$ to remove bubbles, before leaving on a roller mixer for $\gtrsim 4\,\text{h}$ to allow dispersant adsorption and prevent sedimentation.

7.2 Rheological characterisation of a bare calcite suspension

We begin by looking at the behaviour of a bare calcite suspension, that is one with no dispersant, using a combination of steady-shear and shear-reversal rheology. We show that the response is consistent with particles having both frictional and adhesive interactions.

7.2.1 Steady-state flow curves

The steady-state rheology is characterised using an 85 wt.% glycerol-water mixture background solvent, viscosity $\eta_s = 110\,\text{mPa}\,\text{s}$, and the same protocol as used for cornstarch-in-oil suspensions, Ch.6. All results in this chapter are reported from corrected parallel-plate measurements with $R = 20\,\text{mm}$ and $h = 1\,\text{mm}$. Using sandblasted parallel plates and measuring under imposed strain-rate (TA Instruments ARES-G2), we present the results of a single shear-rate up sweep at 5 pts./decade from a minimum shear rate, $\dot{\gamma}_{\text{min}} = 0.1\,\text{s}^{-1}$, to near the fracture stress, $\sigma_{\text{max}} \sim 400\,\text{Pa}$. The time-averaged data is reported with relative

viscosity, η_r, as a function of the corrected stress, σ, from the imposed angular velocity and measured torque, for various volume fractions, ϕ, in Fig. 7.3(a). All shear rates, stresses and hence viscosities reported in this chapter follow this convention, unless explicitly stated otherwise.

The flow curves are indicative of a yield-stress fluid and the steady-state rheology displays two features that are captured by the constraint-based suspension rheology model. Firstly, we identify a yield stress, σ_y, from the stress at the lowest accessed shear rate. With increasing ϕ, σ_y increases exponentially, before appearing to diverge at $\phi \approx 0.51$, Fig. 7.3(b). To interpret these results, we assume for now that the bare calcite particles have a negligible (or zero) onset stress ($\sigma^* \to 0$), so that they are always in frictional contact. Then using the constraint-based model of Ch. 5, we take the yield stress as evidence of adhesive constraints, so that the jamming volume fraction, $\phi_J = \phi_p a(\sigma) + \phi_{\text{rlp}}(1 - a)$, increases with stress from a lower limit, $\phi_p = 0.18$, to an upper limit, $\phi_{\text{rlp}} = 0.51$, controlled by the decreasing fraction of adhesive contacts, $a(\sigma) = 1 - \exp[-(\sigma_a/\sigma)^\kappa]$ ($\sigma_a = 0.6\,\text{Pa}$ and $\kappa = 0.6$). Secondly, in the high-shear-rate limit, suspensions shear thin and approach a plateau viscosity, η_r^∞, which is taken where $\sigma \approx \sigma_{\text{max}}$ or at the highest accessed shear rate. This high-shear viscosity diverges at $\phi = 0.50 \pm 0.01$, Fig. 7.3(c) caption for fit details, a similar volume fraction to the ϕ that captures the divergence of σ_y, $\phi_{\text{rlp}} = 0.51$. With these two features captured, the full flow curves are well-described by the constraint-based model using $\phi_J(\sigma)$ and the Krieger-Dougherty viscosity form determined from the fit to η_r^∞, $\eta_r = (1 - \phi/\phi_J)^{-2.6}$, Fig. 7.3(a).

7.2.2 Shear-reversal response

Although the model captures multiple features of the data, we have tacitly assumed through our choice of notation (ϕ_{rlp} and ϕ_p) that the suspension is frictional. *A priori*, we do not know the physical interpretation of the limiting jamming volume fractions, as one would with monodisperse spheres, or a well-studied model system such as cornstarch. Therefore, we must go beyond steady-state rheology and again look at the transient behaviour upon reversal at stresses below the steady-state yield stress.

In the interpretation of the steady-state rheology data in Fig. 7.3, we have assumed that particles are always in frictional contact ($\sigma^* \to 0$ and $f = 1$). We now perform shear-reversal experiments to show that this assumption is indeed

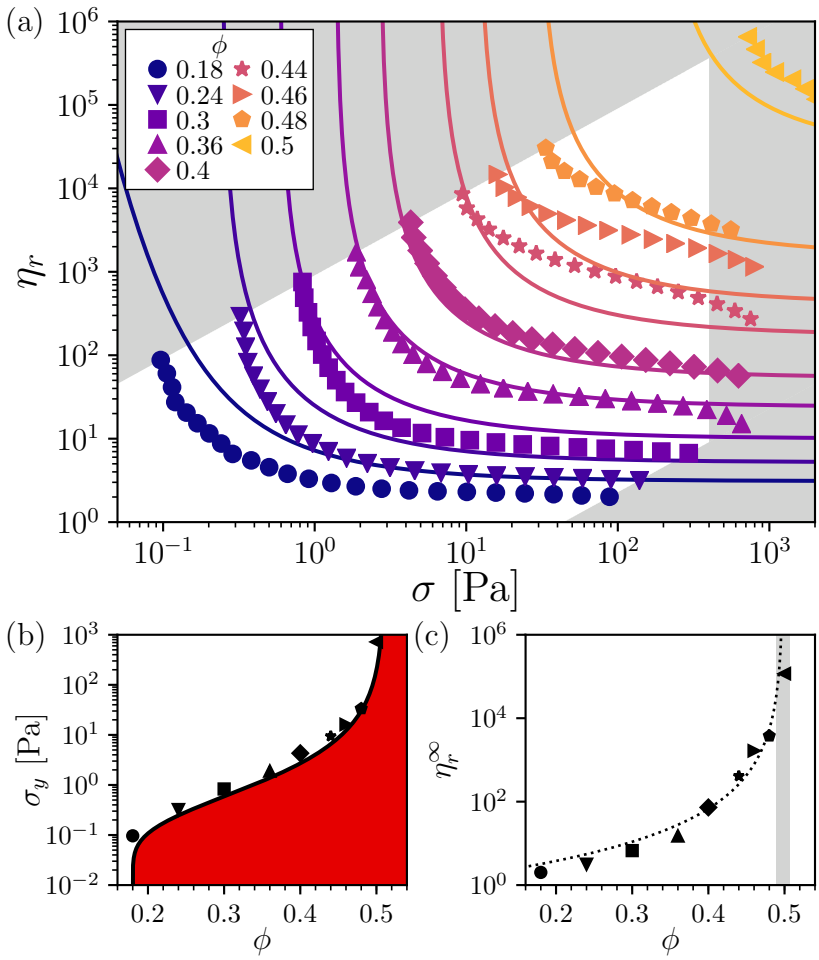

Figure 7.3 Steady-state rheology of an aqueous calcite suspension in an 85 wt.% glycerol-water mixture background solvent. (a) Flow curves: relative viscosity, η_r, as a function of stress, σ, measured under imposed shear rate. Symbols, flow curves for given volume fractions, ϕ, see inset legend. Grey shading represents limit of observable rheological "window", see Ch. 2, $\dot{\gamma}_{\min} = 0.1\,\mathrm{s}^{-1}$ and $\sigma_{\max} = 400\,\mathrm{Pa}$. Lines, fit to constraint-based rheology model, detail in Chs. 5 and 6, parameters: $\phi_{\mathrm{rlp}} = 0.51$, $\phi_p = 0.18$, $\sigma_a = 0.6\,\mathrm{Pa}$ and $\kappa = 0.6$. (b) Yield stress, σ_y, *vs* volume fraction, ϕ. Symbols, experimental yield stress determined dynamically from lowest accessed shear rate, $\sigma_y = \sigma(\dot{\gamma}_{\min} = 0.1\,\mathrm{s}^{-1})$. Solid line, representative fit of σ_y to unjamming stress from constraint-based rheology model, parameters as in (a). Shading: red, jammed at steady state; white, flowing at steady state. (c) High-shear, relative viscosity, η_r^∞, *vs* volume fraction, ϕ. Symbols, relative viscosity at either the maximum accessed shear rate ($\phi \leq 0.30$) or before fracture at $\sigma \approx \sigma_{\max} = 400\,\mathrm{Pa}$ ($\phi \geq 0.36$). Dotted line, fit to a Krieger-Dougherty form, $\eta_r^\infty = (1 - \phi/\phi_{\mathrm{rlp}})^{-l}$, with $\phi_{\mathrm{rlp}} = 0.50 \pm 0.01$ (grey shaded region) and $l = 2.6 \pm 0.3$.

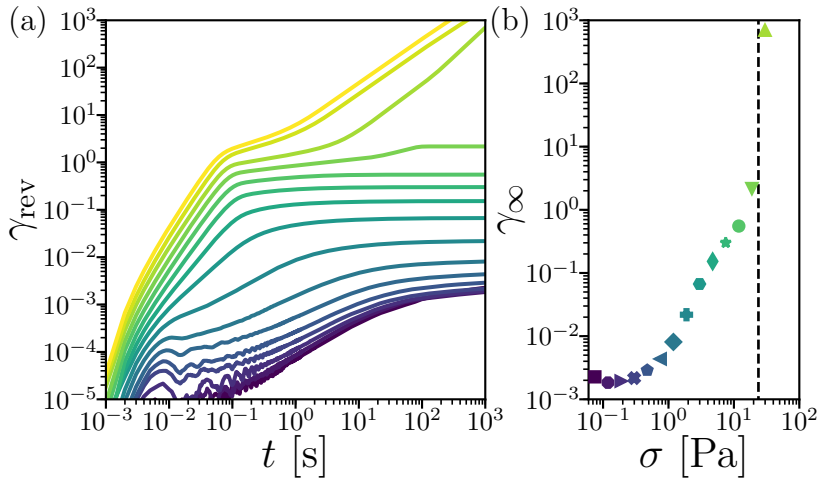

Figure 7.4 Reversal behaviour of a bare calcite suspension at $\phi = 0.46$ in a 50 wt.% glycerol-water mixture. (a) Reversal strain, γ_{rev}, as a function of time, t, after application of a reversal stress, σ. Reversal stresses are applied from 0.075 Pa (purple) to 75 Pa (yellow) logarithmically at 5 pts./decade. (b) Limiting reversal strain, $\gamma_\infty = \gamma_{\mathrm{rev}}(t = 10^3\,\mathrm{s})$, *vs* applied reversal stress, σ, colour of symbol corresponds with strain trace in (a). Dashed line denotes boundary between jammed ($\dot{\gamma} \to 0$ as $t \to \infty$) and flowing ($\dot{\gamma} > 0$ as $t \to \infty$) states, at $\sigma_y = 23\,\mathrm{Pa}$.

correct. By showing that the yield stress takes a strain of $\mathcal{O}(1)$ to develop upon reversal, the presence of a frictional contact network stabilised by adhesive bonds can be inferred. Thus, this justifies our presumptive use of ϕ_p and ϕ_{rlp} as the limiting ϕ_J and, therefore, our interpretation of the steady-state rheology.

Taking a single sample at $\phi = 0.46$ in a 50 wt.% glycerol-water mixture, we investigate the qualitative features of the response to shear reversal. Using a TA Instruments AR-2000 rheometer with cross-hatched parallel plates, we report the rim strain and stress, $\sigma = 3\mathcal{T}/2\pi R^3$, correct at yielding where $\mathrm{d}\ln\sigma/\mathrm{d}\ln\dot{\gamma} = 0$. The sample is first pre-sheared at 75 Pa for 10 s, before being left quiescent for a further 10 s. A stress, σ, is then applied for 1000 s in the reverse shear direction and the strain response following the application, $\gamma_{\mathrm{rev}}(t)$, is reported in Fig. 7.4(a).

As with a suspension of cornstarch in oil, Fig. 6.3, we see a similar series of response types with increasing σ: creep at low stress ($\sigma \lesssim 1\,\mathrm{Pa}$); transient yielding, followed by shear jamming, at intermediate stresses ($1\,\mathrm{Pa} \lesssim \sigma \lesssim 20\,\mathrm{Pa}$); and continuous flow at high stress ($\sigma \gtrsim 20\,\mathrm{Pa}$). This then implies that the system yields from a state which is shear jammed at $\gamma_{\mathrm{rev}} = \mathcal{O}(1)$, which is indicative of a frictional suspension with the stress-dependent breakage of adhesive bonds. This shows that the picture of yielding demonstrated for a cornstarch-in-oil

suspension and the constraint-based rheology model is suitable for describing the more realistic industrial model system of aqueous GCC.

However, plotting the long-time limiting strain, $\gamma_\infty = \gamma_{\text{rev}}(t = 10^3\,\text{s})$, we can see a significant difference in the response compared to that of a cornstarch-in-oil suspension shown in Fig. 6.3: the increase in γ_∞ below continual flow is far more gradual. Instead of a sharp transition in the response from creep to shear jamming, with a corresponding jump in γ_∞, there is now a continuous transition. The origin of this more complex deformation below σ_y is not clear. However, it could be related to the large size polydispersity, as the fines can form a gel-like background at low concentrations [159]. Then at low stresses, the system may behave as non-Brownian particles in a yield-stress background. Although the steady-state rheology of non-Brownian particles in a yield-stress background is known [160], how such a system would respond on reversal has not been investigated. However, the interaction between a fragile contact network of non-Brownian particles and a soft-jammed gel could be expected to be complex and yielding may occur over a broad range of strain and stress.

Before investigating the effect of dispersants, we should ensure that the value of $\phi_{\text{rlp}} \approx 0.51$ we have measured is sensible. While comparable to the value for monodisperse spheres, $\phi_{\text{rlp}} \approx 0.55$ [57], we must consider additional particle details. Eskal 500 is highly polydisperse and in frictionless hard-sphere systems a broad range of sizes is well known to increase the jamming volume fraction: smaller particles pack in the interstices of larger particles, as invoked in Ref. [80]. For frictional particles under shear, significant size variation in the form of bidispersity also increases ϕ_{rlp} [161]. In contrast, ϕ_{rlp} for Eskal 500 is *lower* than that for monodisperse spheres. The decrease in ϕ_{rlp} may instead be due to shape: frictional ellipsoidal particles under shear pack at lower volume fractions than spheres [162].[3] Although direct comparisons are challenging, we can conclude that the critical volume fraction identified at $\phi = 0.51$ is consistent with the frictional jamming point, although without comparison to hard-sphere simulations it is not possible to determine if this is truly the high interparticle friction coefficient limit.

[3]Interestingly, this is in contrast to the effect of asphericity in frictionless packings where it is observed to increase the jamming volume fraction [163].

7.3 Rheological characterisation of a stabilised calcite suspension

Having established that a bare calcite suspension behaves as a frictional and adhesive non-Brownian suspension that is comparable to a cornstarch-in-oil suspension, i.e. $\sigma^* \to 0$ and $\sigma_a > 0$, we now turn to discussion of dispersants and their effect on a calcite suspension. The role of a dispersant in a colloidal suspension is seen as providing a repulsive barrier between particles, either steric or electrostatic, that prevents aggregation or flocculation, e.g. Ref. [164]. Here we seek to investigate the effect of several dispersants on the rheology of a concentrated non-Brownian suspension, first presenting the phenomenology, and then interpreting the results through the constraint-based framework. From this we will go on to deduce the physical effect of a dispersant on the microscopic level. Note that none of the data presented in this section is as 'clean' as that already shown for cornstarch and other model systems. This is to be expected, given the much more near-application nature of GCC suspensions. In particular, few of the comparisons or fits to models work as nicely as in previous chapters or require further fit parameters, and these are only done to extract values for the purpose of indicating trends. Nevertheless, we shall see that the phenomenology can still be interpreted in some detail using the framework we have developed so far and from which we can then deduce 'design principles' for modification of suspension rheology.

7.3.1 Increasing the onset stress and reducing adhesion

We begin by looking at two dispersants, which we shall see behave similarly: both eliminate adhesion ($\sigma_a \to 0$) and introduce a finite onset stress for interparticle friction ($\sigma^* > 0$). The two dispersants used are polyelectrolytes: a low-molecular weight sodium salt of poly-(acrylic acid) (PAA) (5100 Da molecular weight, ~ 54 monomer units, Sigma-Aldrich, approx. radius of gyration ~ 2 nm [165]) and Morwet D-425 (MW425), a sodium salt of alkyl-napthalene sulphonate condensate (supplied by AkzoNobel). Such napthalene sulphonate condensates are widely used as "superplasticisers" in cement, where they can create highly-flowable self-compacting concrete [80]. PAA is also a widely used dispersant and it is known to adsorb to calcite [166]. As PAA lowers the zeta potential of particles [167], PAA is commonly believed to stabilise via electrostatic repulsion.

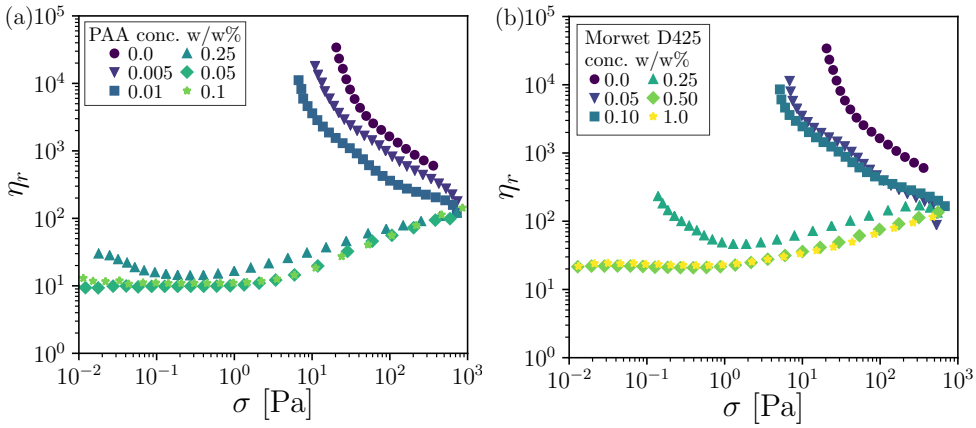

Figure 7.5 Effect of dispersant concentration on calcite suspension rheology. (a) Concentration sweep of poly-(acrylic acid) (PAA) sodium salt (5100 Da molecular weight). Symbols, flow curves, relative viscosity, η_r, as a function of stress, σ, at a volume fraction, $\phi = 0.44$, in a 50 wt.% glycerol-water mixture background, at various concentrations of PAA, see inset legend. Concentrations are given as weight percentages relative to mass of calcite (w/w%). (b) Concentration sweep of alkyl-naphthalene-sulphonate condensate sodium salt (Morwet D-425, MW425), symbols as in (a), for MW 425 concentrations see inset legend.

The effect of these two dispersants is first probed through a concentration sweep on a calcite suspension at $\phi = 0.44$, with a 50 wt.% glycerol-water mixture. The relative mass of PAA added is varied from 0.005 to 0.1 w/w% and of MW425 from 0.05 to 1.0 w/w% We report the relative viscosity as a function of stress from a single rate-controlled up sweep at 6 pts./decade from $\dot{\gamma}_{\min} = 0.1\,\mathrm{s}^{-1}$ to $1000\,\mathrm{s}^{-1}$ for PAA in Fig. 7.5(a) and for MW425 in (b). Data was taken with a 20 s equilibration period and 10 s measurement average per point with sandblasted parallel plates (TA Instruments ARES-G2). Reversibility of the flow curves was ensured between $\dot{\gamma} = 0.1\,\mathrm{s}^{-1}$ and $100\,\mathrm{s}^{-1}$.

With the addition of a small quantity of PAA, ≤ 0.01 w/w%, we see a gradual (sublinear) decrease in the yield stress, $\sigma_y = \sigma(\dot{\gamma}_{\min} = 0.1\,\mathrm{s}^{-1})$: doubling the quantity of PAA from 0.005 w/w% to 0.010 w/w% decreases σ_y from 11 Pa to 7 Pa. However, increasing the quantity of PAA further has a highly non-linear effect: an additional $2^1/_2$-fold increase to 0.025 w/w% causes a drop of at least three orders of magnitude in σ_y. Now at $\dot{\gamma}_{\min}$ yielding is no longer apparent and only weak shear thinning is seen, then at $\sigma > 1$ Pa the suspension begins to shear thicken. The small degree of shear thinning at low stress ($\sigma < 0.1$ Pa) vanishes at 0.05 w/w% PAA, but with higher PAA dosage still (0.1 w/w%) no further change is observed. The same progression is seen with MW425, but with the dispersant

concentrations increased by a factor of 10. We suggest the lack of change with continued increase in dispersant concentration is related to an adsorption limit, where a monolayer of polymeric dispersant is formed [167].[4]

We now focus on the 'stabilised', i.e. well-dispersed, state, varying ϕ, but fixing the dispersant concentration at 0.05 w/w% PAA in a 70 wt.% glycerol-water mixture or 0.5 w/w% MW425 in 85 wt.% glycerol-water mixture. The glycerol proportion in the background solvent was increased to move the shear-thickening seen at high shear rates in Fig. 7.5 into a lower shear-rate range. Measurements are taken under imposed stress (cross-hatched parallel plates, TA Instruments AR2000 for PAA and TA Instruments DHR-2 for MW425) at 10 pts./decade from $\sigma_{\text{app}} = 0.1\,\text{Pa}$ to an upper limit, set by inertial ejection ($\sigma \sim 100\,\text{Pa}$ for $\phi < 0.40$) or sample fracture ($\sigma_{\text{app}} \approx 316\,\text{Pa}$). A single up sweep is reported, with reversibility ensured over a lower stress range. For each measurement point the first 5 s are discarded, to allow equilibration; the total step time is then adjusted to allow sufficient strain for averaging but without allowing sedimentation, details in captions of Figs. 7.6 and 7.7.

We will initially focus on the flow curves of a PAA-stabilised suspension, presented as apparent relative viscosity, $\eta_{r,\text{app}}$ (taken from the apparent stress, $\sigma_{\text{app}} = 2\mathcal{T}/\pi R^3$) *vs* re-scaled shear rate, $\dot{\gamma}\eta_s$, Fig. 7.6(a). With increasing ϕ, the time-averaged flow curves show a transition at $\phi \approx 0.51$ from continuous shear thickening (CST) to discontinuous shear thickening (DST). Remember that DST is shown by the onset of a vertical slope in the flow curve when presented in terms of shear rate. From these flow curves a two-branch shear-thickening phenomenology becomes apparent, Fig. 7.6(b), by plotting as a function of ϕ the minimum relative viscosity [low-shear plateau, $\min(\eta_r)$, black circles] and high-shear plateau viscosity [$\max(\eta_r)$, red squares]. Using a Krieger-Dougherty form [$\eta_r \propto (1-\phi/\phi_J)^{-l}$], we can then extract the high-shear limiting jamming volume fraction [$\phi_J = 0.493 \pm 0.009$ (red shading)] and low-shear limiting jamming volume fraction [$\phi_J = 0.62 \pm 0.03$ (grey shading)], details in Fig. 7.6 caption.[5]

[4] As a rough calculation, assuming monodisperse spherical particles of diameter 4 µm the calcite power has a specific surface area of $\sim 0.5\,\text{m}^2/\text{g}$. At a PAA concentration of 0.05 w/w%, above which no further rheological change is observed, assuming a linear size of 3 nm an area of $0.5\,\text{m}^2/\text{g}$ is also found, suggesting monolayer coverage is plausible at this dispersant concentration (with the caveats that complete adsorption was assumed and a crude estimate of specific surface area was used).

[5] As a note of caution, there is ambiguity in which values of $\max(\eta_r)$ to take as plateau values due to the proximity to fracture [solid symbols in Fig. 7.6(b)]. This drop away from the extrapolated viscosity value has been associated with fracture on the microscopic scale before macroscopic fracture occurs [168]. We exclude $\phi \geq 0.49$ based on observation of the sample

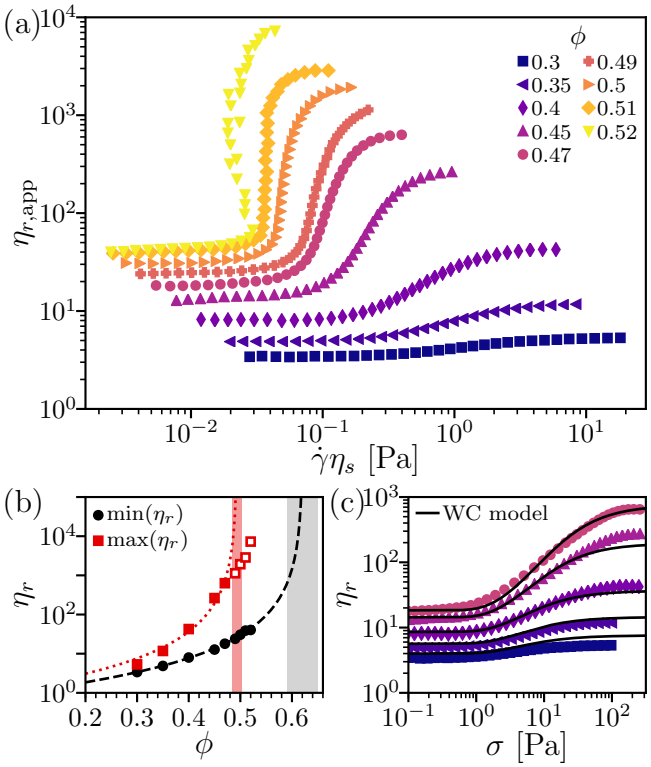

Figure 7.6 Time-averaged rheology of a dispersed calcite suspension, ground calcite suspended in a weak poly-electrolyte solution of a 70 wt.% glycerol-water mixture with 0.05 w/w% a poly-(acrylic acid) sodium salt, concentration of PAA fixed relative to the mass of calcite. (a) Relative (apparent) viscosity, $\eta_{r,\mathrm{app}}$, as a function of the rescaled shear rate, $\eta_s\dot{\gamma}$, at a given volume fraction, ϕ, see inset legend. Suspensions measured under imposed stress at 10 pts./decade from 0.1 Pa, 5 s equilibration time per point with a total step time: 10 s for $\phi \leq 0.40$, 20 s for $0.47 \leq \phi \leq 0.49$ and 30 s for $\phi \geq 0.51$. (b) Plateau viscosity variation with volume fraction. Red squares: high-shear plateau viscosity, $\max(\eta_r)$; black circles, low-shear viscosity, $\min(\eta_r)$. Dotted red line, fit of Krieger-Dougherty form, $\eta_r = (1-\phi/\phi_J)^{-l}$ finding the critical jamming point $\phi_{\mathrm{rlp}} = 0.493 \pm 0.009$ (red shaded region) and $l = 2.2 \pm 0.2$. To the low-shear viscosity a Krieger-Dougherty-like form, including an additional pre-factor, A, can be fitted (black dashed line), to give $\phi_{\mathrm{rcp}} = 0.62 \pm 0.03$ (grey region), with $l = 2.2 \pm 0.4$ and $A = 0.8 \pm 0.1$. (c) Fit of Wyart-Cates model to continuous shear-thickening data for $\phi \leq 0.47$. Symbols, flow curves plotted as relative viscosity, η_r *vs* corrected stress, σ, for ϕ see legend in (a); black lines, fit of WC model in log-space with $\sigma^* = (3.02 \pm 0.15)$ Pa and $\beta = 1.02 \pm 0.03$ using $\phi_{\mathrm{rlp}} = 0.493$ and $\phi_{\mathrm{rcp}} = 0.62$, with $eta_r = [1-\phi/\phi_J]^{-2.2}$. Here, we use Eq. 3.3, $\phi_J(\sigma) = \phi_{\mathrm{rlp}} f(\sigma) + \phi_{\mathrm{rcp}}(1-f(\sigma))$, with the fraction of frictional contacts given by Eq. 3.4, $f(\sigma) = \exp[-(\sigma^*/\sigma)^\beta]$.

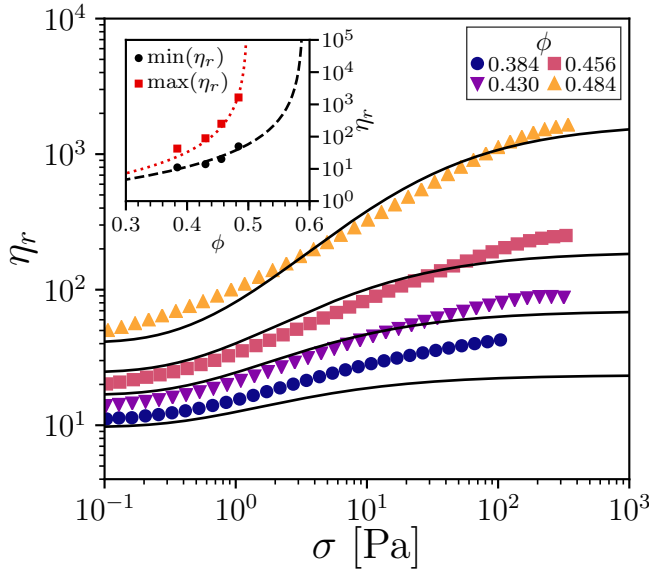

Figure 7.7 Time-averaged flow curves for calcite suspensions in an 85 wt.% glycerol-water mixture background, stabilised by 0.5 w/w% alkyl-naphthalene-sulphonate condensate sodium salt (MW425). Main figure: relative viscosity, η_r, *vs* stress, σ. Symbols, experimental data at a given volume fraction, ϕ, see legend. Measurements taken under imposed stress at 10 pts./decade from 0.1 Pa, 5 second equilibration time and 10 s measurement time step time. Black lines, fit at given ϕ to WC model with $\sigma^* = (1.0 \pm 0.1)$ Pa and $\beta = 0.67 \pm 0.03$, using limiting volume fractions $\phi_{\mathrm{rlp}} = 0.50$ and $\phi_{\mathrm{rcp}} = 0.59$ from high-shear and low-shear plateau viscosity divergences. Inset: plateau viscosities as a function of volume fraction, ϕ. Symbols: red squares, max(η_r), high-shear viscosity; black circles, min(η_r), low-shear viscosity. Lines: red dotted, fit of max(η_r) to Krieger-Dougherty form, $\eta_r = (1 - \phi/\phi_{\mathrm{rlp}})^{-2.2}$, with fixed $l = 2.2$ taken from Fig. 7.6, to give $\phi_{\mathrm{rlp}} = 0.499 \pm 0.003$; black dashed, similar fit to min(η_r) finding $\phi_{\mathrm{rcp}} = 0.59 \pm 0.01$. Note that both errors are likely underestimated due to fixing $l = 2.2$.

The phenomenology is consistent with thickening to a plateau controlled by the frictional jamming point, ϕ_{rlp}. The critical volume fraction extracted from $\max(\eta_r)$ (0.49 ± 0.01) is within error of the value taken from η_r^{∞} in the bare suspension (0.50 ± 0.01). We then deduce that the suspension thickens from a value controlled by the frictionless jamming point, i.e. $\phi_{\mathrm{rcp}} \approx 0.62$.[6] This estimate of ϕ_{rcp} is highly extrapolated, but it is consistent with the result of a preliminary powder compaction test that finds $\phi_{\mathrm{rcp}} \approx 0.60$.[7] The suspension thickens between the frictionless low-shear plateau and frictional high-shear plateau with increasing shear stress, Fig. 7.6(c) (symbols). By replotting the volume fractions that continuously shear thicken to a plateau ($\phi \leq 0.47$) and comparing with the WC model, we can extract an estimate of the critical onset stress, $\sigma^* = (3.0 \pm 0.2)\,\mathrm{Pa}$, see Fig. 7.6 caption for details.[8] The more limited results with MW425 ($0.384 \leq \phi \leq 0.484$), Fig. 7.7 (symbols), are consistent with the same phenomenology and limiting jamming volume fractions (within estimated errors), Fig. 7.7 (inset). Comparison with the WC model (black lines) gives an onset stress of the same magnitude as with PAA, $\sigma^* = (1.0 \pm 0.1)\,\mathrm{Pa}$, fit details in Fig. 7.7 (caption).

7.3.2 Increasing the onset stress alone

We now look at a third dispersant, which we will show has a different effect: increasing σ^* from effectively zero to a finite value, but leaving adhesion relatively unchanged. The dispersant is a comb co-polymer, Agrilan 755 (AG755), provided by AkzoNobel, with a molecular weight of $\sim$ 15,000. The comb co-polymer consists of hydrophilic poly-(ethylene glycol) side chains grafted to a hydrophobic

---

edge; however, this is subjective and the error may be larger than represented by the red-shaded region in Fig. 7.6(b).

[6] The difference in volume fraction between the high-shear and low-shear viscosity divergences, $\Delta\phi = 0.12 \pm 0.03$, is greater than the value for spheres, $\Delta\phi \approx 0.09$ [24], but within error. Although, it should also be noted that for less polydisperse anisotropic systems a greater $\Delta\phi$ is found and that it increases with aspect ratio [169].

[7] The compaction test is carried out using a Rigden apparatus to DS/EN 1097-4:2008 "Tests for mechanical and physical properties of aggregates - Part 4: Determination of the voids of dry compacted filler".

[8] Some inconsistency compared to previously observed behaviour is seen. The onset of discontinuous shear thickening at $\phi = 0.51$, is seen just beyond ϕ_{rlp}, rather than, as predicted, below ϕ_{rlp}. The discrepancy may arise from an error in fitting, it could also be that flow at $\phi > \phi_{\mathrm{DST}} = 0.47$ is inhomogeneous and time-dependent. The observed continuous shear thickening would then only be the bulk time-averaged rheology and no longer represent the local rheology. Tests on the transient flow in this regime would be required to determine if this is the case.

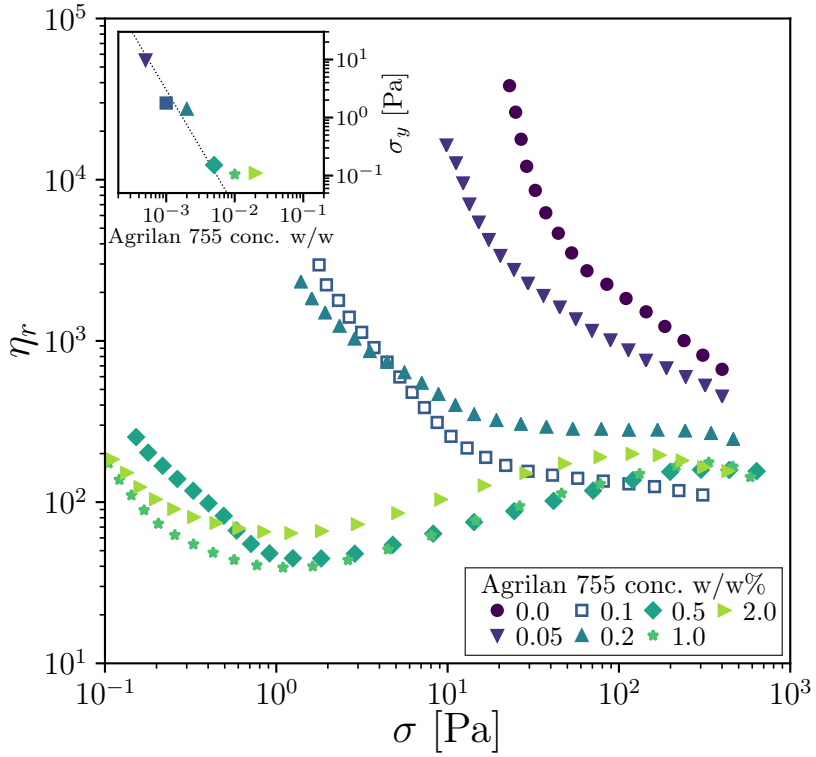

Figure 7.8 Effect of comb co-polymer dispersant (AG755) concentration on calcite suspension rheology. Main figure: flow curves, relative viscosity, η_r, as a function of stress, σ, at a fixed volume fraction, $\phi = 0.44$, in a 50 wt.% glycerol-water mixture background, at various concentrations of AG755 (symbols), see inset legend. Concentrations given as weight percentage relative to mass of calcite (w/w%). flow curves measured under imposed shear rate at 6 pts./decade from $\dot{\gamma}_{\min} = 0.1\,\mathrm{s}^{-1}$. Inset: symbols, yield stress, σ_y, defined from stress at lowest accessed shear rate, $\dot{\gamma}_{\min}$ as a function of dispersant concentration; dotted line, slope of -2 [i.e. $\sigma_y \propto (\text{conc.})^{-2}$] for comparison. Note that samples with a sharp drop in η_r at high σ have been redacted, as they correspond to sample fracture. The data for 0.1 w/w% is also shown with open symbols as an anomalous flow curve. The reduced viscosity could be due to a lower ϕ, because of, e.g., sedimentation, or sample underfilling.

methacrylic acid/methyl-methacrylate backbone. This dispersant is also used as a superplaticiser, as well as in agrochemical formulations [170]. As AG755 is supplied in liquid form a 50 wt.% active fraction is assumed based upon specification and the remainder is taken to be a liquid with the density of water. Using the protocol of §7.3.1, with increasing dispersant dosage there is again a rapid drop in the yield stress, σ_y, in Fig. 7.8 (inset). However, the residual shear thinning left after the drop in σ_y at 0.5 w/w% is not eliminated with a further increase in dispersant concentration to 2.0 w/w%, in contrast to the behaviour in Fig. 7.5.

We now look at the volume fraction dependence of a stabilised suspension, keeping the dosage of AG755 fixed at 1.0 w/w% in a 50 wt.% glycerol-water mixture background.[9] At moderate volume fractions, $\phi \leq 0.47$, flow curves, $\eta_r(\sigma)$, show shear thinning followed by thickening, Fig. 7.9(a) (symbols). These flow curves are reasonably well captured by the second class of flow curves from Ch. 5, in which there is both a finite σ_a and σ^*, with $\sigma_a < \sigma^*$. In this case adhesive bonds are first broken at low stress (ϕ_J increases and flow curves shear thin), before frictional contacts are formed at high stress (ϕ_J decreases and flow curves shear thicken). Parameters extracted from previous tests are used with $\sigma^* = 3\,\mathrm{Pa}$ and $\sigma_a = 0.3\,\mathrm{Pa}$ varied to match the data, see Fig. 7.9 caption for details. At higher volume fractions, $\phi > 0.47$, the residual shear thinning is seen to have a dramatic effect on the rheology. Although the low-stress shear thinning is still captured by the model, the 'fit' breaks down at high stress. Instead of the predicted DST (indicated by the dotted line in Fig. 7.9), a slow increase in η_r with stress is observed. Imaging the marked surface of the sample in this regime reveals significant slip, Fig. 7.9(c). Despite the crude fitting and the inhomogeneous flow at higher volume fractions, we can still conclude there is a σ^* comparable to that for PAA-stabilised suspensions and an adhesion strength similar to, but lower than, the bare suspension.

7.4 Discussing the role of dispersants

Having presented the effect of dispersants on a model calcite suspension, we will now briefly summarise the results, Table 7.1, before showing how they can be used to deduce the microscopic role of a dispersant. Bare ground calcite particles

[9] Usage of a higher glycerol proportion caused the dispersant to precipitate out of solution.

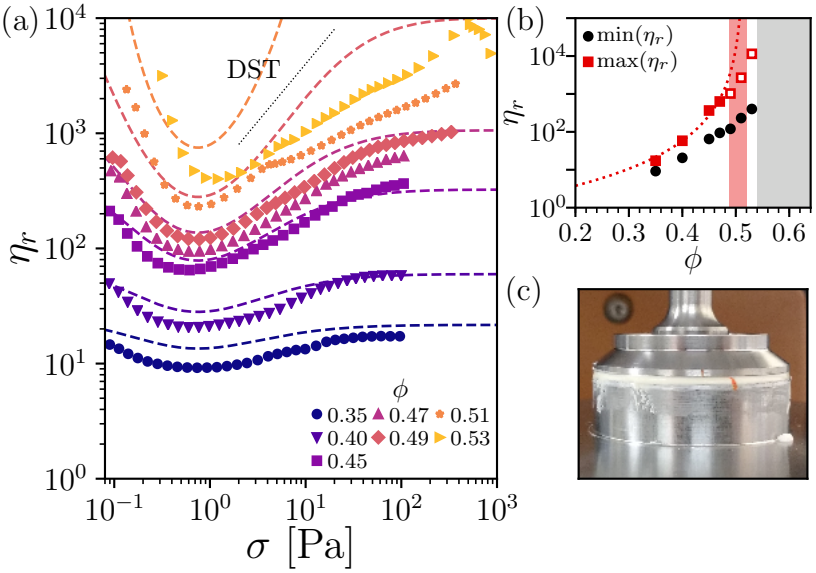

Figure 7.9 Time-averaged rheology of a calcite suspension dispersed using a comb co-polymer. Suspension is ground calcite in a 50 wt.% glycerol-water mixture background with a fixed 1.0 w/w% Agrilan 755 dispersant, relative to calcite mass. (a) Flow curves, relative viscosity, η_r, as a function of stress, σ. Symbols, flow curves at a given volume fraction, ϕ, see inset legend. Dashed lines, a representative fit of the constraint model, for ϕ see colour of symbol in legend. Fit achieved by varying $\sigma^* = 3\,\text{Pa}$ and $\sigma_a = 0.3\,\text{Pa}$ by eye, otherwise using parameters taken from previous fits ($\phi_{\text{rlp}} = 0.50$, $\phi_p = 0.20$, $\phi_{\text{rcp}} = 0.62$, $\kappa = 0.6$, $\beta = 0.7$ and assuming the jamming volume fraction of the adhesive frictionless state, or "adhesive close packing" $\phi_{\text{acp}} = \phi_{\text{rlp}}$ [124]). A power of $l = 2.7$ is used in the Krieger-Dougherty viscosity form, $\eta_r = [1 - \phi/\phi_J]^{-2.7}$, from fitting the high-shear viscosity, see (b). Dotted line, slope of 1, criteria for DST. (b) Plateau viscosity variation with volume fraction. Red squares: high-shear plateau viscosity, $\max(\eta_r)$; black circles, low-shear viscosity, $\min(\eta_r)$. Dotted red line, fit of Krieger-Dougherty form, $\eta_r = (1 - \phi/\phi_J)^{-l}$ finding the critical jamming point $\phi_{\text{rlp}} = 0.51 \pm 0.02$ (red shaded region) and $l = 2.7 \pm 0.1$, open symbols are excluded from the fit due to lack of a clear plateau region. Fitting a Krieger-Dougherty form to the low-shear viscosity was not possible, the range of possible ϕ_{rcp} is indicated by the grey shaded region. (c) Image of slip at high volume fraction, revealed by vertical marking of sample edge (red line) at rest before shearing under imposed stress.

	ϕ_p	ϕ_{rlp}	ϕ_{rcp}	σ_a [Pa]	σ^* [Pa]	κ	β	l
Bare	0.18	0.50(1)	-	0.6	-	0.6	-	2.6(3)
PAA	-	0.49(1)	0.62(3)	-	3.0(2)	-	1.02(03)	2.2(2)
MW425	-	0.499(3)	0.59	-	1.0(1)	-	0.67(3)	(2.2)
AG755	(0.18)	0.51(2)	(0.62)	0.3	1	(0.6)	(0.7)	2.7(1)

Table 7.1 Summary of constraint model parameters for calcite suspensions without dispersant (bare) and stabilised (with listed dispersants). Values for parameters taken from other tests are listed within brackets and estimates by eye are listed without error.

in an aqueous solvent form a yield-stress fluid; the response is consistent with a compressive frictional contact network stabilised by adhesive bonds that are broken with stress. Increasing the dispersant concentration has a highly non-linear effect on the yield stress: addition of a small quantity reduces the yield stress, before a further increase (2.5× for PAA and MW425, 10× for AG755) causes at least a hundredfold decrease in the yield stress. Adding a sufficient amount of dispersant then changes the rheological behaviour from a yield-stress fluid to a shear-thickening suspension. The volume fraction dependence of shear thickening is consistent with a stress-dependent transition from a frictionless to a frictional state. The high-stress limiting jamming volume fraction suggests that the interparticle friction coefficient, μ_p, is unchanged.[10] Finally, the onset stress for shear thickening is found to be a similar magnitude for all dispersants. We will now use the results of this chapter to argue that the dominant effect of a dispersant in eliminating the yield stress in a concentrated non-Brownian suspensions is to create a finite onset stress which prevents frictional contact when adhesion is relevant. We then suggest that the onset stress is consistent with the dispersant desorbing from the surface under shear.

7.4.1 Effect at low stress

We must now address how a dispersant decreases the yield stress and explain why the variation with dispersant concentration is so highly non-linear using the constraint-based rheology model as a framework. For this we use Fig. 7.10 as a guide. In Fig. 7.10(a), the jamming volume fraction is shown as a function of stress at a fixed adhesion strength, $\sigma_a = 0.6\,\mathrm{Pa}$, but with an increasing

[10] Alternatively it may reduce μ_p, but not sufficiently below ≈ 1 to increase ϕ_J [57].

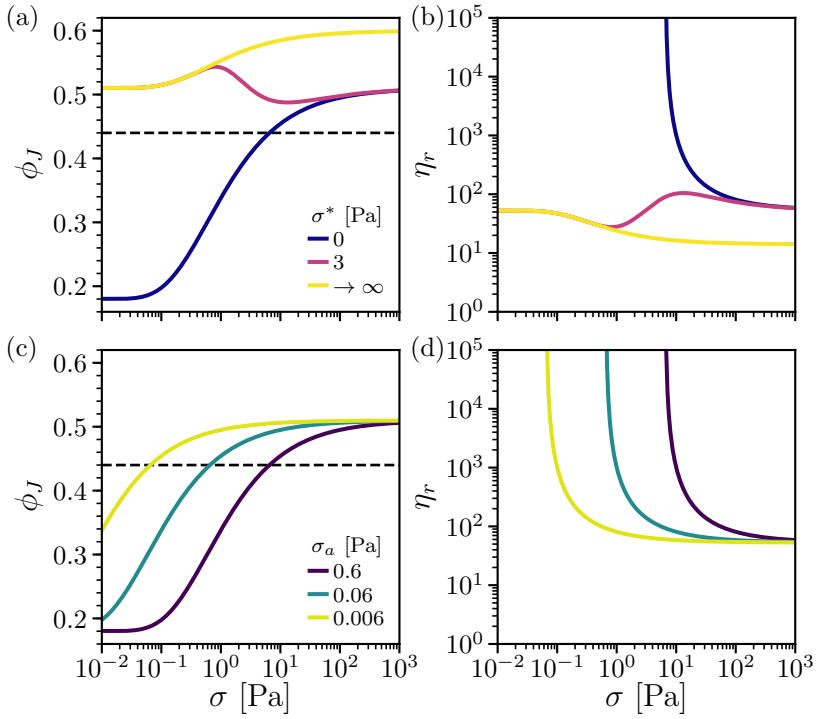

Figure 7.10 Reducing the yield stress within the constraint model: effect of a finite onset stress, σ^*, compared to reducing the adhesion strength, σ_a. (a) and (b) Increasing σ^* with a fixed adhesion strength, $\sigma_a = 0.6\,\text{Pa}$. (a) Jamming volume fraction, ϕ_J, *vs* stress, σ. Solid lines, changing onset stress for frictional contacts between particles, σ^*, see legend. Parameters for constraint model: $\phi_p = 0.18$, $\phi_{\text{acp}} = \phi_{\text{rlp}} = 0.51$, $\phi_{\text{rcp}} = 0.60$, $\beta = 1.0$ and $\kappa = 0.6$. Dashed line, $\phi = 0.44$. (b) Flow curves, relative viscosity as a function of stress, $\eta_r(\sigma)$, for $\phi = 0.44$, see legend in (a) for value of σ^*. (c) and (d) Effect of decreasing adhesion strength, σ_a, with a zero onset stress for frictional contact, $\sigma^* \to 0$. (c) Jamming volume fraction, ϕ_J, as a function of stress, σ, see legend for σ_a. Dashed line, $\phi = 0.44$. Constraint model parameters as in (a), using $\phi_p = 0.18$, $\phi_{\text{rlp}} = 0.51$ and $\kappa = 0.6$. (d) Flow curves, $\eta_r(\sigma)$, for $\phi = 0.44$, at various values of σ_a, see legend in (c).

onset stress, σ^* (purple to gold lines). The volume fraction at which dispersant concentration sweeps were conducted is shown (black dashed line) and the yield stress for this volume fraction is given when $\phi_J(\sigma)$ increases above the indicated ϕ with stress. Therefore, we can see that the yield stress is rapidly removed by increasing the frictional onset stress to the point where $\sigma^* > \sigma_a$, so that the low stress limiting jamming volume fraction goes from the percolation threshold ($\phi_p \approx 0.20$) to 'adhesive close packing' $\phi_{\text{acp}} \sim \phi_{\text{rlp}} \approx 0.50$ [124]. As ϕ_{acp} is likely above the volume fraction of interest, ϕ_J is always above ϕ and the yield stress is removed, see flow curves at $\phi = 0.44$, Fig. 7.10(b).[11] Physically, without a frictional contact network to stabilise and adhesion cannot jam the system at these low volume fractions. We now look at when σ^* remains zero, but the strength of adhesion is reduced, similar to the colloidal view of a dispersant reducing the attraction strength. A reduction in σ_a shifts the rise in ϕ_J to a lower stress, but the low-stress limiting jamming volume fraction remains at $\phi_p \approx 0.20$, Fig. 7.10(c). Thus, in the flow curves at $\phi = 0.44$, the yield stress is shifted to a lower value linearly with the reduction in σ_a, but it is not entirely removed as when σ^* is increased, Fig. 7.10(d). We therefore propose that the dominant physical mechanism for a dispersant reducing the yield stress of a suspension is preventing frictional contact between particles at stresses where adhesion is relevant (i.e. $\sigma^* \gg \sigma_a$) and that it is not just reducing the strength of adhesion.

7.4.2 Effect at high stress

This raises the obvious question as to what microphysics sets the value of σ^* that causes this dramatic reduction in yield stress and controls the shear thickening properties. There are two aspects to the shear-thickening behaviour: the viscosity the suspension thickens to (i.e. ϕ_{rlp}) and the onset stress σ^*. As the limiting jamming volume fraction at high shear is similar across dispersants and matches that for bare particles, Table 7.1, it suggests that the dispersant does not modify the interparticle friction coefficient, μ_p, when they are in contact. Secondly, similar magnitudes of σ^* are seen for all dispersants, Table 7.1. In the WC schema for shear thickening, the onset stress arises from a critical interparticle force [8]. It is therefore highly surprising that the onset stress does not depend sensitively on the type of dispersant, as it is expected that the interparticle force should be sensitive to details such as charge distribution and conformation [171].

[11] There may still be a "colloidal" yield stress (i.e. $\sim \sigma_{\text{osc}}$), but as established in Ch. 6 this is far lower than the unjamming yield stress due to constraint physics.

These details should almost certainly vary between dispersants.

Combining these two observations, we conclude that the dispersant desorbs from the surface as they enter contact, thus leaving μ_p unchanged at high stress. The onset stress would then be set by the desorption process, and hence the adsorption energy. A local critical stress-scale can be estimated from the adsorption energy per unit volume of dispersant.[12] A smaller variation could be expected in the stress-scale set by desorption than the stress-scale set by the peak force, because adsorption interactions for all dispersants are between organic molecules and the calcite substrate, while the larger adsorption energy for bigger molecules would be offset by the greater volume they occupy. One may initially think that there is an inconsistency between the hypothesis that dispersants are pushed off the surface at $\sigma > \sigma^*$ and the fact that the suspension shear thickens reversibly, i.e. that the viscosity increases and decreases the same way with rising and lowering stress. It might be expected that particles with the dispersant removed from the surface would aggregate, so that on lowering the stress instead of the viscosity returning to the low-shear frictionless plateau a large viscosity would be measured due to the presence of aggregated particles. However, as the adhesion between bare particles is weak, $\sigma_a = 0.6\,\mathrm{Pa} < \sigma^* = 3\,\mathrm{Pa}$, as the stress is decreased below the onset stress any aggregates formed would be easily broken up ($\sigma > \sigma_a$) but not reformed ($\sigma < \sigma^*$). Thus, the viscosity returns to that of a well-stabilised suspension.

This local critical stress-scale can be estimated using the binding energy for PAA[13] to give $\sigma^*_{\mathrm{local}} = 10 \times 10^5\,\mathrm{Pa}$. This stress is dramatically higher than the measured σ^*, but we must remember it represents the *local* stress. This would only represent the bulk stress for flat contacting surfaces; when rough surfaces are in contact polymer brush coatings can fail before this stress, with even surface-grafted polymers removed from the surface under shear [172]. Using this local stress-scale, the macroscopic stress (ignoring prefactors) would correspond to a contact area of linear size $\sqrt{\sigma^* d^2/\sigma^*_{\mathrm{local}}} = 20\,\mathrm{nm}$. This estimate lies between the PAA size ($\sim 3\,\mathrm{nm}$) and the particle size ($4\,\mu\mathrm{m}$), it is also similar to the surface roughness found for other non-Brownian particles, e.g. cornstarch [73]. Although these are crude estimates, they demonstrate that this proposed mechanism for

[12] In this calculation it assumes a constant force with separation over the interaction range, accounting for variation of the force with separation, e.g., a linear or quadratic variation, would only introduce a prefactor.

[13] We use the binding energy for a 50,000 MW PAA molecule of $1.4\,\mathrm{kJ\,mol^{-1}}$ [166] and assume that the binding energy is independent of molecular weight for an upper estimate of the stress-scale.

setting σ^* is not implausible.

7.5 Conclusion

In this chapter we have demonstrated the use of a model ground calcite system to study the effect of dispersants in concentrated non-Brownian suspensions. In particular, it has been demonstrated that the addition of a dispersant 'tunes' the suspension between a yield-stress fluid, with adhesive and frictional interactions between particles, similar to cornstarch in oil, to a shear-thickening suspension, similar to cornstarch in water. The constraint-based rheology framework is then used to infer the relevant effect of dispersants on the particle level for concentrated non-Brownian suspensions. Firstly, dispersants reduce adhesion between particles; this is the conventional view of a dispersant from the concept colloidal stability. However, there is a second effect, which could initially be seen as ancillary: that the repulsion removes the particles from mechanical contact. This eliminates sliding friction between particles when adhesion is relevant. The constraint-based rheology model reveals that this is in fact the dominant mechanism for the reduction of the yield stress in a concentrated non-Brownian suspension.

We have then suggested that the onset stress for shear thickening and frictional contact arises from the adsorption energy. This would suggest the focus for dispersant design should be on the strength of adsorption and preventing direct mechanical contact, rather than reducing attraction by further increasing separation. For all studied dispersants the high-shear interparticle friction coefficient is unchanged, so to reduce friction above the onset stress a different type of additive may be required: small molecular-weight surfactants. With a small size, if bound strongly they should remain in contact above the σ^* set by the polymeric dispersant. Such surfactants could then modify the high-shear friction coefficient and, indeed, this effect is observed in model chocolate suspensions [5]. Actually, within Ref. [5] the constraint-based rheology framework was successfully used to interpret the effect of a complex series of steps involving aggregate break-up and the addition of two surfactant types at multiple stages on the yield stress. Thus, it serves as an example of the utility of the framework developed within this thesis.

Part III

Generalising non-Brownian suspension rheology

Chapter 8

Constraint-based approach to non-Brownian suspension rheology

In the previous two chapters we have used the microphysically-motivated model, developed in Ch. 5 and based upon stress-dependent adhesion and friction between particles, to both illuminate the origin of the yield stress in non-Brownian suspensions and the role of dispersants. In the final part of this thesis, comprising this single chapter, we will generalise the WC model in a manner that is agnostic to microphysics, and in doing so try and develop a minimal description of non-Brownian suspension rheology as well as determine what really can be inferred from the steady-state rheology of a suspension.

As we have shown throughout this thesis the steady-state rheology of suspensions can be highly non-Newtonian, but such phenomena occur despite a naïve dimensional analysis suggesting that, with the lack of an intrinsic stress-scale, non-Brownian suspensions should be quasi-Newtonian: with a constant viscosity, η, depending only on solid volume fraction, ϕ. In the case of shear thickening, the additional stress-scale arises because surface details matter: the stabilising force between particles is overcome at a critical stress, σ^*, and the particles enter frictional contact, leading to stress-dependent non-Newtonian behaviour, $\eta(\sigma, \phi)$. However, in non-Brownian suspension rheology shear thickening is not the only behaviour seen. Three broad classes exist in practice, none of which are quasi-Newtonian: shear thinning ($\mathrm{d}\eta/\mathrm{d}\sigma < 0$), class 1; shear thickening ($\mathrm{d}\eta/\mathrm{d}\sigma > 0$), class 2; and combinations thereof (e.g. thinning then thickening), class 3. In each case, at high volume fraction, with changing stress, we can see solid-like behaviour

or unstable flow.

Many cases of non-Newtonian behaviour in non-Brownian suspensions have been explained with bespoke microphysics, specific to the individual suspension. As an illustrative example, thinning of the background fluid at the high shear rates produced between approaching particles has been invoked to explain shear-thinning in suspensions with polymeric background solvents, such as silicone oil [173]. We will address multiple other examples throughout this chapter; for now, note that non-Newtonian behaviour is ubiquitous, suggesting a more general, non-system-specific, underlying mechanism. We therefore set out to extend the conceptual framework of the WC model to describe non-Brownian suspension flow in general and hence capture the salient features of surface details and specifics using a minimal set of 'ingredients'. We show that this approach predicts all three classes of flow curve starting from a single set of assumptions, without the need to resort to bespoke physics in each individual instance.

8.1 Recasting the WC model

To do this we must first examine why the WC model, and relatively simple contact models in DEM simulations, can describe multiple, seemingly disparate, experimental shear-thickening suspensions (e.g. sterically-stabilised [24] and charge-stabilised [56]) despite the prior statement that surface details matter. In the shear-thickening transition, there is a change in contact state: from a lubricated state, which is generic for suspensions of hard-particles in a Newtonian solvent, to a "frictional-contact" state. This begs the question of what friction between particles in a suspension is. In the most simplistic sense it is a force which resists the relative sliding of particles on the timescale of shear, $1/\dot{\gamma}$.[1] The vagueness of the concept suggests why the WC model may be successful: many complex particle-particle interactions are subsumed into the concept of friction that is activated at a critical load. Thus, many interactions, including asperity interlock [78, 119], hydrogen bonding [110], polymer inter-digitation [24], as well as Coulomb friction in DEM simulations [52], can give rise to the same macroscopic shear-thickening phenomenology and so can be considered equivalent for rheological purposes.

[1] Consistent with this statement, simulations incorporating enhanced tangential hydrodynamics have also been shown to reproduce DST [174].

These interactions all constrain sliding, i.e., relative translational motion between particles perpendicular to the line of centres. Note that motion parallel to the line of centres is always considered constrained once particles are in contact, as we are still thinking of hard particles with short-range interactions. This leaves two other modes of relative motion, that are not considered in the WC model: 'rolling' (rotation about an axis perpendicular to the line of centres) and 'twisting' (rotation about the line of centres). Increasing the proportion of contacts where sliding is constrained with stress gives the WC model, but as particles are in mechanical contact with complex surface details it is plausible to consider constraints on other types of relative motion (we will discuss specific microphysics in §8.4). We therefore switch to talking about a general constraint type, $\mathcal{A}$, which is *formed* with stress (where $\mathcal{A}$ = sliding in the WC model), of which Coulomb friction is a prominent instance.

There are two possible contact states: one where $\mathcal{A}$ is unconstrained, A, and a contact state in which $\mathcal{A}$ is constrained, $\bar{A}$. Jamming points, $\phi_J = \phi_A$ and $\phi_{\bar{A}}$, are associated correspondingly with these states. As these jamming points are approached, $\phi \to \phi_J^-$, the viscosity of the suspension diverges, $\eta \to \infty$, and $\dot{\gamma} \to 0^+$; thus, e.g., a suspension with all contacts in state $\bar{A}$ jams at $\phi_{\bar{A}}$. For monodisperse spheres with $\mathcal{A}$ = sliding, these jamming volume fractions return to the previously familiar $\phi_A \equiv \phi_{\mathrm{rcp}} \approx 0.64$ and $\phi_{\bar{A}} \equiv \phi_{\mathrm{rlp}} \approx 0.55$ (ϕ_m in the high μ_p limit). As previously stated, sliding friction lowers ϕ_J ($\phi_{\mathrm{rlp}} < \phi_{\mathrm{rcp}}$) in both isotropic compression [57] and in shear [63].

Under shear, $\mathcal{A}$ is constrained in a stress-dependent manner, such that there is a changing proportion of contacts, $f_{\bar{A}}$, in the state $\bar{A}$, with $\mathcal{A}$ constrained. The proportion of constrained contacts increases with stress, $\mathrm{d}f_{\bar{A}}/\mathrm{d}\sigma > 0$. At low stress, all contacts are in state A, $f_{\bar{A}} = 0$, and the suspension jams at ϕ_A. In the high-stress limit, all contacts are in state $\bar{A}$, $f_{\bar{A}} = 1$, and the suspension jams at $\phi_{\bar{A}}$. The transition from state A to $\bar{A}$ and the *formation* of type-$\mathcal{A}$ constraints, occurs at a characteristic stress, σ_A, e.g. for $\mathcal{A}$ = sliding, $\sigma_A \Rightarrow \sigma^*$. We present predictions using a suitable form, as used in Ch. 4,

$$f_{\bar{A}}(\sigma) = \exp\left[-(\sigma_A/\sigma)^{\alpha}\right], \tag{8.1}$$

where α controls the rapidity of type-$\mathcal{A}$ constraint formation with σ. For $0 < f_{\bar{A}} < 1$, the suspension will jam at an intermediate volume fraction, $\phi_J(f_{\bar{A}})$, between the two limiting jamming volume fractions, ϕ_A and $\phi_{\bar{A}}$. The functional form for all constraint types is not known, we therefore use the WC-form for

constrained sliding, linearly interpolating:

$$\phi_J(f_{\bar{A}}) = f_{\bar{A}}\phi_{\bar{A}} + (1 - f_{\bar{A}})\phi_{\bar{A}}. \tag{8.2}$$

In Ch. 4 we have already shown that this model, with $\mathcal{A}$ being a frictional constraint on sliding, can fit class 2 flow curves of purely shear thickening suspensions. What we have so far done is therefore simply recast the WC model in a more general language. The key step in generalising the WC model is to introduce a second constraint, $\mathcal{B} \neq \mathcal{A}$, which is *released* by stress. The two constraint types, $\mathcal{A}$ and $\mathcal{B}$, now give four possible contact states, AB, $\bar{A}B$, $A\bar{B}$ and $\bar{A}\bar{B}$, where similarly to the notation for constraint $\mathcal{A}$, B means $\mathcal{B}$ is unconstrained and $\bar{B}$ that $\mathcal{B}$ is constrained. Each contact state has an associated jamming volume fraction: ϕ_{AB}, $\phi_{\bar{A}B}$, $\phi_{A\bar{B}}$ and $\phi_{\bar{A}\bar{B}}$. When $\mathcal{B}$ is unconstrained these jamming points return to the previous case: $\phi_{\bar{A}B} \equiv \phi_{\bar{A}}$ or $\phi_{AB} \equiv \phi_A \equiv \phi_{\mathrm{rcp}}$. The random close packing limit is the same for all possible kinds of $\mathcal{A}$ and $\mathcal{B}$ as they are both unconstrained. The other jamming points will, however, depend on the nature of the constraints, $\mathcal{A}$ and $\mathcal{B}$, and in general they are unknown for suspensions under shear. In static packings of *dry* particles, it is found that combining multiple constraint types typically lowers the minimum packing fraction required for mechanical stability [124, 125, 175–177]. We make the assumption, following the WC model, that these trends also apply to the jamming point for sheared suspensions, so that $\phi_{\bar{A}\bar{B}} < \phi_{\bar{A}B},\ \phi_{A\bar{B}} < \phi_{AB}$.

Again, similarly to constraint $\mathcal{A}$, there is a stress-dependent proportion of contacts, $f_{\bar{B}}$, in state $\bar{B}$, with $\mathcal{B}$ constrained, except the proportion of constrained contacts *decreases* with stress, $\mathrm{d}f_{\bar{B}}/\mathrm{d}\sigma < 0$. The jamming point, ϕ_J, will now depend on both $f_{\bar{A}}$ and $f_{\bar{B}}$ with $\phi_J(f_{\bar{A}} = 0, f_{\bar{B}} = 0) = \phi_{AB}$; $\phi_J(f_{\bar{A}} = 1, f_{\bar{B}} = 0) = \phi_{\bar{A}B}$; $\phi_J(f_{\bar{A}} = 0, f_{\bar{B}} = 1) = \phi_{A\bar{B}}$; and, $\phi_J(f_{\bar{A}} = 1, f_{\bar{B}} = 1) = \phi_{\bar{A}\bar{B}}$. The simplest functional form consistent with these limits, extending the linear interpolation of Eq. 8.2, is

$$\begin{aligned}\phi_J(f_{\bar{A}}, f_{\bar{B}}) = (1 - f_{\bar{A}})(1 - f_{\bar{B}})\phi_{AB} + f_{\bar{A}}(1 - f_{\bar{B}})\phi_{\bar{A}B} \\ + (1 - f_{\bar{A}})f_{\bar{B}}\phi_{A\bar{B}} + f_{\bar{A}}f_{\bar{B}}\phi_{\bar{A}\bar{B}}.\end{aligned} \tag{8.3}$$

With multiple constraint types the viscosity should still increase as the jamming point is approached ($\eta \to \infty$ as $\phi \to \phi_J^-$), and η is again, as in earlier chapters,

related to the jamming point using the Maron-Pierce form (Eq. 3.2),

$$\eta_r(\phi, \phi_J) = \frac{\eta}{\eta_s} = \left[1 - \frac{\phi}{\phi_J}\right]^{-2}. \tag{8.4}$$

Finally, to complete the relationship for the stress dependence of η_r, we introduce an expression for the breakage of constraint $\mathcal{B}$ with stress. The proportion of contacts in state $\bar{B}$ (i.e. in either $A\bar{B}$ and $\bar{A}\bar{B}$), $f_{\bar{B}}(\sigma)$, decreases with stress from $f_{\bar{B}}(\sigma = 0) = 1$ to $f_{\bar{B}}(\sigma \to \infty) = 0$, with a characteristic stress, σ_B; we choose

$$f_{\bar{B}} = 1 - \exp\left[-(\sigma_B/\sigma)^{\beta}\right], \tag{8.5}$$

to reflect the form for $f_{\bar{A}}$ and constraint $\mathcal{A}$.[2] Here β controls how rapidly constraint type $\mathcal{B}$ breaks with stress.[3]

Now is an appropriate moment to emphasise the fact that this is a *phenomenological* model: it is neither empirical (we are not deducing a rule from data), nor is it a theory (making non-trivial assumptions, rather than deriving results from first principles). Instead, it is a microscopically motivated model that aims to make testable rheological predictions arising from physics on the particle level. The choice of functional forms is therefore an illustrative rather than prescriptive choice, as stated in the WC model [8], because we are interested in general behaviour and trends rather than exact numerical values. For example Eqs. 8.1 and 8.5, are chosen to have two 'tuneable' features: a critical stress and a range of stress the constraint state changes over (small exponents α and β lead to a larger stress range). While the microscopic origins of the stress-scale may be clear (e.g. a repulsive force for an increasing constraint and a bond strength for a decreasing constraint), α and β are less well understood. Their values may be affected by a distribution of critical loads on the particle level (e.g. Ref. [73])[4] or the nature of the contact-force distribution, which could vary when applying the model beyond paradigmatic monodisperse spheres, e.g., to polydisperse or non-spherical particles.

[2]For simulations of dry packings, rolling friction causes the torque distribution to have a similar exponential tail (from which the expression is derived) to the tangential force distribution for packings with sliding friction alone [122].

[3]Note that the exponent β introduced here is in fact equivalent to κ from Ch. 5 and *not* β from the WC model.

[4]$\alpha = 1$ was derived for the proportion of contact forces above a single critical force, a distribution of critical forces should broaden this transition, $\alpha < 1$.

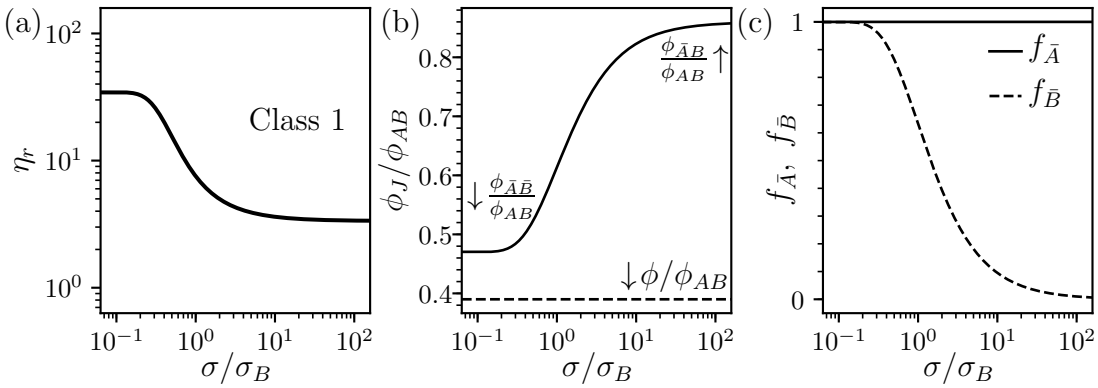

Figure 8.1 Model prediction for class 1 (shear thinning) flow curves, $\sigma_A \lll \sigma_B$. Limiting jamming volume fractions $\phi_{\bar{A}B} = 0.86\phi_{AB}$ and $\phi_{\bar{A}\bar{B}} = 0.47\phi_{AB}$; model parameters, $\sigma_A = 0$ and $\beta = 1$ ($\alpha \neq 0$). (a) Relative viscosity, η_r, as a function of dimensionless stress, σ/σ_B for $\phi/\phi_{AB} = 0.39$. (b) Corresponding relative jamming volume fraction, ϕ_J/ϕ_{AB}, also indicating the two limiting $[\phi_J(\sigma/\sigma_B \to 0) = \phi_{\bar{A}\bar{B}}$ and $\phi_J(\sigma/\sigma_B \to \infty) = \phi_{\bar{A}B}]$ values and relative volume fraction, $\phi/\phi_{AB} = 0.39$, for $\eta_r(\sigma)$ in (a). (c) Underlying constraint fraction. Proportion of contacts with $\mathcal{A}$ constrained, $f_{\bar{A}} = 1$ (solid line), and proportion with $\mathcal{B}$ constrained, $f_{\bar{B}}(\sigma)$ from Eq. 8.5 (dashed line).

8.2 Predicted flow curves

We now explore variation of the multiple parameters in the model and the rich variety of predicted flow curves, which are sensitive to the interplay between the two types of constraint. This interplay is broadly controlled by two ratios: σ_A/σ_B and α/β. These two ratios control the broad class of flow curves modelled. The exact rheology depends on the values of the jamming points; however, here we present qualitative phenomenology, which simply depends on the reasonable assumption that $\phi_{\bar{A}\bar{B}} < \phi_{\bar{A}B},\ \phi_{A\bar{B}} < \phi_{AB}$. To understand the representative classes of flow curves and make substantive predictions we use $\phi_{\bar{A}B} = \phi_{A\bar{B}} = 0.86\phi_{AB}$ and $\phi_{\bar{A}\bar{B}} = 0.47\phi_{AB}$ (so that if $\phi_{AB} \equiv \phi_{\mathrm{rcp}} = 0.64$, $\phi_{\bar{A}B} = \phi_{A\bar{B}} = 0.55$ and $\phi_{\bar{A}\bar{B}} = 0.30$), presenting all plots in terms of a dimensionless stress, σ/σ_B.

8.2.1 Shear-thinning flow curves: Class 1

Class 1 behaviour (shear thinning) is obtained when $\sigma_A/\sigma_B \lll 1$, independent of the value of α/β, Figs. 8.1.[5] For stresses $\mathcal{O}(\sigma_B)$, σ_A is far exceeded and so $\mathcal{A}$ is always constrained, $f_{\bar{A}} = 1$, Fig. 8.1(c). The shape of ϕ_J, Fig. 8.1(b), and hence the flow curve $\eta_r(\sigma)$, Fig. 8.1(a), is set by $f_{\bar{B}}(\sigma)$ alone. Far below σ_B, all contacts remain in state $\bar{A}\bar{B}$, and there is a viscosity plateau, set by $\phi_J = \phi_{\bar{A}\bar{B}}$. Approaching σ_B, type-$\mathcal{B}$ constraints begin to break, $f_{\bar{B}}$ decreases [Fig. 8.1(c)], and ϕ_J increases [Fig. 8.1(b)]. The distance to the jamming point, $|\phi_J - \phi|$, is increased and the viscosity is lowered: the suspension shear thins. For $\sigma \gg \sigma_B$, $f_{\bar{B}} = 0$, all type-$\mathcal{B}$ constraints have been released and an upper viscosity plateau is reached, set by $\phi_{\bar{A}B}$.

8.2.2 Shear-thickening flow curves: Class 2

To reproduce shear thickening (class 2) requires $\sigma_A/\sigma_B \ggg 1$. In the limit of $\sigma_B \to 0$, the model mathematically reduces to the WC model, as $f_{\bar{B}} = 0$. When considering $\mathcal{A}$ = sliding, it is then equivalent ($\sigma_A \Rightarrow \sigma^*$, *etc.*), see Ch. 3.

8.2.3 Non-monotonic flow curves: Class 3

Much more interesting behaviour results when the two stress-scales are comparable, importantly reproducing non-monotonic flow curves (class 3). We will discuss how multiple classes arise from the model when varying the ratios σ_A/σ_B and α/β.

Thinning then thickening: Class 3a

Class 3a (thinning then thickening) is captured by the model when $\sigma_A/\sigma_B \gg 1$ and $\alpha/\beta \lesssim 1$, Fig. 8.2. The two stress-scales are well separated, so type-$\mathcal{B}$ constraints are almost entirely released before the formation of type-$\mathcal{A}$ constraints, Fig. 8.2(c). The jamming volume fraction therefore first increases from $\phi_{A\bar{B}}$, peaking as almost all contacts are unconstrained (in state AB), before

[5] When precisely σ_A/σ_B can be considered small will depend on α/β, a smaller ratio of exponents requires greater separation between σ_A and σ_B, with $\sigma_A/\sigma_B \ll 1$ required when $\alpha/\beta \approx 1$.

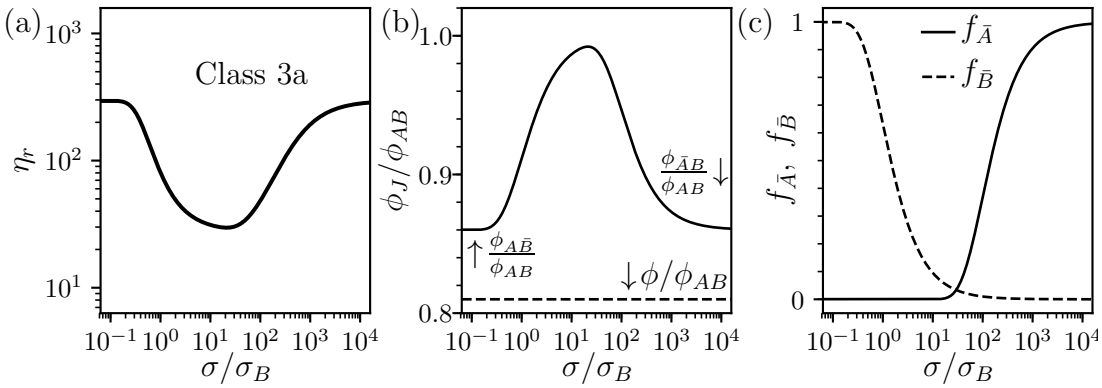

Figure 8.2 Model prediction for class 3a flow curves (thinning then thickening), $\sigma_A/\sigma_B \gg 1$ and $\alpha/\beta \lesssim 1$. Limiting jamming volume fractions $\phi_{A\bar{B}} = \phi_{\bar{A}B} = 0.86\phi_{AB}$; model parameters, $\sigma_A/\sigma_B = 10^2$ and $\alpha/\beta = 1$. (a) Relative viscosity, η_r, as a function of dimensionless stress, σ/σ_B for $\phi/\phi_{AB} = 0.81$. (b) Corresponding relative jamming volume fraction, ϕ_J/ϕ_{AB}, also indicating the two limiting values $[\phi_J(\sigma/\sigma_B \to 0) = \phi_{A\bar{B}}$ and $\phi_J(\sigma/\sigma_B \to \infty) = \phi_{\bar{A}B}]$ and the relative volume fraction, $\phi/\phi_{AB} = 0.81$, for $\eta_r(\sigma)$ in (a). (c) Underlying constraint fraction. Proportion of contacts with type-$\mathcal{A}$ constraints, $f_{\bar{A}}$ (solid line) from Eq. 8.1, and proportion with type-$\mathcal{B}$ constraints, $f_{\bar{B}}(\sigma)$ from Eq. 8.5 (dashed line).

decreasing to $\phi_{\bar{A}B}$, Fig. 8.2(b). The relative viscosity reflects this, first thinning to a viscosity minimum before shear thickening, Fig. 8.2(a). From the flow curve shown, if σ_A is reduced further, thinning and thickening become more clearly separated by a viscosity plateau. Eventually the thinning is on a far lower stress-scale to thickening, and class 2 thickening behaviour could be considered in isolation.

Thickening then thinning: Class 3b

Class 3b (thickening then thinning) behaviour requires much more specific parameter ratios than the cases so far outlined, only occurring when $\sigma_A/\sigma_B \sim 1$. The two constraint fractions change over the same stress range and the behaviour is not immediately apparent from the trends in the two constraint fractions, $f_{\bar{A}}$ and $f_{\bar{B}}$. This fine balance between the two types of constraint results in sensitivity to the precise parameters. We explore the effect on the height of the viscosity peak on both the ratio of the stress-scales (σ_A/σ_B, Fig. 8.3) and the ratio of the stretch exponents (α/β, Fig. 8.4). With α/β fixed, reducing the onset stress for the formation of type-$\mathcal{A}$ constraints, relative to the strength of type-$\mathcal{B}$ constraints, from $\sigma_A/\sigma_B = 1.0$ (yellow Fig. 8.3) to $\sigma_A/\sigma_B = 0.4$ (purple) causes over a 10-fold

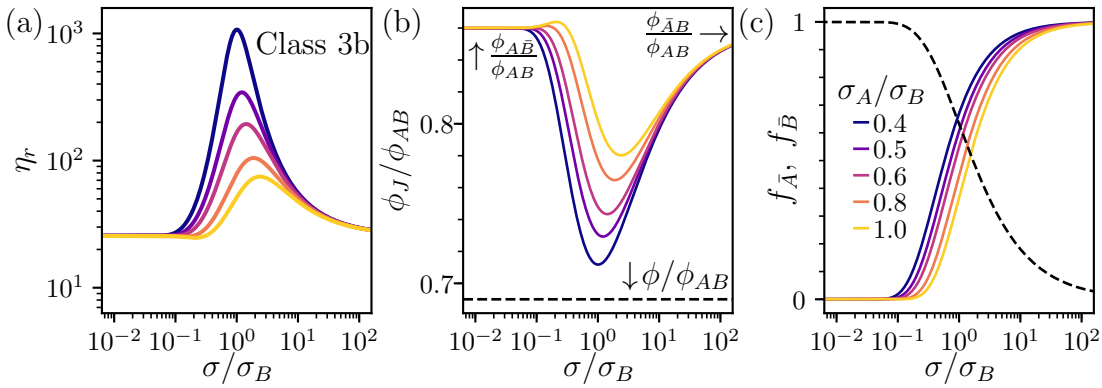

Figure 8.3 Model prediction for class 3b flow curves (thickening then thinning) varying $\sigma_A/\sigma_B \sim 1$. Limiting jamming volume fractions $\phi_{A\bar{B}} = \phi_{\bar{A}B} = 0.86\phi_{AB}$ and $\phi_{\bar{A}\bar{B}} = 0.47\phi_{AB}$; model parameters, $\alpha = 1$ and $\beta = 0.7$ with $\phi/\phi_{AB} = 0.69$ at different σ_A/σ_B [see legend in (c)]. (a) Relative viscosity, η_r, as a function of dimensionless stress, σ/σ_B. (b) Corresponding relative jamming volume fraction, ϕ_J/ϕ_{AB}, also indicating the same two limiting values as from Fig. 8.2(b) and the relative volume fraction, $\phi/\phi_{AB} = 0.69$, for $\eta_r(\sigma)$ in (a). (c) Underlying constraint fraction. Proportion of contacts with type-$\mathcal{A}$ constraints, $f_{\bar{A}}$ (coloured solid lines, see legend for σ_A/σ_B value) from Eq. 8.1, and proportion with type-$\mathcal{B}$ constraints, $f_{\bar{B}}(\sigma)$ from Eq. 8.5 (dashed line).

increase in the peak value of η_r, Fig. 8.3(a). At $\sigma_A/\sigma_B = 0.4$ type-$\mathcal{A}$ constraints can form before type-$\mathcal{B}$ constraints are released, lowering the jamming point and raising the viscosity.

There is similar sensitivity to changes in the ratio of stretch exponents when keeping the stress ratio fixed. With $\sigma_A/\sigma_B = 0.45$, increasing α/β from 0.6 to 1.8 gives rise to again a ∼10-fold increase in the height of the viscosity peak, Fig. 8.4(a). With type-$\mathcal{A}$ constraints more rapidly formed, Fig. 8.4(c), the system approaches state $\bar{A}\bar{B}$, with a significant proportion of the most constrained type of contact ($\mathcal{A}$ and $\mathcal{B}$) and the lowest jamming point, Fig. 8.4(b). In all cases explored there is an extended high-stress region of shear thinning controlled by progressive release of constraints on $\mathcal{B}$, $f_{\bar{B}} \to 0$, with constraints on $\mathcal{A}$ saturated, $f_{\bar{A}} \approx 1$.

The sensitivity of flow curve behaviour to model parameters is consistent with experiments where, such peaked flow curves are dependent on seemingly inconsequential details, e.g. particle size [178] or background solvent [179]. In changing such details, alterations to the particle surface presumably perturb the stress-dependent microphysics, and the resulting macroscopic parameters of the

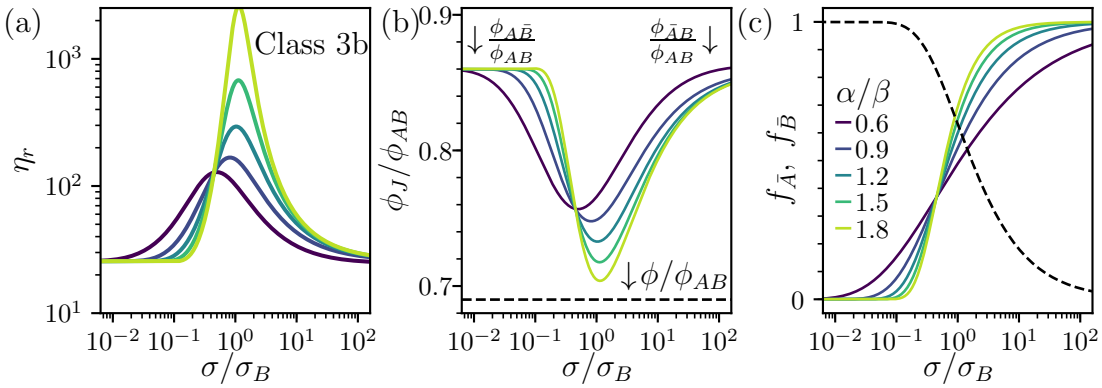

Figure 8.4 Model prediction for class 3b flow curves (thickening then thinning) varying $\alpha/\beta \sim 1$. Limiting ϕ_J and relative volume fraction, $\phi/\phi_{AB} = 0.69$, as in Fig. 8.3. Other model parameters: $\sigma_A/\sigma_B = 0.45$ and with $\beta = 0.7$ at different α corresponding to an increasing ratio (purple to chartreuse) [see legend in (c)]. (a) Relative viscosity, η_r, as a function of dimensionless stress, σ/σ_B. (b) Corresponding relative jamming volume fraction, ϕ_J/ϕ_{AB}, indicating limiting values and relative volume fraction, ϕ/ϕ_{AB}, for (a). (c) Underlying constraint fractions. Proportion of contacts with type-$\mathcal{A}$ constraints, $f_{\bar{A}}$ (coloured solid lines) from Eq. 8.1, and proportion with type-$\mathcal{B}$ constraints, $f_{\bar{B}}(\sigma)$ from Eq. 8.5 (dashed line).

model, leading to large variations in $\eta_r(\sigma)$.

More complex combinations: Class 3c

Using our chosen functional forms for $f_{\bar{A}}$, Eq. 8.1, and $f_{\bar{B}}$, Eq. 8.5, the model also predicts more varied combinations of thickening and thinning (class 3c). Class 3c(i), "thins, thickens and thins," arises when $\sigma_A/\sigma_B \gg 1$ and $\alpha/\beta \gtrsim 1$ (remember class 3a is reproduced when $\alpha/\beta \lesssim 1$). Now type-$\mathcal{B}$ constraints are released much more slowly than type-$\mathcal{A}$ constraints are formed: $f_{\bar{A}}$ goes from ≈ 0 to ≈ 1 while $f_{\bar{B}}$ is still decreasing. Fig. 8.5(a) shows a series of representative flow curves for different α/β (see caption for parameters). Finally, class 3c(ii), "thickens, thins and thickens," is reproduced whenever $\sigma_A/\sigma_B \sim 1$ and α/β is small, for the chosen parameters $\lesssim 0.5$. For larger values of α/β class 3b behaviour is recovered (a viscosity peak, with no subsequent trough). Again, a set of representative flow curves for a series of α/β values is shown in Fig. 8.5(b). Flow curves of class 3c(i) have been widely reported in the literature, e.g. Refs. [44, 180, 181], although this is not the case for type 3c(ii).

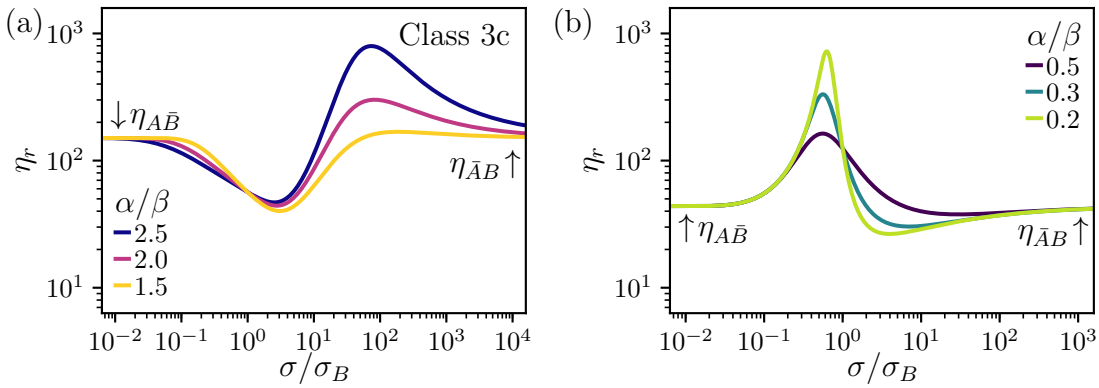

Figure 8.5 Class 3c flow curves, varied combinations of thickening and thinning. Jamming points as Fig. 8.3. (a) "Thins, thickens and thins." Model parameters $\phi/\phi_{AB} = 0.79$, $\sigma_A/\sigma_B = 10$ and $\alpha = 1$ with β corresponding to given ratios from $\alpha/\beta = 2.5$ (indigo) to 1.5 (golden yellow) (see legend). Limiting plateau viscosities: $\sigma/\sigma_B \to 0$, $\eta_r \to \eta_{A\bar{B}} \equiv \eta_r(\phi, \phi_J = \phi_{A\bar{B}})$; and, $\sigma/\sigma_B \to \infty$, $\eta_r \to \eta_{\bar{A}B} \equiv \eta_r(\phi, \phi_J = \phi_{\bar{A}B})$. (b) "Thickens, thins and thickens." Model parameters $\phi/\phi_{AB} = 0.73$, $\sigma_A/\sigma_B = 1$ and $\alpha = 0.5$ with β corresponding to given ratios from $\alpha/\beta = 0.5$ (purple) to 0.2 (chartreuse) (see legend). Limiting plateau viscosities as in (a).

8.2.4 Determining constraint physics

Exploring variation in the model parameters by tuning the ratios of the characteristic stresses (σ_A/σ_B) and the stretch exponents (α/β), we have shown how the interplay of two constraint types can reproduce all experimentally observed classes of flow curve, summarised in Fig. 8.6(a) with increasing σ_A/σ_B (indigo to golden-yellow). In this schema system-specific inter-particle interactions are expressed in terms of constraints on relative sliding, rolling or twisting which are then either formed (type-$\mathcal{A}$) or broken (type-$\mathcal{B}$) with stress. Such constraints control the jamming point, $\phi_J(\sigma)$, with stress and hence, at fixed ϕ, the distance to jamming, which controls the viscosity, $\eta_r(\sigma)$. We should stress that many interactions do not necessarily constrain relative motion; for example, with hard spheres, conservative (or equivalently potential) interactions, such as electro-static or depletion forces. Such interactions are well known to still give rate or stress-dependent rheology [37, 130]: so, how do we then determine whether the rheology is constraint driven?

Key to answering this question is the jamming phase diagram. At fixed-ϕ the system can be in one of two states, flowing [$\phi < \phi_J(\sigma)$] or, if $\phi > \phi_J(\sigma)$, jammed, with $\eta_r \to \infty$. Although non-constraint physics can also arrest flow, the

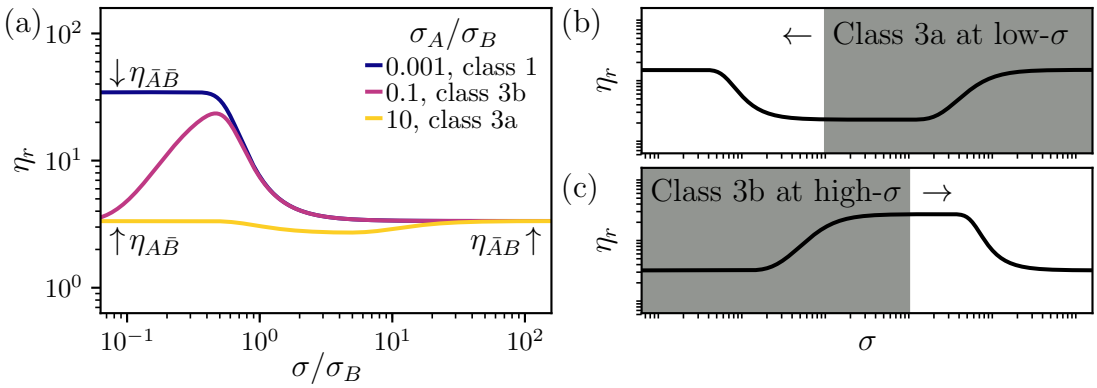

Figure 8.6 Determining constraint physics. (a) Transition with increasing σ_A/σ_B from class 1 (indigo, $\sigma_A/\sigma_B = 0.001$), via class 3b (magenta, $\sigma_A/\sigma_B = 0.1$), to class 3a (golden-yellow, $\sigma_A/\sigma_B = 10$). Limiting jamming points as in Fig. 8.2 with $\phi/\phi_{AB} = 0.39$ and $\alpha = \beta = 2$. Labelled limiting viscosities in plotted range of σ/σ_B: $\eta_{\bar{A}\bar{B}} \equiv \eta_r(\phi, \phi_J = \phi_{\bar{A}\bar{B}})$, $\eta_{A\bar{B}} \equiv \eta_r(\phi, \phi_J = \phi_{A\bar{B}})$ and $\eta_{\bar{A}B} \equiv \eta_r(\phi, \phi_J = \phi_{\bar{A}B})$. (b) and (c) Schematic effect of a limited range of experimentally-accessible stress, grey shaded region inaccessible. (b) Shear-thinning from the low-stress regime of class 3a behaviour, higher stress unobservable due to, e.g. sample fracture. (c) Shear thinning as the high-stress behaviour of class 3b flow curves, lower stress unobservable due to, e.g. instrument resolution.

model makes specific predictions for viscosity divergences, which are not otherwise expected to arise generically. Plotting the jamming point relative to random close packing as a function of stress can be used to reveal this behaviour.

A prerequisite to this is measurement of random close packing, or ϕ_{AB}, which must be done through means other than steady-state rheology, i.e. dry compressed packing density or the 'glossy' suspension to 'matt' granule transition (at this point there is not enough liquid to immerse the particles and particles protrude through the interface) [182]. Reference relative to this volume fraction is needed due to the limited experimental "window," the observable range of stresses and shear rates set by: $\sigma_{\min}$, rheometer resolution; $\sigma_{\max}$, sample fracture; $\dot{\gamma}_{\min}$, experiment time; and, $\dot{\gamma}_{\max}$, inertial sample ejection [24]. Such a limited "window" on the complete flow curve raises an issue; for example, one could be observing thinning before type-$\mathcal{A}$ constraints have formed [white region of Fig. 8.6(b), low-stress range of class 3a] or before [Fig. 8.6(c) white region, high-stress range of class 3b]. Similar considerations exist for thickening: class 2 or the low-stress range of class 3b, Fig. 8.6(c) grey region.[6] Despite the seeming

[6]This latter example has not been reported experimentally, corresponding to strong thickening in (comparatively) low-volume-fraction suspensions of spherical particles. Such low-

similarity within the "window", the constraint physics is very different (state A *vs* $\bar{A}$). Plotting a jamming phase diagram, relative to random close packing, resolves this ambiguity and allows the constraint physics to be determined, testing the model.

8.3 Jamming phase diagrams

We now explore the predicted jamming phase diagram in σ-ϕ space for two examples, class 1 and class 3a, comparing to literature and experimental data.

8.3.1 Class 1

The jamming phase diagram in σ-ϕ space for a class 1 system is shown in Fig. 8.7(a). Two "phases" or states exist; the red region denotes jammed states, $\phi > \phi_J(\sigma)$, and the white region flowing states, $\phi < \phi_J(\sigma)$. The boundary, $\sigma_J(\phi)$ (black solid line), is defined by $\phi_J(\sigma_J) = \phi$, calculating numerically from Eqs. 8.1, 8.3 and 8.5. Above ϕ_{AB} is coloured maroon, where dispersion is predicted to be not possible, i.e., air must be incorporated [182].

Flow curves are then generated from this jamming phase diagram, shown at various volume fractions in Fig. 8.7(b) (solid lines, legend for ϕ). The form of $\eta_r(\sigma)$ with respect to singularities can be deduced from tracing a vertical line in Fig. 8.7(a). For $\phi > \phi_{\bar{A}\bar{B}}$, with increasing σ a critical stress must be reached, $\sigma_J(\phi)$, for the system to flow, the suspension has a yield stress, $\sigma_y = \sigma_J$. The yield stress increases with ϕ, diverging at $\phi_{\bar{A}B}$. Above σ_J, the distance to jamming increases and so the viscosity drops, suspensions shear thin.

Such behaviour, as we have earlier addressed, is ubiquitous in industrial suspensions, including molten chocolate [5] and mineral slurries [135], but here we turn to a literature data for a model suspension of quasi-monodisperse hard-spheres of (unstabilised) PMMA (diameter, $d = 5\,\mu\text{m}$) in silicone oil ($\eta_s = 225\,\text{mPa s}$) [184]. For near monodisperse spheres random close packing (and random loose packing) are known from separate measurements (e.g. packing simulations [57]). A yield stress emerges at $\phi \approx 0.20$, which we take to be $\phi_{\bar{A}\bar{B}}$,

volume-fraction strong thickening has only been reported for fractal aggregates [183] or highly anisotropic particles [44].

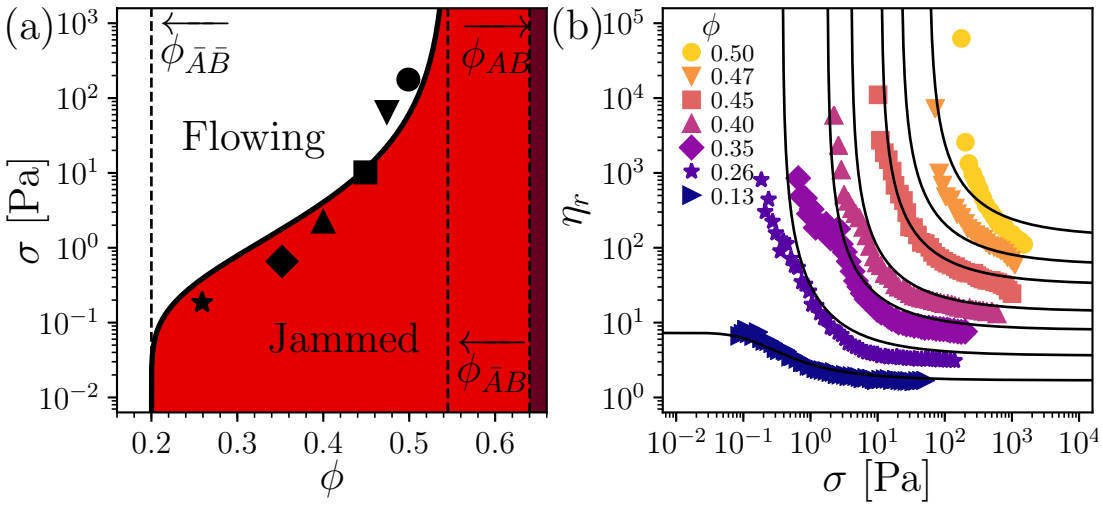

Figure 8.7 Singular behaviour of class 1 flow curves. (a) σ-ϕ jamming phase diagram, showing jammed states [red, $\phi > \phi_J(\sigma)$] and flowing states [white, $\phi < \phi_J(\sigma)$]. Maroon region, $\phi > \phi_{AB} = 0.64$, denotes region where dispersal is not possible (based on random close packing of monodisperse spheres [57]). Dashed lines denote limiting jamming volume fractions, as labelled, with $\phi_{\bar{A}\bar{B}} = 0.20$ and $\phi_{\bar{A}B} = 0.545$. Solid black line: jamming stress, $\sigma_J(\phi)$, for $\beta = 0.5$, $\sigma_B = 1.2\,\mathrm{Pa}$ and $f_{\bar{A}} = 1$. Solid black symbols, yield stress for $d = 5\,\mu\mathrm{m}$ PMMA (unstabilised) in silicone oil suspension, data from Ref. [184] using WebPlotDigitizer for capture [185]. Yield stress estimated from lowest stress for which continuous flow was reported. (b) Flow curves for a class 1 system: relative viscosity, η_r *vs* stress, σ. Symbols, full flow curve for suspensions with yield stresses reported in (a), see legend for volume fraction, ϕ. Black lines: model predictions of η_r at corresponding ϕ with $\eta_s = 225\,\mathrm{mPa\,s}$ (from reported $\phi = 0$ data) and model parameters as in (a).

and diverges at $\phi \approx 0.55$ which we take as $\phi_{\bar{A}B}$. Appropriate values of σ_B ($= 1.2\,\mathrm{Pa}$) and β ($= 0.5$) for a representative fit are then found through manual variation.[7] With the yield stress diverging at $\phi_{\bar{A}B} = 0.545$ close to random loose packing ($\phi_{\mathrm{rlp}} \approx 0.55$) this suggests that $\mathcal{A}$ = sliding.

Suspensions of glass or polymer spheres in silicone oil (at $\phi \lesssim 0.40$) are commonly used in the study of non-Brownian suspensions (e.g. Refs. [186–188]). Shear thinning has been universally noted and has recently been attributed to shear thinning of the background silicone oil in the narrow particle gaps due to the enhanced shear rates [173]. In the experimental data shown in Fig. 8.7, shear thinning follows un-jamming, the suspensions have a yield stress and $\dot{\gamma} \to 0$ at stress below this. This rules out non-Newtonian behaviour of the suspension being driven by the high shear rate behaviour of the background fluid. The weak shear thinning seen in many experiments would then constitute a weaker example (effectively the high-stress residual shear thinning) of the non-Newtonian behaviour shown in Ref. [184].

8.3.2 Class 3a

For this class (thinning then thickening), the phase diagram is more complex, as one would expect from the non-monotonic flow curves; we plot an example for $\phi_{A\bar{B}} < \phi_{\bar{A}B}$, Fig. 8.8(a). As before, there are still jammed (red) and flowing (white) regions, but there are now *multiple* features which produce distinctive viscosity signatures.

With increasing ϕ, $\sigma_J(\phi)$ is first single valued, with an unjamming event above $\phi_{A\bar{B}}$, a yield stress σ_y [Fig. 8.8(a), solid line]. Above $\phi_{\bar{A}B}$, $\sigma_J(\phi)$ is now double valued: with increasing σ there is first yielding, before re-jamming (dotted line) occurs at higher σ.[8] With further increasing ϕ, the range of flowing stresses between the yield stress and the re-jamming stress shrinks, with the two meeting at ϕ_{max}. Above ϕ_{max}, and up to ϕ_{AB}, there is then a range of volume fractions in which no (steady homogeneous) flow is possible at any stress. ϕ_{max} is not directly associated with a limiting jamming volume fraction, occurring when type-$\mathcal{A}$ constraints have already been formed before enough type-$\mathcal{B}$ constraints can be

[7] We are interested in showing that the model can capture the experimental behaviour, rather than finding precise well-determined fits.

[8] For $\phi_{\bar{A}B} = \phi_{A\bar{B}}$, $\sigma_J(\phi)$ is immediately double valued; whereas, for $\phi_{\bar{A}B} < \phi_{A\bar{B}}$ shear jamming appears before the emergence of a yield stress with increasing ϕ.

broken.

In the grey region in Fig. 8.8(a), $\phi < \phi_J(\sigma)$, but also $\mathrm{d}\dot{\gamma}/\mathrm{d}\sigma < 0$ [or when plotting η_r *vs* σ on logarithmic axes: $\mathrm{d}\ln\eta_r/\mathrm{d}\ln\sigma > 1$], so that this the region of discontinuous shear thickening (DST). In this region, steady shear flow is expected to be unstable [189], see Ch. 4. The boundary of this region, $\sigma_{\mathrm{DST}}(\phi)$ (dash-dotted line), meets $\sigma_J(\phi)$ at ϕ_{max} and $\phi_{\bar{A}B}$ as $\sigma \to \infty$.[9] Under imposed $\dot{\gamma}$, σ_{DST} should also represent the maximum stress for stable, steady flow.

The most systematic work on non-Brownian suspensions showing class 3a behaviour (thinning then thickening) has been performed using aqueous cornstarch suspensions ($d \approx 14\,\mu\mathrm{m}$) [15, 82, 95]. Under imposed-σ, in a wide-gap Couette, the only comprehensive study [95] found strong shear thinning, followed by discontinuous shear thickening ($\mathrm{d}\dot{\gamma}/\mathrm{d}\sigma < 0$) and further followed by a shear jammed state. The jammed state was identified by a novel method, probing the solidity of the suspension by dropping a ball bearing onto the surface and simply observing whether it bounces ($\Rightarrow$ shear jammed) or sinks (DST). Such "phase" behaviour is consistent with the predictions of the model [cf. Ref. [95] and Fig. 8.9(a)].

Typical flow-curves under imposed shear rate are shown in Fig. 8.8(b) (symbols), from Ref. [15]. Overlaid is shown a representative fit of the model for the measured ϕ (black lines, parameters given in caption). At all available ϕ, with increasing $\dot{\gamma}$, strong shear thinning is observed, indicative of a yield stress, σ_y. We take the stress at the lowest accessed shear rate to be the yield stress [solid symbols, Fig. 8.8(a)], which increases strongly with ϕ. Beyond this the suspension begins to weakly shear thicken, before rapidly thickening, with the flow becoming unstable and separating into bands (density variations observed through magnetic resonance imaging), the maximum steady stress being shown in Fig. 8.8(a) (open symbols). For the model, above σ_{DST} the 'jump' in σ and η_r, predicted under imposed-$\dot{\gamma}$, is plotted (dotted lines). The stress at the onset of unsteady flow [open symbols, Fig. 8.8(a)] reasonably corresponds to $\sigma_{\mathrm{DST}}(\phi)$, this stress decreases sharply with ϕ. The two critical stresses (maximum and minimum σ for imposed-$\dot{\gamma}$ stable flow) then appear to converge approximately at the predicted ϕ_{max}. This volume fraction significantly below both the predicted $\phi_{AB} = 0.51$ as well as the maximum packing fraction identified from both the tapped density and the highest density reached during unstable flow experimentally. The existence of

[9] Found numerically by solving the condition $\mathrm{d}\dot{\gamma}/\mathrm{d}\sigma = 0$, with Eqs. 8.1, 8.3, 8.4 and 8.5.

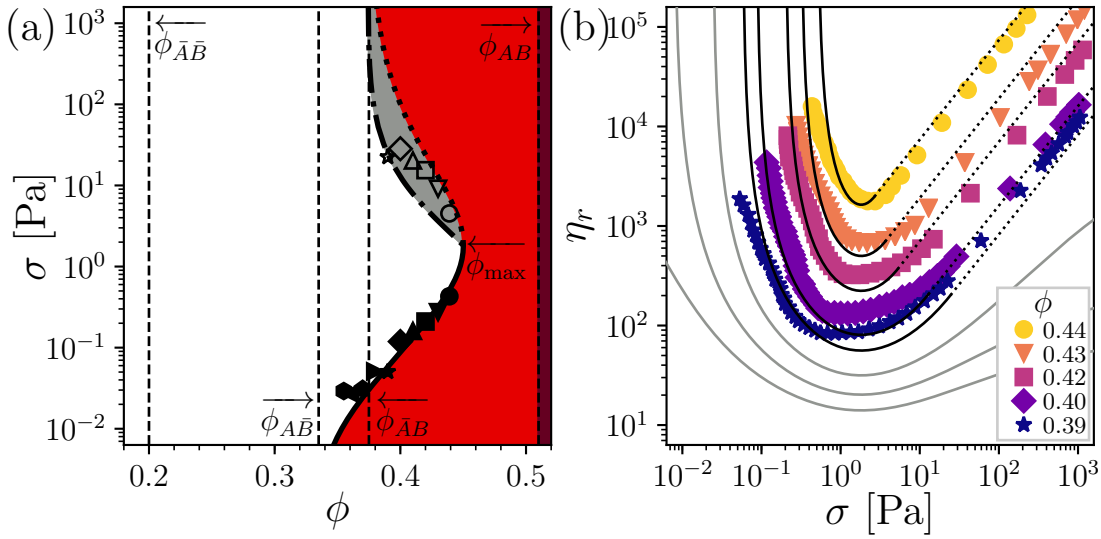

Figure 8.8 Singular behaviour of class 3a flow curves, suspensions of cornstarch in demineralised water. (a) σ-ϕ jamming phase diagram, showing jammed states (red), stable flowing states ($\mathrm{d}\dot{\gamma}/\mathrm{d}\sigma > 0$, white) and unstable flowing states ($\mathrm{d}\dot{\gamma}/\mathrm{d}\sigma < 0$, grey). Maroon region, $\phi > \phi_{AB}$, denotes region where dispersal is not possible. Solid line, unjamming or yielding ($\mathrm{d}\phi_J/\mathrm{d}\sigma > 0$, $\sigma_J(\phi) = \sigma_y$); dotted line, rejamming ($\mathrm{d}\phi_J/\mathrm{d}\sigma < 0$); dot-dashed line $\sigma_{\mathrm{DST}}(\phi)$, where $\mathrm{d}\dot{\gamma}/\mathrm{d}\sigma = 0$. Symbols, data from Ref. [15]: solid, yield stress estimated from stress at lowest accessed $\dot{\gamma}$; and, open, stress at onset of unstable (banded) flow. Model parameters: $\sigma_A = 10\,\mathrm{Pa}$, $\sigma_B = 0.085\,\mathrm{Pa}$, $\alpha = 0.5$, and $\beta = 0.38$; and limiting jamming points (dashed lines): $\phi_{AB} = 0.51$ $\phi_{\bar{A}B} = 0.375$, $\phi_{A\bar{B}} = 0.335$, and $\phi_{\bar{A}\bar{B}} = 0.20$. Maximum volume fraction with flowing state $\phi_{\max} = 0.45$. (b) Flow curves for a class 3a system: relative viscosity, η_r, *vs* stress, σ. Symbols: flow curves under imposed shear rate, reported in Ref. [15] at multiple volume fractions, ϕ, see legend. η_s (unreported) is taken to be 1 mPa s. Lines: representative model predictions for parameters of (a). Solid black, steady flow; dotted lines, predicted 'jump' in η_r and σ ($\mathrm{d}\ln\eta_r/\mathrm{d}\ln\sigma = 1$) under imposed-$\dot{\gamma}$; and, grey, predictions for lower ϕ (0.37, 0.35, 0.33 and 0.30, top to bottom).

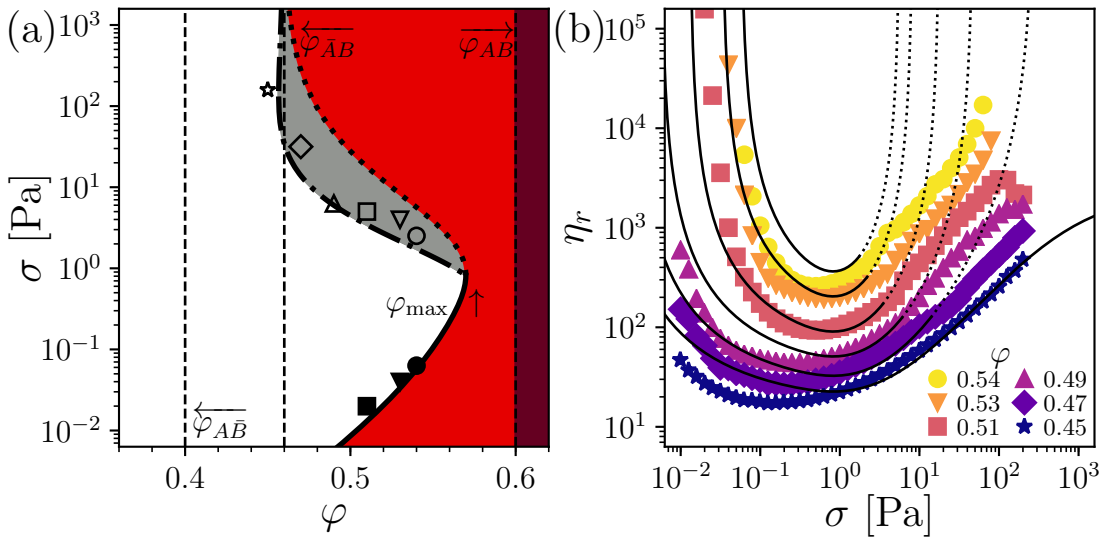

Figure 8.9 Geometry independence of Class 3a behaviour, rheology of cornstarch suspensions in 50 wt.% glycerol-water, measured under imposed stress with a parallel-plate geometry. (a) Stress-weight fraction, σ-φ, jamming phase diagram, key as in Fig. 8.8(a). Symbols: filled symbols, yield stress defined from lowest σ with measurable flow; open symbols, onset of DST, minimum stress where $\mathrm{d}\dot{\gamma}/\mathrm{d}\sigma < 0$. Model parameters: $\sigma_A = 7\,\mathrm{Pa}$, $\sigma_B = 0.003\,\mathrm{Pa}$, $\alpha = 0.6$ and $\beta = 0.35$. Limiting jamming points: $\varphi_{AB} = 0.60$, $\varphi_{\bar{A}B} = 0.46$, $\varphi_{A\bar{B}} = 0.40$, and $\varphi_{\bar{A}\bar{B}} = 0.30$. (b) Flow curves: relative viscosity, η_r, *vs* stress, σ. Points, experimental data at given weight fraction, φ (see legend). Lines, model fit at corresponding φ: solid, stable state; and, dotted, unstable region.

a range of fully jammed volume fractions below random close packing proved a puzzle for the authors of Ref. [15], yet this feature arises naturally in our model.

Before closing this section, a short caveat is in order. The data of Fig. 8.8 was taken using Couette cylinders with non-density matched particles. In such a situation, sedimentation may cause the measured rheology to differ from the local rheology. As sedimentation would increase ϕ in the lower section of the gap until the jamming point is reached, this can cause the measurement of an apparent yield stress for samples (which when well-mixed) do not possess one [13]. To show that this is not the origin of the yield stress we performed similar experiments to Ref. [15] but in a parallel plate geometry. In this set up, sedimentation would be expected to have the opposite effect, leading to shear-thickening when the viscous stress is sufficient to resuspend the particles [17].

Suspensions are prepared as in Ch. 4, and measured with roughened parallel plates (radius $R = 20\,\mathrm{mm}$ and gap height $h = 1\,\mathrm{mm}$) using a TA Instruments

DHR-2 applying a fixed torque, $\mathcal{T}$, while measuring angular velocity, Ω. From this we report apparent stress, $\sigma = 2\mathcal{T}/(\pi R^3)$, and rim shear rate, $\dot{\gamma} = \Omega R/h$. Flow curves, Fig. 8.9(b), are taken with decreasing σ, from just below fracture to 0.01 Pa at 10 pts./decade, holding for 30 s/pt . and averaging the final 10 s. With repeated increasing and decreasing σ, qualitatively similar phenomenology is found. Due to the swelling of cornstarch particles in glycerol-water [96], we report weight fractions, φ.

Crucially the two sets of experiments, in different geometries, show the same qualitative behaviour, i.e. compare Figs. 8.8(b) and 8.9(b), with yielding to discontinuous shear thickening. This suggests that such flow curves are intrinsic to aqueous cornstarch suspensions. Below the onset of unsteady flow, $\eta_r(\sigma)$ can again be captured by the model, Fig. 8.9(b) (see caption for parameters). In the phase diagram, Fig. 8.9(a), we take σ_y (filled symbols) to be the lowest stress with measurable flow[10] and also report the minimum σ at which $\mathrm{d}\ln\eta_r/\mathrm{d}\ln\sigma > 1$ (open symbols). This phase diagram is again comparable to the one obtained in a Couette geometry, Fig. 8.8(a).

8.3.3 Class 3b

As a final example we present the jamming phase diagram for class 3b (thickening then thinning), Fig. 8.10(a), the most distinctive feature of which is a 'nose'. The minimum in $\phi_J(\sigma) = \phi_{\mathrm{nose}}$, occurs as type-$\mathcal{A}$ constraints have formed before type-$\mathcal{B}$ constraints break. The unsteady region [grey, Fig. 8.10(a)] meets $\sigma_J(\phi)$ at ϕ_{nose}.[11] In the flow curves, below ϕ_{nose}, $\eta_r(\sigma)$ is peaked. Above ϕ_{nose}, jamming followed by unjamming or yielding is predicted. While peaked flow curves at moderate ϕ (~ 0.40) have been measured, see §8.2.3, the behaviour at higher volume fractions has not been reported. Experimental validation of this distinctive jamming-unjamming process with stress would strongly support the model.

[10] 'Measurable' flow is defined as $\dot{\gamma}$ greater than the standard deviation in $\dot{\gamma}(t)$, $\sim 10^{-4}$

[11] For class 3c(i) systems the unsteady region goes between the minima and maxima of $\phi_J(\sigma)$, i.e. ϕ_{max} and ϕ_{nose}.

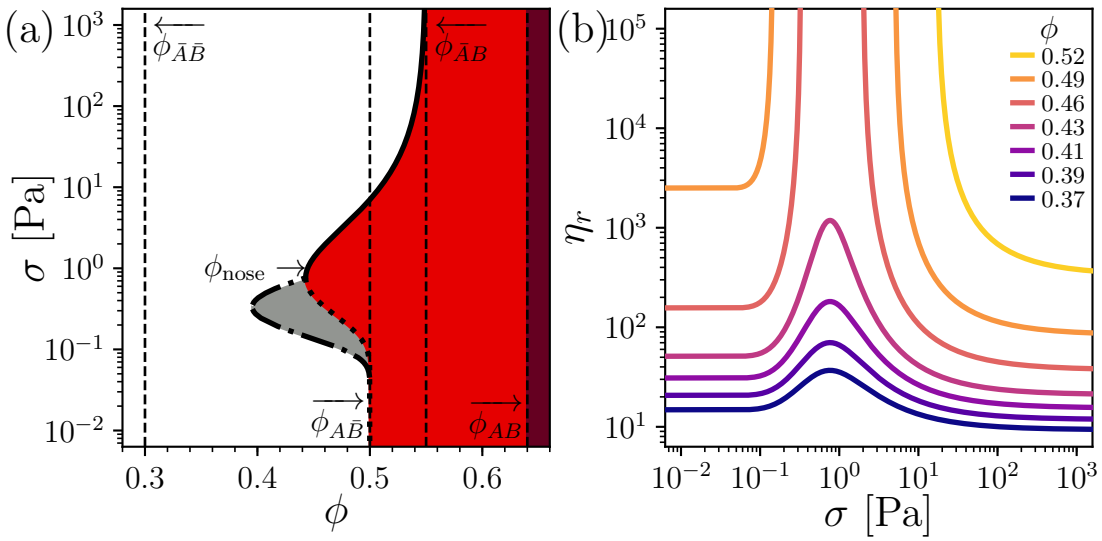

Figure 8.10 Predicted singular behaviour of class 3b flow curves. (a) Jamming phase diagram, key as in Fig. 8.8. Example model parameters: $\sigma_A = 0.4\,\text{Pa}$, $\sigma_B = 1\,\text{Pa}$, $\alpha = 1$ and $\beta = 0.7$. Limiting ϕ_J: $\phi_{AB} = 0.64$ $\phi_{\bar{A}B} = 0.55$, $\phi_{A\bar{B}} = 0.50$, and $\phi_{\bar{A}\bar{B}} = 0.30$ (b) Flow curves: relative viscosity, η_r, *vs* stress, σ, at given volume fractions, ϕ, see legend, using paramters of (a).

8.4 Microphysics

For most of this chapter we have been agnostic about microphysics, simply stating that there are two types of constraint ($\mathcal{A}$ and $\mathcal{B}$). Ultimately this reflects a physical limitation: by measuring $\eta_r(\sigma)$, $\phi_J(\sigma)$ can be determined and therefore how constrained particle contacts are, but the physical process through which relative motion is constrained cannot be directly probed through rheology. Instead, one can only motivate a consistent physical picture. The origin of type-$\mathcal{A}$ constraints, in the form of restricted sliding, has been widely discussed, with speculation on and investigation of the presence of asperity interlock [78, 119], hydrogen bonding [110] and polymer inter-digitation [24]. We now turn to consider what plausible contact-level mechanisms could lead to the presence of type-$\mathcal{B}$ constraints and their breakage with increasing stress.

If sliding is already the type-$\mathcal{A}$ constraint, the type-$\mathcal{B}$ constraint must be either rolling or twisting (as stated in §8.1 radial motion is always considered constrained). To restrict such modes of relative motion requires a torque about the line of centres between two contacting particles, not just a force. To produce a torque that resists rolling or twisting needs both a force and a lengthscale and,

therefore, a finite area of contact between particles is required.[12] For the type-$\mathcal{B}$ constraint to be broken with stress an additional stress-scale, σ_B, is also needed.[13]

A suitable contact model, capturing the relevant physics, is a modified Johnson, Kendall and Roberts (JKR) contact model, although we are not suggesting that this is the only possible contact description. A JKR contact adds a surface energy term to elastic contact between spheres, so that a pull-off force is required to break the contact [190]. The JKR model was later modified such that when rolling the contact line could only move in discrete steps because of the surface topography creating a pinning lengthscale [120]. By creating an asymmetric pressure distribution across the contact, this restricts rolling below a critical rolling moment, M^*, which is equal to the pull-off force times the pinning length. Hence, a type-$\mathcal{B}$ constraint on rolling is introduced with a critical stress, $\sigma_B \sim M^*/d^3$.[14] This modified JKR-contact model has been verified to apply to contacting dry micrometre-sized silica particles, with the the pinning length given by the surface roughness [121]. A critical rolling moment has also been shown to exist between particles in a colloidal gel [191], suggesting that such contact mechanics could apply to non-Brownian suspensions. Other pinning lengthscales could be provided by facetting or shape [192]. This contact model is what we introduced as *adhesion*, back in Ch. 5.

The work of this chapter, through formulating a type-$\mathcal{B}$ constraint and contact state $\bar{A}\bar{B}$, more thoroughly introduces adhesion and constrained rolling into suspensions than our *ad hoc* model of Ch. 5. This also further extends the use of dry tribology into suspension physics; however, a contact in state $A\bar{B}$ (rolling constrained, sliding unconstrained) has no obvious dry analogue.[15] This is not necessarily a barrier; as now, in a suspension, the presence of a background solvent provides the possibility of new interaction mechanisms, e.g. a second immiscible fluid phase in capillary suspensions [114] or hysteretic interaction potentials [193]. Whatever the mechanism, this suggests that contact physics in suspensions will

[12]Here we are assuming short-range interactions, with, e.g., long-range dipolar interactions a torque could be induced between particles without a finite contact area.

[13]If rolling or twisting constraints are not broken with stress but instead formed (i.e., $\mathcal{A}$ = sliding and rolling), shear thickening could be enhanced with $\phi_{\bar{A}} < \phi_{\mathrm{rlp}}$. This could plausibly occur for 'bumpy' particles with asperity interlock, where such anomalous shear thickening has been observed [78].

[14]As there is a finite contact radius twisting would require sliding within the contact, so twisting would be constrained in state $\bar{A}\bar{B}$, although the stress-scale for mobilisation could be separate to rolling. In the literature, twisting has not been investigated separately, so we restrict ourselves to discussion of rolling only in this section.

[15]The ambiguity in defining rolling when sliding is unconstrained is discussed in Appendix D.

contain surprises.

8.5 Attraction within the constraint model

Throughout the last several chapters we have specifically used the term 'adhesion' to refer to the extra rolling constraint that is in addition to the sliding constraint of the WC model. As stated when introducing the term 'adhesion', we distinguish it from attraction, i.e a conservative interparticle force that is expressible in the form of $F = -\nabla U$, and is a function of the relative positions. Attraction acting along the line of centres will clearly not introduce an additional constraint, as for contacting hard particles this degree of freedom is already constrained. The question therefore arises: what effect does potential-based attraction have on a non-Brownian suspension, and how is it different from the effect of adhesion?

In this section we will briefly review what is known about the effect of attraction on non-Brownian hard-particle systems, with the caveat that the literature for suspensions is sparse and inconclusive, as there has yet been a systematic study to answer this question. However, we can try and deduce the possible effect based upon these disparate results. From the outset, we must distinguish the aggregative effect of attraction in non-Brownian systems from the effect in Brownian systems. In the latter thermal case, a homogeneous system will aggregate by itself due to diffusion. However, for short-ranged attraction in the athermal case, below ϕ_{rcp} the particles do not contact each other and cannot aggregate [194]. For particles to encounter one another and aggregate the system must be strained.

We know of a single focussed study on the rheology of an attractive non-Brownian hard-sphere system without friction, in this case a quasi-static simulation (i.e. $\dot{\gamma} \to 0$) [195]. A weak yield stress was measured, however in the range of volume fractions studied this did not depend sensitively on ϕ, remaining finite at ϕ_{rcp} (consistent with $\propto \phi^2$ and depending on contact number density). Such yielding was also found to be reversal symmetric. To infer the effect of friction on an attractive non-Brownian suspension we again turn to dry attractive, or cohesive, granular materials. Here attraction increases the shear strength of a packing (i.e., a smaller confining pressure is needed to support a given shear stress), and attraction simply acts to increase the internal frictional forces [196]. Attraction then increases the effective friction coefficient between particles, but

only at low stress. Given our previous discussion, it should be clear that such a system could shear jam and then yield, but only above ϕ_{rlp} and below $\phi_m(\mu_p)$ (as the effective interparticle friction coefficient is $\gg 1$ at low stress, but it drops back to the actual interparticle friction coefficient, μ_p, at high stress).

We therefore conclude that the experimental phenomenology presented throughout this thesis would not be captured by the effects of attraction alone, including both the volume fraction dependence of the yield stress (Figs. 6.2, Fig. 8.7 and Fig. 7.3) or the reversal response, Fig. 6.10. Instead, we propose that the constraint-based rheology model developed in this chapter captures the relevant effects of particle-particle interactions in non-Brownian suspensions. Nevertheless, it remains the case that the effect of attraction in non-Brownian suspensions has not been systematically studied, so that both identifying a suitable experimental model system as well as simulating such suspensions should be fruitful directions for further work. Indeed, it is not until such work has been done that a comparison with our hypothesis of adhesive contacts can be finally made.

8.6 Conclusion and outlook

To conclude, we have developed a phenomenological model, based on a simple set of physical assumptions, which captures all known classes of experimental flow curve, including combinations of thinning and thickening encountered in industrial applications. Multiple non-trivial predictions, for singular viscosity behaviour follow from these simple assumptions, these are seen to be borne out by comparison with literature data. The underlying constraint physics of these examples was demonstrated by construction of a jamming phase diagram. Comparison with yield-stress suspension data made the surprising prediction that sliding friction played a vital role in yield-stress suspensions, a prediction that was tested and found to be correct in Part II. Ultimately, the concept of the detailed particle-contact-level physics entering only on the level of constraints is powerful. The concept shows how multiple disparate systems may be described by the same model and frames future questions about how particle level details may influence non-Newtonian behaviour in non-Brownian suspensions, e.g. particle roughness in shear thickening.

Many challenges still exist, most important of which remains the question first

raised in Ch. 3: the link to dissipation. Do rolling (or type-$\mathcal{B}$ in general) constraints only increase the viscosity through driving additional non-affine motion, or is there direct dissipation? There is then the generalised question as to the effects of having a lower sliding than static friction coefficient: when the critical particle-level force is exceeded, and the contact mobilised, is the constraint is 'broken' (the resisting force drops) or simply displaced (the resisting force remains constant)? Couching such questions in terms of constraints could help obliviate the need to consider all particle contact level details on an individual basis, and help tame a seemingly insurmountable task.

Chapter 9

Conclusion and further work

9.1 Synopsis

In this final chapter, we draw together the main results of the thesis. Underlying this whole thesis is the idea that the response of a non-Brownian suspension is controlled by finite-area mechanical contacts between particles. These contacts can constrain relative interparticle motion, dependent on stress, and have a physical effect through lowering the jamming volume fraction under shear. We extended this framework to describe both time-dependence in shear-thickening suspensions and to more varied types of particle interaction. Throughout, our approach and physical picture of suspension behaviour contrasts with the traditional 'colloidal' view of suspensions with which this thesis began in Ch. 3. In this colloidal view, the response is controlled by particle interactions 'at a distance', described by hydrodynamic lubrication forces and interparticle potentials [25]. After reviewing the results presented in this thesis, we conclude with a suggestion for a scheme of future work.

9.1.1 Dynamic behaviour of shear-thickening suspensions

The thesis began with describing how the understanding of steady-state shear thickening in concentrated suspensions of non-Brownian particles has been transformed. The increase in viscosity is now understood to be a stress-dependent transition from a lubricated regime to a regime with frictional contact

between particles [70, 71, 73]. This schema is captured by the phenomenological model of Wyart and Cates [8], which captures the steady-state continuous shear thickening of several model nearly-hard-sphere suspensions [24, 56], but also predicts $\mathcal{S}$-shaped and shear-jamming flow curves at higher volume fractions as a consequence. Such negative constitutive relationships ($\mathrm{d}\dot{\gamma}/\mathrm{d}\sigma < 0$) are predicted to be unstable [62] and the flow of shear-thickening suspensions at these volume fractions is expected to be both inhomogeneous and time dependent [82]. In experiment, the time-averaged bulk response will not necessarily match the local response, and indeed DST is observed in the predicted shear jamming regime when time averaging. However, looking at the time-dependent response large temporal fluctuations can be observed.

Following previous work [64, 94], and mirroring concurrent work [92], we extended the WC model to time-dependent flows. This represents a first step to the understanding of spatio-temporally varying flows as we showed how large shear-rate oscillations under controlled stress arise from a competition between a fast contact-dynamics timescale and a slow system timescale, using geometry inertia as a paradigmatic example. This work extended the knowledge of shear-thickening suspensions threefold: experimentally verifying a dynamic extension to the WC model; establishing the existence of shear-jamming flow curves,[1] and measuring a quiescent contact-relaxation time through the introduction of an additional explicit time-dependence in the evolution f.

Capturing the system with a single ratio of timescales that depends on the various system parameters through changing the viscosity, we verified the presence of a critical ratio, which controls the presence of large shear-rate oscillations. As such, it provides a guide for tuning the presence of instabilities in shear-thickening suspensions. More generally, the graphical dynamical-systems approach presented could be used to qualitatively describe and understand the time-dependent flow of shear thickening-suspensions more generally.

Time-dependent spatially-varying flow of suspensions is an area of active investigation, with teh study of, e.g. vorticity banding [92]. This instability

[1]Note, however, that we cannot measure such flow curves using the rapid shear rate oscillations. During the rapid drop in shear rate, as the suspension approaches jamming, due to the diverging viscosity the 'slow variable' actually changes faster than the contact dynamics, the fraction of frictional contacts is therefore no longer quasi–steady-state. While our model has zero spatial dimensions, a similar argument can be made for the work of Ref. [197], suggesting why higher shear rates than predicted by the steady-state WC model can be observed in the propagation of a shear front.

was studied in a very simplified geometry and bridging the gap to comparison with experiment may prove highly challenging as instabilities are often observed in the flow direction [82, 198]. In this case the formalism developed in Ref. [199] to study gradient and vorticity instabilities under shear no longer applies due to the advective term in the flow direction. Therefore, it may be that a qualitative analysis identifying a slow 'system' timescale and conducting a phase-portrait analysis to identify the physical steps in the instability and how it can be controlled may be the most detailed analysis currently possible.

9.1.2 A minimal model to capture varied particle interactions

At the start of the second part of the thesis, using a microphysical motivation we introduced a WC-like model, or "constraint-based model", to describe suspensions with more varied interactions than pure repulsion. As finite-area contacts are now 'allowed' in suspensions, short-range attraction could conceivably create a critical rolling talk between particles, which we term an "adhesive constraint". This introduces a critical stress-scale, σ_a. We argued that such constraints on relative motion lower the jamming volume fraction under shear, taking results from the dry granular literature [124]. Combining adhesive contact mechanics that prevent relative rolling between particles and are broken with stress with frictional constraints, which prevent sliding and are formed with stress, allowed us to describe a broader variety of flow curves. In this chapter we briefly outlined "weak adhesion", where adhesive contacts are broken before frictional contacts are formed so that suspension first shear thin and then thicken, in addition to "strong adhesion", where adhesive bonds are broken after frictional contacts have formed and suspensions yield to a high-shear plateau.

9.1.3 Revealing the role of friction in yield-stress suspensions

In the following two chapters we then explored the implications of the phenomenological model we introduced in Ch. 5. In Ch. 6, we explored the properties of a model yield-stress suspension, cornstarch in oil. Experimentally we showed that the steady-state yield stress emerged at percolation and diverged at random loose packing. By comparison with the constraint-based model, we suggested that the steady-state rheology and yielding was driven by breakage of adhesive constraints in a frictional suspension. We then supported this suggestion by demonstrating

that upon reversal of the direction of shear the steady-state yield stress takes strain to develop. By comparison with reversal experiments on non-adhesive frictional suspensions, we argued that this is consistent with the formation of a percolating compressive frictional contact network stabilised by adhesive bonds. To test this hypothesis we prepared a state with the compressive frictional contact networks relaxed by oscillatory shear, analogous to removing the effect of friction by shaking a powder to compact it. Correspondingly, this state possessed a strength much lower than the steady-state yield stress, revealing the importance of frictional contacts to the yield stress. Yielding to a flowing state in a non-Brownian yield-stress suspension is then unjamming from a shear-jammed state, in contrast to the colloidal view of a yield stress arising from potential attraction in an isotropic state [118]. This insight has important implications for the handling of such suspensions, suggesting that techniques for frictional suspensions, such as applying vibrations [152] or orthogonal shear [153], should be successful.

9.1.4 Interpreting the role of dispersants

In the final chapter of Part II and the last experimental results chapter, we further explored the implications of the model introduced in Ch. 5: interpreting the role of dispersants on non-Brownian suspensions. To do this we first developed a model suspension closer to industrially-relevant suspensions to which dispersants can adsorb on the surface, an aqueous suspension of ground calcite. Although the rheological results were not as clean as with previous model systems, the framework we have developed relies upon interpretation of trends, rather than precise fits, an important aspect when dealing with more complex industrially-relevant suspensions.

With the bare calcite particles forming a yield-stress suspension comparable to the cornstarch-in-oil model system, we studied the effects of two types of dispersant. One type of dispersant was observed to both eliminate adhesion and introduce a finite onset stress, σ^*, for friction, while a second predominantly increased σ^*, leaving significant adhesion. However, both types of dispersant were observed to rapidly decrease the yield stress at a fixed volume fraction. Using the constraint-based framework we demonstrated that the relevant physical mechanism for a dispersant reducing the yield stress in a non-Brownian suspension is preventing frictional contact when adhesion is relevant, i.e. $\sigma^* > \sigma_a$. In the phenomenological model this increases the low-stress jamming volume fraction from percolation to

"adhesive close packing", possibly close to random loose packing. Physically, if there is no percolating compressive frictional contact network to stabilise then adhesion cannot jam the system and there is no yield stress. Finally, we suggested that the onset stress is due to desorption and therefore that in designing dispersants to remove the yield stress in non-Brownian suspensions the focus should be on stronger adsorption to prevent frictional contact rather than purely reducing adhesion, as might be the typical colloidal view of stabilisation with dispersants.

9.1.5 Constraint-based approach to suspension rheology

In the final part of the thesis we had a change of tone: having used a simple microphysically-motivated model based upon friction and adhesion in Part III, we returned to the model to generalise. In Ch. 8, we argued that non-Brownian suspension rheology is controlled by stress-dependent constraints on relative particle motion. By combining constraints that increase with stress and decrease with stress we could reproduce all experimentally observed classes of flow curve. Exploring the model, we predicted several non-trivial features that we compare (predominantly) to literature data. In addition to a yield stress which diverges below random close packing, as earlier explored, we also predicted that for suspensions which shear thin and then thicken that there should be a range of volume fractions in which dispersion is possible (below random close packing), but for which no steady-flowing state exists. Indeed, this is observed for suspensions of cornstarch in aqueous solvents [15]. We also predicted the existence of peaked flow curves that should be sensitive to precise details, resulting from a delicate interplay of two constraints, and again this is seen in the literature [179].

Ultimately, the work presented in this chapter provides a paradigm for understanding how particles level details transform to bulk rheology in suspensions. Simplifying complex surface topographies and interactions to thinking in terms of constraints may allow an intuitive understanding, even beyond the model we have outlined, for example explaining the effect of macroscopic roughness [78, 119], which could additionally constrain rolling or twisting as well as sliding, enhancing their shear-thickening effect.

9.2 Outlook and future work

In this thesis we have taken the concept of mechanical contact between particles controlling the response of non-Brownian suspensions and extended its application to more complex time-dependent flow or to particles with more varied interactions than a short-range repulsive force. There are two distinct possible avenues for further work that are suggested by the results of this thesis: continued development of the phenomenological models used to describe time-dependent flow and investigation of the fundamental physics behind the response of a suspension. More minor suggestions for further work directly related to presented results have been summarised at the end of various results chapters and these will not be recapped.

Continuing to develop and test the phenomenological models used so far, the constraint-based model could be seen to require a comparison with DEM simulations using a suitable contact model, see Ch. 8. Of particular interest would be the reversal response of a frictional and adhesive suspension just below ϕ_{rlp}; the approach of combined phenomenological modelling, experiment and simulation have proved of great utility in studying shear-thickening suspensions, e.g., Refs. [70, 152].

This has left out perhaps the most obvious extension of the work in this direction: combining multiple constraints (i.e. adhesion and friction) with time-dependence. A dynamic model incorporating multiple constraints could be applied to homogeneous flows, but, perhaps more interestingly, it could also focus on gradient banding in the flow of yield-stress suspensions. Introducing particle migration (following Ref. [200]) and time-dependent adhesion (possibly following methods developed in the modelling of thixotropic systems [201]) may allow the comparison of the model with experimental data from quantitative imaging of the sample edge, following the preliminary images of banding during steady-shear shown in Appendix C.

The future work suggested above, extending the comparison of experiment and phenomenological model, misses a more fundamental question, as they are intrinsically phenomenological models. We have, in some sense, treated the fraction of frictional contacts, f, (or the proportion for any constraint) as an "order parameter", completely describing the response of the system.[2]

[2]This, of course, only considers the shear response. In general flow can also be extensional

The form of f is robust to changes in the suspension, including bidispersity and the introduction of rolling resistance [123] and this is initially supportive of f as an order parameter. However, in the bidisperse case the fraction of frictional contacts no longer correctly interpolates between the low-shear and high-shear viscosities through the shear-thickening transition, i.e. a contact between small particles is not equivalent to a contact between large particles [161], suggesting that it should also fail in the polydisperse case. It may therefore be that the models we have presented, which use highly polydisperse solid particles for experimental comparison, simply represent convenient interpolations, without the precise physical interpretation of f that we began with. Clearly this raises the question as to what a more general "order parameter" could possibly be. Complex tensorial descriptions are likely to fail [97]. It has been suggested that a description in force space may be suitable [203], because with friction the force between particles no longer depends solely upon their relative position. Working with a thermodynamic-like description in terms of the macroscopic friction coefficient, $\mu = \sigma/p$ (given by the shear stress normalised by the particle pressure), this description may be more robust to changes such as polydispersity as μ is independent of the size distribution in frictional materials [204]. It may therefore represent a promising direction for future work with a more fundamental focus.

and may depend on normal stress differences; however, in steady flow there is no suggestion that similar interpolations using a scalar parameter would not work as well, for normal forces [84] or in extensional flow [202].

Appendix A

Suspension-rheology regimes

In Ch. 3 we assumed the existence of the intermediate-size regime between the colloidal (thermal) and granular (inertial) regimes. This is implicilty an assumption that the shear stress at which thermal motion becomes negligible, small Pe $\propto \eta_s d^3/k_\mathrm{B}T$, is much lower and well separated from the stress at which inertia becomes important, large $\mathrm{Re}_p \propto \dot{\gamma} d^2/\eta_s$. For physical viscosities and densities this is thought to hold true [28]. Due to the size dependence of the stresses, when considering an observable stress region (*e.g.* 0.1 Pa to 1000 Pa) this also defines a range of particle sizes, the intermediate size regime and non-Brownian suspensions.

Within the non-Brownian suspension regime, the WC-model assumes an additional transition at an onset stress, σ^*, from a frictionless regime, Fig. A.1(ii), to

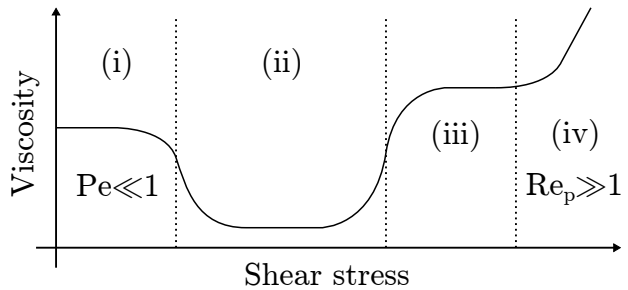

Figure A.1 Schematic representation of suspension rheology regimes at $\phi \sim 0.5$. (i) Colloidal regime: Brownian suspension, thermal physics dominate. (ii) Frictionless non-Brownian suspension, hydrodynamics dominate. (iii) Frictional non-Brownian suspension, frictional contact forces dominate. (iv) Granular regime: inertial forces dominate.

a frictional regime, Fig. A.1(iii). The overlap with the thermal limit, Fig. A.1(i), has been considered in Ref. [24]. As σ^* is found to scale $\propto d^{-2}$ for sterically-stabilised particles, while the stress at which a suspension shear thins is $\propto d^-3$, as the particle size decreases regime (i) will 'shift' closer to σ^* and regime (iii). For small particles there is then a transition directly from shear thinning to thickening [24].

We can also consider the limit of the granular regime, Fig. A.1(iv), which begins at a stress $\propto \eta_s^2/d^2$. With a strong dependence on the solvent viscosity, this suggests that for sufficiently low η_s there may be a transition directly to a granular inertial shear-thickening regime from regime (ii), rather than between two viscous regimes. Such a transition has in fact been reported in both cornstarch in water [14] and stabilised quartz flour suspensions in water [77]. However, throughout the thesis we use non-Brownian particles (high Pe at observable stresses) in viscous background solvents, and therefore consider all regimes to be well-separated throughout and focus on viscous non-Brownian suspensions. Viscous background solvents (*i.e.* compared to water) were chosen to prevent sedimentation; in both previously mentioned experiments great effort had to be made to avoid sedimentation through other means, density matching with salt or using a twin-helix-rotor geometry respectively.

Appendix B

Supplemental material for: Competing timescales lead to oscillations in shear-thickening suspensions

B.1 Linear stability analysis

The Jacobian, J, describing the phase-plane behavior, is given by

$$J = \begin{bmatrix} \frac{\partial g_1}{\partial \dot{\Gamma}} & \frac{\partial g_1}{\partial f} \\ \frac{\partial g_2}{\partial \dot{\Gamma}} & \frac{\partial g_2}{\partial f} \end{bmatrix} = \begin{bmatrix} -\eta_r & -\dot{\Gamma}\frac{\mathrm{d}\eta_r}{\mathrm{d}f} \\ \frac{\dot{\Gamma}}{\epsilon}\frac{\partial \hat{f}}{\partial \dot{\Gamma}} & \frac{\dot{\Gamma}}{\epsilon}\left(\frac{\partial \hat{f}}{\partial f} - 1\right) \end{bmatrix} = \begin{bmatrix} -\eta_r & -\dot{\Gamma}\frac{\mathrm{d}\eta_r}{\mathrm{d}f} \\ \frac{\dot{\Gamma}\eta_r}{\epsilon}\frac{\mathrm{d}\hat{f}}{\mathrm{d}\Sigma} & \frac{\dot{\Gamma}}{\epsilon}\left(\dot{\Gamma}\frac{\mathrm{d}\eta_r}{\mathrm{d}f}\frac{\mathrm{d}\hat{f}}{\mathrm{d}\Sigma} - 1\right) \end{bmatrix}. \tag{B.1}$$

Evaluating J at the fixed point, this simplifies to

$$\begin{bmatrix} -\eta_r & -\dot{\Gamma}\frac{\mathrm{d}\eta_r}{\mathrm{d}\hat{f}} \\ \frac{\dot{\Gamma}\eta_r}{\epsilon}\frac{\mathrm{d}\hat{f}}{\mathrm{d}\Sigma_E} & \frac{\dot{\Gamma}}{\epsilon}\left(\dot{\Gamma}\frac{\mathrm{d}\eta_r}{\mathrm{d}\Sigma_E} - 1\right) \end{bmatrix}, \tag{B.2}$$

with expressions from Eqs. 1-3 in dimensionless form and where derivatives are evaluated at the fixed point ($g_2 = 0,\ g_1 = 0$). The behavior about the fixed point is determined by the eigenvalues of the matrix, $\lambda_{1,2}$, given by the roots of the

equation

$$\epsilon\lambda^2 + \lambda\frac{\eta_r}{\dot{\Gamma}}\left(\epsilon + \frac{\dot{\Gamma}}{\eta_r}\left(1 - \dot{\Gamma}\frac{\mathrm{d}\eta_r}{\mathrm{d}\Sigma_\mathrm{E}}\right)\right) + \frac{\eta_r}{\dot{\Gamma}} = 0. \tag{B.3}$$

When the real part of either λ is positive, $\Re(\lambda) > 0$, the fixed point becomes unstable.

There are now two possibilities for the solution to this equation in the form, $a\lambda^2 + b\lambda + c = 0,\ \lambda_{1,2} = \left(-b \pm \sqrt{b^2 - 4ac}\right)/2a$. Firstly, $b^2 - 4ac < 0$: the fixed point becomes unstable when b becomes negative; $\Re(\lambda_1),\ \Re(\lambda_2) > 0$ and a sink becomes a source. Secondly $b^2 - 4ac > 0$, *i.e.,* the fixed point becomes unstable when only $\Re(\lambda_1) > 0$ and the sink becomes a saddle point. In the latter case, this requires: $-b + \sqrt{b^2 - 4ac} > 0$, or $-4ac > 0$. However, as $a = \epsilon$ and $c = \eta_r/\dot{\Gamma}$ are strictly positive, this condition is not possible. We therefore return to the first case: the fixed point becomes unstable when $b < 0$. The instability criterion is then

$$\frac{\eta_r}{\dot{\Gamma}}\left(\epsilon + \frac{\dot{\Gamma}}{\eta_r}\left(1 - \dot{\Gamma}\frac{\mathrm{d}\eta_r}{\mathrm{d}\Sigma_E}\right)\right) < 0,$$

$$\epsilon < \frac{\dot{\Gamma}}{\eta_r}\left(\dot{\Gamma}\frac{\mathrm{d}\eta_r}{\mathrm{d}\Sigma_E} - 1\right) = \dot{\Gamma}\left(\frac{\Sigma_E}{\eta_r^2}\frac{\mathrm{d}\eta_r}{\mathrm{d}\Sigma_E} - \frac{1}{\eta_r}\right) = -\dot{\Gamma}\frac{\mathrm{d}}{\mathrm{d}\Sigma_E}\left(\frac{\Sigma_E}{\eta_r}\right).$$

Written finally as

$$\epsilon < -\dot{\Gamma}\frac{\mathrm{d}\dot{\Gamma}}{\mathrm{d}\Sigma_\mathrm{E}}. \tag{B.4}$$

This result, as both $\Re(\lambda)$ become positive simultaneously, also means that all bifurcations must be Hopf bifurcations.

B.2 Steady-state rheology of alternate shear-thickening suspensions

In this section of the appendix we present the time-averaged rheology for systems used in Ch. 4, other than the cornstarch in 50 wt.% glycerol-water mixture.

B.2.1 Cornstarch in an 85 wt.% glycerol-water mixture

For the cornstarch suspensions in an 85 wt.% glycerol-water mixture slow swelling is visibly apparent over 2 h. For reproducibility samples were measured after ~ 4 h

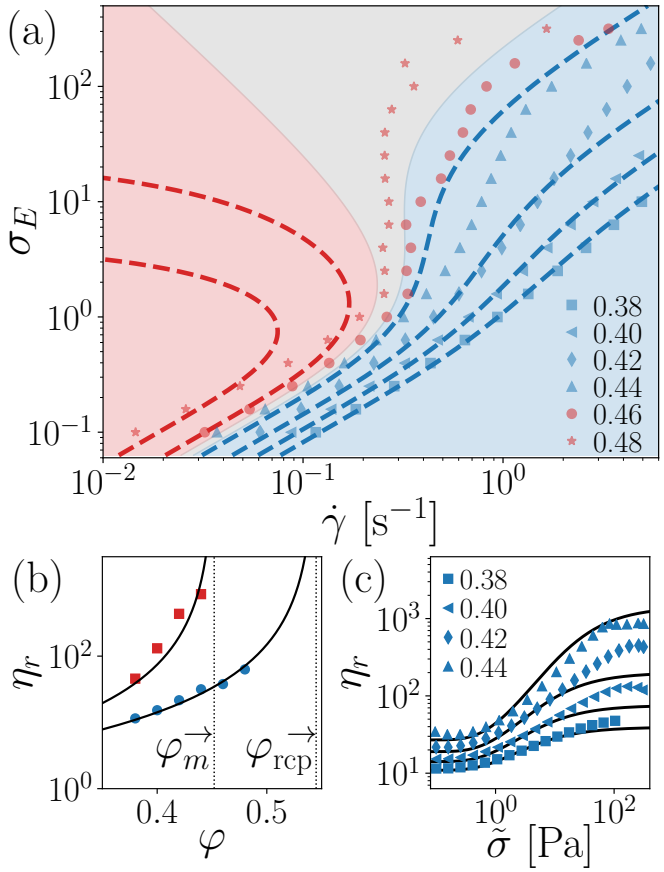

Figure B.1 Cornstarch in an 85 wt.% glycerol-water mixture, time-averaged rheology under imposed stress. (a) Flow curves: applied stress *vs* average shear rate, $\sigma_E(\dot{\gamma})$, at given weight fractions, φ. Dashed lines: WC model for $\varphi_m = 0.452$, $\varphi_{\rm rcp} = 0.545$, $\beta = 0.81$ ($\Rightarrow \varphi_{\rm DST} = 0.445$) and $\sigma^\star = (1.3 \pm 0.2)$ Pa at given φ. Blue, $\varphi < \varphi_{\rm DST}$; grey, $\varphi_{\rm DST} < \varphi < \varphi_m$; red, $\varphi > \varphi_m$. Symbols: Σ_E *vs* time-averaged $\dot{\Gamma}$ for cornstarch suspensions in 85 wt.% glycerol-water. (b) Limiting viscosity states as a function of weight fraction, φ. Symbols: red squares, maximum relative viscosity [$\max(\eta_r)$] without fracture (for $\varphi \leq 0.44$); blue circles, minimum relative viscosity [$\min(\eta_r)$]. Lines, fits to Eq. 4.3: from $\max(\eta_r)$, $\varphi_m = 0.452 \pm 0.004$ and from $\min(\eta_r)$, $\varphi_{\rm rcp} = 0.545 \pm 0.003$. Note that as these are plateau values the apparent viscosity is equal to the viscosity measured including the parallel plate correction. (c) Fit of rheological data to WC model. Symbols, relative viscosity as a function of corrected stress, $\tilde{\sigma}$, for $\varphi < \varphi_m$, see (a) for symbols. Using least squares fitting in log space, $\beta = 0.81 \pm 0.07$ and $\sigma^* = (1.3 \pm 0.2)$ Pa.

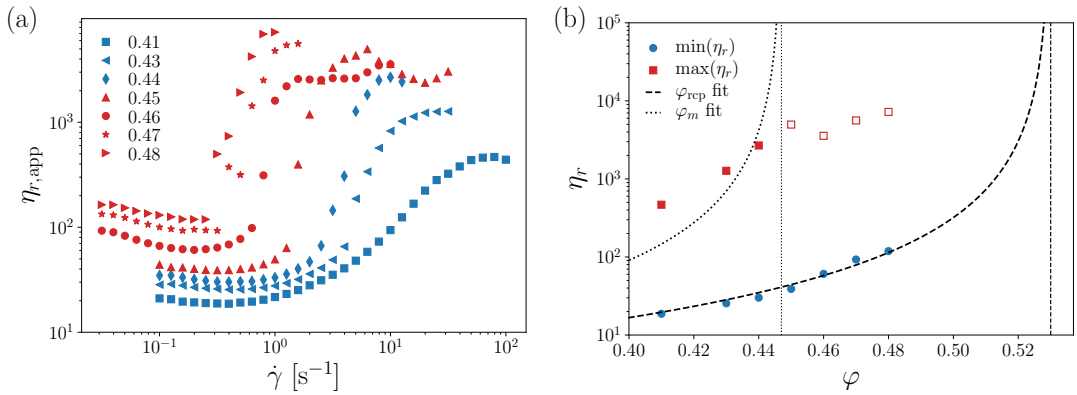

Figure B.2 Cornstarch in a 67 wt.% glycerol-water mixture, time-averaged rheology under imposed shear rate. (a) Flow curves: apparent relative viscosity *vs* average shear rate, $\eta_{r,\mathrm{app}}(\dot{\gamma})$, at given weight fractions, φ, see legend. Symbols: blue, $\varphi < \varphi_m = 0.447$; and red, $\varphi > \varphi_m$. (b) Limiting viscosity states as a function of weight fraction, φ. Symbols: red squares, maximum relative viscosity [max(η_r)] without fracture (for $\varphi \leq 0.44$), open symbols with visible edge fracture; blue circles, minimum relative viscosity [min(η_r)]. Lines, fits to Eq. 4.3: dotted lines, from max(η_r), $\varphi_m = 0.447 \pm 0.003$ and from min(η_r) (dahsed lines), $\varphi_{\mathrm{rcp}} = 0.530 \pm 0.002$. Note that as these are plateau values the apparent viscosity is equal to the viscosity measured including the parallel-plate correction.

resting, using a roller bank to prevent sedimentation. The background solvent viscosity, η_s, was measured at 75 mPa s from the supernatant of centrifuged samples at $\varphi = 0.40$. Rheological measurements were made with the sample protocol and geometry as for cornstarch in a 50 wt.% glycerol-water mixture background solvent, but with a 15 s equilibration time and 15 s measurement time to account for the reduced shear rates. The results are reported in Fig. B.1 (symbols), with a representative fit of the WC model (dashed lines). For fitting procedure see Figs. B.1(b) and (c), along with their respective captions.

B.2.2 Cornstarch in a 67 wt.% glycerol-water mixture

For cornstarch in a 67 wt.% glycerol-water mixture background solvent, samples were rested for 1 h after mixing on a roller mixer. Although swelling was not apparent, this resting period was precautionary and due to the occurrence of swelling for cornstarch in an 85 wt.% glycerol-water mixture. The background viscosity was measured, $\eta_s = 17$ mPa s, from both a centrifuged supernatant and from the stock solution. Steady-state flow curves were measured using a TA

Instruments ARES-G2 with sandblasted parallel plates, from which we report rim shear rates and apparent viscosities. Measurements were taken under imposed shear rate from $0.1\,\mathrm{s}^{-1}$ for $\varphi \leq 0.45$, or $0.0316\,\mathrm{s}^{-1}$ for $\varphi \geq 0.46$, till fracture, with a single up-sweep at 10 pts./decade with a 20 s delay and 10 s averaging time per point. Again, weight fractions are reported due to particle swelling or porosity. Limiting φ_J ($\varphi_m = 0.447 \pm 0.003$ and $\varphi_{\mathrm{rcp}} = 0.530 \pm 002$) were determined using only the steady high-stress viscosities without edge fracture (seen for $\varphi \leq 0.44$), see Fig. B.2 (caption) for details. Fitting $\eta_r(\sigma)$ to the WC model with the given φ_m and φ_{rcp} using corrected stresses, we find $\sigma^* = 2.3\,\mathrm{Pa}$ and $\beta = 0.94$, which gives $\varphi_{\mathrm{DST}} = 0.436$.

B.2.3 Silica particles

The experimental results, figure and figure caption presented here, Fig. B.3, are the work of John Royer, based upon predictions of the model. They are included to support the results of the model. For experimental details please see the Supplemental Material of Ref. [1].

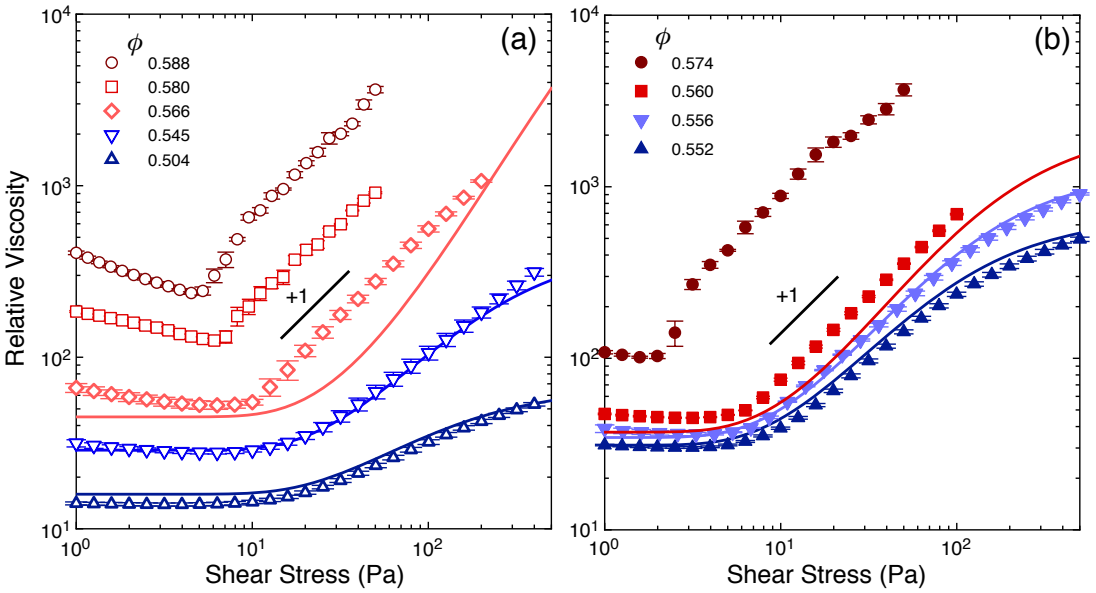

Figure B.3 Flow curves, $\eta_r(\sigma)$, for suspensions of $d = 4\,\mu\text{m}$ silica spheres at various volume fractions, ϕ suspended in: (a) an 80 wt.% DMSO-water mixture, (b) an 87 wt.% glycerol-water mixture. Error bars give the standard deviation from two up and down stress sweeps. Solid lines show WC-model flow curves with $\phi_{\text{rcp}} = 0.67$, $\phi_m = 0.57$, $\beta = 1$, and $\sigma^* = 14.5\,\text{Pa}$ for suspensions in a DMSO-water mixture, (a), and $\sigma^* = 40\,\text{Pa}$ for suspensions in a glycerol-water mixture, (b).

Appendix C

Supplemental material for: Yielding in adhesive non-Brownian suspensions

C.1 Flow-curve details

C.1.1 Time dependence

Much research has been conducted into the time-dependent flows of yield-stress fluids, focussing in particular on 'thixotropy', the gradual drop in viscosity over time with applied shear [201]. Briefly probing the time-evolution of the system under continuous shear and selecting a single volume fraction ($\phi = 0.51$), we see that upon repeated 'sweeps' of the applied shear rate that the flow curve appears reversible, although some scatter in the data points is noticeable at low shear rates, see Fig. C.1. During pre-shear at $\dot{\gamma} = 10\,\mathrm{s}^{-1}$, there is a minimal drop in the measured stress, from a peak of 160 Pa to 150 Pa. The response of the system therefore does not appear to be dominated by thixotropy or controlled by long-term structural evolution [25].

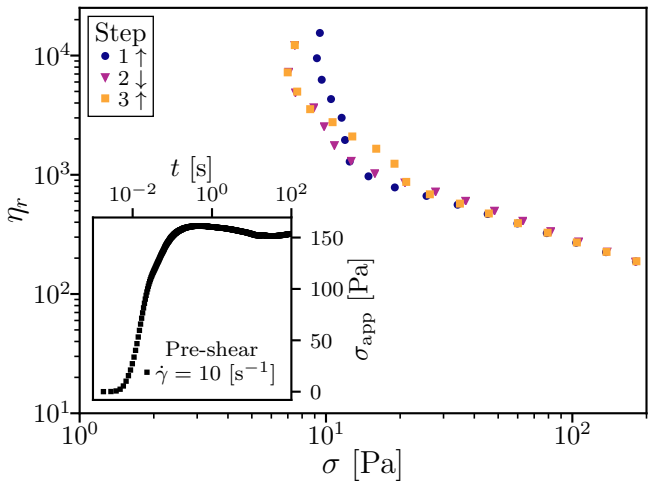

Figure C.1 Flow curve reversibility at $\phi = 0.51$. Symbols, repeated shear rate sweeps following the protocol of Fig. 6.2, see legend for step. Inset: time dependence of pre-shear. Black trace: apparent stress, $\sigma_{\rm app} \equiv 2\mathcal{T}/\pi R^3$, *vs* time, t, at $\dot{\gamma} = 10\,\mathrm{s}^{-1}$.

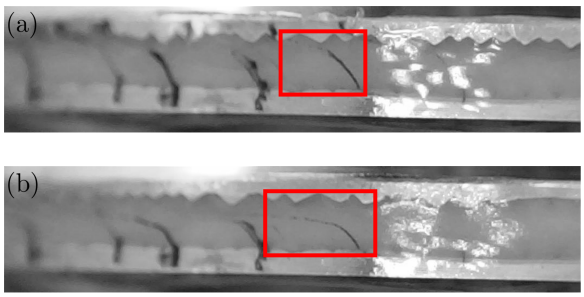

Figure C.2 Banding at $\phi = 0.50$. Direction of shear is right to left. (a) Image of suspension edge under shear at $\sigma_{\rm app} = 20\,\mathrm{Pa}$. Markings are carbon black in sunflower oil placed vertically on the suspension at rest, most recent marking is highlighted by the red box. Due to imaging considerations a controlled-stress Anton-Paar MCR 302 rheometer was used with cross-hatched parallel plates ($R = 20\,\mathrm{mm}$ and $h = 1.0\,\mathrm{mm}$), applying a stepped, logarithmically increasing stress. Yield stress measured under imposed rate, $\sigma_{y,\rm app}^{(\rm d)} = 9\,\mathrm{Pa}$. (b) Image of marked suspension edge at $\sigma_{\rm app} = 120\,\mathrm{Pa} \gg \sigma_{y,\rm app}^{(\rm d)}$.

C.1.2 Gradient banding

In addition to temporal variation, spatial variation of yield stress fluid flows has also been widely investigated, particularly in the form of gradient banding: a coexistence of solid and fluid bands [205]. We can crudely investigate this phenomenon through imaging of a line marked on the sample edge before shearing from rest. Taking a sample at $\phi = 0.50$, under a constant applied stress, $\sigma_{\text{app}} = 20\,\text{Pa} \gtrsim \sigma_{y,\text{app}}^{(\text{d})} = 9\,\text{Pa}$, we see clear signs of banding, see Fig. C.2. The lower portion of the edge marking remains visible and close to vertical, while a layer close to the top plate flows with the marking slanted and progressively less visible. As the applied stress is raised further above the yield stress, $\sigma_{\text{app}} = 120\,\text{Pa}$, the flowing band appears to increase in size. The banding may lie at the root of the scatter observed in the measured stress at low shear rates, see Fig. C.1, although detailed investigation of this phenomenon lies beyond the scope of this thesis. With an inhomogeneous shear rate across the gap, η_r now only represents an apparent viscosity, rather than a material property. Despite this limitation, our strongly shear-thinning flow curves are still indicative of a yield stress fluid.

Although the macroscopic shear rate no longer represents the local shear rate, the stress should not be similarly affected.[1] We then simply estimate the yield stress from the lowest accessed macroscopic shear rate, $\sigma_y^{(\text{d})} = \sigma(\dot{\gamma}_{\text{min}})$, but this could also be estimated from extrapolation using a fit to an empirical model, e.g., Herschel-Bulkley. Although the flow is banded, and the viscosity is now only an apparent viscosity, $\sigma_y^{(\text{d})}$ should still represent a material property. Caution should, however, be taken for flows which are entirely localised at the boundary, or 'slip', where the measured 'yield stress' becomes dependent on the surface properties of the plate [206].

C.2 Repeated shear reversal

We can make the apparent reversal asymmetry explicit by repeated reversal of the applied shear stress. For a test at a given stress, σ, the suspension is first prepared in a reproducible state, shearing at a high stress, 100 Pa, for 100 s, to erase the previous shear history, followed by 100 s at $+\sigma$ and 10 s at 0 Pa. Once

[1] In the low Re limit the torque across the gap must be constant, a small error may arise in conversion to a stress due to uncertainty in the local shear rate and hence the $\text{dln}\,\mathcal{T}/\text{dln}\,\Omega$ term.

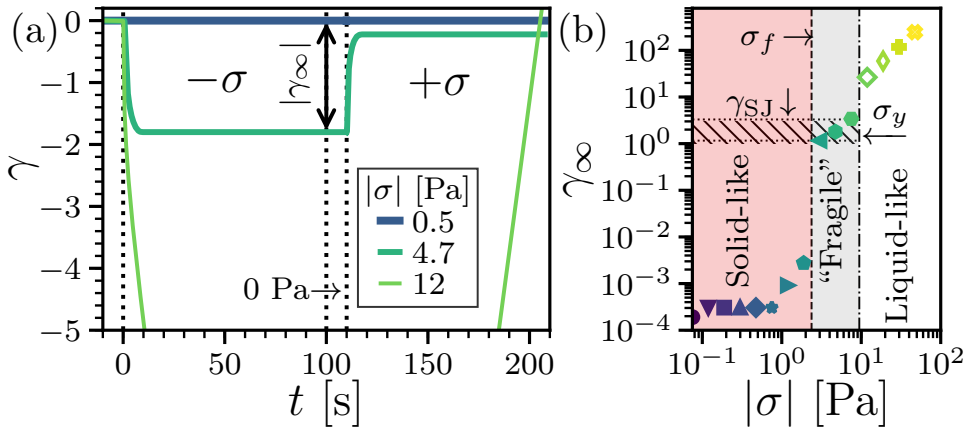

Figure C.3 Repeated stress-reversal response at $\phi = 0.51$. (a) Stress traces, $\gamma(t)$, from $t = 0$, the time of the first stress reversal to a stress -σ, see legend for $|\sigma|$ value. Dotted lines, changes in stress, as labelled. Bold arrow, definition of reversal strain, γ_∞. (b) Reversal strain, γ_∞, *vs* stress magnitude, $|\sigma|$. Symbols, logarithmically spaced results at 5pts./decade; closed symbols, jammed states with $\dot{\gamma} \to 0$, and open symbols, flowing states, $\dot{\gamma} > 0$. Dashed line: onset of apparent fragility at σ_f, from $\max(\log \gamma_\infty / \log \sigma)$; dot-dashed line: onset of flowing states at the yield stress, σ_y. Hatched region, range of shear jamming strains.

a reproducible state has been reached, the applied stress, σ, is then repeatedly applied in an alternating direction, each time for 100 s followed by a 10 s recovery period with zero applied stress. The strain response, $\gamma(t)$, is shown starting from the first reversal of the applied stress, for a sample at $\phi = 0.51$, see Fig. C.3(a). At low stress, e.g., $\sigma = 0.5$ Pa, the suspension behaves as a rigid isotropic solid, with minimal deformation ($|\gamma| = 3 \times 10^{-4}$) in either the reverse (-σ) or forward ($+\sigma$) directions, see Fig. C.3(a) (bold, blue trace). At a higher stress of 4.7 Pa, the system at first rapidly deforms, however the strain stops increasing after $t \approx 10$ s, reaching $|\gamma(t = 100\,\text{s})| \equiv \gamma_\infty = 1.8$, see Fig. C.3(a) (green trace). The deformation is plastic, as in Fig. 6.3, with no measurable elastic strain recovered upon removal of the stress, see 0 Pa region indicated in Fig. C.3(a). When the direction of stress is again reversed, the suspension flows in the $+\gamma$ direction, before re-jamming. The systems appears "fragile" at this stress. Finally, when the stress is higher still at $|\sigma| = 12$ Pa, the suspension behaves as liquid-like, flowing continually ($|\gamma| \gg 10$) upon application of stress in both the forward and reverse directions, see Fig. C.3(a) (fine, light green trace).

The transitions between these qualitatively different behaviors can be identified from $\gamma_\infty(\sigma)$, the magnitude of the change in strain during the first stress reversal step, as a function of stress magnitude. The transition from solid-like to apparent

"fragility", at σ_f, is identified by the sharp change in γ_∞, Fig. C.3 (b) [dashed line]. The second jump in strain to flowing states (open symbols) again identifies the yield stress, σ_y. The form of $\gamma_\infty(\sigma)$ is similar to the strain response after a high-stress pre-shear, cf. Fig. 6.3(b). This shows that the response we identified in §6.1.2 is due to reversal and not due to the high pre-shear stress.

C.3 Comparison of constraint model with flow curves

In this section we present a comparison of the full experimental flow curves, $\eta_r(\sigma, \phi)$, with the constraint model, Fig. C.4. The experimental data is identical to that presented in Fig. 6.2. For the constraint model the relative viscosity is determined from the jamming volume fraction (Eqs. 6.1 and 6.2) and the Maron-Pierce equation, $\eta_r = (1-\phi/\phi_J)^{-2}$. The fit parameters are as used Ch. 6, and they are also detailed in Fig. C.4 (caption). Particular attention should be drawn to the agreement between model and experiment in the high-shear viscosity plateau for $\phi \leq 0.49$.

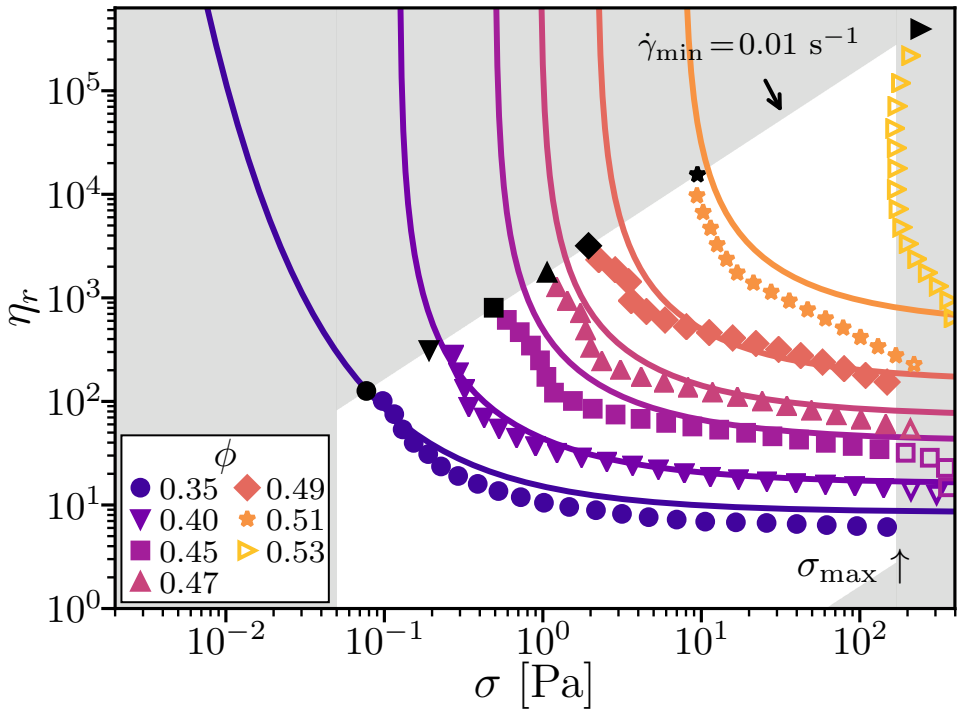

Figure C.4 Steady-state rheology of an adhesive suspension compared to the constraint-based model. Symbols, cornstarch-in-oil flow curves under imposed shear rate, $\dot{\gamma}$: relative viscosity, $\eta_r = \eta/\eta_s$, *vs* shear stress, σ, at volume fractions, ϕ, see legend. Open symbols, $\sigma > \sigma_{\max}$; black points, $\sigma(\dot{\gamma}_{\min}) \equiv \sigma_y^{(\mathrm{d})}$. Solid lines, corresponding flow curves for the constraint-based model, Eqs. 6.1 & 6.2. Stress-dependent jamming volume fraction: $\phi_J(\sigma) = \phi_{\mathrm{rlp}}(1-a) + \phi_{\mathrm{alp}}a$, $a(\sigma) = 1 - \exp(-(\sigma_a/\sigma)^\kappa)$ with $\phi_{\mathrm{rlp}} = 0.533$, $\phi_{\mathrm{p}} = 0.35$, $\sigma_a = 0.2\,\mathrm{Pa}$ & $\kappa = 0.55$. Relative viscosity for $\phi < \phi_J$ given by Maron-Pierce form: $\eta_r = [1 - \phi/\phi_J(\sigma)]^{-2}$. Note that banding was observed during steady shear, see Fig. C.2, and data for η_r should be taken as an effective viscosity rather than a material property.

Appendix D

Defining a constraint on rolling

Although when sliding is constrained defining a constraint on rolling is straight forward (the particles must stay co-linear as they rotate together forming a rigid pair), when sliding is unconstrained it is more nuanced and it is necessary to outline how it may defined. The first attempt, could be to simply keep the orientation of the two particles aligned, as in the case with sliding constrained, see Fig. D.1(a) with particle orientation indicated by arrows. This does not, as it first appears, introduce an additional constraint. In the static limit (i.e., without lubrication forces) there are no tangential forces for frictionless spheres and the particle orientations would not change, even without imposing a constraint on their relative orientations. It is then commensurately observed that introducing such a "constraint" in the form of rolling resistance, without constraining sliding, does not lower the jamming volume fraction [122].

To define a constraint on rolling we must consider the angle, θ, through which the two particles have slid relative to one another while in contact. Consider a particle with a contact pinning length-scale that prevents rolling, shown as a facet in Fig. D.1(b), sliding along another (smooth) particle. Such a contact would prevent the facetted particle rolling, and therefore impose a rotation on the particle as it slides. To constrain rolling would then require keeping the angle between the particle orientations equal to the angle, θ, through which the particles have slid relative to one another. In Fig. D.1(b) we have shown two dissimilar particles to enable a clearer physical description; however, the constraint on the relative orientations deduced from this picture does not have such an asymmetry.

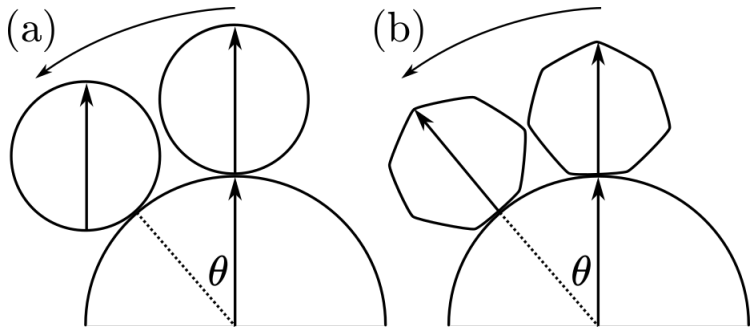

Figure D.1 Defining constraints on rolling when sliding. (a) A schematic of particle motion during sliding through an angle θ between two particles (curved arrow). The possible relative orientation of the particles (straight arrows) without rolling constrained is shown, i.e., with conventionally defined rolling resistance. (b) Schematic of particle orientation during sliding of particle with rolling constrained, a facetted particle is shown for effect.

Bibliography

[1] J. A. Richards, J. R. Royer, B. Liebchen, B. M. Guy, and W. C. K. Poon, Competing timescales lead to oscillations in shear-thickening suspensions, Phys. Rev. Lett. **123**, 038004 (2019).

[2] J. A. Richards, B. M. Guy, E. Blanco, M. Hermes, G. Poy, and W. C. K. Poon, The role of friction in the yielding of adhesive non-brownian suspensions (2019), arXiv:1910.07958 .

[3] B. M. Guy, J. A. Richards, D. J. M. Hodgson, E. Blanco, and W. C. K. Poon, Constraint-based approach to granular dispersion rheology, Phys. Rev. Lett. **121**, 128001 (2018).

[4] P. Banfill, Rheology of fresh cement and concrete, in *Rheology Reviews 2006* (British Society of Rheology, 2006) pp. 61–130.

[5] E. Blanco, D. J. M. Hodgson, M. Hermes, R. Besseling, G. L. Hunter, P. M. Chaikin, M. E. Cates, I. Van Damme, and W. C. K. Poon, Conching chocolate is a prototypical transition from frictionally jammed solid to flowable suspension with maximal solid content, Proc. Natl. Acad. Sci. U.S.A. , 201901858 (2019).

[6] T. J. Carneim and D. J. Green, Mechanical properties of dry-pressed alumina green bodies, J. Am. Ceram. Soc. **84**, 1405 (2001).

[7] A. Lemaître, J.-N. Roux, and F. Chevoir, What do dry granular flows tell us about dense non-Brownian suspension rheology?, Rheol. Acta **48**, 925 (2009).

[8] M. Wyart and M. E. Cates, Discontinuous shear thickening without inertia in dense non-Brownian suspensions, Phys. Rev. Lett. **112**, 098302 (2014).

[9] C. W. Macosko, *Rheology: principles, measurements, and applications*, Advances in interfacial engineering (VCH Publishers, Inc., 1993).

[10] M. Smith, R. Besseling, M. Cates, and V. Bertola, Dilatancy in the flow and fracture of stretched colloidal suspensions, Nat. Commun. **1**, 114 (2010).

[11] F. Boyer, E. Guazzelli, and O. Pouliquen, Unifying suspension and granular rheology, Phys. Rev. Lett. **107**, 188301 (2011).

[12] A. Deboeuf, G. Gauthier, J. Martin, Y. Yurkovetsky, and J. F. Morris, Particle pressure in a sheared suspension: A bridge from osmosis to granular dilatancy, Phys. Rev. Lett. **102**, 108301 (2009).

[13] A. Fall, F. Bertrand, G. Ovarlez, and D. Bonn, Yield stress and shear banding in granular suspensions, Phys. Rev. Lett. **103**, 178301 (2009).

[14] A. Fall, A. Lemaitre, F. Bertrand, D. Bonn, and G. Ovarlez, Shear thickening and migration in granular suspensions, Phys. Rev. Lett. **105**, 268303 (2010).

[15] A. Fall, F. Bertrand, D. Hautemayou, C. Mezière, P. Moucheront, A. Lemaître, and G. Ovarlez, Macroscopic discontinuous shear thickening versus local shear jamming in cornstarch, Phys. Rev. Lett. **114**, 098301 (2015).

[16] R. E. O'Neill, J. R. Royer, and W. C. K. Poon, Liquid migration in shear thickening suspensions flowing through constrictions, Phys. Rev. Lett. **123**, 128002 (2019).

[17] E. Brown and H. M. Jaeger, The role of dilation and confining stresses in shear thickening of dense suspensions, J. Rheol. **56**, 875 (2012).

[18] F. Blanc, E. D'Ambrosio, L. Lobry, F. Peters, and E. Lemaire, Universal scaling law in frictional non-Brownian suspensions, Phys. Rev. Fluids **3**, 114303 (2018).

[19] P. Coussot, Experimental procedures and problems in paste viscometry, in *Rheometry of Pastes, Suspensions, and Granular Materials* (John Wiley & Sons, Inc. Hoboken, NJ, USA, 2005) pp. 81–152.

[20] C. Carotenuto, A. Vananroye, J. Vermant, and M. Minale, Predicting the apparent wall slip when using roughened geometries: A porous medium approach, J. Rheol. **59**, 1131 (2015).

[21] H. A. Barnes, Measuring the viscosity of large-particle (and flocculated) suspensions — a note on the necessary gap size of rotational viscometers, J. Non-Newton. Fluid **94**, 213 (2000).

[22] A. Yoshimura and R. K. Prud'homme, Wall slip corrections for couette and parallel disk viscometers, J. Rheol. **32**, 53 (1988).

[23] R. H. Ewoldt, M. T. Johnston, and L. M. Caretta, Experimental challenges of shear rheology: how to avoid bad data, in *Complex fluids in biological systems* (Springer, 2015) pp. 207–241.

[24] B. M. Guy, M. Hermes, and W. C. K. Poon, Towards a unified description of the rheology of hard-particle suspensions, Phys. Rev. Lett. **115**, 088304 (2015).

[25] J. Mewis and N. J. Wagner, *Colloidal suspension rheology* (Cambridge University Press, 2012).

[26] H. A. Barnes and K. Walters, The yield stress myth?, Rheol. Acta **24**, 323 (1985).

[27] H. A. Barnes, The 'yield stress myth?' paper – 21 years on, Appl. Rheol. **17**, 43110 (2007).

[28] J. J. Stickel and R. L. Powell, Fluid mechanics and rheology of dense suspensions, Annu. Rev. Fluid Mech. **37**, 129 (2005).

[29] S.-E. Phan, W. B. Russel, Z. Cheng, J. Zhu, P. M. Chaikin, J. H. Dunsmuir, and R. H. Ottewill, Phase transition, equation of state, and limiting shear viscosities of hard sphere dispersions, Phys. Rev. E **54**, 6633 (1996).

[30] W. C. K. Poon, E. R. Weeks, and C. P. Royall, On measuring colloidal volume fractions, Soft Matter **8**, 21 (2012).

[31] E. Brown and H. M. Jaeger, Shear thickening in concentrated suspensions: phenomenology, mechanisms and relations to jamming, Rep. Prog. Phys. **77**, 046602 (2014).

[32] R. A. Bagnold, Experiments on a gravity-free dispersion of large solid spheres in a Newtonian fluid under shear, Proc. R. Soc. Lond. A Math. Phys. Sci. **225**, 49 (1954).

[33] H. A. Barnes, Shear-thickening ("dilatancy") in suspensions of nonaggregating solid particles dispersed in Newtonian liquids, J. Rheol. **33**, 329 (1989).

[34] N. J. Wagner and J. F. Brady, Shear thickening in colloidal dispersions, Physics Today **62**, 27 (2009).

[35] B. J. Maranzano and N. J. Wagner, The effects of interparticle interactions and particle size on reversible shear thickening: Hard-sphere colloidal dispersions, J. Rheol. **45**, 1205 (2001).

[36] M. Trulsson, M. Bouzid, J. Kurchan, E. Clément, P. Claudin, and B. Andreotti, Athermal analogue of sheared dense Brownian suspensions, EPL (Europhysics Letters) **111**, 18001 (2015).

[37] R. Mari, R. Seto, J. F. Morris, and M. M. Denn, Discontinuous shear thickening in Brownian suspensions by dynamic simulation, Proc. Natl. Acad. Sci. U.S.A. **112**, 15326 (2015).

[38] É. Guazzelli, J. F. Morris, and S. Pic, *A Physical Introduction to Suspension Dynamics*, Cambridge Texts in Applied Mathematics (Cambridge University Press, 2011).

[39] D. R. Foss and J. F. Brady, Structure, diffusion and rheology of Brownian suspensions by Stokesian dynamics simulation, J. Fluid Mech. **407**, 167–200 (2000).

[40] J. R. Melrose and R. C. Ball, Continuous shear thickening transitions in model concentrated colloids – the role of interparticle forces, J. Rheol. **48**, 937 (2004).

[41] N. Frankel and A. Acrivos, On the viscosity of a concentrated suspension of solid spheres, Chem. Eng. Sci. **22**, 847 (1967).

[42] J. Melrose and R. Ball, The pathological behaviour of sheared hard spheres with hydrodynamic interactions, EPL (Europhysics Letters) **32**, 535 (1995).

[43] D. Lootens, H. van Damme, Y. Hémar, and P. Hébraud, Dilatant flow of concentrated suspensions of rough particles, Phys. Rev. Lett. **95**, 268302 (2005).

[44] E. Bertrand, J. Bibette, and V. Schmitt, From shear thickening to shear-induced jamming, Phys. Rev. E **66**, 060401 (2002).

[45] A. Fall, N. Huang, F. Bertrand, G. Ovarlez, and D. Bonn, Shear thickening of cornstarch suspensions as a reentrant jamming transition, Phys. Rev. Lett. **100**, 018301 (2008).

[46] A. Fall, F. Bertrand, G. Ovarlez, and D. Bonn, Shear thickening of cornstarch suspensions, J. Rheol. **56**, 575 (2012).

[47] A. B. Metzner and M. Whitlock, Flow behavior of concentrated (dilatant) suspensions, Transactions of the Society of Rheology **2**, 239 (1958).

[48] R. L. Hoffman, Discontinuous and dilatant viscosity behavior in concentrated suspensions. I. Observation of a flow instability, Transactions of the Society of Rheology **16**, 155 (1972).

[49] J. N. Israelachvili, *Intermolecular and surface forces* (Academic press, 2011).

[50] B. Persson, *Sliding Friction: Physical Principles and Applications* (Springer Science & Business Media, 2000).

[51] V. L. Popov, *Contact mechanics and friction* (Springer, 2010).

[52] R. Seto, R. Mari, J. F. Morris, and M. M. Denn, Discontinuous shear thickening of frictional hard-sphere suspensions, Phys. Rev. Lett. **111**, 218301 (2013).

[53] H. J. Wilson and R. H. Davis, Shear stress of a monolayer of rough spheres, J. Fluid Mech. **452**, 425 (2002).

[54] R. H. Davis, Y. Zhao, K. P. Galvin, and H. J. Wilson, Solid–solid contacts due to surface roughness and their effects on suspension behaviour, Philos. Trans. A Math. Phys. Eng. Sci. **361**, 871 (2003).

[55] E. Lerner, G. Düring, and M. Wyart, A unified framework for non-Brownian suspension flows and soft amorphous solids, Proc. Natl. Acad. Sci. U.S.A. **109**, 4798 (2012).

[56] J. R. Royer, D. L. Blair, and S. D. Hudson, Rheological signature of frictional interactions in shear thickening suspensions, Phys. Rev. Lett. **116**, 188301 (2016).

[57] L. E. Silbert, Jamming of frictional spheres and random loose packing, Soft Matter **6**, 2918 (2010).

[58] G. Y. Onoda and E. G. Liniger, Random loose packings of uniform spheres and the dilatancy onset, Phys. Rev. Lett. **64**, 2727 (1990).

[59] S. H. Maron and P. E. Pierce, Application of Ree-Eyring generalized flow theory to suspensions of spherical particles, J. Colloid Sci. **11**, 80 (1956).

[60] D. Quemada, Rheology of concentrated disperse systems and minimum energy dissipation principle, Rheol. Acta **16**, 82 (1977).

[61] F. Radjai, M. Jean, J.-J. Moreau, and S. Roux, Force distributions in dense two-dimensional granular systems, Phys. Rev. Lett. **77**, 274 (1996).

[62] P. D. Olmsted, Perspectives on shear banding in complex fluids, Rheol. Acta **47**, 283 (2008).

[63] R. Mari, R. Seto, J. F. Morris, and M. M. Denn, Shear thickening, frictionless and frictional rheologies in non-Brownian suspensions, J. Rheol. **58**, 1693 (2014).

[64] R. Mari, R. Seto, J. F. Morris, and M. M. Denn, Nonmonotonic flow curves of shear thickening suspensions, Phys. Rev. E **91**, 052302 (2015).

[65] M. E. Cates, M. D. Haw, and C. B. Holmes, Dilatancy, jamming, and the physics of granulation, J. Phys. Condens. Matter **17**, S2517 (2005).

[66] M. E. Cates and M. Wyart, Granulation and bistability in non-Brownian suspensions, Rheol. Acta **53**, 755 (2014).

[67] D. J. M. Hodgson, M. Hermes, and W. C. K. Poon, Jamming and the onset of granulation in a model particle system (2015), arXiv:1507.08098 .

[68] F. Peters, G. Ghigliotti, S. Gallier, F. Blanc, E. Lemaire, and L. Lobry, Rheology of non-Brownian suspensions of rough frictional particles under shear reversal: A numerical study, J. Rheol. **60**, 715 (2016).

[69] C. Ness and J. Sun, Two-scale evolution during shear reversal in dense suspensions, Phys. Rev. E **93**, 012604 (2016).

[70] N. Y. C. Lin, B. M. Guy, M. Hermes, C. Ness, J. Sun, W. C. K. Poon, and I. Cohen, Hydrodynamic and contact contributions to continuous shear thickening in colloidal suspensions, Phys. Rev. Lett. **115**, 228304 (2015).

[71] C. Clavaud, A. Bérut, B. Metzger, and Y. Forterre, Revealing the frictional transition in shear-thickening suspensions, Proc. Natl. Acad. Sci. U.S.A. **114**, 5147 (2017).

[72] B. Andreotti, Y. Forterre, and O. Pouliquen, *Granular Media: Between Fluid and Solid* (Cambridge University Press, 2013).

[73] J. Comtet, G. Chatté, A. Niguès, L. Bocquet, A. Siria, and A. Colin, Pairwise frictional profile between particles determines discontinuous shear thickening transition in non-colloidal suspensions, Nat. Commun. **8**, 15633 (2017).

[74] B. Andreotti, J.-L. Barrat, and C. Heussinger, Shear flow of non-Brownian suspensions close to jamming, Phys. Rev. Lett. **109**, 105901 (2012).

[75] M. Trulsson, E. DeGiuli, and M. Wyart, Effect of friction on dense suspension flows of hard particles, Phys. Rev. E **95**, 012605 (2017).

[76] C. Heussinger, Shear thickening in granular suspensions: Interparticle friction and dynamically correlated clusters, Phys. Rev. E **88**, 050201 (2013).

[77] N. Fernandez, R. Mani, D. Rinaldi, D. Kadau, M. Mosquet, H. Lombois-Burger, J. Cayer-Barrioz, H. J. Herrmann, N. D. Spencer, and L. Isa, Microscopic mechanism for shear thickening of non-Brownian suspensions, Phys. Rev. Lett. **111**, 108301 (2013).

[78] C.-P. Hsu, S. N. Ramakrishna, M. Zanini, N. D. Spencer, and L. Isa, Roughness-dependent tribology effects on discontinuous shear thickening, Proc. Natl. Acad. Sci. U.S.A. **115**, 5117 (2018).

[79] R. I. Tanner, C. Ness, A. Mahmud, S. Dai, and J. Moon, A bootstrap mechanism for non-colloidal suspension viscosity, Rheol. Acta **57**, 635 (2018).

[80] H. V. Damme, Concrete material science: Past, present, and future innovations, Cem. Concr. Res. **112**, 5 (2018).

[81] D. V. Boger, Rheology and the resource industries, Chem. Eng. Sci. **64**, 4525 (2009).

[82] M. Hermes, B. M. Guy, W. C. K. Poon, G. Poy, M. E. Cates, and M. Wyart, Unsteady flow and particle migration in dense, non-Brownian suspensions, J. Rheol. **60**, 905 (2016).

[83] E. J. Hemingway and S. M. Fielding, Edge-induced shear banding in entangled polymeric fluids, Phys. Rev. Lett. **120**, 138002 (2018).

[84] A. Singh, R. Mari, M. M. Denn, and J. F. Morris, A constitutive model for simple shear of dense frictional suspensions, J. Rheol. **62**, 457 (2018).

[85] R. J. Larsen, J.-W. Kim, C. F. Zukoski, and D. A. Weitz, Fluctuations in flow produced by competition between apparent wall slip and dilatancy, Rheol. Acta **53**, 333 (2014).

[86] S.-i. Nagahiro, H. Nakanishi, and N. Mitarai, Experimental observation of shear thickening oscillation, EPL (Europhysics Letters) **104**, 28002 (2013).

[87] G. Bossis, P. Boustingorry, Y. Grasselli, A. Meunier, R. Morini, A. Zubarev, and O. Volkova, Discontinuous shear thickening in the presence of polymers adsorbed on the surface of calcium carbonate particles, Rheol. Acta **56**, 415 (2017).

[88] G. Bossis, Y. Grasselli, A. Meunier, and O. Volkova, Tunable discontinuous shear thickening with magnetorheological suspensions, J. Intell. Material Syst. Struct. , 1045389X17704915 (2017).

[89] D. Lootens, H. Van Damme, and P. Hébraud, Giant stress fluctuations at the jamming transition, Phys. Rev. Lett. **90**, 178301 (2003).

[90] V. Rathee, D. L. Blair, and J. S. Urbach, Localized stress fluctuations drive shear thickening in dense suspensions, Proc. Natl. Acad. Sci. U.S.A. **114**, 8740 (2017).

[91] B. Saint-Michel, T. Gibaud, and S. Manneville, Uncovering instabilities in the spatiotemporal dynamics of a shear-thickening cornstarch suspension, Phys. Rev. X **8**, 031006 (2018).

[92] R. N. Chacko, R. Mari, M. E. Cates, and S. M. Fielding, Dynamic vorticity banding in discontinuously shear thickening suspensions, Phys. Rev. Lett. **121**, 108003 (2018).

[93] M. E. Cates, J. P. Wittmer, J.-P. Bouchaud, and P. Claudin, Jamming, force chains, and fragile matter, Phys. Rev. Lett. **81**, 1841 (1998).

[94] H. Nakanishi, S.-i. Nagahiro, and N. Mitarai, Fluid dynamics of dilatant fluids, Phys. Rev. E **85**, 011401 (2012).

[95] I. R. Peters, S. Majumdar, and H. M. Jaeger, Direct observation of dynamic shear jamming in dense suspensions, Nature **532**, 214 (2016).

[96] E. Han, N. Van Ha, and H. M. Jaeger, Measuring the porosity and compressibility of liquid-suspended porous particles using ultrasound, Soft Matter **13**, 3506 (2017).

[97] R. N. Chacko, R. Mari, S. M. Fielding, and M. E. Cates, Shear reversal in dense suspensions: the challenge to fabric evolution models from simulation data, J. Fluid Mech. **847**, 700–734 (2018).

[98] J. Läuger and H. Stettin, Effects of instrument and fluid inertia in oscillatory shear in rotational rheometers, J. Rheol. **60**, 393 (2016).

[99] E. Scheinerman, *Invitation to Dynamical Systems* (Prentice Hall, 1996).

[100] L. Isa, R. Besseling, A. N. Morozov, and W. C. K. Poon, Velocity oscillations in microfluidic flows of concentrated colloidal suspensions, Phys. Rev. Lett. **102**, 058302 (2009).

[101] E. Jones, T. Oliphant, P. Peterson, *et al.*, SciPy: Open source scientific tools for Python (2001–).

[102] G. Bossis, O. Volkova, Y. Grasselli, and O. Gueye, Discontinuous shear thickening in concentrated suspensions, Philosophical Transactions of the Royal Society A: Mathematical, Physical and Engineering Sciences **377**, 20180211 (2019).

[103] R. Maharjan and E. Brown, Giant deviation of a relaxation time from generalized Newtonian theory in discontinuous shear thickening suspensions, Phys. Rev. Fluids **2**, 123301 (2017).

[104] L. Oyarte Gálvez, S. de Beer, D. van der Meer, and A. Pons, Dramatic effect of fluid chemistry on cornstarch suspensions: Linking particle interactions to macroscopic rheology, Phys. Rev. E **95**, 030602 (2017).

[105] M. Krupa and P. Szmolyan, Relaxation oscillation and canard explosion, J. Differ. Equ. **174**, 312 (2001).

[106] T. A. Strivens, The shear thickening effect in concentrated dispersion systems, J. Colloid Interface Sci. **57**, 476 (1976).

[107] Z. Pan, H. de Cagny, B. Weber, and D. Bonn, S-shaped flow curves of shear thickening suspensions: Direct observation of frictional rheology, Phys. Rev. E **92**, 032202 (2015).

[108] N. C. Crawford, S. K. R. Williams, D. Boldridge, and M. W. Liberatore, Shear thickening of chemical mechanical polishing slurries under high shear, Rheol. Acta **51**, 637 (2012).

[109] Y. S. Lee, E. D. Wetzel, and N. J. Wagner, The ballistic impact characteristics of kevlar® woven fabrics impregnated with a colloidal shear thickening fluid, J. Mater. Sci. **38**, 2825 (2003).

[110] N. M. James, E. Han, R. A. L. de la Cruz, J. Jureller, and H. M. Jaeger, Interparticle hydrogen bonding can elicit shear jamming in dense suspensions, Nat. Mater. **17**, 965 (2018).

[111] S. von Kann, J. H. Snoeijer, D. Lohse, and D. van der Meer, Nonmonotonic settling of a sphere in a cornstarch suspension, Phys. Rev. E **84**, 060401 (2011).

[112] P. Kanehl and H. Stark, Self-organized velocity pulses of dense colloidal suspensions in microchannel flow, Phys. Rev. Lett. **119**, 018002 (2017).

[113] S. Paul, Water-borne acrylic emulsion paints, Prog. Org. Coat. **5**, 79 (1977).

[114] E. Koos and N. Willenbacher, Capillary forces in suspension rheology, Science **331**, 897 (2011).

[115] R. G. Larson, *The Structure and Rheology of Complex Fluids*, Topics in Chemical Engineering (OUP USA, 1999).

[116] V. Gopalakrishnan and C. F. Zukoski, Effect of attractions on shear thickening in dense suspensions, J. Rheol. **48**, 1321 (2004).

[117] D. Bonn, M. M. Denn, L. Berthier, T. Divoux, and S. Manneville, Yield stress materials in soft condensed matter, Rev. Mod. Phys. **89**, 035005 (2017).

[118] A. Singh, S. Pednekar, J. Chun, M. M. Denn, and J. F. Morris, From yielding to shear jamming in a cohesive frictional suspension, Phys. Rev. Lett. **122**, 098004 (2019).

[119] L. C. Hsiao, S. Jamali, E. Glynos, P. F. Green, R. G. Larson, and M. J. Solomon, Rheological state diagrams for rough colloids in shear flow, Phys. Rev. Lett. **119**, 158001 (2017).

[120] C. Dominik and A. G. G. M. Tielens, Resistance to rolling in the adhesive contact of two elastic spheres, Philos. Mag. A **72**, 783 (1995).

[121] L.-O. Heim, J. Blum, M. Preuss, and H.-J. Butt, Adhesion and friction forces between spherical micrometer-sized particles, Phys. Rev. Lett. **83**, 3328 (1999).

[122] N. Estrada, A. Taboada, and F. Radjaï, Shear strength and force transmission in granular media with rolling resistance, Phys. Rev. E **78**, 021301 (2008).

[123] R. Mari and R. Seto, Force transmission and the order parameter of shear thickening, Soft Matter **15**, 6650 (2019).

[124] W. Liu, Y. Jin, S. Chen, H. A. Makse, and S. Li, Equation of state for random sphere packings with arbitrary adhesion and friction, Soft Matter **13**, 421 (2017).

[125] W. Liu, S. Li, A. Baule, and H. A. Makse, Adhesive loose packings of small dry particles, Soft Matter **11**, 6492 (2015).

[126] H. Vinutha and S. Sastry, Disentangling the role of structure and friction in shear jamming, Nat. Phys. **12**, 578 (2016).

[127] E. Brown, N. A. Forman, C. S. Orellana, H. Zhang, B. W. Maynor, D. E. Betts, J. M. DeSimone, and H. M. Jaeger, Generality of shear thickening in dense suspensions, Nat. Mater. **9**, 220 (2010).

[128] E. O. Afoakwa, A. Paterson, and M. Fowler, Factors influencing rheological and textural qualities in chocolate – a review, Trends Food Sci. Technol. **18**, 290 (2007).

[129] G. Ovarlez, F. Mahaut, S. Deboeuf, N. Lenoir, S. Hormozi, and X. Chateau, Flows of suspensions of particles in yield stress fluids, J. Rheol. **59**, 1449 (2015).

[130] K. N. Pham, G. Petekidis, D. Vlassopoulos, S. U. Egelhaaf, P. N. Pusey, and W. C. K. Poon, Yielding of colloidal glasses, Europhys. Lett. **75**, 624 (2006).

[131] Q. D. Nguyen, T. Akroyd, D. C. De Kee, and L. Zhu, Yield stress measurements in suspensions: an inter-laboratory study, Korea Aust. Rheol. J. **18**, 15 (2006).

[132] F. S. Merkt, R. D. Deegan, D. I. Goldman, E. C. Rericha, and H. L. Swinney, Persistent holes in a fluid, Phys. Rev. Lett. **92**, 184501 (2004).

[133] H. Freundlich and H. L. Röder, Dilatancy and its relation to thixotropy, Trans. Faraday Soc. **34**, 308 (1938).

[134] T. C. Halsey and J. E. Martin, Electrorheological fluids, Scientific American **269**, 58 (1993).

[135] J. Z. Q. Zhou, P. H. T. Uhlherr, and F. T. Luo, Yield stress and maximum packing fraction of concentrated suspensions, Rheol. Acta **34**, 544 (1995).

[136] T. Divoux, D. Tamarii, C. Barentin, and S. Manneville, Transient shear banding in a simple yield stress fluid, Phys. Rev. Lett. **104**, 208301 (2010).

[137] D. Z. Chen, H. Zheng, D. Wang, and R. P. Behringer, Discontinuous rate-stiffening in a granular composite modeled after cornstarch and water, Nat. Commun. **10**, 1283 (2019).

[138] R. Seto, A. Singh, B. Chakraborty, M. M. Denn, and J. F. Morris, Shear jamming and fragility in dense suspensions, Granul. Matter **21**, 82 (2019).

[139] S. Gallier, E. Lemaire, F. Peters, and L. Lobry, Percolation in suspensions and de Gennes conjectures, Phys. Rev. E **92**, 020301 (2015).

[140] S. Gallier, *Numerical simulation of frictional suspensions. Application to solid propellants*, Ph.D. thesis, Université Nice Sophia Antipolis (2014).

[141] H. Tsurusawa, M. Leocmach, J. Russo, and H. Tanaka, Direct link between mechanical stability in gels and percolation of isostatic particles, Sci. Adv. **5**, eaav6090 (2019).

[142] F. Gadala-Maria and A. Acrivos, Shear-induced structure in a concentrated suspension of solid spheres, J. Rheol. **24**, 799 (1980).

[143] L. Corte, P. M. Chaikin, J. P. Gollub, and D. J. Pine, Random organization in periodically driven systems, Nat. Phys. **4**, 420 (2008).

[144] E. Moghimi, A. R. Jacob, N. Koumakis, and G. Petekidis, Colloidal gels tuned by oscillatory shear, Soft Matter **13**, 2371 (2017).

[145] J. Baker and A. Kudrolli, Maximum and minimum stable random packings of Platonic solids, Phys. Rev. E **82**, 061304 (2010).

[146] G. J. Donley, W. W. Hyde, S. A. Rogers, and F. Nettesheim, Yielding and recovery of conductive pastes for screen printing, Rheol. Acta **58**, 361 (2019).

[147] M. Yang, L. E. Scriven, and C. W. Macosko, Some rheological measurements on magnetic iron oxide suspensions in silicone oil, J. Rheol. **30**, 1015 (1986).

[148] H. J. Walls, S. B. Caines, A. M. Sanchez, and S. A. Khan, Yield stress and wall slip phenomena in colloidal silica gels, J. Rheol. **47**, 847 (2003).

[149] R. N. Zia, B. J. Landrum, and W. B. Russel, A micro-mechanical study of coarsening and rheology of colloidal gels: Cage building, cage hopping, and Smoluchowski's ratchet, J. Rheol. **58**, 1121 (2014).

[150] C. Ness, Z. Xing, and E. Eiser, Oscillatory rheology of dense, athermal suspensions of nearly hard spheres below the jamming point, Soft Matter **13**, 3664 (2017).

[151] A. Ahuja and C. Gamonpilas, Dual yielding in capillary suspensions, Rheol. Acta **56**, 801 (2017).

[152] N. Y. Lin, C. Ness, M. E. Cates, J. Sun, and I. Cohen, Tunable shear thickening in suspensions, Proc. Natl. Acad. Sci. U.S.A. **113**, 10774 (2016).

[153] C. Ness, R. Mari, and M. E. Cates, Shaken and stirred: Random organization reduces viscosity and dissipation in granular suspensions, Sci. Adv. **4**, eaar3296 (2018).

[154] J. A. Koch, D. I. Castaneda, R. H. Ewoldt, and D. A. Lange, Vibration of fresh concrete understood through the paradigm of granular physics, Cem. Conc. Res. **115**, 31 (2019).

[155] British Calcium Carbonates Federation, Calcium Carbonate – modern day uses of GCC (2019), accessed 2019-08-15.

[156] *eskal 500 datasheet*, KSL Staubtechnik GmbH (2007).

[157] V. Rathee, S. Arora, D. L. Blair, J. S. Urbach, A. K. Sood, and R. Ganapathy, Unraveling the role of frictional contacts and particle orientational order during shear-thickening in suspensions of colloidal rods (2019), arXiv:1906.06356 .

[158] Glycerine Producers Association and others, *Physical properties of glycerine and its solutions* (Glycerine Producers' Association, 1963).

[159] T. Liberto, M. Le Merrer, C. Barentin, M. Bellotto, and J. Colombani, Elasticity and yielding of a calcite paste: Scaling laws in a dense colloidal suspension, Soft Matter **13**, 2014 (2017).

[160] F. Mahaut, X. Chateau, P. Coussot, and G. Ovarlez, Yield stress and elastic modulus of suspensions of noncolloidal particles in yield stress fluids, J. Rheol. **52**, 287 (2008).

[161] B. M. Guy, C. Ness, M. Hermes, L. J. Sawiak, J. Sun, and W. C. K. Poon, Testing the Wyart–Cates model for non-Brownian shear thickening using bidisperse suspensions, Soft Matter **16**, 229 (2020).

[162] M. Trulsson, Rheology and shear jamming of frictional ellipses, J. Fluid Mech. **849**, 718–740 (2018).

[163] A. Donev, I. Cisse, D. Sachs, E. A. Variano, F. H. Stillinger, R. Connelly, S. Torquato, and P. M. Chaikin, Improving the density of jammed disordered packings using ellipsoids, Science **303**, 990 (2004).

[164] A. Guy, Coatings components beyond binders, in *The Chemistry and Physics of Coatings (2)*, Vol. 1, edited by A. Marrion (The Royal Society of Chemistry, 2004) pp. 267–316.

[165] D. Reith, B. Müller, F. Müller-Plathe, and S. Wiegand, How does the chain extension of poly (acrylic acid) scale in aqueous solution? A combined study with light scattering and computer simulation, J. Chem. Phys. **116**, 9100 (2002).

[166] D. J. Sparks, M. E. Romero-González, E. El-Taboni, C. L. Freeman, S. A. Hall, G. Kakonyi, L. Swanson, S. A. Banwart, and J. H. Harding, Adsorption of poly acrylic acid onto the surface of calcite: an experimental and simulation study, Phys. Chem. Chem. Phys. **17**, 27357 (2015).

[167] R. Eriksson, J. Merta, and J. B. Rosenholm, The calcite/water interface: I. Surface charge in indifferent electrolyte media and the influence of low-molecular-weight polyelectrolyte, J. Colloid Interface Sci. **313**, 184 (2007).

[168] S. Dhar, S. Chattopadhyay, and S. Majumdar, Signature of jamming under steady shear in dense particulate suspensions, J. Phys. Condens. Matter **32**, 124002 (2019).

[169] R. G. Egres and N. J. Wagner, The rheology and microstructure of acicular precipitated calcium carbonate colloidal suspensions through the shear thickening transition, J. Rheol. **49**, 719 (2005).

[170] T. F. Tadros, Disperse systems in pesticidal formulations, Adv. Colloid Interface Sci. **32**, 205 (1990).

[171] R. Flatt, Y. Houst, P. Bowen, H. Hofmann, J. Widmer, U. Sulser, *et al.*, Electrosteric repulsion induced by superplasticizers between cement particles-an overlooked mechanism?, ACI Special Publications **195**, 29 (2000).

[172] S. Lee and N. D. Spencer, Sweet, hairy, soft, and slippery, Science **319**, 575 (2008).

[173] A. Vázquez-Quesada, R. I. Tanner, and M. Ellero, Shear thinning of noncolloidal suspensions, Phys. Rev. Lett. **117**, 108001 (2016).

[174] J. Brady, A hydrodynamic mechanism for discontinuous shear thickening (2018).

[175] S. Luding, Contact models for very loose granular materials, in *IUTAM Symposium on Multiscale Problems in Multibody System Contacts* (Springer, 2007) pp. 135–150.

[176] F. A. Gilabert, J.-N. Roux, and A. Castellanos, Computer simulation of model cohesive powders: Influence of assembling procedure and contact laws on low consolidation states, Phys. Rev. E **75**, 011303 (2007).

[177] F. A. Gilabert, J.-N. Roux, and A. Castellanos, Computer simulation of model cohesive powders: Plastic consolidation, structural changes, and elasticity under isotropic loads, Phys. Rev. E **78**, 031305 (2008).

[178] C. Gamonpilas, J. F. Morris, and M. M. Denn, Shear and normal stress measurements in non-Brownian monodisperse and bidisperse suspensions, J. Rheol. **60**, 289 (2016).

[179] I. E. Zarraga, D. A. Hill, and D. T. Leighton, The characterization of the total stress of concentrated suspensions of noncolloidal spheres in Newtonian fluids, J. Rheol. **44**, 185 (2000).

[180] G. Chatté, J. Comtet, A. Niguès, L. Bocquet, A. Siria, G. Ducouret, F. Lequeux, N. Lenoir, G. Ovarlez, and A. Colin, Shear thinning in non-Brownian suspensions, Soft Matter **14**, 879 (2018).

[181] D. P. Kalman, B. A. Rosen, and N. J. Wagner, Effects of particle hardness on shear thickening colloidal suspension rheology, AIP Conf. Proc. **1027**, 1408 (2008).

[182] D. J. M. Hodgson, M. Hermes, E. Blanco, and W. C. K. Poon, Granulation and suspension rheology: a unified treatment (2019), arXiv:1907.10980 .

[183] S. R. Raghavan and S. A. Khan, Shear-thickening response of fumed silica suspensions under steady and oscillatory shear, J. Colloid Interface Sci. **185**, 57 (1997).

[184] L. Heymann, S. Peukert, and N. Aksel, On the solid-liquid transition of concentrated suspensions in transient shear flow, Rheol. Acta **41**, 307 (2002).

[185] A. Rohatgi, Webplotdigitizer (2008).

[186] R. I. Tanner, Aspects of non-colloidal suspension rheology, Phys. Fluids **30**, 101301 (2018).

[187] J. Y. Moon, S. Dai, L. Chang, J. S. Lee, and R. I. Tanner, The effect of sphere roughness on the rheology of concentrated suspensions, J. Non-Newton. Fluid **223**, 233 (2015).

[188] S.-C. Dai, E. Bertevas, F. Qi, and R. I. Tanner, Viscometric functions for noncolloidal sphere suspensions with Newtonian matrices, J. Rheol. **57**, 493 (2013).

[189] J. Yerushalmi, S. Katz, and R. Shinnar, The stability of steady shear flows of some viscoelastic fluids, Chem. Eng. Sci. **25**, 1891 (1970).

[190] K. L. Johnson and K. L. Johnson, *Contact mechanics* (Cambridge University Press, 1987).

[191] J. P. Pantina and E. M. Furst, Elasticity and critical bending moment of model colloidal aggregates, Phys. Rev. Lett. **94**, 138301 (2005).

[192] N. Estrada, E. Azéma, F. Radjai, and A. Taboada, Identification of rolling resistance as a shape parameter in sheared granular media, Phys. Rev. E **84**, 011306 (2011).

[193] S. Krijt, C. Dominik, and A. Tielens, Rolling friction of adhesive microspheres, J. Phys. D Appl. Phys. **47**, 175302 (2014).

[194] D. J. Koeze and B. P. Tighe, Sticky matters: Jamming and rigid cluster statistics with attractive particle interactions, Phys. Rev. Lett. **121**, 188002 (2018).

[195] W. Zheng, H. Liu, and N. Xu, Shear-induced solidification of athermal systems with weak attraction, Phys. Rev. E **94**, 062608 (2016).

[196] M. Badetti, A. Fall, F. Chevoir, and J.-N. Roux, Shear strength of wet granular materials: Macroscopic cohesion and effective stress, Eur. Phys. J. E **41**, 68 (2018).

[197] E. Han, N. M. James, and H. M. Jaeger, Stress controlled rheology of dense suspensions using transient flows, Phys. Rev. Lett. **123**, 248002 (2019).

[198] V. Rathee, D. L. Blair, and J. S. Urbach, Localized transient jamming in discontinuous shear thickening (2019), arXiv:1908.02856 .

[199] V. Schmitt, C. M. Marques, and F. Lequeux, Shear-induced phase separation of complex fluids: The role of flow-concentration coupling, Phys. Rev. E **52**, 4009 (1995).

[200] R. Besseling, L. Isa, P. Ballesta, G. Petekidis, M. E. Cates, and W. C. K. Poon, Shear banding and flow-concentration coupling in colloidal glasses, Phys. Rev. Lett. **105**, 268301 (2010).

[201] R. G. Larson and Y. Wei, A review of thixotropy and its rheological modeling, J. Rheol. **63**, 477 (2019).

[202] O. Cheal and C. Ness, Rheology of dense granular suspensions under extensional flow, J. Rheol. **62**, 501 (2018).

[203] J. E. Thomas, K. Ramola, A. Singh, R. Mari, J. F. Morris, and B. Chakraborty, Microscopic origin of frictional rheology in dense suspensions: Correlations in force space, Phys. Rev. Lett. **121**, 128002 (2018).

[204] C. Voivret, F. Radjaï, J.-Y. Delenne, and M. S. El Youssoufi, Multiscale force networks in highly polydisperse granular media, Phys. Rev. Lett. **102**, 178001 (2009).

[205] G. Ovarlez, S. Rodts, X. Chateau, and P. Coussot, Phenomenology and physical origin of shear localization and shear banding in complex fluids, Rheol. Acta **48**, 831 (2009).

[206] P. Coussot, Yield stress fluid flows: A review of experimental data, J. Non-Newton. Fluid **211**, 31 (2014).